UNIVERSITAT DE BARCELONA

The Petrogenesis of the ophiolitic mélange of Central Cuba: origin and evolution of oceanic litosphere from abyssal to subduction and suprasubduction zone settings

Lidia Butjosa Molines

ADVERTIMENT. La consulta d'aquesta tesi queda condicionada a l'acceptació de les següents condicions d'ús: La difusió d'aquesta tesi per mitjà del servei TDX (**www.tdx.cat**) i a través del Dipòsit Digital de la UB (**diposit.ub.edu**) ha estat autoritzada pels titulars dels drets de propietat intel·lectual únicament per a usos privats emmarcats en activitats d'investigació i docència. No s'autoritza la seva reproducció amb finalitats de lucre ni la seva difusió i posada a disposició des d'un lloc aliè al servei TDX ni al Dipòsit Digital de la UB. No s'autoritza la presentació del seu contingut en una finestra o marc aliè a TDX o al Dipòsit Digital de la UB (framing). Aquesta reserva de drets afecta tant al resum de presentació de la tesi com als seus continguts. En la utilització o cita de parts de la tesi és obligat indicar el nom de la persona autora.

ADVERTENCIA. La consulta de esta tesis queda condicionada a la aceptación de las siguientes condiciones de uso: La difusión de esta tesis por medio del servicio TDR (**www.tdx.cat**) y a través del Repositorio Digital de la UB (**diposit.ub.edu**) ha sido autorizada por los titulares de los derechos de propiedad intelectual únicamente para usos privados enmarcados en actividades de investigación y docencia. No se autoriza su reproducción con finalidades de lucro ni su difusión y puesta a disposición desde un sitio ajeno al servicio TDR o al Repositorio Digital de la UB. No se autoriza la presentación de su contenido en una ventana o marco ajeno a TDR o al Repositorio Digital de la UB (framing). Esta reserva de derechos afecta tanto al resumen de presentación de la tesis como a sus contenidos. En la utilización o cita de partes de la tesis es obligado indicar el nombre de la persona autora.

WARNING. On having consulted this thesis you're accepting the following use conditions: Spreading this thesis by the TDX (**www.tdx.cat**) service and by the UB Digital Repository (**diposit.ub.edu**) has been authorized by the titular of the intellectual property rights only for private uses placed in investigation and teaching activities. Reproduction with lucrative aims is not authorized nor its spreading and availability from a site foreign to the TDX service or to the UB Digital Repository. Introducing its content in a window or frame foreign to the TDX service or to the UB Digital Repository is not authorized (framing). Those rights affect to the presentation summary of the thesis as well as to its contents. In the using or citation of parts of the thesis it's obliged to indicate the name of the author.

The Petrogenesis of the ophiolitic mélange of Central Cuba:

Origin and evolution of oceanic lithosphere from abyssal to subduction and suprasubduction zone settings

PhD Thesis

Lidia Butjosa Molines

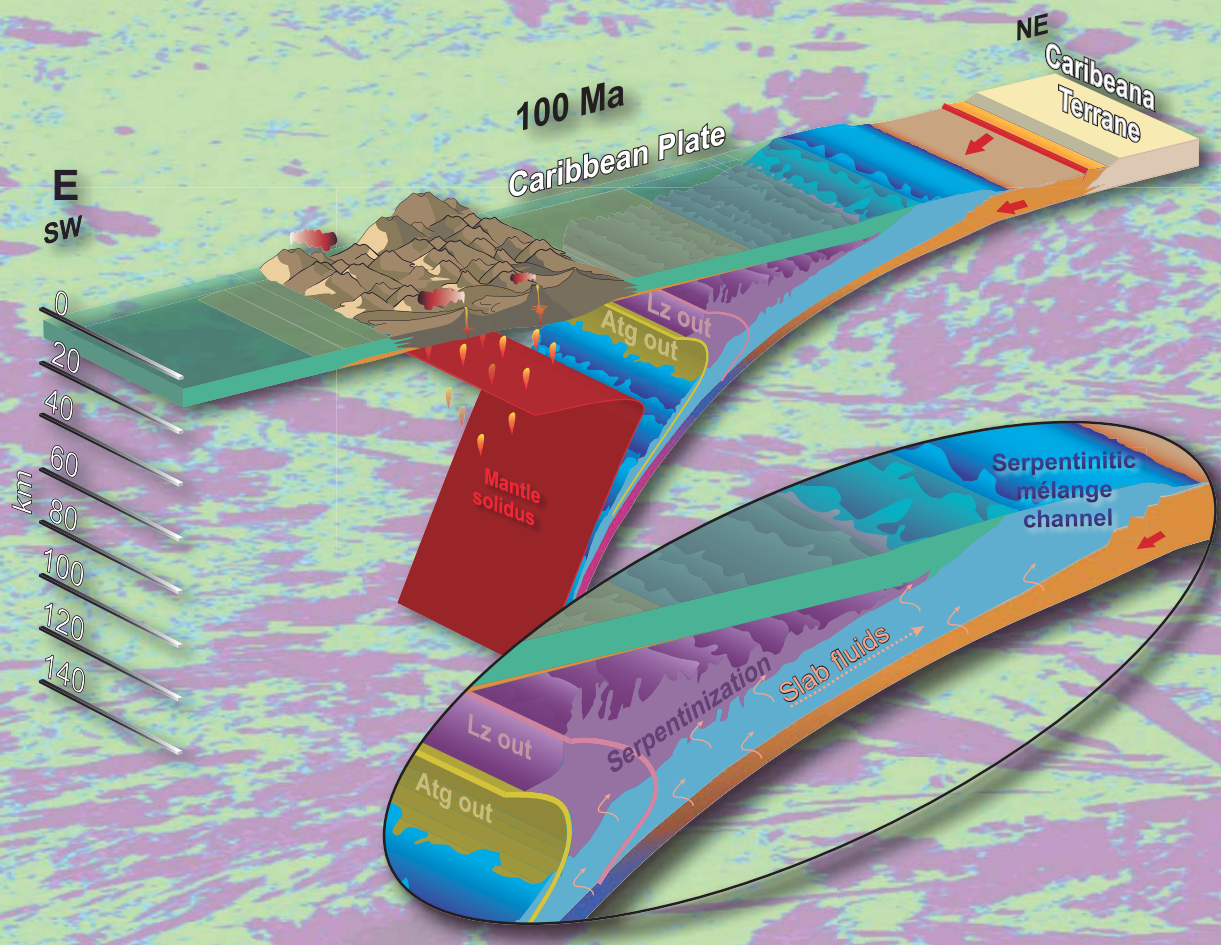

January 2018

UNIVERSITAT DE BARCELONA

B:KC Barcelona Knowledge Campus
Campus d'Excel·lència Internacional

UNIVERSITAT DE BARCELONA
B:KC Barcelona Knowledge Campus
Campus d'Excel·lència Internacional

The Petrogenesis of the ophiolitic mélange of Central Cuba: Origin and evolution of oceanic lithosphere from abyssal to subduction and suprasubduction zone settings

Lidia Butjosa Molines

ADVERTIMENT

La consulta d'aquesta tesi queda condicionada a l'acceptació de les següents condicions d'ús: La difusió d'aquesta tesi per mitjà del servei TDX (www.tesisenxarxa.net) ha estat autoritzada pels titulars dels drets de propietat intel·lectual únicament per a usos privats emmarcats en activitats d'investigació i docència. No s'autoritza la seva reproducció amb finalitats de lucre ni la seva difusió i posada a disposició des d'un lloc aliè al servei TDX. No s'autoritza la presentació del seu contingut en una finestra o marc aliè a TDX (framing). Aquesta reserva de drets afecta tant al resum de presentació de la tesi com als seus continguts. En la utilització o cita de parts de la tesi és obligat indicar el nom de la persona autora.

ADVERTENCIA

La consulta de esta tesis queda condicionada a la aceptación de las siguientes condiciones de uso: La difusión de esta tesis por medio del servicio TDR (www.tesisenred.net) ha sido autorizada por los titulares de los derechos de propiedad intelectual únicamente para usos privados enmarcados en actividades de investigacióny docencia. No se autoriza su reproducción con finalidades de lucro ni su difusión y puesta a disposición desde un sitio ajeno al servicio TDR. No se autoriza la presentación de su contenido en una ventana o marco ajeno a TDR (framing). Esta reserva de derechos afecta tanto al resumen de presentación de la tesis como a sus contenidos. En la utilización o cita de partes de la tesis es obligado indicar el nombre de la persona autora.

WARNING

On having consulted this thesis you're accepting the following use conditions: Spreading this thesis by the TDX (www.tesisenxarxa.net) service has been authorized by the titular of the intellectual property rights only for private uses placed in investigation and teaching activities. Reproduction with lucrative aims is not authorized neither its spreading and availability from a site foreign to the TDX service. Introducing its content in a window or frame foreign to the TDX service is not authorized (framing). This rights affect to the presentation summary of the thesis as well as to its contents. In the using or citation of parts of the thesis it's obliged to indicate the name of the author.

UNIVERSITAT DE BARCELONA

Universitat de Barcelona

Departament de Mineralogia, Petrologia i Geologia Aplicada

Facultat de Ciències de la Terra

The Petrogenesis of the ophiolitic mélange of Central Cuba: Origin and evolution of oceanic lithosphere from abyssal to subduction and suprasubduction zone settings

Tesi doctoral presentada per

Lidia Butjosa Molines

Memòria presentada per optar al títol de doctora per la Universitat de Barcelona

amb Menció Internacional

Tesi realitzada dins del Programa de Doctorat de Ciències de la Terra de la Universitat de Barcelona, sota la direcció del Dr. Antonio García Casco i el Dr. Joaquín A. Proenza Fernández

La Doctoranda — Els Directors

Lidia Butjosa Molines **Antonio García Casco** **Joaquín A. Proenza Fernández**

Barcelona, gener de 2018

Aquesta tesi ha estat financiada pels projectes CGL2012-36263 (Ministerio de Economía y Competitividad) i CGL2015-65824 (plan Nacional I+D+i). El grup d' Investigació de Recursos Minerals: Jaciments, Aplicacions, Sostenibilitat (2014 SGR 1661). La Universitat de Granada ha cofinançat els anàlisis realitzats en aquesta tesi. La doctoranda ha disfrutat la beca del programa de Formación del Personal Investigador (FPI; BES-2013-063205) del Ministerio de Economía y Competitividad. S'han pogut realizar estades nacionals i internacionals gràcies al finançament de la beca de la Fundació Universitària Agustí Pedro Pons, beques de suport per a la mobilitat de Joves investigadors de la facultat de Ciències de la Terra (Modalitat FR- UB) i les dues ajudes a la movilidad predoctoral para la realización de estancias breves en centros de I+D españoles y extranjeros (EEBB-I-15-09573 y EEBB-I-16-10837) del Ministerio de Economía y Competitividad.

A la família i amics

“La vida és un Tango, hay que saber bailarlo y balancearlo”

Lidia Jubany

Agraïments

La veritat que podria semblar fàcil escriure quatre línies per agrair a tots aquells que han format part del camí. Però és difícil expressar amb paraules tots els sentiments, moments i anècdotes que he viscut amb tots vosaltres durant aquests 4 anys, tot i així ho intentaré ^.^

Primer vull agrair als meus directors de tesi Joaquín A. Proenza (Joa) i Antonio García Casco l'oportunitat que m'han donat per poder desenvolupar aquest treball d'investigació, també per la seva amistat i confiança que m'heu donat al llarg de la tesi. Moltes gràcies Joa per introduir-me en el món de les roques ultramàfiques, contribuir al esperit crític de l' investigació i donar-me la possibilitat de formar part d'aquest grup d'investigació "CALOR". Muchas gracias Antonio por la paciencia, las discusiones petrológicas, los momentos de picar en tu despacho y decir: "se puede?" y siempre estar disponible. Siempre quedará el momento café, dónde solucionamos el mundo y salen las mejores ideas. Gracias por la acogida en Granada, que he hecho de ella mi segunda casa. También por los buenos momentos pasados en la facultad y fuera de ella.

Aquesta tesi no es podria haver realitzat sense el suport del Departament de Mineralogia, Petrologia y Geologia Aplicada de la Universitat de Barcelona. Gràcies a tot l'equip de secretaria i al director Albert Soler Gil. També al Centre Científic i Tecnològic de la Universitat de Barcelona d'on forma part Eva Prats (SEM), Tariq Jawhari (raman) i en especial al Xavier Llovet (Microsonda) que sempre està disposat a reptes nous. Al servei de làmina prima: Dolors Barso, Montse Sibila, Fadoua Zoura i Vicenç Planella. Agrair a tots els companys que hem compartit despatx, moments d'estrès i riures: Sandra (sempre amb un somriure), Amaia (a punt per l'aventura), Jingyao (amb el rebost a punt). No em puc deixar a Cristina Vilanova, Marc Campeny, Lisard Torró, Montgarri i les últimes en arribar Núria i Júlia. Agrair al Thomas Ailgsperger les converses enriquidores que hem compartit en tots els viatges!

Vull agrair també al Pere Enrique per descobrir-me el món de la petrologia ígnea i fer-me aquelles preguntes que fan pensar i ser crític amb un mateix. A la Gumer Galán per tots els consells i ensenyar-me a ser metòdica.

Cómo no agradecer al Departamento de Mineralogía y Petrología de la Universidad de Granada, que ha puesto todas las facilidades durante mis estancias en Granada (Nicolás Velilla director y Inés secretaria). Gracias por los momentos del café: Aitor, Juan Antonio Moreno, Concha, Lozano, Claudio, Vicente, Idael, Jose María, Encarni, Patricia y Antonio Sanchez Navas. Agradecer a los que siempre están disponibles para resolver dudas José Francisco Molina, Pilar Montero y Olga Cazalla (ICP CIC-UGR) siempre preparada para analizar muestras complicadas.

Os pensabais que me iba a dejar a la familia Granaina: Juanito, Concha, Faouziya, Aitor, Thaís, Thales, Carol, Antonio, Belén, Nacho y Luís. Juanito gracias por hacerme sentir como en casa. Concha siempre con un: “buenos días, café?”. Faouziya, gracias por hacerme reír y haber compartido tan buenos momentos. Aitor, amigo que te puedo decir… gracias por toda la ayuda, la paciencia, los momentos de diversión, las paellas Murcianas, las discusiones enriquecedoras y por enseñarme a ser eficiente y paciente. Ya sabes que aún tengo que saldar mi deuda … XD! Thaís, amiga gracias por formar parte de mi camino y ser tan generosa, la mejor consejera que puedo tener! Thales gracias por los momentos de desconexión. No pueden faltar las acuario Belén y Carol gracias por ser auténticas! Nacho y Luís gracias por abrirme vuestra casa, sois la alegría de la casa.

A mis compañeras de Piso que tan buenos momentos hemos compartido en el balcón de Pedro Antonio. Stefania, Ana, Vicky, Jose, Francesca y en especial a Anna (la pequeña de la casa) que siempre pregunta “Que hacemos hoy de comer?”, gracias por hacerme reír, cuidarme tanto y por nuestras conversaciones de después de cenar.

Ringrazio le persone del CNR di Pisa, in particolare quelli del laboratorio del TIMS. La vostra accoglienza ed ospitalità mi ha permesso di sentirmi come a casa mia: Samuele, Paolo Mercury (XD), Noemi, Mattia, Chiara y Maddalena.

Gràcies als companys i amics que sempre han estat al costat quan els he necessitat. Ja sigui donant una volta a Gallecs, fent randoris, anant d’excursió a la muntanya o simplement trobar-nos per fer una bona calçotada. Gràcies a la família del Judo al complet, també a Sunna, Enrique, Itxi, Romén, Luz, David, Sergi, Diana, Clara (i les nostres converses d’Skype), Carmen, Olga, Alba i Marta. Diana gràcies per la hora catàrtica del dinar. Gràcies a la tesi he pogut conèixer gent fantàstica com Manuel Menzel, Irene Novo, Anfisa i Alice.

Ja per acabar no em podia oblidar de “Danieladas Varies” i tots els seus membres que cada matí em feu posar un somriure. Gràcies als avis (Angeleta, Josep i Lídia) i a la Família Butjosa-Molines. En especial als pares (Bartomeu i Lídia) per confiar en les meves decisions, fent una carrera de geologia (que no coneixien) i després amb la tesi. La il·lusió, la constància i amor l’he tret de vosaltres i per això us dono les gràcies. A la meva germana sempre disponible per escoltar i amb la maleta a punt per anar les dues a qualsevol lloc. Saps que aquest viatge l’hem fet juntes! També vull recordar-me d’aquells que si avui estiguessin aquí (avi Pascual i tiet Siscu), estarien orgullosos del que per ells era una afició, la seva neta i neboda ho ha convertit en la seva passió que es la geologia.

Això va per a tots vosaltres Companys, Amics i Família!

Contents

Resum 18

Abstract 20

1. Introduction 25

1.1. Objectives 28

2. The geologic evolution of the Caribbean Realm 31

2.1 Summary of Cuban Geology 32

2.1.1. The Geology of Central Cuba 34

2.1.1.1. The Villa Clara Serpentinitic Mélange (VCSM) 36

3. Sample and Methods 41

3.1. Sample preparation 41

3.2. Micro-Raman spectroscopy 42

3.3. Electron Micro Probe Analysis (EMPA) 42

3.4. X-ray Fluorescence (XRF) 43

3.5. Inductively Coupled Plasma Mass Spectrometry (ICP-MS) 43

3.6. Thermal Ionitzation Mass Spectrometry (TIMS) 43

3.7. Condensation of compositional space 45

3.8. Pseudosection modelling 45

3.9. Melting modelling 46

3.10. Isotopic modelling 47

4. The serpentinitic matrix of Villa Clara serpentinitic mélange **53**

4.1. Field relations 53

4.2. Petrography 55

4.3. Mineral chemistry 59

4.3.1. Spinel group minerals 59

4.3.2. Olivine 61

4.3.3. Pyroxenes 63

4.3.4. Serpentine group minerals 67

4.3.5. Chlorite 70

4.4. Whole-rock composition 71

4.4.1. Major elements 71

4.4.2. Trace elements 77

4.4.3. Platinum-group elements 79

4.4.4. Nd-Sr-Pb-B isotope systematics 79

4.5. Discussion of serpentinitic matrix of VCSM 81

4.5.1. Enrichment processes in the serpentinitic matrix of VCSM 81

4.5.2. Role of serpentinization and fluid reservoirs in a subduction context 83

4.5.3. Geochemical fingerprints of mantle source and partial melting processes 87

5. The mafic crust of the Villa Clara serpentinitic mélange **95**

5.1. Field relations 95

5.2. Sub-volcanic unit: diabase and microgabbro 98

5.2.1. Petrography 98

5.2.2. Mineral chemistry 100

5.2.2.1. Minerals of magmatic assemblage 100

5.2.2.2. Minerals of the metamorphic assemblage 105

5.2.3. Whole-rock chemistry 111

5.2.3.1. Major elements 111

5.2.3.2. Trace elements 117

5.2.3.3. Nd-Sr isotope systematics 118

5.3. Plutonic unit: layered gabbros and ol-gabbros 119

5.3.1. Petrography 119

5.3.2 Mineral chemistry 120

5.3.2.1. Minerals of the magmatic assemblage 120

5.3.2.2. Minerals of the metamorphic assemblage 125

5.3.3. Whole-rock chemistry 132

5.2.3.1. Major elements 132

5.2.3.2. Trace elements 134

5.2.3.4. Nd-Sr isotope systematics 135

5.4 Discussion of mafic crust of the VCSM 136

5.4.1. Sub-volcanic unit of the VCSM 136

5.4.1.1. Element behaviour and metamorphism of the sub-volcanic unit 136

5.4.1.2. Petrogenesis of sub-volcanic unit of the VCSM 138

5.4.1.3. Melting modelling of sub-volcanic unit of the VCSM 141

and their link with peridotites of VCSM

5.4.1.4. Correlations of sub-volcanic unit of the VCSM 144

with other crustal sections of the Caribbean.

5.4.2. Plutonic unit of the VCSM 146

6. An exotic ultramafic block in the Villa Clara serpentintic mélange 151
6.1. Field relations 151
6.2. Petrography 153
6.3. Mineral chemistry 155
6.4. Whole-rock chemistry 166
6.4.1. Major elements 166
6.4.2. Trace elements and Nd-Sr isotope systematics 169
6.5. P-T Conditions 172
6.6. Discussion of exotic ultramafic block of the VCSM 174
6.6.1. Nature of the dolomite-bearing Atg-serpentinite and Atg-serpentinite protolith 174
6.6.2. Origin of the serpentinizing- and vein-forming fluid 175
6.6.3. Blackwall formation model 177
6.6.4. Exchange of matter 180
7. General discussion 185
7.1. Petrogenesis of serpentinitic matrix and mafic crust rocks of the VCSM 185
7.2. Ocean-floor metamorphism and supra-subduction zone metasomatism in VCSM 189
7.3. Geodynamic setting evolution of VCSM: from fracture zone to subduction zone setting 192
8. Conclusions 201
9. References 205

Resum/Abstract

Resum

Aquesta tesi doctoral tracta sobre la matriu serpentinítica, escorça màfica i els blocs exòtics ultramàfics de la mélange serpentinítica de Villa Clara situada a Cuba Central. El propòsit és avaluar l'evolució de la litosfera oceànica. Cadascuna d'aquestes unitats proporciona informació sobre la composició original del mantell, l'origen de la escorça oceànica i la seva relació amb el mantell, el metamorfisme de fons oceànic, el metasomatisme i el flux de fluids en la zona de subducció.

L'estudi de la matriu serpentinítica ha permès l' identificació de dos protòlits de peridotita. El grup A, amb composicions fèrtils (alt Al_2O_3 i baix Cr# en piroxens i espinela, així com un enriquiment dels elements de les terres rares pesades) i el grup B, que mostra composicions refractàries (baix Al_2O_3 i alt Cr# en piroxens i espinela, així com un empobriment en els elements de les terres rares mitjanes i pesades). El grup A es pot relacionar amb peridotites abissals/ zona de fractura, mentre que el grup B té composicions típiques d'avantarc. Els models de fusió mostren que el grup A és el resultat de la fusió a graus de fusió baixos (*c.* 4-8%), mentre que el grup B pot arribar fins a *c.* 14-22% de fusió després d'una fusió en dos passos, la primera a partir d'un mantell empobrit i la segona per una fusió d'un protòlit similar a les roques del grup A.

L'escorça màfica aquí estudiada inclou roques d'origen subvolcànic (diabasa i microgabre) i plutònic (acumulats de gabre i gabre olivínic). La unitat subvolcànica mostra que hi ha dos tipus de magma màfic; grup 1 mostra una signatura típica de basalts d'avantarc (FAB; baix ràtio Ti/V) i el grup 2 amb una composició de toleïtes d'arc d'illes (IAT; ràtio intermèdia Ti/V), ambdós amb anomalia positiva de Th i negativa de Nb en comparació a composicions N-MORB. Aquestes composicions a més de la composició isotòpica de la unitat plutònica (baix $^{143}Nd/^{144}Nd$ i $^{87}Sr/^{86}Sr$) indica la presència d'un component subductiu. Hi ha evidències geoquímiques que recolzen una relació genètica entre els protòlits de la matriu serpentinítica i la unitat subvolcànica de l'escorça màfica. Una evidència indirecta és l'enriquiment de terres rares lleugeres en les peridotites del grup B. Aquest enriquiment s'interpreta com a resultat de la reequilibració de fosos basàltics que percolen en el mantell, aquests podrien estar representats per la unitat subvolcànica de l'escorça màfica. També els models de fusió dels fosos primitius de la escorça màfica (grup 1- FAB) prediuen el *c.* 8-10 % de fusió d'un mantell abissal, com el de les peridotites tipus A que produeix un residu equivalent al de les peridotites tipus B.

D'altra banda, el metamorfisme de fons oceànic afecta a l'escorça màfica, que mostra associacions minerals típiques de fàcies d'esquistos verds i amfibolites. Això permet establir una pressió baixa i una temperatura baixa a intermèdia típica de condicions someres. Aquest procés té un impacte directe en la concentració dels elements mòbils. Diferents processos metasomàtics/enriquiment es veuen registrats en la geoquímica dels elements traça i els isòtops estables i radiogènics (B, Nd, Sr i Pb) de la matriu serpentinítica. Les relacions isotòpiques apunten a la presència de fluids provinents de la desvolatilització de la placa subduent on es forma l'agent metasomatizador. Aquests fluids estan compostos per diferents proporcions de fluids

provinents de l'escorça oceànica alterada, sediments subduïts i sediments terrígens. La combinació d'aquests tres reservoris isotòpics amb un mantell ja hidratat en el fons oceànic, reprodueix la signatura isotòpica de la matriu serpentinítica de la mélange serpentinítica de Villa Clara. Aquest resultat està en consonància amb l'evidència proveïda pels blocs exòtics ultramàfics d'alta pressió de la mélange serpentinítica de Villa Clara. Ja que aquests mostren composicions isotòpiques similars indicant la interacció amb un fluid similar en un context de subducció.

Les característiques petrològiques i geoquímiques dels blocs exòtics ultramàfics permeten distingir dos tipus de serpentinites: i) antigoritita i ii) antigoritita amb dolomita. Ambdues representen peridotites subduïdes que deriven d'un protòlit localment enriquit en CaO com a resultat de l' infiltració d'una mescla de fluids amb H_2O-CO_2. L'infiltració de fluids en el canal de subducció és el detonant per la serpentinització/carbonatació i formació de dominis de reemplaçament i venes de tremolita en la antigoritita. El zonat mineralògic i químic observat en els dominis de reemplaçament (domini de Atg + Chl + Tr en direcció a la antigoritita i el domini Chl + Tr en direcció a la vena) confirmen els canvis metasomàtics de la composició del fluid durant l'interacció fluid-roca. Les diferències de composició química entre els dominis i la antigoritita mostren que el fluid que s'infiltra estava enriquit en Ca, Al, elements litòfils de gran radi iònic i terres rares lleugeres. La modelització de la pseudosecció realitzada en el domini Atg + Chl + Tr indica que la seva formació va tenir lloc a *c.* 450ºC i *c.* 10kbar.

Tots aquests resultats permeten constrènyer l'evolució geodinàmica de la mélange serpentinítica en el context de la regió del Carib. La matriu serpentinítica demostra la presència de dos ambients geodinàmics diferents. Les peridotites del grup A format en un ambient abissal/zona de fractura en la conca oceànica del Proto-Carib, mentre que les peridotites del grup B, els blocs exòtics ultramàfics i l'escorça màfica apunten cap a un ambient d'avant arc. Els dos escenaris coexisteixen en un model geodinàmic del Jurassic Superior-Cretaci Inferior amb la formació de litosfera oceànica després del trencament de Pangea i el posterior inici de la subducció, en un ambient de zona de fractura. L'inici de la subducció en el Cretaci inferior i posterior desenvolupament de la serpentinització de la zona d'avantarc i el canal de subducció durant el Cretaci Inferior-Superior fins al final emplaçament del conjunt (mélange serpentinitic) durant Cretaci Superior-Eocè.

Abstract

This PhD is about the serpentinitic matrix, mafic crust and exotic ultramafic blocks of the Villa Clara serpentinitic mélange (VCSM) in central Cuba in an attempt to evaluate the evolution of oceanic lithosphere. Each of these units bears witness of mantle source composition, origin of oceanic crust and its relation to the mantle, ocean floor metamorphism, metasomatism and fluid flux in the subduction zone.

The study of the serpentinitic matrix allowed the identification of two peridotite protoliths. Group A, with fertile compositions (high Al_2O_3 and low Cr# in pyroxene and spinel and enriched in heavy rare earth elements) and group B, displaying refractory compositions (low Al_2O_3 and higher Cr# in pyroxene and spinel compositions and depleted in middle and heavy rare earth elements). Group A can be related to typical abyssal/fracture zone peridotite, whereas group B is typical of forearc peridotite. Melting modelling shows that, group A resulted from low melting degrees (*c.* 4-8%) of a depleted mantle source, whereas group B reached up to *c.* 14-22% melting upon a two-stage melting of a depleted mantle followed by melting of a protolith similar to group A.

The studied mafic crust includes rocks of sub-volcanic (diabase and microgabbro) and plutonic origin (cumulate gabbro and olivine gabbro). The sub-volcanic unit attests for two types of mafic magma: group 1 displays forearc basalts signature (FAB; low Ti/V ratio) and group 2 island arc tholeiite composition (IAT; medium Ti/V ratio), both with positive Th and negative Nb anomalies in comparison to N-MORB compositions. These compositions as well as the isotopic signature of the plutonic unit (low $^{143}Nd/^{144}Nd$ and low $^{87}Sr/^{86}Sr$) point to a subduction-related imprint. Geochemical evidence supports a genetic relationship between the protoliths of the serpentinitic matrix rocks and the sub-volcanic mafic crust. An indirect evidence is the light rare earth element enrichment of group B peridotites, which is commonly interpreted as a result of re-equilibration with percolating basaltic melts like those represented by the sub-volcanic mafic crust. Also, melting modelling of primitive melts of the mafic crust (group 1-FAB related) results in *c.* 8-10 % melting of an abyssal mantle source like group A peridotites that produced a residue like group B peridotites.

On the other hand, ocean floor metamorphism affected the mafic crust, which displays greenschist to amphibolite facies assemblages that attest for low pressure/low to medium temperature at shallow depths. This process had an impact on the concentration of mobile elements. A different metasomatic/enrichment process is recorded by trace element geochemistry and stable and radiogenic isotopes (B, Nd, Sr and Pb) in the serpentinitic matrix. The isotopic relations point to a slab fluid formed after devolatilitzation of the subducting plate as the source of metasomatic agent. The slab fluid is composed of diverse proportions of altered oceanic crust fluid (AOCF), global subducting sediment fluid (GLOSSF) and terrigenous fluid (TERF). The combination of these three isotopic reservoirs with an already serpentinized mantle related to ocean floor hydration reproduces the isotopic signature of the serpentinitic matrix of the VCSM. This result is in agreement with evidence provided by the high-pressure exotic ultramafic block of the VCSM, which shows

similar isotopic composition indicating interaction with a similar fluid in a context of subduction.

The petrological and geochemical characteristics of the exotic ultramafic block allow distinguishing two types of serpentinite: i) antigorite-serpentinite and ii) dolomite-bearing antigorite serpentinite. Both represented a subducted peridotite that derives from a peridotite protolith locally CaO-enriched as a result of infiltration of a H_2O-CO_2 fluid mixture. Fluid infiltration in the subduction channel triggered serpentinization /carbonation and formation of tremolite veins and associated blackwalls developed in host antigorite-serpentinite. Mineralogical and chemical zoning in the blackwall (Atg + Chl + Tr towards the host serpentinite and Chl + Tr towards the vein) attest for metasomatic changes in fluid composition during fluid-rock interaction. The differences in chemical composition between blackwall and antigorite-serpentinite show that the infiltrating fluid was enriched in Ca, Al, LILE and LREE. Pseudosection modelling in the vein structure indicates that their formation took place at *c.* 450ºC and *c.* 10 kbar.

All these findings allow constraining the geodynamic evolution of the Villa Clara serpentinitic mélange in the context of the Caribbean realm. The serpentinitic matrix attests for two contrasting geodynamic settings. Group A peridotites formed at an abyssal/fracture zone setting in the Proto-Caribbean oceanic basin, whereas group B peridotites, exotic ultramafic block and mafic crust are pointing to a forearc setting. Both scenarios are reconciled in a geodynamic model of Upper Jurassic-Lower Cretaceous oceanic lithosphere formation upon break-up of Pangea followed by subduction initiation, likely at a fracture zone setting, during the early Cretaceous, and further development of a serpentinized forearc mantle and associated subduction channel during Lower-Upper Cretaceous time until final emplacement of the ensemble (serpentinitic mélange) during the latest Cretaceous-Eocene.

Chapter 1

Introduction

1.1. Objectives

1. Introduction

Ophiolitic complexes are remnants of ancient oceanic lithosphere accreted to continental margins and volcanic arcs. The ideal ophiolite is composed of a pseudostratigraphically arranged oceanic crust (sedimentary cover, pillow lavas, sheeted dyke, and isotropic and layered gabbros) and mantle, generally of harzburgitic composition (e.g. Anonymous, 1972; Dilek and Furnes, 2011 and references therein). Dilek and Furnes (2011, 2014) and Furnes and Dilek (2017) propose an ophiolite classification based on geochemical characteristics, internal structure, thickness (vary with the spreading rate), proximity to plume or trenches, mantle temperature, mantle fertility and availability of fluids. The classification distinguishes two groups: subduction related and subduction un-related ophiolites (Fig C1_1). The subduction related group includes ophiolites that are controlled by slab devolatilization with associated mantle metasomatism, the melting of slab areas and continuous partial melting of peridotites. This group comprises suprasubduction zone and volcanic arc types. On the other hand, subduction un-related ophiolites exhibit magmatic processes that are not influenced by subduction, encompassing continental margin, mid-ocean-ridge and plume type ophiolites. Throughout the geotectonic evolution of a given oceanic region it is common to pass through different geodynamic scenarios and ophiolite types. An additional complexity that masks the petrogenetic and geodynamic evolution of ophiolites is the existence of ophiolitic mélanges, where original pseudostratigraphic relations are completely distorted (e.g. Shervais et al., 2011; Blanco-Quintero et al., 2011a; Uysal et al., 2016; Cárdenas-Párraga et al., 2017).

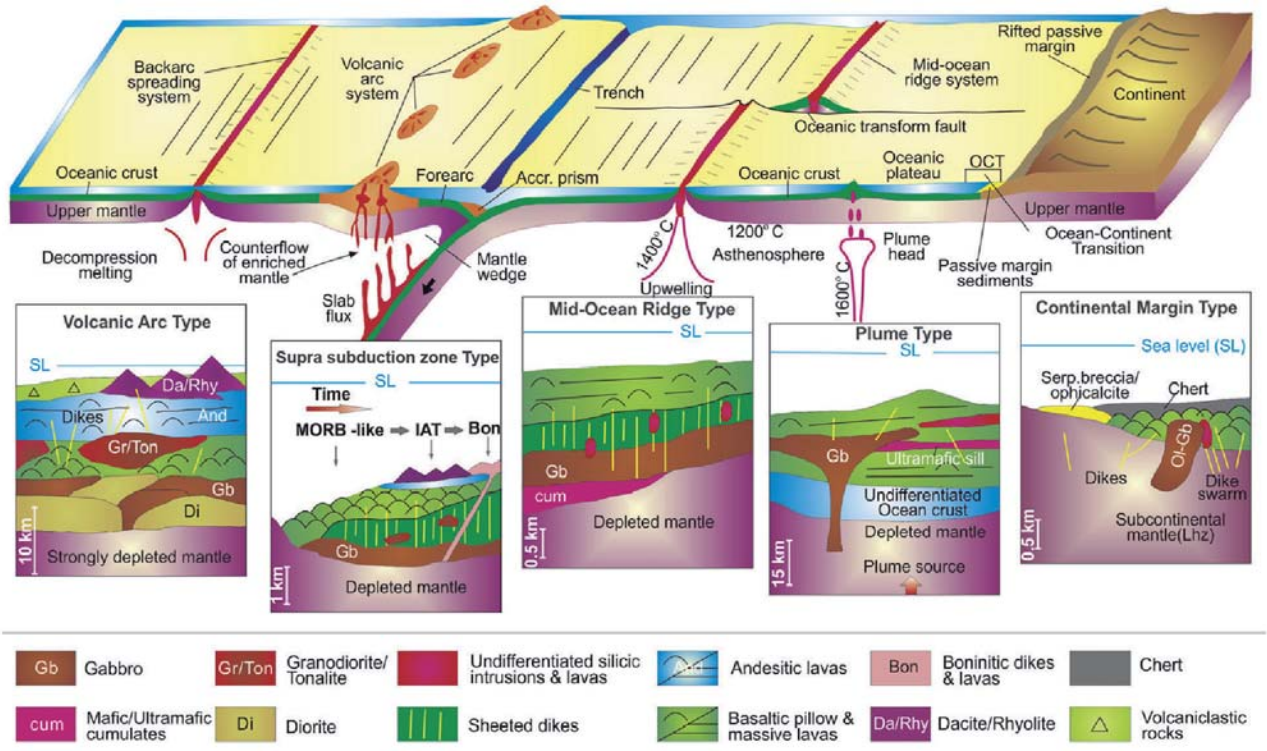

Figure C1_1. *Plate tectonic sketch depicting ophiolite classification from Dilek and Furnes (2011) and Furnes and Dilek (2017).*

The term mélange has been applied as a descriptive and non-genetic definition not limited to the rock types involved (igneous, metamorphic or sedimentary) and the contacts between them, which can be tectonic, stratigraphic or intrusive, and controlled by the process of mélange formation (e.g. Wood, 1974; Raymond, 1984; Cowan, 1985; Festa et al., 2012 and references therein). The mélanges are complex units with pervasively deformed matrix that could contain blocks of diverse origin and lithology. There are different types of mélanges depending on the lithology involved (e.g. sedimentary, serpentinitic), contacts between the host rocks (tectonic, stratigraphic) and site of formation (Festa et al., 2012 and references therein).The geodynamic setting that provides the largest amount of mélanges is in subduction environments. Such mélanges typically form in subduction channels, where rocks of diverse lithological type and metamorphic grade mix together (Shreve and Cloos, 1996; Cloos and Shreve, 1988a and 1988b; Guillot et al., 2009; Bebout and Penniston-Dorland, 2016). The subduction channel promotes slab decoupling in the interface between the subducting and the hanging wall plates, allowing the exhumation of high pressure blocks at shallow levels (Fig. C1_2; e.g. Guillot et al., 2009; Angiboust et al., 2011).

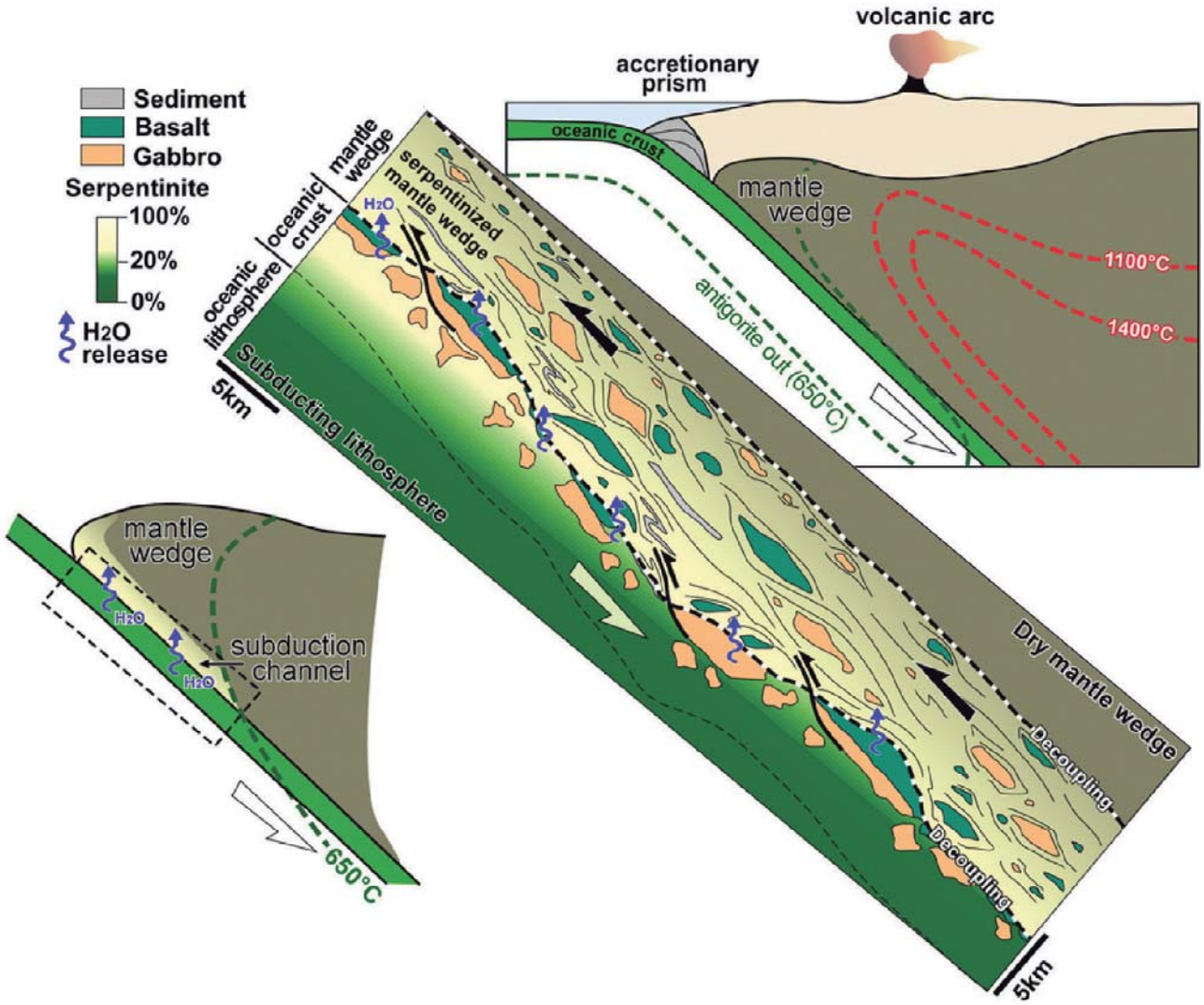

Figure C1_2. *Sketch of subduction zone setting showing the nature of the subduction channel mélange. Note that fragments of diverse lithology mix all together with an enveloping serpentintic matrix (from Guillot et al., 2015).*

Exhumed subduction channel mélanges are natural laboratories for the study of fluid-rock interaction and mass transfer of elements along the subduction interface, as well as the melting of mantle wedge favoured by devolatilitzation reactions (e.g. Zack and John, 2007; Bouilhol et al., 2012; Green et al., 2014; Taetz et al., 2016). Fluid flow and fluid-rock interaction are responsible for suprasubduction metasomatism (Bebout and Penniston-Dorland, 2016 and references therein). H_2O-rich fluid in the subduction environment is a metasomatic agent able to transport elements over large distances under variable pressure and temperature conditions (e.g. Zack and John, 2007; Konrad-Schmolke et al., 2011; Spandler et al., 2011; Angiboust et al., 2014). Tracking fluid flow and determining potential fluid sources is possible after inspection of appropriate subducted lithologies. In general terms, the fluid cycle in the subduction environment can be characterized as follows. At oceanic transform fault zones and core-complexes, during bending and related faulting of the downgoing oceanic plates at trenches, seawater is introduced deep in the subduction plate, promoting hydration of basalt, gabbro and peridotite (Molina and Poli, 2000; Ranero et al., 2003; Deschamps et al., 2011). These rock units are transformed into greenschist, blueschist, eclogite and serpentinite (lizardite-serpentinite and antigorite-serpentinite) upon subduction. Devolatilization of these rocks and associated metasediments gives rise to fluids/melts of variable composition depending on source lithologies and the temperature regime during subduction (e.g. Bebout, 1991; Plank and Langmuir, 1998; Padrón-Navarta et al., 2011; Lázaro et al., 2011; Spandler and Pirard, 2013; Marchesi et al., 2013; Schmidt and Poli, 2014). Fluid/rock interactions among these various lithologies may produce a hybrid fluid whose endmember compositions are difficult to quantify. Nevertheless, a complete study of all units involved in a subduction zone setting will shed light on the possible endmember fluids and the consequences of fluid-rock interactions.

The evolved fluid infiltrates in the downgoing and upper plates following diffuse and channelized flow, triggering fluid-rock interactions that transform the infiltrated rocks and allow melting in the mantle wedge (e.g. Green et al., 2014). The melt resulting from mantle partial melting displays a characteristic geochemical signature attested by HFSE/HREE ratios (e.g., Th/Yb, Nb/Yb). Such hints have been used to track magma provenance and subduction-derived fluid interactions (e.g. Pearce, 2008 and 2014). These geochemical “fingerprints” make it possible to distinguish diverse igneous rock types, such as fore-arc basalts, island arc tholeiites, ocean island basalts and backarc basin basalts. Various studies have focused on major and trace element patterns and isotopic compositions of oceanic crust, mantle section and subduction-related blocks, characterizing their role in subduction-derived fluids, mantle metasomatism and melt-mantle interactions in the subduction environment (e.g. Bédard, 1999; Scambelluri et al., 2001a, 2004b; Saha et al., 2005; Marchesi et al., 2006, 2011; Harlow and Sorensen, 2005; Cárdenas-Párraga et al., 2012; Angiboust et al., 2014; Le Roux et al., 2014; Vitale-Brovarone et al., 2014; Harlow et al., 2015; Uysal et al., 2016).

The internal structure of subduction mélanges and the geochemical signature of their enclosed units record petrologic, geochemical, tectonic and geodynamic processes that operate during their origin and evolution until they accrete onto continental margins. The paleomargin of the Caribbean plate offers a natural

laboratory to study subduction mélanges, as it bears several examples of ophiolitic units and subduction mélanges in Guatemala, Cuba, the Dominican Republic and Puerto Rico (e.g. Harlow et al., 2004; Blanco-Quintero et al., 2010; Blanco-Quintero et al., 2011a; Marchesi et al., 2011; Roehrig et al., 2015; Cárdenas-Párraga et al., 2017). The study of these geological bodies contributes to our understanding of ocean-floor metamorphism, sources of mantle metasomatism, and melting of mantle source. In order to study all these processes, this PhD thesis focuses on central Cuba, characterized by a serpentinitic mélange where the petrogenesis of ultramafic rocks and oceanic crust units can be related to the geodynamic evolution of the Caribbean from the mid-ocean ridge to the subduction zone settings.

1.1. Objectives

The main goal of this PhD is to describe the petrogenesis and geochemical/isotopic signature of the serpentinitic matrix of the mélange, mafic crust and exotic ultramafic blocks from the Villa Clara serpentinitic mélange (VCSM) in central Cuba. These issues have not been studied since the 1970's. This work is the first to provide the mineral composition along with the major, trace element and isotopic (radiogenic and stable) compositions of the serpentinitic matrix, mafic crust and exotic ultramafic rocks of this region. These data allow one to extract information regarding mantle source composition, degree of melting, ocean-floor metamorphism, and suprasubduction-zone-related metasomatism.

In particular we aim to:

i. Determine the petrogenetic evolution of the protoliths of the serpentinitic matrix, mafic crust rocks and exotic ultramafic blocks of the VCSM.

ii. Determine the melting degrees of the mantle source from the protoliths of the serpentinitic matrix and mafic crust, and find evidence of a potential genetic relationship between the two units.

iii. Characterize the geochemical effects of ocean floor metamorphism.

iv. Assess the metasomatic processes involved throughout the geologic history of the serpentinitic mélange and identify the nature of the slab component involved.

v. Study the processes of fluid infiltration, fluid-rock interaction and fluid-driven mass transfer at depth in the subduction channel, as attested by blackwall domains of high temperature antigorite-serpentinite; and propose a blackwall formation model to explain the exchange of matter between host rock and vein.

vi. Propose an integrated geodynamic evolution of the Villa Clara serpentinitic mélange within the framework of Caribbean evolution.

To sum up, the study of the VCSM is intended to contribute to our knowledge about the evolution of oceanic lithosphere from the mid-ocean ridge to the subduction settings, as well as offer an integrated geodynamic model of formation.

Chapter 2

Geologic evolution of the Caribbean realm

2.1. Summary of Cuban Geology

2.1.1. The Geology of Central Cuba

2.1.1.1. The Villa Clara Serpentinitic Mélange (VCSM)

2. The geologic evolution of the Caribbean realm

The geodynamic evolution of the Caribbean region started with the rupture of Pangea during Jurassic times, which involved the drifting apart of the North American plate and the inception of the Proto-Caribbean oceanic basin in between the Americas (e.g. Pindell et al., 2005, 2009, 2012; Iturralde-Vinent, 2006a; Boschman et al., 2014 and references therein). In the early Cretaceous the Proto- Caribbean basin started to subduct beneath the Pacific (Farallon) plate, favoured by the inter-American transform (*ca.* 135 Ma; Rojas-Agramonte et al., 2011; Pindell et al., 2012; Boschman et al., 2014; Cárdenas-Párraga et al., 2017). These events led to the formation of back-arc, forearc and arc settings in the leading edge of the Caribbean plate where the ophiolitic and arc units formed (cf., Garcia-Casco et al., 2008a, Pindell and Kennan, 2009; Escuder et al., 2011; Rojas-Agramonte et al., 2011, Pindell et al., 2012; Escuder et al., 2014; Rojas-Agramonte et al., 2016 and references therein). The convergence was a long-lasting process that finished when the volcanic arc collided with the passive margin of North America during latest Cretaceous - Tertiary times (Garcia-Casco et al., 2008; Iturralde-Vinent et al., 2008 and references therein). The result was the exhumation of high pressure complexes and ophiolite suites, which were tectonically emplaced above the margin. The high pressure complexes, volcanic arc units and ophiolite suites that crop out along the Caribbean realm bear witness to the long-lasting subduction setting of the region, which continues today in the Lesser Antilles (Fig. C2_1). These rock units have been recognized along Guatemala, Cuba, Hispaniola, Trinidad-Tobago, the northern part of Venezuela and northwestern Colombia.

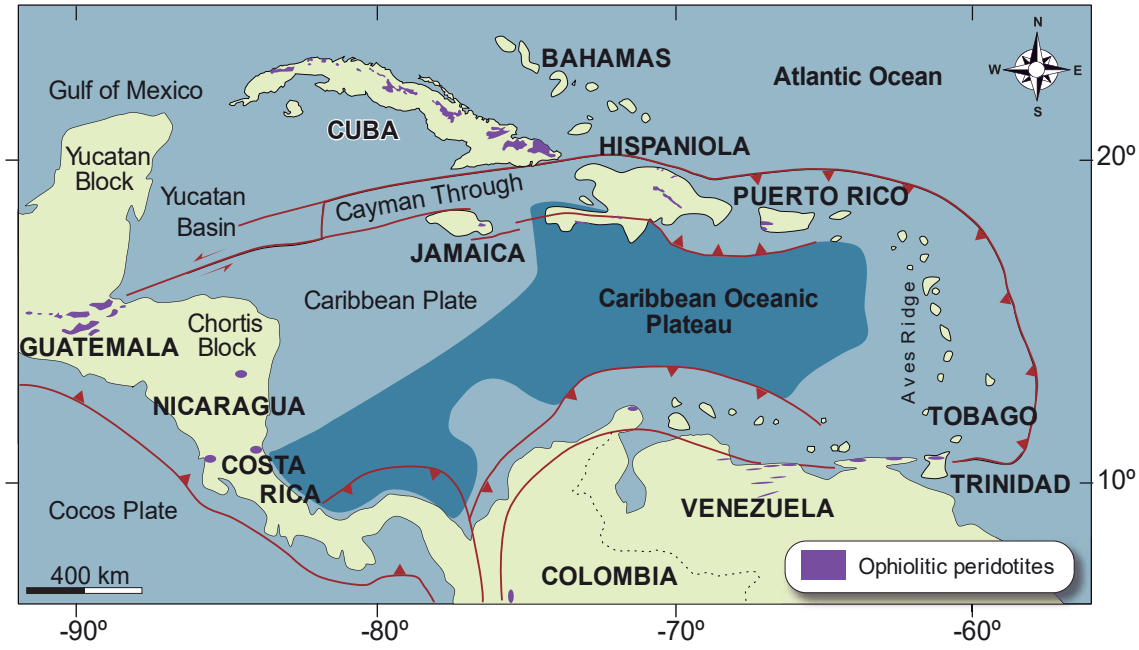

Figure C2_1. *Present plate tectonic configuration of the Caribbean region, including ophiolitic peridotites and Cretaceous-Tertiary suture zones (from Garcia-Casco et al., 2006; Lewis et al., 2006).*

2.1. Summary of Cuban Geology

The evolution of the Caribbean region is recorded in the island of Cuba, where the following main geological features crop out: i) North American passive margin, ii) Caribeana metamorphic terranes, iii) volcanic arc units (Cretaceous and Paleogene), and iv) ophiolitic massifs and associated subduction mélanges (Fig. C2_2).

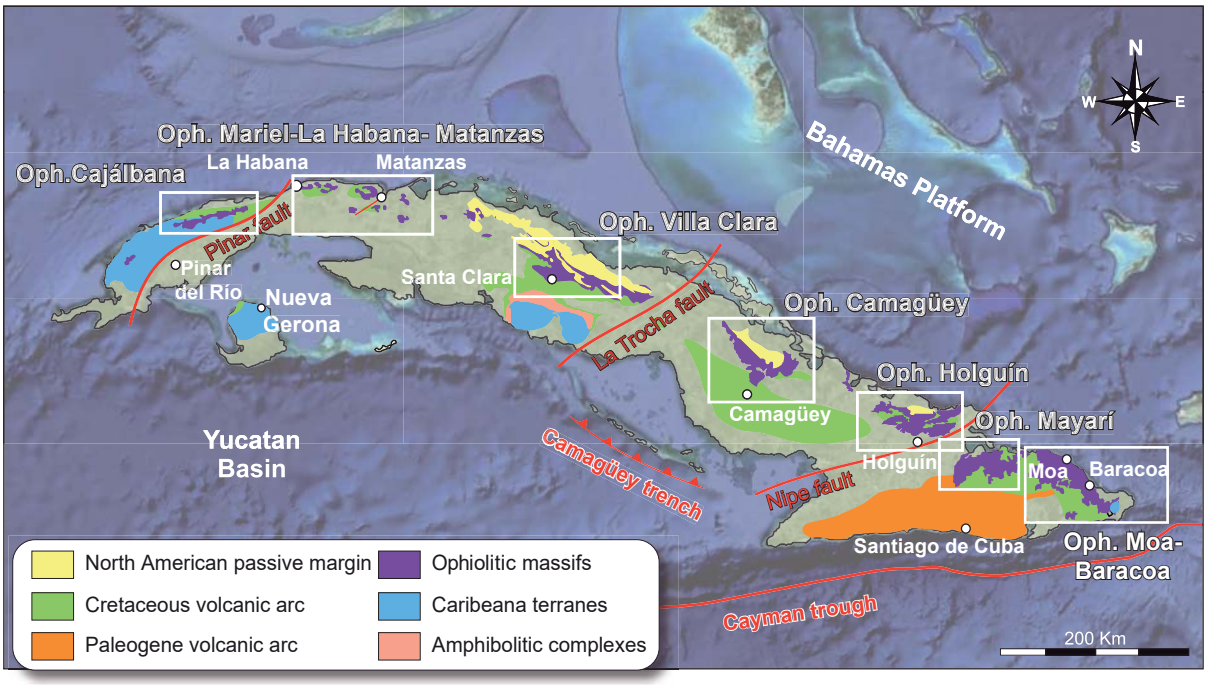

Figure C2_2. *Geological sketch of Cuba showing main geologic features including passive margin, volcanic arc, ophiolitic massifs, Caribeana terranes (high pressure terranes) and amphibolitic complexes (modified after Iturralde -Vinent, 1996a).*

The North American passive margin includes the continental margin of the Bahamas platform, which consists of shallow, external and deep marine platform sediments that were accreted in the Middle to Late Eocene (*ca.* 48-40 Ma; Pszczólkowski, 1986; Iturralde-Vinent, 1996a; Iturralde-Vinent et al., 2016). The Caribeana terranes were a sedimentary prism that extended southeast into the Proto-Caribbean basin. They comprise a Jurassic-Cretaceous passive margin and associated oceanic crust that were subducted, obducted and seated during Late Cretaceous to Tertiary (Garcia-Casco et al., 2008a; Despaigne-Díaz et al., 2016 and references therein). The Caribeana is constituted of different terranes that crop out along the island (from east to west): Cangre, Pinos, Escambray and Asunción (Somin and Millán, 1981; Garcia-Casco et al., 2008a; Despaigne-Díaz et al., 2016). They all have experienced greenschist to eclogite facies conditions (Fig. C2_2).

During Early Cretaceous the development of a volcanic arc began, then continued until the Tertiary. It has a heterogeneous geochemical signature: from low K tholeiitic, calc-alkaline to shoshonitic (Fig. C2_2; Hall et al., 2004; Marchesi et al., 2007; Garcia-Casco et al., 2008b; Rojas-Agramonte et al., 2011; Lázaro et al., 2015

and references therein). The volcanic arc was tectonically imbricated by thrust faults with ophiolitic units. Yet the Paleogene volcanic arc, which is composed of Danian–Middle Eocene arc lavas and volcaniclastic deposits, crops out only in eastern Cuba (Fig. C2_2; Cobiella 1988; Cazañas et al., 1998; Kysar-Mattietti, 2001; Rojas-Agramonte et al., 2006). Since the Paleogene, the subduction has migrated eastward as a result of strike-slip faults, leading to its present geographic position in the Lesser Antilles.

The Northern Cuban ophiolite belt presents slices of oceanic lithosphere obducted onto the North American continental paleomargin in Latest Cretaceous to Late Eocene times, during collision with the leading edge of the Caribbean plate (Iturralde-Vinent, 1996a; Garcia-Casco et al., 2008a). The Northern Cuban ophiolite belt is exposed over more than 1000 km along Cuba (Fig. C2_2). It contains seven ophiolite massifs (from west to east): Cajálbana (western Cuba), Mariel-La Habana-Matanzas, Villa Clara, Camagüey, Holguín (central Cuba), Mayarí-Cristal and Moa-Baracoa (eastern Cuba). However, Iturralde-Vinent et al. (2006b) distinguished west-central Cuba ophiolites (from Cajálbana to Holguín) and eastern Cuba ophiolites (Mayarí-Cristal and Moa-Baracoa) due to differences in their structural location and emplacement. Still, the two ophiolite groups display similarities in terms of lithology and geochemistry. The ophiolites include serpentinized peridotites, layered and isotropic gabbros, basalts, and oceanic sediments.

The west-central ophiolites as well as the eastern ophiolites are outcropping basalts, diabase and gabbros, which display compositions of typical mid-ocean ridge basalts (MORB; interpreted as Proto-Caribbean basin) and island arc tholeiites (IAT; suggesting supra subduction setting; Andó et al., 1996; Iturralde-Vinent, 1996b; Kerr et al., 1999; Proenza et al., 1999, 2006; Marchesi et al., 2006, 2007; Llanes et al., 2016). The eastern ophiolites show the same lithology as in west-central Cuba. Some authors agree that geochemical compositions of the Mayarí-Cristal ophiolitic massif are typical of forearc settings (MORB, boninites, IAT rock types; Gervilla et al.,2005; Marchesi et al., 2006; Proenza et al., 2006; Blanco–Quintero et al., 2011a), whereas the Moa-Baracoa massif depicts a backarc environment (backarc basin basalts: BABB; Proenza et al., 1999; Lázaro et al., 2015). Petrological and geochemical data suggest that Cuban ophiolites include both mid-ocean ridge and supra-subduction zone types (Kerr et al., 1999; Proenza et al., 1999, 2006; Marchesi, 2006, 2007; Lázaro et al., 2015; Cárdenas-Párraga et al., 2017).

The ages of ophiolite massifs along Cuba range from *c.*135 to *c.*60 Ma (Rutten et al., 1938; Iturralde-Vinent et al., 1996c; Llanes et al., 1998; Proenza et al., 1999; Marchesi et al., 2006; Garcia-Casco et al., 2008b; Rojas-Agramonte et al., 2010, 2011, 2013, 2016; Lázaro et al., 2015), whereas the subduction-related high pressure tectonic blocks included in the ophiolite massifs have an age range of *c.*126 to *c.*60 Ma (K-Ar in whole-rock, amphibole and micas, cf., Somin et al., 1992; Iturralde-Vinent, 1996c; Millán, 1996a; Schneider, 2000). These ages are in good agreement with those obtained from tectonic blocks of high-pressure melanges from eastern Cuba (*c.*123-75 Ma zircon SHRIMP U-Pb and amphiboles Ar-Ar ages; Lázaro et al., 2009; Cárdenas-Párraga et al., 2012; Lázaro et al., 2016) and from high-pressure coherent terranes in

central Cuba (Escambray complex, Despaigne-Díaz et al., 2016 and references therein). The ages described from Cuban ophiolites are in line with those reported from the Cretaceous volcanic arc that crops out along Cuba (W to E; *c.*100-60 Ma K-Ar amphibole, micas, feldspar and whole-rock, SHRIMP zircon U-Pb ages; Iturralde-Vinent, 1996b; Iturralde-Vinent et al. 2006b; Marchesi et al. 2006; Marchesi et al. 2007; Rojas-Agramonte et al., 2010).

Hence, available geochronological data support the Early Cretaceous to Late Cretaceous subduction of the Proto-Caribbean lithosphere and the formation of subduction channel mélanges and coherent complexes (central Cuba: Villa Clara serpentinitic mélange, in this PhD volume; eastern Cuba: La Corea and Sierra del Convento mélanges, Blanco-Quintero et al., 2011a; Cárdenas-Párraga et al., 2017). Early Cretaceous to Tertiary whole-rock K-Ar ages (*c.* 126-60 Ma) of high pressure blocks from ophiolitic complexes may represent a late-stage incorporation of subducted rocks into the mélange and/or variable resetting (Garcia-Casco et al., 2002).

2.1.1. The Geology of Central Cuba

Central Cuba displays the most complete geological units of Cuba Island. These units are: North American margin, volcanic arc sequences, Mabujina amphibolites, Escambray complex and Villa Clara ophiolitic massif (Fig. C2_3A).

In central Cuba, the North American margin is made up of different belts cropping out north and northeast of Santa Clara city (from NE-SW): Cayo Coco, Remedios, Camajuaní and Placetas (Fig. C2_3A). The Cayo Coco and Remedios belts consist of shallow to deep marine intra-platform channels that constitute the carbonate platform (e.g. Iturralde-Vinent, 1998; Iturralde et al., 2016). The Camajuaní belt and Placetas platform contain deep marine sediments, representing the continental slope of the Proto-Caribbean oceanic basin. The Placetas platform shows a series of NW-SE elongated bodies intercalated within the Villa Clara ophiolitic massif (Fig. C2_3B).

The volcanic arc sequences in central Cuba are formed by volcanic, plutonic and volcano-sedimentary sequences from the pre-Albian (Primitive Island arc, Los Pasos formation; Rojas- Agramonte et al., 2011) to Campanian (Cretaceous volcanic arc). They contain tholeiitic, calc-alkaline and high-alkaline rocks (Rojas-Agramonte et al., 2011). The volcanic arc overlies the Villa Clara ophiolitic massif and the Mabujina amphibolite complex (Fig. C2_3B). The Mabujina amphibolite complex is made of arc-derived rocks that were deformed and metamorphosed into greenschist and amphibolite facies (Somin and Millán, 1981; Blein et al., 2003). Associated arc-related granitoid plutons occur from *c.*133 to 83 Ma (Grafe et al., 2001; Rojas-Agramonte et al., 2011). Some authors (Somin and Millán, 1981; Dublan et al., 1986; Millán, 1996b) interpreted that the Mabujina amphibolite complex represents the metamorphosed base of the Cretaceous volcanic arc. Blein et al. (2003) and Rojas-Agramonte et al. (2011) interpreted it as a different arc system accreted from the Pacific. However, the Mabujina complex is tectonically underlain by the

Escambray complex (Fig. C2_3B).

The Escambray complex belongs to the Caribeana metamorphic terranes that crop out across Cuba (Fig. C2_3A). It comprises a mixture of metasediment and metaophiolite rocks (e.g. Garcia-Casco et al., 2008a; Despaigne-Díaz et al., 2016 and references therein). They were metamorphosed under high-intermediate pressure and low-medium temperature conditions related to the subduction and collision-exhumation of the accretionary wedge from the Late Cretaceous to the Early Eocene (Despaigne-Díaz et al., 2016 and references therein).

The Villa Clara ophiolitic massif is tectonically disrupted, occurring mostly as tectonic mélange characterized by blocks of mafic and ultramafic rocks within serpentinized peridotite/serpentinite or, commonly, as exotic blocks of subduction-related high-pressure rocks (Somin and Millán, 1981; Millán, 1996a; García-Casco et al., 2002; 2006 and references therein). Hence, a more appropriate term for the 'Villa Clara ophiolitic massif' is suggested: the Villa Clara serpentinitic mélange (VCSM).

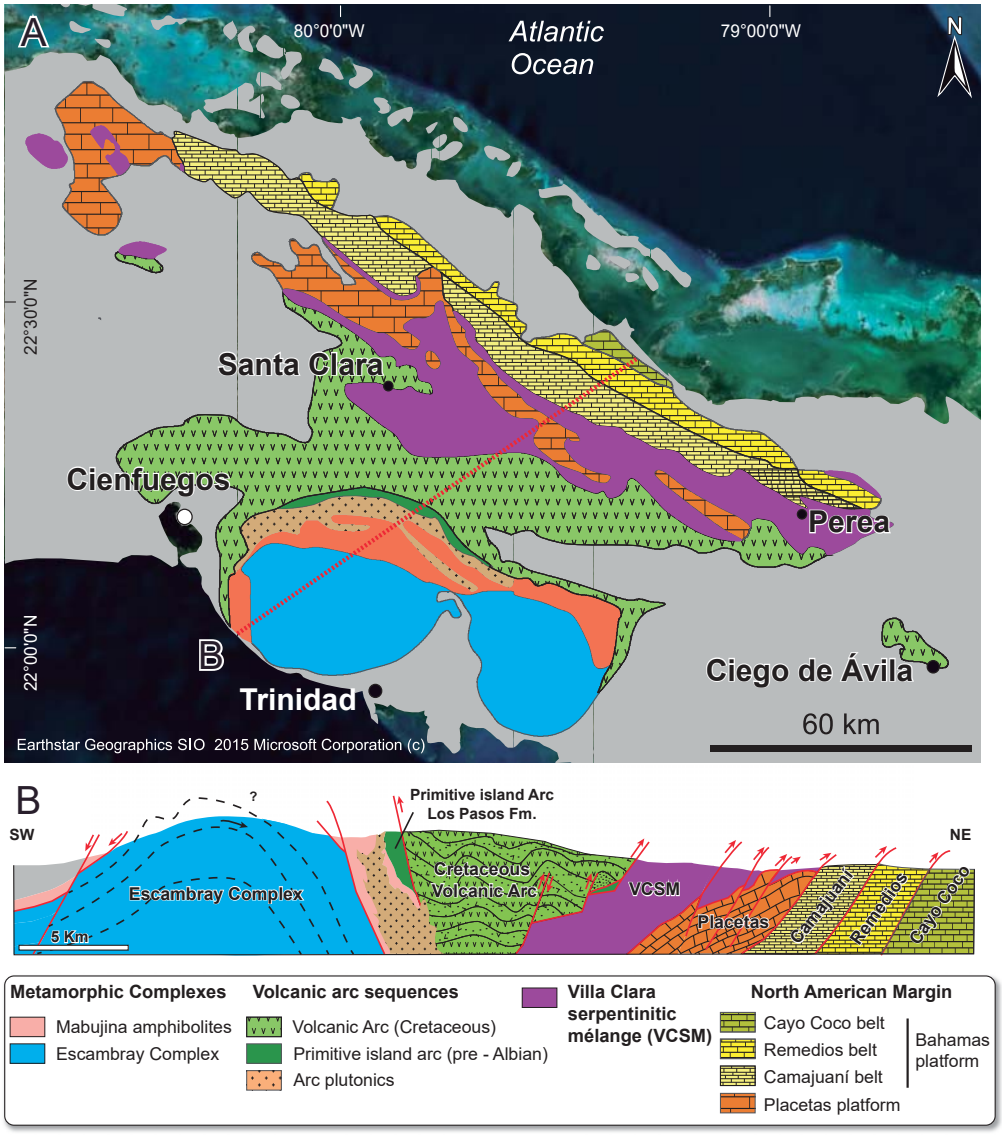

Figure. C2_3. *Geological map and cross-section of central Cuba showing the basic geological features (after Iturralde-Vinent, 1996a).*

2.1.1.1. The Villa Clara Serpentinitic Mélange (VCSM)

The Villa Clara serpentinitic mélange (central Cuba) is constituted by meter- to kilometer-sized bodies of a dismembered ophiolitic sequence including mafic crust (basalts, diabase dykes and layered gabbros), a serpentinitic matrix (serpentinized peridotites and serpentinites) and exotic blocks of: a) high pressure rocks of metabasite (eclogite and blueschist), metaultramafic (antigorite-serpentinite, chloritite) and metasedimentary (quartzite, schists) compositions; b) arc-derived volcanic and sedimentary rocks; and c) Bahamas platform-derived sedimentary rocks (Kanchev et al., 1978; Somin and Millán, 1981; Garcia-Casco et al., 2002, 2003, 2006). The rock mixture allows the whole ensemble to be characterized as a serpentinite mélange having a mixture of blocks from shallow geologic formations and from a subduction channel mélange. In fact, Garcia-Casco et al. (2002; 2006) suggested that eclogite blocks were exhumed close to the Earth's surface within a serpentinitic subduction channel (mélange) at *c.* 110 Ma, pointing to a first stage of mélange formation during Early Cretaceous, previous to a second main stage of mélange formation during arc-continent collision and ophiolite obduction at *c.* 70 Ma (Garcia-Casco et al., 2008b). In this regard, Álvarez et al. (1991) subdivided the Villa Clara ophiolitic mélange into the Descanso and Santa Clara mélanges. The Descanso mélange is composed of serpentinites enclosing ophiolitic, volcanic-arc and platform sedimentary rocks from the nearby North American passive margin (Ducloz and Vuagnat, 1962). The Santa Clara mélange comprises serpentinites enclosing high-pressure subduction-related rocks (Fig. C2_4). However, our observations and other studies (Rutten et al., 1938; Kanchev et al., 1978) have recognised high-pressure subduction-related blocks in both mélanges (as mapped by Álvarez et al., 1991) adjacent to (a few meters apart) low-P/unmetamorphosed blocks, thereby questioning the mapped boundary between the two mélanges. Given these considerations, the Villa Clara serpentinitic mélange (VCSM) will be treated as one whole geologic unit.

The extension of the VCSM is limited to the northeast, overlapping with the North American passive margin, which includes the synorogenic basins, and the Bahamas and Placetas platforms. To the southwest, the VCSM is overthrusted by volcanic arc sequences (Fig. C2_4). Most outcrops of the VCSM are strongly serpentinized peridotites, which form the serpentinitic matrix (see chapter 4). The rocks of the mafic crust of the ophiolite are represented by layered gabbros, sub-volcanic bodies of diabase, and basalts (Fig. C2_4 and chapter 5; Rutten et al., 1938; Kanchev et al., 1978; Garcia-Casco et al., 2006). These rocks occur as metric to kilometric bodies surrounded by serpentinites, suggesting a tectonic mélange. Basalts and sub-volcanic bodies are generally partially metamorphosed in the amphibolite and greenschist facies conditions at low pressure (< 2 kbar) under static conditions, and most bodies do not show signs of deformation (more details in chapter 5; Rutten et al., 1938; Kanchev et al., 1978; Somin and Millán, 1981; Álvarez et al., 1991; García-Casco et al., 2003).

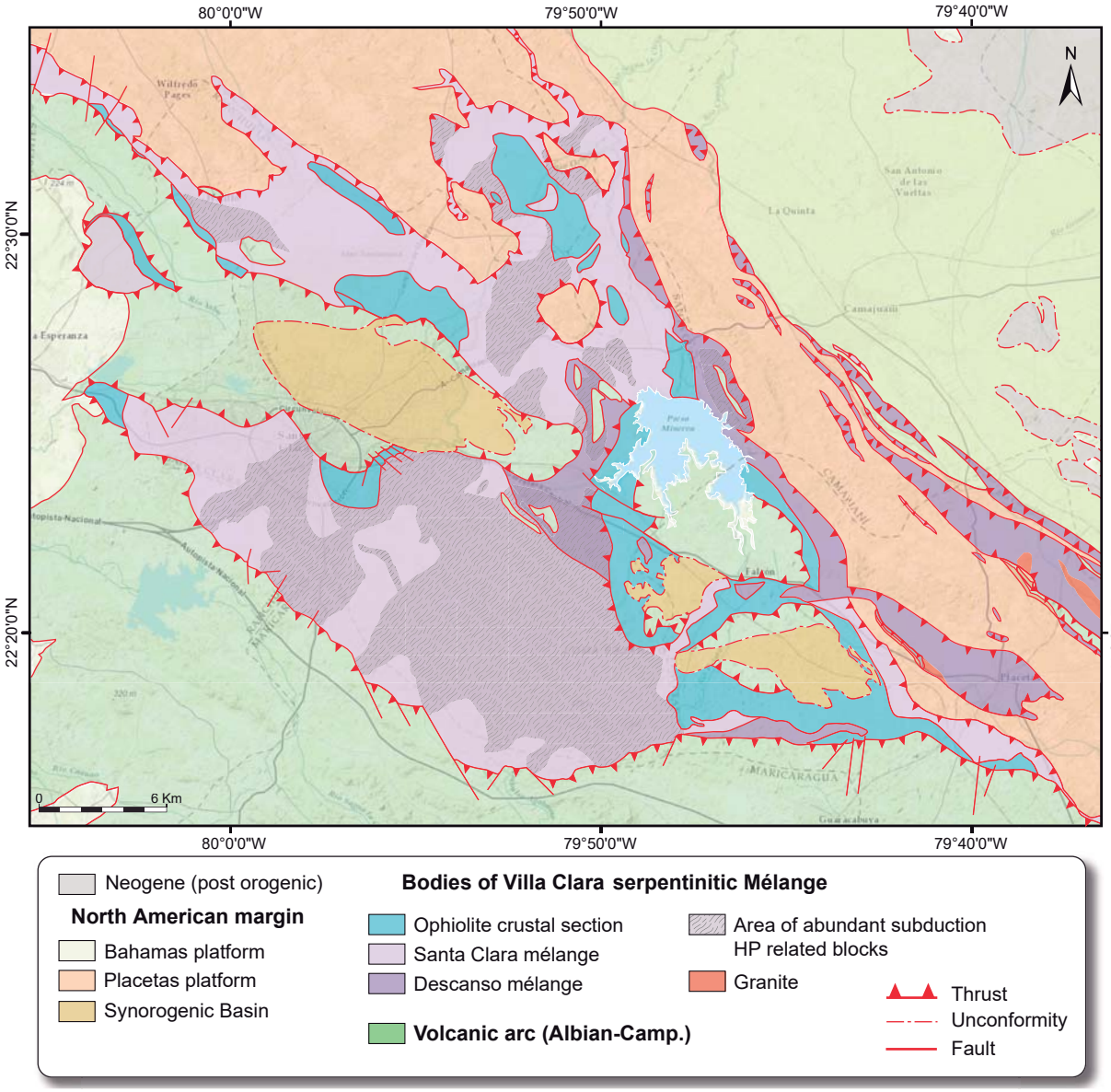

Figure. C2_4. *Geological map of Las Villas 1:100000 (modified from Kanchev et al., 1978; Álvarez et al., 1991 and García et al., 1998).*

Blocks derived from the overlying volcanic arc as well as from the underlying Bahamas platform units also occur, surrounded by serpentinite, suggesting a tectonic mélange formed during arc-continent collision and ophiolite obduction (see region of subduction-related blocks in Fig. C2_4 García-Casco et al., 2008; Iturralde-Vinent et al., 2008; Van Hinsbergen et al., 2009). Moreover, subduction-related tectonic blocks of high-pressure rocks, including MORB-derived eclogite, garnet amphibolite, blueschist facies rocks and massive strongly foliated antigorite-serpentinite (Fig. C2_4; Rutten et al., 1938; Kanchev et al., 1978; Somin and Millán, 1981; Álvarez et al., 1991; Garcia-Casco et al., 2002, 2006) are dispersed within the serpentinitic body. The blocks of eclogite formed at *ca.* 600 ºC, 20 kbar (ca. 60-70 km depth; Garcia-Casco et al., 2002) and are generally surrounded by blackwalls of chloritite, enclosed within massive high-pressure antigorite-serpentinite (Atg-serpentinite), that lack resemblance with the surrounding undeformed or weakly deformed serpentinized peridotite and the serpentinite of serpentinitic matrix (Álvarez et al., 1991; Somin and Millan, 1991; see chapter 6).

Chapter 3

Sample and Methods

3.1. Sample preparation

3.2. Micro-Raman spectroscopy

3.3. Electron Micro Probe Analysis (EMPA)

3.4. X-ray Fluorescence (XRF)

3.5. Inductively Coupled Plasma Mass Spectrometry (ICP-MS)

3.6. Thermal Ionitzation Mass Spectrometry (TIMS)

3.7. Condensation of compositional space

3.8. Pseudosection modelling

3.9. Melting Modelling

3.10. Isotopic Modelling

3. Sample and Methods

This study is based on 75 samples (see Table C3_1) from the Villa Clara serpentinitic mélange (VCSM). A representative selection of the different rock groups is presented and analysed in this manuscript, comprising samples of: serpentinitic matrix (20 serpentinites and serpentinized peridotites), mafic crust (14 samples of sub-volcanic unit and 7 samples of plutonic unit) and exotic ultramafic blocks (3 samples of dolomite-bearing Atg-serpentinites, 3 samples of Atg-serpentinites and 3 blackwall domains and tremolite vein) of the Villa Clara serpentinitic mélange (see field relations in chapters 4, 5 and 6). Mineral assemblages and textures were first studied on 75 polished thin sections by transmitted and reflected light optical microscopy.

	Serpentinitic matrix	**Mafic crust**		**Exotic ultramafic block**
		Sub-volcanic unit	Plutonic unit	
Thin section	20	25	18	12
XRF	20	14	7	9
ICP-MS	20	14	7	9
PGE	4	-	-	1
EMPA	15	4	5	4
Raman	2	-	-	1
$^{87}Sr/^{86}Sr$ TIMS	12	9	4	3
$^{143}Nd/^{144}Nd$ TIMS	5	9	4	3
$^{206}Pb/^{204}Pb$ TIMS	12	-	-	-
$^{207}Pb/^{204}Pb$ TIMS	12	-	-	-
$^{208}Pb/^{204}Pb$ TIMS	12	-	-	-
$\delta^{11}B$ TIMS	7	-	-	-
Total samples	20	25	18	12

Table C3_1. *Summary of samples and methods used in this PhD thesis.*

3.1. Sample preparation

Samples were processed at Servei de Làmina Prima at the University of Barcelona (SLP-UB). All selected samples were sawed, using a diamond saw, to remove surface alteration and secondary veins. The small pieces were crushed in steel mortar and quartered several times by a riffle-splitter to achieve a (10 g) representative sample aliquot. Whole-rock powders (< 2mm grained) were obtained by pulverizing these aliquots in an agate ring mill. Samples of the vein and blackwall domains enclosed in Pelo Malo megablock (exotic ultramafic block in chapter 6) were separated by manual fragmentation and powdered with an agate mortar in Atg + Chl + Tr, Chl + Tr domains, and Tr-vein.

3.2. Micro-Raman spectroscopy

The serpentine group minerals in the serpentinitic matrix and exotic ultramafic block of the VCSM (Fig. C4_10 in chapter 4 and Fig. C6_3C in chapter 6) were identified using Micro-Raman spectra acquired at the Centres Científics i Tecnològics of Barcelona University (CCITUB). The spectra were obtained from polished thin sections, with a HORIBA Jobin Yvon LabRam-HR800 dispersive spectrometer equipped with an Olympus BXFM optical microscope (using a 100x objective lens), and a 600 mm focal length spectrograph equipped with CCD 5 mW laser power, working at 785 nm. The laser beam size was set to 10 µm and the spectra were acquired using 8 scans of 30 s per spectral region, processed using NGS-Labspec software (version. 5.33.14). An automatic baseline subtraction was performed. Serpentine phases were identified based on the spectral characteristics reported by Rinaudo et al. (2003) and Groppo et al. (2006).

3.3. Electron Micro Probe Analysis (EMPA)

Electron images, mineral compositions and X-Ray mapping were obtained from polished thin sections using a JEOL JXA-8230 microprobe with a five wavelengths dispersive (WDS) spectrometer (20 keV accelerating potential and 20 nA beam current) at CCiTUB (Spain), and a CAMECA SX–100 with five WDS (15 keV and 15 nA) at the University of Granada (Centro de Instrumentación Científica, CIC-UGR, Spain). Analytical standards and lines used for analyses at CCiTUB were: wollastonite (Si Kα), wollastonite (Ca Kα), Fe_2O_3 (Fe Kα), rutile (Ti Kα), periclase (Mg Kα), rhodonite (Mn Kα), Al_2O_3 (Al Kα), chromite (Cr Kα), NiO (Ni Kα), albite (Na Kα), ortoclase (K Kα), apatite (P Kα), NaCl (Cl Kα) and fluorite (F Kα). Analytical standards used at CIC-UGR were: SiO_2 (Si Kα), diopside (Ca Kα), Fe_2O_3 (Fe Kα), TiO_2 (Ti Kα), periclase (Mg Kα), $MnTiO_3$ (Mn Kα), Al_2O_3 (Al Kα), Cr_2O_3 (Cr Kα), NiO (Ni Kα), albite (Na Kα), sanidine (K Kα), apatite (P Kα), vanadinite (Cl Kα), SO_4Ba (Ba Kα) and CaF_2 (F Kα).

The mineral formulas were normalized to certain oxygens, depending on each mineral, as elements per formula unit (p.f.u.). The pyroxenes were normalized to 6 oxygens, olivine and spinel to 4 oxygens, feldspars (plagioclase and alkali feldspar) to 8 oxygens, amphibole to 23 oxygens, epidote to 12.5 oxygens, serpentine to 14 oxygens, chlorite to 28 oxygens, prehnite to 11 oxygens and ilmenite to 3 oxygens. Serpentine group minerals and chlorite mineral formula were determined considering total Fe as Fe^{2+} per formula (cf. Debret et al., 2014). In the case of epidote, feldspars (plagioclase and alkaline feldspar), ilmenite and prehnite, total Fe was considered as Fe^{3+}. The estimation of ferric iron (Fe^{3+}) proportions in amphiboles was calculated as in Schumacher (1997). In the other minerals, ferric iron was calculated as the stoichiometric proportion. Mineral and endmember abbreviations are after Whitney and Evans (2010).

Elemental X-ray mapping (WDS: Si, Ca, Fe, Mg, Al and Cr; see chapter 6.3) of blackwall domains enclosed in exotic ultramafic Pelo Malo megablock and back-scattered electron (BSE) images were obtained with the CAMECA SX–100 microprobe (at CIC-UGR, Spain) operated at 15 keV and 300 nA, a focused beam, step (pixel) size of 14 µm and counting time of 30 ms/pixel. The images were processed with DWImager software

(Torres-Roldán and Garcia-Casco, unpublished). The quantification of X-ray maps to weight percent of oxides was done using internal standards and the ZAF correction procedure of Bence and Albee (1968). In order to show the textural position and composition of the mineral of interest in the composite vein structure, the quantified XR maps of the elements (colour-coded; expressed in wt %) were clipped to avoid (mask out) holes, polish defects and all other mineral phases, and the masked images were overlain onto the corresponding BSE image that contains the textural information of the scanned area.

3.4. X-ray Fluorescence (XRF)

Whole-rock major element compositions of 50 selected samples were analysed on glass beads using Philips Magix Pro (PW-2440) X-ray fluorescence (XRF) equipment after fusion with lithium tetraborate ($Li_2B_4O_7$). Typical precision of XRF analyses was better than ± 1.5-2% for an analyte concentration of ≥10 wt.% and ± 4% (relative error) for concentrations of <10 wt.%. Zirconium was determined by X-ray fluorescence on the same glass beads with a precision better than ± 0.2% for 5 ppm Zr. Loss of Ignition (LOI) was determined by weight difference before and after ignition of samples in a furnace. Analyses were performed at the University of Granada (Centro de Instrumentación Científica, CIC-UGR, Spain).

3.5. Inductively Coupled Plasma Mass Spectrometry (ICP-MS)

Whole-rock trace elements (Li, Be, Co, Ni, Zn, Cr, Cu, Rb, Sr, Y, Nb, Cs, Ba, rare earth elements, Hf, Pb, Th, U, V, Ga, Mo, Sc, Sn, Tl) were analysed in 50 selected samples using a quadrupole NEXION 300d Inductively Coupled Mass Spectrometry (ICP-MS) at the University of Granada (CIC-UGR, Spain). The ICP-MS spectrometry determinations were made after HNO_3+HF digestion of 0.1000 g of sample powder in a Teflon-lined vessel at 180°C and 200 psi for 30 min, evaporation to dryness, and subsequent dissolution in 100 ml of 4 vol.% HNO_3; the precision was better than ±5 % for analyte concentrations of 10 ppm. The concentration of Hf was calculated from the ICPMS-determined Zr/Hf and the XRF-determined Zr concentration.

The platinum group element (PGE) compositions were analysed by ICP-MS after fire assay nickel sulphide collection (detection limits, 1ppb for Ir, Ru, Rh, Os, Pd, Pt and 2 ppb for Au) at Intertek Genalysis (Maddington, Western Australia), following the method described by Chan and Finch (2001). All analysed sample powders (50 g each) were previously homogenized by quartering of a larger initial sample.

3.6. Thermal Ionization Mass Spectrometry (TIMS)

Radiogenic isotopes (Nd, Sr and Pb) and stable isotopes (B) were measured using whole-rock powders. A total of 28 samples were analysed, including 12 of serpentinitic matrix, 13 of mafic crust and 3 of exotic ultramafic block.

The Nd isotopes of all samples were determined at Granada University (Spain) in the CIC-UGR. The Sr isotopes of mafic crust and exotic ultramafic blocks were also analysed at CIC-UGR. In turn, Sr, Pb and B isotopes of serpentinitic matrix samples were analysed at Istituto di Geoscienze e Georisorse- Consiglio

Nazionale delle Ricerche (IGG-CNR) of Pisa (Italy).

The procedure for Nd and Sr isotopes entailed digestion of the powdered sample with HNO_3+HF using ultra-clean reagents, with analysis by Thermal Ionization Mass Spectrometry (TIMS) in a Finnigan MAT 262 spectrometer after chromatographic separation with ion-exchange resins at CIC-UGR, Granada (Spain).

Normalization values were $^{146}Nd/^{144}Nd$=0.7219 and $^{86}Sr/^{88}Sr$=0.1194. Blanks were 0.09 ng for Nd and 0.6 ng for Sr. The external precision (2σ), estimated by analysing 10 replicates of the standard WS–E (Govindaraju, 1994) was better than ± 0.0015 % for $^{143}Nd/^{144}Nd$ and ± 0.003 % for $^{87}Sr/^{86}Sr$. $^{147}Sm/^{144}Nd$ and $^{87}Rb/^{86}Sr$ were directly determined by ICP-MS following the method developed by Montero and Bea (1998), with a precision better than ± 0.9 % for $^{147}Sm/^{144}Nd$ and ± 1.2 % (2σ) for $^{87}Rb/^{86}Sr$.

The Sr isotope compositions of serpentinitic matrix samples were analysed by TIMS using a Finnegan MAT 262 multicollector mass-spectrometrer running in dynamic mode at Istituto di Geoscienze e Georisorse-Consiglio Nazionale delle Ricerche (IGG-CNR) of Pisa (Italy). The Samples were attacked with HNO_3+HF, and purified in ion-exchange columns with Sr-spec resin. Measured $^{87}Sr/^{86}Sr$ ratios were normalized to $^{86}Sr/^{88}Sr$=0.1194. Replicate analysis of the NBS-987 standard was performed and gave an average value of 0.710232 ±27 (2σ, n=51). Published values are adjusted to $^{87}Sr/^{86}Sr$=0.710250. The Pb isotope analyses were performed at IGG-CNR by TIMS using Finnegan MAT 262 multicollector mass-spectrometrer operated in static mode. Samples were attacked with HNO_3+HF. The Pb extraction was carried out by chromatographic ion exchange in Dowex 1 anion resin, using HBr and HCl elution procedures. Replicate analysis of Pb isotope ratios are accurate to within 0.025% (2σ) per mass unit, after applying mass discrimination corrections of 0.05±0.01% per mass unit relative to the NBS-987 standard reference composition of Todt et al. (1993).

The Nd, Sr and Pb isotopic compositions are age-corrected in all samples to the eclogitic metamorphic peak event in Santa Clara serpentinitic mélange that indicates pre-Aptian subduction c. 125Ma (Garcia-Casco et al., 2002; Rojas Agramonte et al., 2012).

The B contents were determined by prompt gamma neutron activation (PGNA) in Activation Laboratories Ltd. (Actlabs, Canada) with a limit detection of 0.5ppm. B isotopic compositions were measured via Cs_2BO^{2+} in Pisa (CNR-IGG) using a VG Isomass 54E positive ion thermal ionization mass spectrometer (TIMS) running in dynamic mode. Boron extraction was accomplished by alkaline fusion and purification via an ion-exchange procedure described by Tonarini et al. (1997). Samples (c. 1µg B) were loaded to preconditioned tantalum filaments with graphite layer. The accuracy of B isotope composition, of about ± 0.5‰, is based on the repeated analysis of a standard NIST SRM 951 and full chemistry of the standard at the same time as samples. The conventional notation for B isotopic compositions of the samples is reported in delta notation ($\delta^{11}B$) as permil (‰) deviation from accepted composition of NBS-951 (certified $^{11}B/^{10}B$=4.04362 ± 0.00137 (2σ); Catanzaro et al., 1970).

3.7. Condensation of compositional space

Whole rock compositions of serpentinitic matrix and exotic ultramafic blocks of the VCSM were plotted in ternary diagram olivine-orthopyroxene-clinopyroxene (Fig C4_5 in chapter 4 and Fig. C6_11A in chapter 6) using the singular value decomposition of Fisher (1989, 1993). This is an algebraic method that condenses a compositional space of 9 components (SiO_2, TiO_2, Al_2O_3, Cr_2O_3, FeO, MnO, MgO, NiO and CaO) to a new system of 3 components (forsterite- enstatite- diopside). Compositional space is defined by pure endmember compositions calculated in oxi-equivalent units (forsterite, enstatite, diopside and spinel) and exchange vectors ($Fe_2TiMg_{-1}Al_{-2}$, $CrAl_{-1}$, $FeMg_{-1}$, $MnFe_{-1}$ and $NiMg_{-1}$) considering all iron as Fe^{2+}. This calculation makes it possible to depict the full composition space close to volume proportions of olivine, orthopyroxene and clinopyroxene in rocks that have lost their primary minerals due to serpentinization process. The CSpace software (Torres-Roldán et al., 2000) was used for condensation of compositional space and projection of the resulting calculations in the ternary diagram.

The MASH diagram, which models blackwall assemblage formation (Fig. C6_15A in chapter 6) by means of algebraic methods (Singular Value Decomposition: SVD; Fisher, 1989, 1993) using software CSpace (Torres-Roldán et al., 2000). The SVD led to the condensation of compositional space from a 12-component system (SiO_2, Al_2O_3, Cr_2O_3, FeOT, MnO, MgO, NiO, CaO, Na_2O, F and H_2O) to 4-component system in a tetrahedron of M-A-S-H. It was carried out with projection points (average composition of analysed tremolite) and projection vectors $CrAl_{-1}$, $FeMg_{-1}$, $MnFe_{-1}$, $NiMg_{-1}$, $NaAl(CaMg)_{-1}$, $F(OH)_{-1}$. All relations involving the composition of the fluid are hypothetical. Fe is considered as Fe^{2+} total.

3.8. Pseudosection modelling

Two pseudosections were modelled in this study: i) antigorite + chlorite + tremolite (Atg + Chl + Tr) blackwall domain phase diagram in the system CFMASH (chapter 6); and ii) harzburgite phase diagram in the system CFMAS (chapter 7.1).

The P-T phase diagram (pseudosection) of blackwall domain was calculated for antigorite + chlorite + tremolite blackwall domain (enclosed in exotic Atg-serpentinites of Pelo Malo megablock) in the system CFMASH (CaO-FeO-MgO-Al_2O_3-SiO_2-H_2O) using PERPLE_X software (Connolly, 1990, 2005; version 6.6.8). The standard state thermodynamic data are from Holland and Powell (1998, 2011), and the following solid solution models were used: olivine (ideal, Holland and Powell, 1998), antigorite (Padrón-Navarta et al., 2013), orthopyroxene (Holland and Powell, 1996), clinopyroxene (Holland and Powell, 1996), chlorite (Holland et al., 1998), talc (Holland and Powell, 1998), and tremolite and anthophilite (Holland and Powell, 1998). The major element compositions of the Atg + Chl + Tr domain used for pseudosection calculation were calculated by means of the quantified XRay-maps of EMPA for higher precision using 2308565 pixels (CaO = 4.13 wt% ± 0.02, FeO = 5.49 wt% ± 0.01, MgO = 29.13 wt% ± 0.01, Al_2O_3 = 9.31 wt% ± 0.02, and SiO_2 = 41 wt% ± 0.01; error 2σ calculated at 95% of confidence interval).

The P-T harzburgite pseudosection diagram was calculated by means of Theriak-Domino software (De Capitani and Petrakakis, 2010; version 04.02.2017) for a harzburgite composition (Fig. C7_2B in chapter 7.1) that pertains to a representative analysis of group A peridotites of serpentinitic matrix in the system SiO_2-MgO-CaO-FeO-Al_2O_3. The bulk composition used was Si (39.64) Al (7) Mg (51.69) Ca (0.06) Fe (5.58) H (1.1) in elemental moles. The thermodynamic database used was tcds61 from Holland and Powell (2011) and following solution models of orthopyroxene (White et al., 2014a and White et al., 2014b), Clinopyroxene (Green et al., 2007), spinel (Holland and Powell, 1998), garnet (White et al., 2007) and olivine (ideal, Holland and Powell, 1998).

3.9. Melting Modelling

The melting modelling was performed in the serpentinitic matrix (chapter 4) and mafic crust (chapter 5) of the VCSM.

Initial assumptions were made in order to carry out melting modelling: i) the use of fixed partition coefficients, ii) use of fixed melting reaction, iii) use of depleted mantle as the source composition and iv) a non-modal melting modelling equation. Fixed partition coefficients and melt reaction were chosen in view of the closest conditions of our rocks due to partition coefficients; the melting reaction varies with pressure, temperature, composition, oxygen fugacity, crystal chemistry and water content. Although a depleted mantle does not represent the heterogeneities of the mantle, it is the best fit approximation. The non-modal melting equation offered the best fit approximation to natural processes. The melting modelling entailed non-modal fractional melting following the equation (Eq. 1-4) of Shaw (2000).

$$\frac{C_i{}^s}{C_i{}^o} = \frac{1}{(1-F)} * \left[1 - \left(\frac{P*F}{D_i{}^o}\right)\right]^{\frac{1}{P}} \quad \text{(Eq. 1)}$$

$$\frac{C_i{}^l}{C_i{}^o} = \frac{1}{D_i{}^o} * \left[1 - \left(\frac{P*F}{D_i{}^o}\right)\right]^{(\frac{1}{P}-1)} \quad \text{(Eq. 2)}$$

$$D_i{}^o = \sum D_i{}^a * X_{o,a} \quad \text{(Eq. 3)}$$

$$P = \sum D_i{}^a * p_a{}^o \quad \text{(Eq. 4)}$$

Where C_i^o is the initial composition of element i in the initial rock, in this case the depleted mantle source being from Salters and Stracke (2004). C_i^s is the composition of element i in the solid residue after melting. C_i^l is the composition of element i in the melt after melting. D_i^o is the initial bulk rock partition coefficient of element i (Eq. 3), made of the sum of all distribution coefficients of mineral a (D_i^a), which are multiplied by the initial abundance of each mineral a in the rock ($X_{o,a}$). P is the weighted partition coefficient of the mineral phase entering in the liquid (Eq. 4). P is expressed as the sum of the distribution coefficient of

mineral a (D_i[a]) multiplied by the proportion of mineral a entering in the liquid (p_a). F is the degree of melting. The distribution coefficients of minerals for a given element are from a compilation of Bédard (1999) and Jean et al. (2010) (see Table C3_2). The mineral source modes in spinel and garnet peridotite field were from Jean et al. (2010) (see Table C3_2). The mineral melt modes of spinel- peridotite wet/dry and garnet peridotite were taken from Jean et al. (2010).

Table C3_2. *Input parameters for non-modal fractional melting modelling.*

	Source Composition [a]	Distribution coefficients in Spl-peridotites [b]				Distribution coefficients in Grt-peridotites [c]			
	DM (ppm)	$D_{Cpx/l}$	$D_{Opx/l}$	$D_{Ol/l}$	$D_{Spl/l}$	$D_{Cpx/l}$	$D_{Opx/l}$	$D_{Ol/l}$	$D_{Grt/l}$
La	0.234	0.0536	0.0031	0.0003	0.0006	0.04	0.00048	0.00001	0.003
Ce	0.772	0.0858	0.0021	0.0003	0.0006	0.07	0.00097	0.00001	0.005
Pr	0.131	0.1	0.0026	0.0003	0.0006	-	-	-	-
Nd	0.713	0.1873	0.0023	0.0002	0.0006	0.178	0.00343	0.00007	0.052
Sm	0.27	0.291	0.0037	0.00018	0.0006	0.293	0.00923	0.0007	0.25
Eu	0.107	0.3288	0.009	0.0002	0.0006	0.32	0.01302	0.00095	0.6
Gd	0.395	0.367	0.0065	0.00025	0.0006	0.34	0.01752	0.0015	1.2
Tb	0.075	0.404	0.008	0.000475	0.00105	0.35	0.02761	0.0025	1.8
Dy	0.531	0.38	0.011	0.0007	0.0015	0.38	0.03769	0.004	2.2
Ho	0.122	0.4145	0.016	0.00122	0.0023	0.375	0.04893	0.0065	3
Er	0.371	0.387	0.021	0.00174	0.003	0.37	0.06233	0.009	4
Tm	0.06	0.4085	0.029	0.00348	0.00375	0.385	0.08937	0.015	5.2
Yb	0.401	0.43	0.038	0.00522	0.0045	0.4	0.1164	0.023	6.6
Lu	0.063	0.433	0.046	0.00852	0.0045	0.4	0.15309	0.025	7.2

	Source Modes [d]		Melt Mode [e]		
	Spl-Peridotite	Grt-peridotite	Spl-Peridotite wet	Spl-Peridotite dry	Grt-Peridotite
Ol	0.56	0.57	-0.25	-0.22	0.08
Opx	0.25	0.21	0.51	0.38	-0.19
Cpx	0.18	0.16	0.62	0.71	0.81
Spl	0.02		0.12	0.13	
Grt		0.06			0.3

[a] Source composition od Depleted Mantle by Salters and Stracke (2004)

[b] Distribution coefficients compiled by Bédard (1999)

[c] Distribution coefficients compiled by Jean et al. (2010)

[d] Source modes from Jean et al.(2010)

[e] Melt mode from Jean et al. (2010)

We modellize two cases of melting for protoliths of serpentinitic matrix and mafic crust of the VCSM, which best fit their compositions: case X and case Y. Case X modelling started at garnet peridotite facies in the first step melting, whereas second and third step melting were carried out in the spinel facies conditions (using melt modes of spinel peridotite dry and wet, respectively). In contrast, case Y modelling was for first and second step melting at spinel peridotite facies.

3.10. Isotopic Modelling

The element concentrations of isotope endmembers are in Table C3_3. The isotopic endmembers were: depleted mantle (DM), altered oceanic crust fluid (AOCF), global subducting sediment fluid and melt (GLOSSF and GLOSSM), terrigenous fluid (TERF) and seawater (SW). The DM element concentration of Sr, Nd, Pb and isotopic ratios of $^{87}Sr/^{86}Sr$, $^{143}Nd/^{144}Nd$, $^{206}Pb/^{204}Pb$, $^{207}Pb/^{204}Pb$ and $^{208}Pb/^{204}Pb$ were adopted from Rehkämper and Hofmann (1997); B and $\delta^{11}B$ were from Chaussidon and Marty (1995). Altered oceanic crust fluid (AOCF) was taken from element concentrations (Sr, Nd, Pb) calculated with partition coefficients ($D_{sol/fluid}$) from Johnson and Plank (1999), with element concentrations of altered oceanic crust from Kelley et

al. (2003). In turn, B fluid composition was calculated using $D_{sol/fluid}$ from Tonarini et al. (2007), with the B concentrations of Leeman et al. (2004). The $^{143}Nd/^{144}Nd$ average was adopted from Staudigel et al. (1995), $^{87}Sr/^{86}Sr$, $^{206}Pb/^{204}Pb$, $^{207}Pb/^{204}Pb$ and $^{208}Pb/^{204}Pb$ from Leeman et al. (2004), and $\delta^{11}B$ of AOC fluid from Leeman et al. (2004). Average subducting sediment fluid (GLOSSF) element concentrations (Sr, Nd, Pb) were calculated using the partition coefficients ($D_{sol/fluid}$) of Johnson and Plank (1999) and Tonarini et al. (2007) with element concentrations of Plank (2014). The element concentration of global subducting sediment melt (GLOSSM) was obtained after 0.26% of melting, using partition coefficients ($D_{sol/melt}$; from Johnson and Plank, 1999) that correspond to 0.26% melting based on the initial element concentrations of Plank (2014). Isotope ratios of Nd, Sr, Pb were from Plank (2014) and B isotopes from Leeman et al. (2004) for GLOSSF and GLOSSM. Terrigenous fluid element concentrations (Sr, Nd, Pb) were calculated with partition coefficients ($D_{sol/fluid}$) of Johnson and Plank (1999), while element concentrations of average continental crust were taken from Rudnick and Gao (2003). B fluid composition was calculated using $D_{sol/fluid}$ from Tonarini et al. (2007), with the B concentrations of Rudnick and Gao (2003). $^{87}Sr/^{86}Sr$, $^{143}Nd/^{144}Nd$, $^{206}Pb/^{204}Pb$, $^{207}Pb/^{204}Pb$ and $^{208}Pb/^{204}Pb$ were obtained based on calculations of Stracke et al. (2003a) and Willbold and Stracke (2006), with a 1.2 Ga of crust formation. $\delta^{11}B$ of continental crust fluid was from Cannaó et al. (2016). Serpentinized peridotites (SPER) have element concentrations (Sr, Nd, Pb and B) from Savov et al. (2005) and Cannaó et al. (2016). The Sr and Nd isotopic ratios were from Tonarini et al. (2007), and Pb isotopic ratios and $\delta^{11}B$ from Cannaó et al. (2016).

The seawater endmember has Nd and $^{143}Nd/^{144}Nd_{T=125Ma}$ from Keto and Jacobsen (1988), B and $\delta^{11}B$ from Spivack and Edmond (1987). Sr and $^{87}Sr/^{86}Sr_{T=125Ma}$ come from Veizer et al. (1999), and $^{206}Pb/^{204}Pb$, $^{207}Pb/^{204}Pb$, $^{208}Pb/^{204}Pb$ from Paul et al. (2015). Mixing lines were calculated using the equation of isotopic mixture from Faure and Mensing (2005) (Eq. 5).

$$[X]_M = [X]_A * f_A + [X]_B * (1 - f_A) \quad \text{(Eq. 5)}$$

The $[X]_M$ is the isotopic relation in a mixture M of components A and B, $[X]_{A,B}$ is the isotopic relation in the components A and B, respectively, and f_A is the weight fraction of component A in the mixture M.

The seawater-DM mixing line was calculated with the equation of McCulloch et al. (1981).

$$\frac{W}{R} = \left[\frac{\epsilon_r^f - \epsilon_r^i}{\epsilon_w^i - \epsilon_r^i}\right] * \left[\frac{C_r^i}{C_w^i}\right] \text{(Eq. 6)}$$

The W/R is the water/rock ratio by weight, where is the concentration of isotope element in initial rock and is the concentration of isotope element in water. The is the value of the isotopic ratio of the rock before exchange, is the final value of isotopic relation of the rock after exchange, is the value of water isotopic ratio before exchange and is the modified value of water isotopic ratio.

Table C3_3 *Endmembers and partition coefficients used for isotope mixing calculations.*

	DM [a]	Fluid AOC [b]	Fluid GLOSS [c]	Melt GLOSS [c]	Fluid TER [d]	Sea water [e]	Serpentinized Peridotite [f]
B (ppm)	0.05	260	679	-	110	4.5	32.2
Sr (ppm)	11.300	324.306	569.811	592.157	603.774	101.600	19.460
Nd (ppm)	1.120	3.494	8.466	197.386	6.135	9.240	0.012
Pb (ppm)	0.049	0.650	33.125	234.109	17.188	-	0.128
$d^{11}B$	-10.00	5.50	-2.00	-	-3.70	39.50	30.30
$^{87}Sr/^{86}Sr$	0.7025	0.7052	0.7124	0.7124	0.7105	0.7092	0.7051
$^{143}Nd/^{144}Nd$	0.51320	0.51306	0.51221	0.51221	0.51202	0.51205	0.51310
$^{206}Pb/^{204}Pb$	18.00	18.91	18.93	18.93	18.09	18.17	18.13
$^{207}Pb/^{204}Pb$	15.43	15.58	15.69	15.69	15.58	15.63	15.54
$^{208}Pb/^{204}Pb$	37.70	38.54	39.12	39.12	38.22	38.09	37.98
$^{87}Sr/^{86}Sr_t$	0.7025	0.7046	0.7109	0.7109	0.7098	0.7075	0.7050
$^{143}Nd/^{144}Nd_t$	0.51303	0.51289	0.51210	0.51210	0.51192	0.51225	0.51301
$^{206}Pb/^{204}Pb_t$	17.82	18.45	18.83	18.83	17.96	-	18.09
$^{207}Pb/^{204}Pb_t$	15.42	15.55	15.69	15.69	15.57	-	15.54
$^{208}Pb/^{204}Pb_t$	37.55	38.36	38.96	38.96	38.03	-	37.94

	Partition coefficients		
	$D_{sol/fluid\ TON}$ [g]	$D_{sol/fluid\ SED}$ [h]	$D_{sol/melt\ SED}$ [i]
B (ppm)	0.10	-	-
Sr (ppm)	0.50	0.53	0.51
Nd (ppm)	2.00	3.26	1.53
Pb (ppm)	-	0.64	1.29

[a] DM: Depleted mantle; Rehkämper and Hofmann (1997) and Chaussidon and Marty (1995).

[b] AOCF: Altered Oceanic Crust fluid; Staudigel et al. (1995), Kelley et al. (2003) and Leeman et al. (2004).

[c] GLOSSF/GLOSSM.: Global Subducting Sediment fluid; Leeman et al. (2004) and Plank (2014).

[d] TERF: Terrigenous fluid; Rudnick and Gao (2003), Stracke et al. (2003), Willbold and Stracke (2006) and Cannaó et al. (2016).

[e] SW: Seawater; Spivack and Edmond (1987), Keto and Jacobsen (1988), Viezer et al. (1999)and Paul et al. (2015).

[f] SPER: Serpentinized peridotite; Savov et al. (2005); Cannaó et al. (2016) and Tonatini et al. (2007).

[g] Partition Coefficients of $D_{sol/fluid}$ from Tonarini et al. (2007)

[h] Partition Coefficients of $D_{sol/fluid}$ from Johnson and Plank (1999).

[i] Partition Coefficients of $D_{sol/melt}$ from Johnson and Plank (1999).

Chapter 4

Serpentinitic matrix of VCSM

4.1. Field relations

4.2. Petrography

4.3. Mineral chemistry

4.4. Whole-rock composition

4.5. Discussion of serpentinitic matrix of VCSM

4. The serpentinitic matrix of Villa Clara serpentinitic mélange

4.1. Field relations

The Villa Clara serpentinitic mélange overlaps tectonic units of the North American margin and it is overthrust by the Cretaceous volcanic arc sequences in its southern area (Fig C4_1, García et al., 1998). The serpentinitic matrix crops out all along the area of Villa Clara serpentinitic mélange (VCSM, Fig C4_1). This is closely associated with the ophiolitic mafic crust by tectonic contacts. Both units belong to the serpentinitic mélange. It is common to find blocks of the mafic crust inside the matrix of serpentinitic mélange (for more details see chapter 5). The VCSM moreover contains subduction-related high-pressure blocks such as eclogite, garnet-amphibolite, blueschist facies rocks and antigorite-serpentinite (see details for Atg-serpentinites in chapter 6).

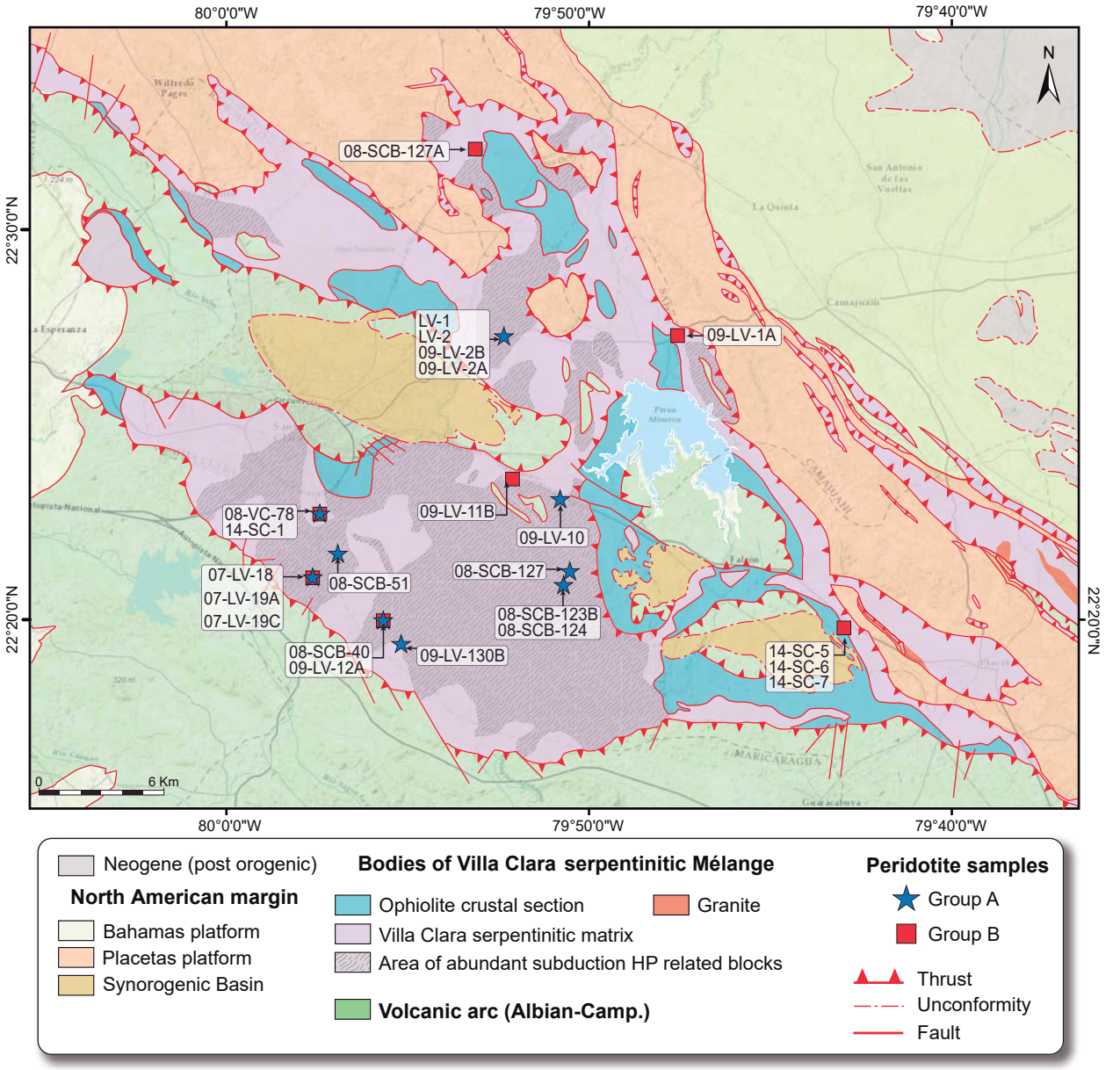

Figure. C4_1. *Geological map of Las Villas 1:100000, indicating the main geologic features and sample locations from the serpentinitic matrix (Group A and B peridotites) of the VCSM (modified from Kanchev et al., 1978; Álvarez et al., 1991 and García et al., 1998).*

The serpentinitic matrix comprises serpentinized peridotites and serpentinites. These show foliated, brecciated and massive unsheared fabrics (cf., Kanchev et al., 1978; (Fig. C4_2). Brecciated fabric (Figs. C4_2A and C4_2B) is characterized by a number of slip planes/foliations, with local penetrative foliation and mylonitization (Fig. C4_2B). Deformed and undeformed veins composed of serpentine group minerals are common. At outcrop scale, both brecciated and massive serpentinized peridotites and serpentinites have a compact appearance, with green-dark grey to dark brown colour. Relicts of primary minerals (Fig. C4_2C and C4_2D) are common following the mantle foliation. These varieties of serpentinite do not compare with high-pressure blocks of massive Atg-serpentinite, due to the fact that they lack primary minerals and pseudomorphic textures (see chapter 6).

Figure. C4_2. *Field relations of serpentinized peridotites and serpentinites of VCSM. A) Field view of brecciated textures; B) Detail of brecciated serpentinites showing foliation; C) Massive appearance of serpentinized peridotites and serpentinites; D) Massive serpentinites with Cr-spinel relicts following the mantle foliation and macroscopic mesh texture matrix of the serpentinite.*

4.2. Petrography

In the serpentinitic matrix, two rock groups of serpentinized peridotites and serpentinites could be distinguished on the basis of mineral and whole-rock composition.

Group A serpentinized peridotites and serpentinites locally preserve relicts of olivine, orthopyroxene, clinopyroxene and spinel (Figs C4_3). Relict orthopyroxene (c. 1-8 mm) and clinopyroxene are porphyroclastic, indicating plastic deformation at mantle depths (Figs C4_3A and C4_3B). Larger crystals of clinopyroxene showing ondulose extinction are mantle relicts (*c.* 0.5-1 mm; Fig. C4_3B). Smaller crystals of clinopyroxene (*c.* < 300 µm) that do not show deformation and tend to surround orthopyroxene porphyroclast are neoformed (Fig. C4_3A and C4_3B). Olivine appears as large crystals (*c.* 500 µm to 2 mm) with porphyroclastic texture (Fig. C4_3C). Accessory pale-brownish Cr-spinel shows anhedral shape (*c.*200-400 µm; Fig. C4_3D). Serpentine-group minerals display replacement textures including mesh texture in olivine (Fig. C4_3E and C4_3F) and bastite texture after orthopyroxene (Fig. C4_3E). Cr-spinel is commonly replaced by ferrian chromite and magnetite, the latter rimmed by chlorite (Fig. C4_3F).

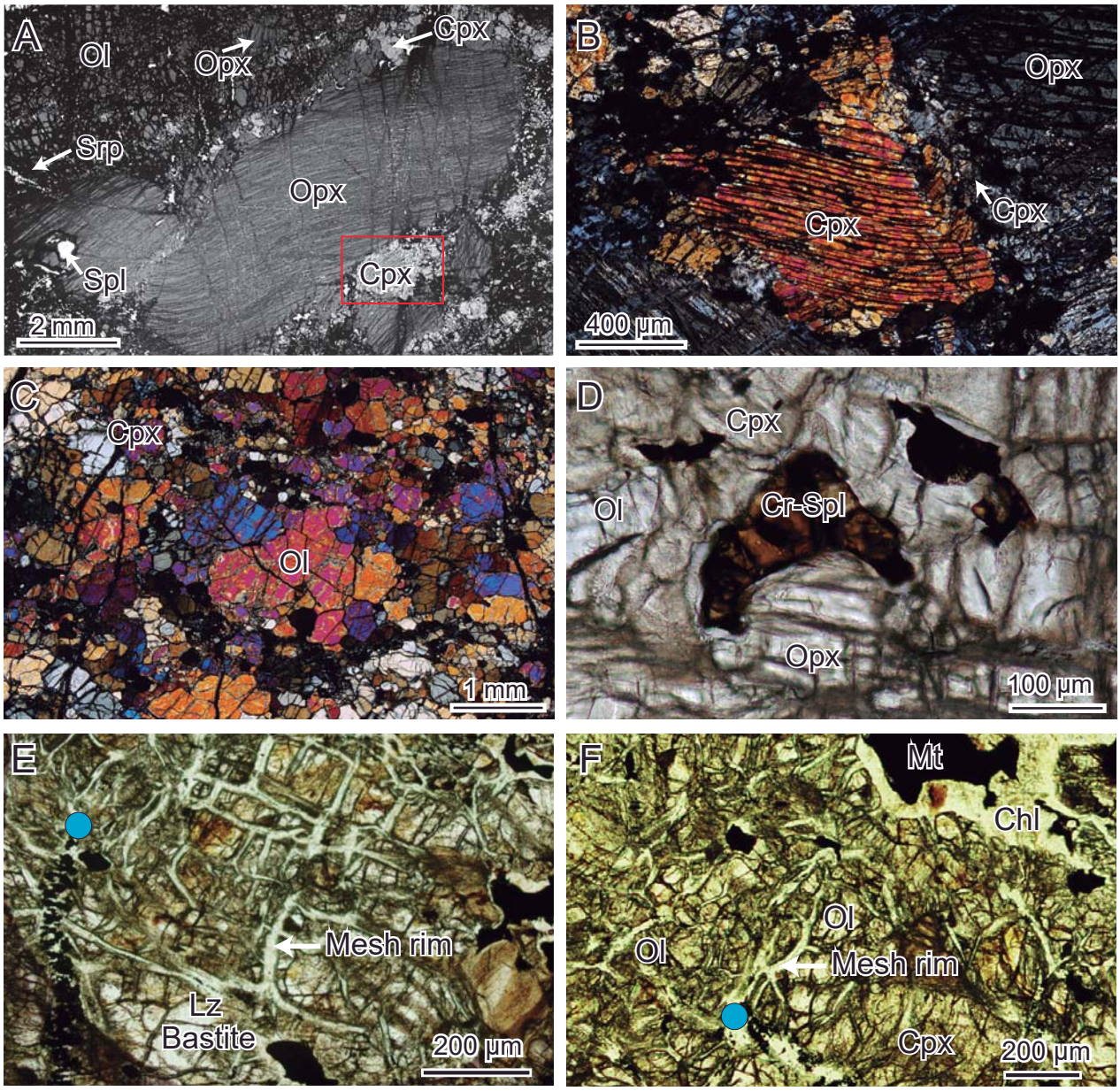

Figure. C4_3. *Back-scatter electron images (BSE) and optical photographs of group A serpentinized peridotites and serpentinites of VCSM. A) Porphyroclastic texture with highly deformed orthopyroxene porphyroclast replaced by serpentine (dark grey) and clinopyroxene surrounding orthopyroxene. B) Detail of image A) with deformed clinopyroxene showing oscillatory zoning, with surrounding small crystals of clinopyroxene. C) Porphyroclasts of olivine with crosscutting veins of serpentine. D) Cr-spinel with pale brownish colour with hypidiomorphic texture. E) Serpentine after olivine with mesh rim and bastite textures after orthopyroxene. F) Mesh rim textures and magnetite + chlorite as alteration product of Cr-spinel. Blue spot indicates the location of micro-Raman analysis obtained in these samples.*

Group B serpentinized peridotites and serpentinites display porphyroclastic texture. These show a higher degree of serpentinization (>80%), although relict mantle olivine, orthopyroxene and Cr-spinel are locally preserved (Figs C4_4).

Orthopyroxene porphyroclasts (*c.* 1-3 mm) are strongly affected by serpentinization (bastite pseudomorphs, Fig. C4_4A). In group B, clinopyroxene always appear as small crystals (*c.* <200 µm) in the

serpentinized matrix and do not display ondulose extinction (Fig. C4_4A); they could be interpreted as neoformed clinopyroxenes. Olivine tends to appear in the mesh center (*c.* 100 µm; Fig. C4_4B). Cr-spinel is anhedral and locally idiomorphic (*c.* 100-700 µm), showing a brown to reddish colour typical of Cr-spinel (Fig. C4_4C and C4_4D) and it are often completely replaced by magnetite surrounded by chlorite. Mesh textures commonly show typical lizardite sweeping extinction (black), interrupted by subdomains with different optical orientation (white) in the mesh center, and a mesh rim with magnetite (Figs. C4_4E and C4_4F).

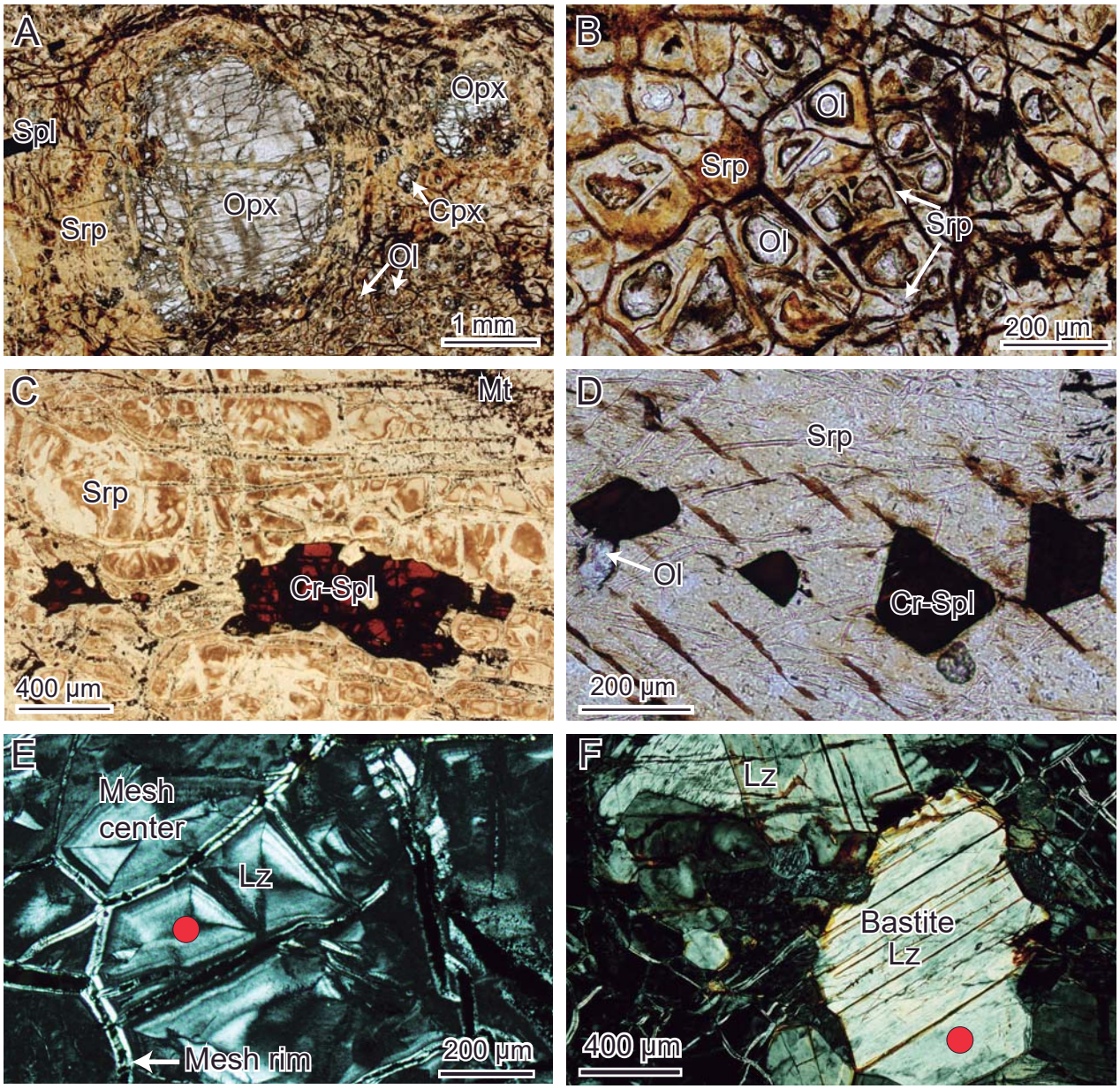

Figure. C4_4. *Optical photographs of group B serpentinized peridotites and serpentinites of VCSM. A) Porphyroclasts of orthopyroxene, olivine and Cr-spinel showing characteristic porphyroclastic texture with small crystals of neoformed clinopyroxene in the serpentine matrix. Serpentine (yellow) in the matrix replaces mantle minerals. B) Typical mesh texture, complete to partial serpentinitzation of olivine. Relicts of olivine are preserved in the mesh centre. C) Xenomorphic Cr-spinel with serpentine in a matrix of mesh texture. D) Idiomorphic Cr-spinel showing dark brown to reddish colour; note olivine relict in contact with Cr-spinel. E) Mesh center and mesh rim with magnetite. F) Bastite texture, lizardite replaces pyroxene. Lizardite red spot is the location of micro-Raman analysis obtained in these samples.*

The serpentinized peridotites and serpentinites of VCSM were classified in the Ol-Opx-Cpx ternary diagram (Fig. C4_5). Because the samples are completely or partially serpentinized, we use an algebraic method (SVD; Fisher, 1989 and 1993) to obtain mineral proportions of each sample using whole-rock geochemical data. This method allows one to condense the compositional space in a three component system: forsterite-enstatite-diopside (more details in Chapter 3). Group A and B rocks display a harzburgitic protolith (Fig. C4_5) indicating low contents of endmember clinopyroxenes confirmed by petrographic analysis in the less serpentinized peridotites (Fig. C4_3 and C4_4). However, group A has higher amounts of clinopyroxene (*c.* 2 %) than group B rocks (*c.* 0.4 %) (More details in Table C4_1).

Table C4_1. *Oxi-equivalent proportions of endmembers olivine, orthopyroxene and clinopyroxene of serpentinized peridotites and serpentinites from VCSM.*

Sample	Group type	Modes (Oxi-equivalent units %)			
		Olivine	Orthopyroxene	Clinopyroxene	Spinel
LV-2	A	55.2	36.5	3.2	5.1
08-VC-78	A	45.2	50.6	0.2	4
08-VC-130B	A	58.9	36.8	0.2	4.1
09-LV-10	A	50.4	43.9	1.9	3.8
09-LV-12A	A	54.5	40.8	0.3	4.4
7-LV-18	A	41.8	49.4	3.8	5
08-SCB-51	A	48	47.8	0.7	3.5
08-SCB-123B	A	47.2	48.7	1.4	2.7
08-SCB-124	A	44	50.4	0.5	5.1
08-SCB-127	A	42.7	48.4	3.2	5.7
09-LV-1A	B	57.1	40.4	0.4	2.1
09-LV-11B	B	46.8	52.2	0.3	0.7
7-LV-19A	B	46.9	51	0.2	1.9
7-LV-19C	B	45.6	51.3	0.3	2.8
08-SCB-40	B	47.4	49.8	0.2	2.6
08-SCB-127A	B	55.2	43	0.5	1.3
14-SC-1	B	49.4	49.1	0.7	0.8
14-SC-5	B	46.2	51.9	0.3	1.6
14-SC-6	B	50	48	0.5	1.5
14-SC-7	B	51.8	46.4	0.5	1.3

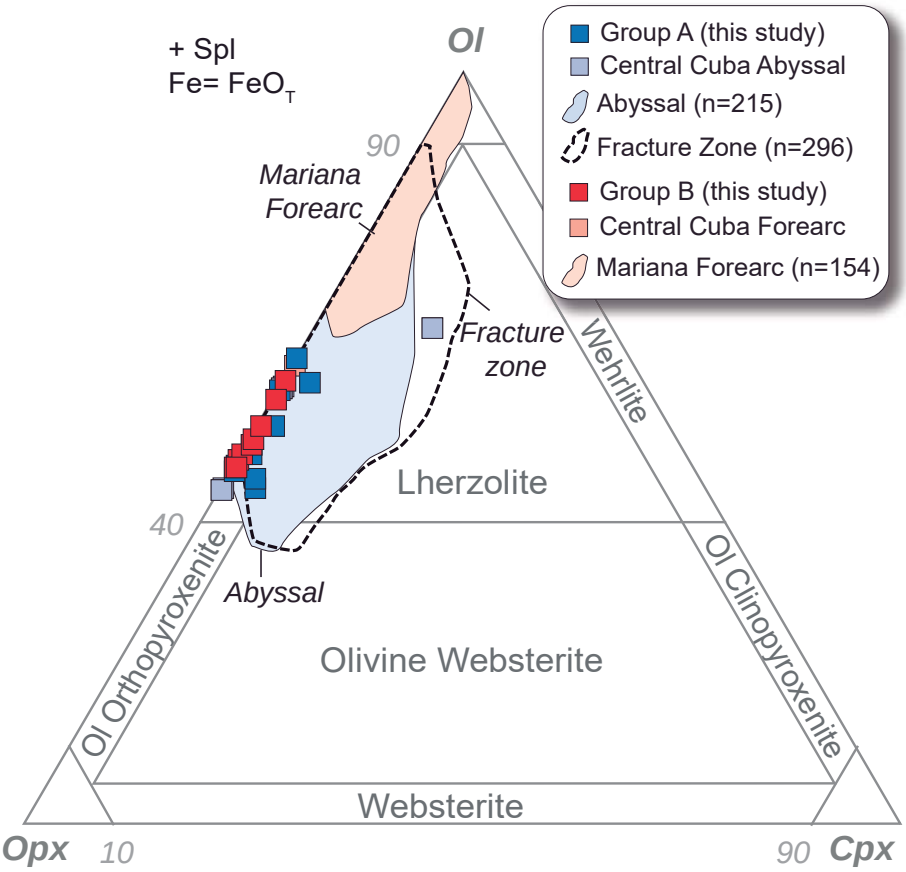

Figure. C4_5. *Classification diagram of ultramafic rocks (Le Maître et al., 2002) using whole-rock compositions plotted as oxi-equivalent proportions of olivine, orthopyroxene and clinopyroxene. Fields of abyssal peridotites and serpentinites (Niu, 2004; Paulick et al., 2006; Boschi et al., 2008; Kodolányi et al., 2012), fracture zone (PetDB compilation, Lehnert et al., 2000), forearc (Ishii et al., 1992; Savov et al., 2007; Kodolányi et al., 2012) and Central Cuba (Hattori and Guillot, 2007) are plotted for reference. See text for details.*

4.3. Mineral chemistry

Mineral compositions of spinel group minerals, olivine, pyroxene, serpentine group minerals and chlorite are displayed below. The mineral formula was normalized to certain oxygens, depending on each mineral, as elements per formula unit (p.f.u.). The olivine and spinel group minerals are normalized to 4 oxygens, pyroxenes to 6 oxygens, serpentine to 14 oxygens and chlorite to 28 oxygens (more details in chapter 3).

4.3.1. Spinel group minerals

The spinel group minerals display contrasting compositions in Cr-spinel in group A versus B rocks (Fig. C4_6A, Table C4_2). Figure C4_6B shows spinel group minerals that can be distinguished in Cr-spinel and magnetite.

Table C4_2. *Representative analyses of spinel group minerals from serpentinitic matrix.*

Sample	08-SCB-127	08-SCB-127	08-SCB-127	LV-2	08-SCB-127A	14-SC-5	14-SC-1	7-LV-19A
Rock type	Harzburgite			Serpentinite	Serpentinite		Harzburgite	Serpentinite
Group	A	A	A	A	B	B	B	B
Mineral	Cr-spinel			Magnetite	Cr-spinel			Magnetite
Major elements (wt%)								
SiO_2	0.06	b.d.l	0.09	0.89	0.01	0.01	0.02	0.41
TiO_2	0.08	0.02	0.07	0.38	0.07	b.d.l	0.05	0.09
Al_2O_3	49.79	56.44	51.45	1.22	31.44	31.80	21.04	0.10
Cr_2O_3	15.57	10.33	15.58	11.15	36.09	36.70	45.22	2.07
V_2O_3	0.13	0.08	0.13	b.d.l	0.18	0.12	0.22	0.03
FeOT*	12.38	13.27	12.12	77.94	16.38	15.81	20.94	92.16
MnO	0.18	0.17	0.13	0.96	0.25	0.18	0.53	0.10
ZnO	0.35	0.20	0.19	b.d.l	b.d.l	0.17	0.27	b.d.l
MgO	19.98	20.10	19.27	1.71	15.51	16.13	11.22	0.49
NiO	0.43	0.36	0.33	0.03	0.11	0.08	0.02	0.02
CaO	0.05	b.d.l	b.d.l	0.01	0.02	b.d.l	b.d.l	0.02
Total	99	100.98	99.36	94.31	100.07	100.99	99.52	95.59
Formula based 4 oxygens								
Si	0.00	-	0.00	0.03	0.00	0.00	0.00	0.02
Ti	0.00	0.00	0.00	0.01	0.00	-	0.00	0.00
Al	1.60	1.71	1.62	0.05	1.08	1.09	0.78	0.00
Cr	0.33	0.21	0.33	0.33	0.83	0.83	1.12	0.06
V	0.00	0.00	0.00	-	0.00	0.00	0.01	0.00
Fe^{+3}	0.06	0.08	0.05	1.53	0.08	0.07	0.09	1.90
Fe^{+2}	0.22	0.21	0.22	0.92	0.32	0.31	0.46	0.98
Mn	0.00	0.00	0.00	0.03	0.01	0.00	0.01	0.00
Zn	0.00	0.00	0.00	-	-	0.00	0.01	-
Mg	0.77	0.78	0.77	0.10	0.67	0.68	0.52	0.03
Ni	0.01	0.01	0.01	0.00	0.00	0.00	0.00	0.00
Ca	0.00	-	-	0.00	0.00	-	-	0.00
Cr#	0.17	0.11	0.17	0.86	0.44	0.43	0.59	0.93
Mg#	0.78	0.79	0.77	0.09	0.68	0.69	0.53	0.03
Fe^{+3}#	0.03	0.04	0.02	0.80	0.04	0.04	0.05	0.97

*FeOT expressed as FeO, Mg#=Mg/(Mg+Fe2+); Cr#=Cr/(Cr+Al); Fe3+#= Fe3+/(Cr+Al+Fe3+); b.d.l: below detection limit.

The composition of Cr-spinel shows substantial differences. In group A it is rich in Al (Fig. C4_6A) and Mg#=[Mg/(Mg+Fe^{2+})] = 0.75-0.79 and poor in Cr#=[Cr/(Cr+Al)] = 0.11-0.19, TiO_2 (0.02-0.08 wt %) and NiO (<0.43 wt %), while in group B it shows higher Cr, Cr# (0.39-0.61), lower Mg# (0.53-0.69) and NiO (<0.18 wt %) with similar TiO_2 (<0.11 wt %) (Fig. C4_6C and 6D). In figure C4_6C and 6D the group A Cr-spinels plot in the field of abyssal spinels, whereas group B plots in the forearc field. In light of the calculated melt extraction from fertile MORB mantle (FMM, from Choi et al., 2008), group A Cr-spinels show a lower melting degrees (less than 10% melting), than group B (> 15% melting).

The magnetite that formed after alteration of Cr-spinel has Cr_2O_3 <11.15wt%, TiO_2 <0.38wt% and NiO < 1.31 wt% contents. It has high values of Cr# (0.77-0.97) and Fe^{3+}#= [Fe^{3+}/(Cr+Al+Fe^{3+})] = 0.80-1 compared to primary mantelic Cr-spinel (Fig. C4_6B), which attests to the alteration path toward magnetite compositions of Cr-spinel in groups A and B.

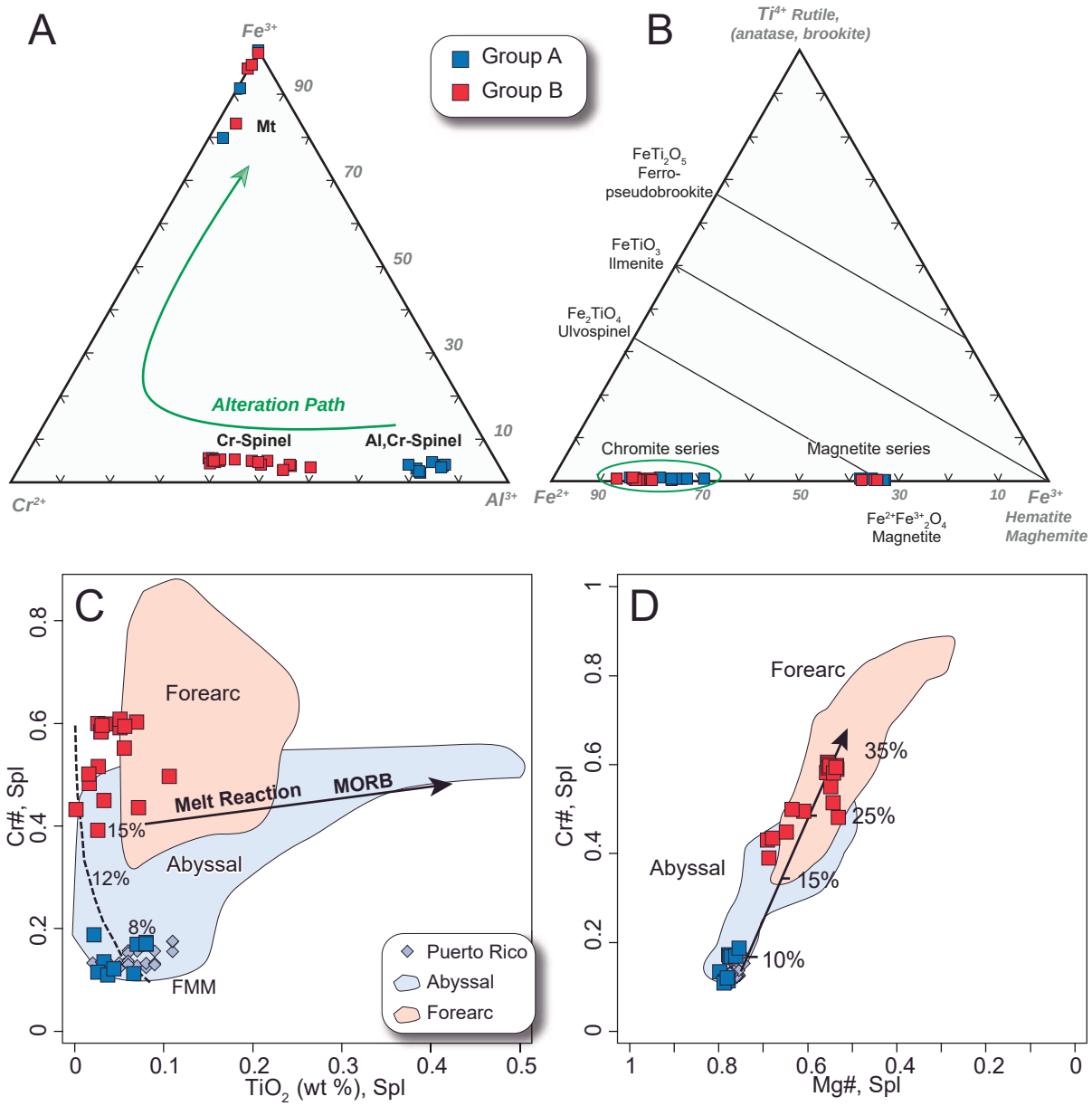

Figure. C4_6 *Composition of spinel group minerals from the serpentinitic matrix of VCSM. A) Ternary diagram Ti^{4+}-Fe^{2+}-Fe^{3+} calculated based on 3 cations per formula unit. B) Ternary diagram Fe^{3+}- Cr^{3+}- Al^{3+} based on 3 cations per formula unit. C) Cr#= Cr/(Cr+Al) vs TiO_2 in Cr-spinel. Dashed line indicates melt extraction from Fertile MORB Mantle (FMM) from Choi et al. (2008); D) Cr# vs Mg#=Mg/(Mg + Fe^{2+}) of Cr-spinel. Black arrow indicates percentage of melting (Dupuis et al., 2005). Field of abyssal Cr-spinel from Dick and Bullen (1984), Dick (1989), Dick et al. (2010). Field of forearc Cr-spinel from Ishii et al. (1992), Parkinson and Pearce (1998). The Puerto Rico Cr-spinel compositions are selected from Marchesi et al. (2011).*

4.3.2. Olivine

Forsterite content in olivine is lower in group A rocks (Fo_{90-92}) than in group B (Fo_{92-93}), with similar NiO (0.27-0.47 wt % group A and 0.35-0.44 wt% group B) (Fig. C4_7 and Table C4_3). Cr# in spinel and Fo in olivine are correlated with higher values in group B (Fig. C4_7).

Table C4_3. *Representative analyses of olivine from serpentinitic matrix.*

Sample	08-SCB-127	08-SCB-127	08-SCB-127	08-SCB-127	14-SC-1	14-SC-1	14-SC-1	14-SC-1
Rock type	Harzburgite				Harzburgite			
Group	A	A	A	A	B	B	B	B
Mineral	Olivine							
Major elements (wt%)								
SiO_2	40.35	40.35	40.78	40.67	40.84	40.73	40.75	40.80
TiO_2	b.d.l	0.01	b.d.l	b.d.l	b.d.l	0.02	0.01	0.03
Al_2O_3	0.01	b.d.l	b.d.l	b.d.l	b.d.l	b.d.l	b.d.l	0.01
Cr_2O_3	0.02	b.d.l	0.01	b.d.l	b.d.l	0.02	b.d.l	b.d.l
V_2O_3	n.a	b.d.l	b.d.l	b.d.l	0.01	b.d.l	0.01	0.02
FeO*	9.78	10.29	10.20	10.24	8.71	8.78	8.85	9.04
MnO	0.12	0.20	0.13	0.13	0.05	0.05	0.04	0.11
ZnO	n.a	b.d.l	b.d.l	b.d.l	b.d.l	0.04	b.d.l	b.d.l
MgO	48.42	49.59	49.48	49.58	49.97	50.89	50.88	50.37
NiO	0.44	0.47	0.38	0.35	0.41	0.42	0.40	0.41
CaO	0.02	b.d.l	0.01	0.01	0.01	0.01	0.02	0.01
Total	99.16	100.90	100.99	100.98	100.00	100.96	100.95	100.81
Formula based 4 oxygens								
Si	1.00	0.98	0.99	0.99	1.00	0.98	0.99	0.99
Ti	-	0.00	-	-	-	0.00	0.00	0.00
Al	0.00	-	-	-	-	-	-	0.00
Cr	0.00	-	0.00	-	-	0.00	-	-
V	-	-	-	-	0.00	-	0.00	0.00
Fe^{+3}	0.00	0.04	0.02	0.02	0.01	0.03	0.03	0.02
Fe^{+2}	0.20	0.17	0.19	0.18	0.17	0.14	0.15	0.16
Mn	0.00	0.00	0.00	0.00	0.00	0.00	0.00	0.00
Zn	-	-	-	-	-	0.00	-	-
Mg	1.79	1.80	1.79	1.79	1.82	1.83	1.82	1.82
Ni	0.01	0.01	0.01	0.01	0.01	0.01	0.01	0.01
Ca	0.00	-	0.00	0.00	0.00	0.00	0.00	0.00
Fo	0.90	0.92	0.91	0.91	0.91	0.93	0.92	0.92

*FeOT expressed as FeO, Fo=Mg/(Mg+Fe+2); n.a: not analyzed; b.d.l: below detection limit.

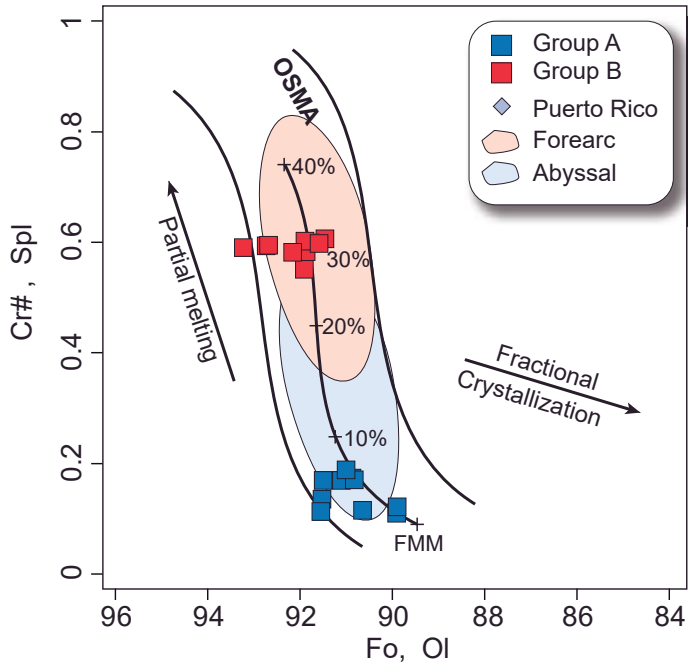

Figure. C4_7 *Compositions of Cr-spinel and olivine in equilibrium from the serpentinitic matrix of VCSM. Diagram Cr# of Cr-spinel vs Fo in olivine. Olivine-Spinel Mantle Array (OSMA) plotted as reference, from Choi et al. (2008). Field for abyssal Cr-spinel and olivine from Dick and Bullen (1984), Dick (1989), Dick et al. (2010). Field for forearc Cr-spinel and olivine from Ishii et al. (1992), Parkinson and Pearce (1998). The Puerto Rico spinel and olivine compositions were selected from Marchesi et al. (2011).*

4.3.3. Pyroxenes

Group A orthopyroxene (En_{86-90} Wo_{1-4} Fs_{9-11}; Mg# = 90-91) is richer in Al_2O_3 (2.43-6.13 vs 0.99-1.52 wt %), TiO_2 (<0.15 wt % vs <0.04 wt %) and Cr_2O_3 (0.15-0.83 vs 0.18-0.54 wt %), but poorer in Cr# (4-11 vs 11-20) than group B rocks (En_{89-90} Wo_{1-2} Fs_{8-9}, Mg# = 91) (Fig. C4_8 and Table C4_4).

Meanwhile, group A clinopyroxene has diopside-augite compositions (En_{48-59} Wo_{36-48} Fs_{4-6}) with high Al_2O_3 (3.71-4.89 wt %), TiO_2 (0.21-0.36 wt %), and Na_2O (0.49-0.81 wt %), with Mg# (92-93) and low Cr# (6-8) (Fig. C4_8 and Table C4_4), though group B clinopyroxene only shows diopsidic composition (En_{49-50} Wo_{46-48} Fs_{3-4}) with lower Al_2O_3 (1.01-1.62 wt%), TiO_2 (0.02-0.07 wt%), and Na_2O (<0.06), but higher Mg# (93-94) and Cr# (16-25) than group A clinopyroxene (Fig. C4_8). In group A two types of clinopyroxene can be distinguished by petrography and mineral chemistry. Augite appears as large porphyroclasts, whereas diopside occurs as small crystals without deformation (Fig. C4_3A and C4_3B). Furthermore, group B clinopyroxenes (only diopside; Fig. C4_4A) display the same petrographic appearance as diopsides of group A.

The clinopyroxenes and orthopyroxenes of both rock types were plotted in the Wo-En-Fs diagram (Fig. C4_8E). The diagram reflects pyroxene solvus relations and tie-lines (after Lindsley, 1983) at different temperatures under constant 5 kbar pressure. Diopsides of group A and B display compositions that fall in the low temperature solvus region, indicating that such clinopyroxenes are not primary, as petrography

would indicate. Nonetheless, augitic compositions point to tie-lines (augite-orthopyroxene pairs) in a high temperature solvus region (1000 to 1200ºC) showing compositions of primary clinopyroxene. In order to constrain the origin of the mantle protoliths, we will therefore consider only high-T clinopyroxenes in between 1000 to 1200ºC, i.e. only augitic ones (Fig. C4_8E).

Table C4_4. *Representative analyses of orthopyroxene and clinopyroxene from serpentinitic matrix.*

Sample	08-SCB-127	08-SCB-127	08-SCB-127	08-SCB-127	14-SC-1	14-SC-1	14-SC-1	14-SC-1
Rock type	Harzburgite				Harzburgite			
Group	A	A	A	A	B	B	B	B
Mineral	Enstatite				Enstatite			
Major elements (wt%)								
SiO_2	53.39	52.70	53.92	53.26	56.99	57.31	57.16	56.69
TiO_2	0.08	0.12	0.15	0.13	b.d.l	0.02	0.01	0.01
Al_2O_3	5.89	5.71	5.90	5.60	1.41	1.05	1.19	1.32
Cr_2O_3	0.67	0.66	0.56	0.57	0.49	0.21	0.38	0.40
V_2O_3	b.d.l	0.07	0.02	b.d.l	0.02	b.d.l	0.03	0.02
FeO*	6.56	6.52	6.67	6.83	5.91	6.01	5.81	5.93
MnO	0.17	0.23	0.19	0.14	0.14	0.08	0.14	0.20
ZnO	0.02	0.04	0.02	b.d.l	0.04	b.d.l	b.d.l	0.03
MgO	32.67	32.49	31.71	32.71	34.49	35.36	35.01	34.96
NiO	0.04	0.13	0.15	0.12	0.11	0.08	0.08	0.08
CaO	0.46	0.36	1.21	0.51	0.87	0.54	0.76	0.61
Na_2O	0.01	0.02	0.08	0.04	0.03	b.d.l	b.d.l	0.01
Total	99.96	99.06	100.59	99.91	100.50	100.66	100.57	100.26
Formula based 6 oxygens								
Si	1.84	1.83	1.86	1.84	1.95	1.96	1.96	1.94
Ti	0.00	0.00	0.00	0.00	-	0.00	0.00	0.00
Al	0.24	0.24	0.24	0.23	0.06	0.04	0.05	0.05
Cr	0.02	0.02	0.02	0.02	0.01	0.01	0.01	0.01
V	-	0.00	0.00	-	0.00	-	0.00	0.00
Fe^{+3}	0.05	0.07	0.03	0.07	0.02	0.04	0.03	0.05
Fe^{+2}	0.14	0.12	0.17	0.13	0.15	0.13	0.14	0.12
Mn	0.00	0.01	0.01	0.00	0.00	0.00	0.00	0.01
Zn	0.00	0.00	0.00	-	0.00	-	-	0.00
Mg	1.68	1.69	1.63	1.69	1.76	1.80	1.79	1.79
Ni	0.00	0.00	0.00	0.00	0.00	0.00	0.00	0.00
Ca	0.02	0.01	0.04	0.02	0.03	0.02	0.03	0.02
Na	0.00	0.00	0.01	0.00	0.00	-	-	0.00
Wo %	0.90	0.72	2.39	0.99	1.63	0.99	1.40	1.12
En %	88.83	88.92	87.03	88.43	89.55	90.29	90.02	90.01
Fs %	10.26	10.36	10.57	10.57	8.82	8.72	8.58	8.86
Mg#	89.88	89.88	89.45	89.51	91.23	91.30	91.48	91.31
Cr#	7.06	7.24	5.98	6.38	18.78	11.93	17.85	17.03

*FeOT expressed as FeO, Mg#=Mg/(Mg+Fe2+); Cr#=Cr/(Cr+Al); b.d.l: below detection limit.

Table C4_4. *Continued.*

Sample	08-SCB-127	08-SCB-127	08-SCB-127	08-SCB-127	14-SC-1	14-SC-1	14-SC-1	14-SC-1
Rock type	Harzburgite				Harzburgite			
Group	A	A	A	A	B	B	B	B
Mineral	Augite		Diopside		Diopside			
Major elements (wt%)								
SiO_2	52.70	51.86	52.31	52.20	54.25	54.32	54.18	54.04
TiO_2	0.29	0.31	0.24	0.31	0.02	b.d.l	0.05	0.04
Al_2O_3	4.52	4.45	3.71	4.18	1.14	1.25	1.25	1.37
Cr_2O_3	0.50	0.49	0.48	0.40	0.39	0.49	0.50	0.59
V_2O_3	n.a	n.a	0.03	0.09	0.01	0.02	0.01	0.04
FeO*	2.78	2.96	2.40	2.67	2.23	2.13	2.03	1.98
MnO	0.07	0.10	0.11	0.08	0.09	b.d.l	b.d.l	0.02
MgO	18.29	18.65	16.24	16.42	18.35	18.12	17.74	17.54
NiO	0.05	0.05	0.06	b.d.l	0.05	0.04	0.05	0.07
CaO	21.23	19.92	22.99	22.94	23.69	23.73	23.95	24.12
Na_2O	0.56	0.72	0.78	0.81	0.05	0.04	0.06	0.04
Total	100.99	99.52	99.36	100.09	100.27	100.14	99.82	99.85
Formula based 6 oxygens								
Si	1.88	1.87	1.91	1.89	1.96	1.97	1.97	1.96
Ti	0.01	0.01	0.01	0.01	0.00	-	0.00	0.00
Al	0.19	0.19	0.16	0.18	0.05	0.05	0.05	0.06
Cr	0.01	0.01	0.01	0.01	0.01	0.01	0.01	0.02
V	-	-	0.00	0.00	0.00	0.00	0.00	0.00
Fe^{+3}	0.06	0.09	0.06	0.07	0.02	0.00	0.00	0.00
Fe^{+2}	0.02	0.00	0.02	0.01	0.04	0.06	0.06	0.06
Mn	0.00	0.00	0.00	0.00	0.00	-	-	0.00
Mg	0.97	1.00	0.88	0.88	0.99	0.98	0.96	0.95
Ni	0.00	0.00	0.00	-	0.00	0.00	0.00	0.00
Ca	0.81	0.77	0.90	0.89	0.92	0.92	0.93	0.94
Na	0.04	0.05	0.05	0.06	0.00	0.00	0.00	0.00
Wo %	43.41	41.27	48.35	47.86	46.42	46.89	47.69	48.16
En %	52.04	53.77	47.52	47.67	50.03	49.82	49.15	48.73
Fs %	4.66	4.95	4.13	4.47	3.55	3.29	3.16	3.12
Mg#	92.14	91.83	92.34	91.64	93.62	93.81	93.97	94.04
Cr#	6.91	6.92	8.03	6.06	18.67	20.82	21.16	22.41

*FeOT expressed as FeO, Mg#=Mg/(Mg+Fe2+); Cr#=Cr/(Cr+Al); n.a: not analyzed; b.d.l: below detection limit.

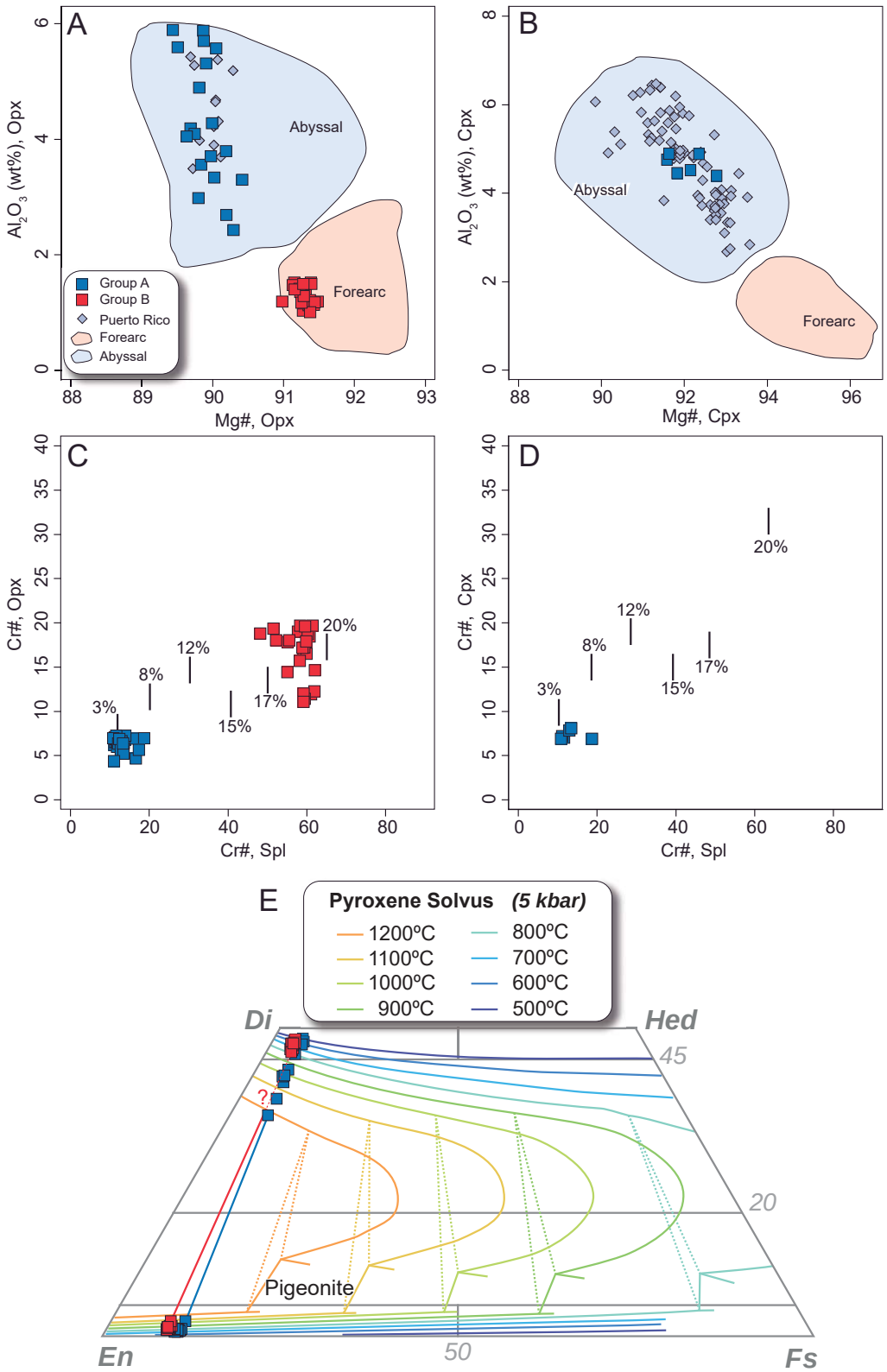

Figure. C4_8 *Orthopyroxene and clinopyroxene compositions from the serpentinitic matrix of VCSM. A) Al_2O_3 content vs Mg# of Opx. B) Al_2O_3 content vs Mg# of Cpx. C) Cr# of Opx vs Cr# of Spl. D) Cr# of Cpx vs Cr# of Spl. E) Pyroxene quadrilateral diagram with tie-lines and curves of pyroxene solvus at different temperatures for a constant 5 kbar pressure (solvus and tie-lines by Lindsley, 1983). In diagrams A) to D) primary pyroxenes are plotted, whereas in diagram E) Primary and secondary pyroxenes are plotted. Melt fractions plotted in C) and D) taken from Choi et al. (2008). Abyssal field from Dick (1989), Johnson et al. (1990), Pearce et al. (2000), Dick et al. (2010). Forearc field from Ishii et al. (1992), Parkinson and Pearce (1998), Pearce et al. (2000). The Puerto Rico pyroxene compositions were selected from Marchesi et al. (2011).*

4.3.4. Serpentine group minerals

Serpentine from group A has high Al_2O_3 (1.60-4.11 wt.%) and low FeO_t (2.67-4.10 wt.%) (Fig. C4_9A), pointing to the tschermak exchange vector (Si(Mg, Fe)-Al_{-2}) as the main control on Al contents (Table C4_5). The negative correlation between Fe and Mg denotes the $FeMg_{-1}$ exchange vector (Fig. C4_9B). Group B serpentine is depleted in Al_2O_3 (<0.67 wt.%) and enriched in FeO_t (1.54-8.26 wt.%) relative to Group A serpentine, whereas Mg# is similar in the two groups (group A: 0.94-0.96; group B: 0.88-0.98; Fig. C4_9B).

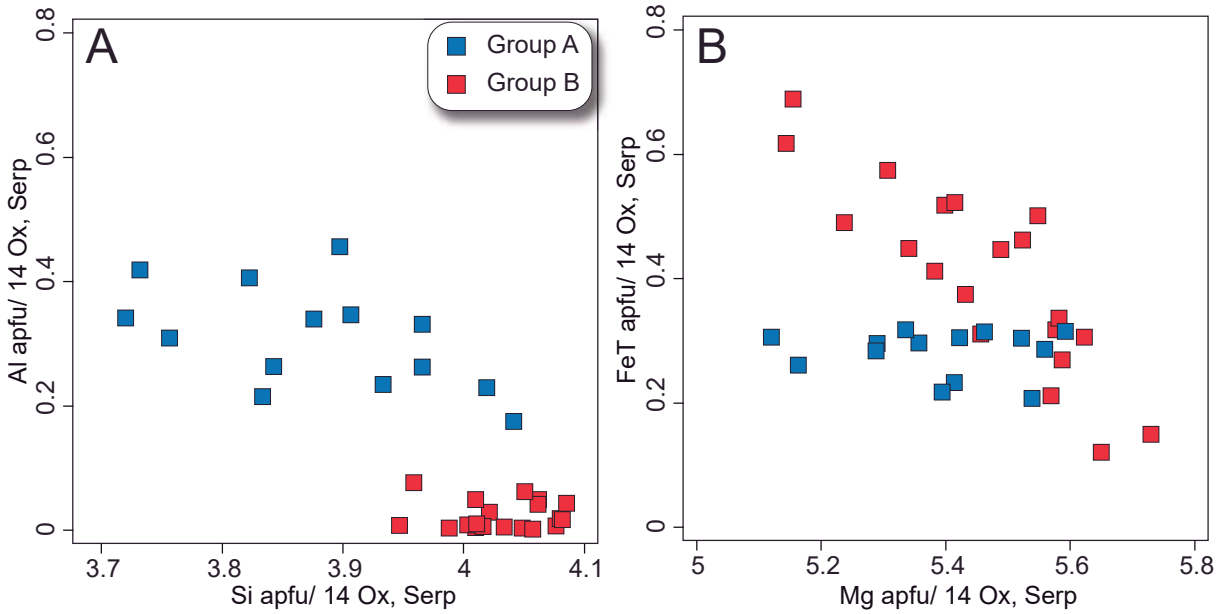

Figure. C4_9 *Serpentine group mineral composition of group A and B rocks from the serpentinitic matrix of VCSM. A) Al vs Si. B) Fe vs Mg.*

Raman spectroscopy allows lizardite to be characterized as the most abundant phase in bastite and mesh textures (Fig. C4_10A and C4_10B) from both groups, though rare antigorite is locally present (Fig. C4_10C). Late serpentine veins of group A are formed by chrysotile (Fig. C4_10D).

Table C4_5. *Representative analyses of serpentine group minerals from serpentinitic matrix .*

Sample	09-LV-12A	LV-2	LV-2	08-SCB-127	09-LV-11B	14-SC-5	09-LV-1A	14-SC-1
Rock type	Serpentinite			Harzburgite	Serpentinite			Harzburgite
Group	A	A	A	A	B	B	B	B
Mineral	Serpentine				Serpentine			
Major elements (wt%)								
SiO_2	41.07	41.41	41.53	42.58	42.44	42.94	43.75	41.54
TiO_2	0.08	0.04	0.04	0.04	b.d.l	b.d.l	b.d.l	b.d.l
Al_2O_3	2.91	4.11	3.09	2.39	b.d.l	0.26	0.17	0.03
Cr_2O_3	0.86	0.48	0.58	0.08	0.03	0.02	b.d.l	b.d.l
V_2O_3	b.d.l	n.a	n.a	0.01	b.d.l	0.03	b.d.l	0.02
FeO*	3.23	3.89	3.80	2.99	5.56	1.91	2.71	5.76
MnO	0.08	0.06	0.11	0.03	0.03	b.d.l	b.d.l	b.d.l
ZnO	b.d.l	n.a	n.a	0.01	b.d.l	0.05	b.d.l	0.04
MgO	35.87	36.49	38.50	38.99	37.15	41.04	40.06	38.59
NiO	0.36	0.27	0.07	0.07	0.15	0.27	0.33	0.29
CaO	0.03	0.09	0.02	0.05	0.08	0.06	0.06	0.03
Na_2O	b.d.l	0.02	b.d.l	b.d.l	b.d.l	b.d.l	b.d.l	0.02
K_2O	b.d.l	b.d.l	b.d.l	n.a	b.d.l	b.d.l	0.01	n.a
Cl	n.a	0.07	b.d.l	0.02	n.a	n.a	n.a	0.04
Total	84.49	86.93	87.73	87.26	85.44	86.62	87.09	86.36
Formula based 14 oxygens								
Si	3.97	3.90	3.88	3.97	4.09	4.02	4.08	3.99
Ti	0.01	0.00	0.00	0.00	-	-	-	-
Al	0.33	0.46	0.34	0.26	-	0.03	0.02	0.00
Cr	0.07	0.04	0.04	0.01	0.00	0.00	-	-
V	-	-	-	0.00	-	0.00	-	0.00
Fe^{+2}	0.26	0.31	0.30	0.23	0.45	0.15	0.21	0.46
Mn	0.01	0.00	0.01	0.00	0.00	-	-	-
Zn	-	-	-	0.00	-	0.00	-	0.00
Mg	5.16	5.12	5.36	5.41	5.34	5.73	5.57	5.52
Ni	0.03	0.02	0.01	0.01	0.01	0.02	0.02	0.02
Ca	0.00	0.01	0.00	0.00	0.01	0.01	0.01	0.00
Na	-	0.00	-	-	-	-	-	0.00
K	-	-	-	-	-	-	0.00	-
Cl	-	0.01	-	0.00	-	-	-	0.01
Mg#	0.95	0.94	0.95	0.96	0.92	0.97	0.96	0.92
Mg+Fe+Mn+Ni	5.46	5.45	5.67	5.65	5.80	5.90	5.81	6.01

*FeOT expressed as FeO, Mg#=Mg/(Mg+Fe2+); n.a: not analyzed; b.d.l: below detection limit.

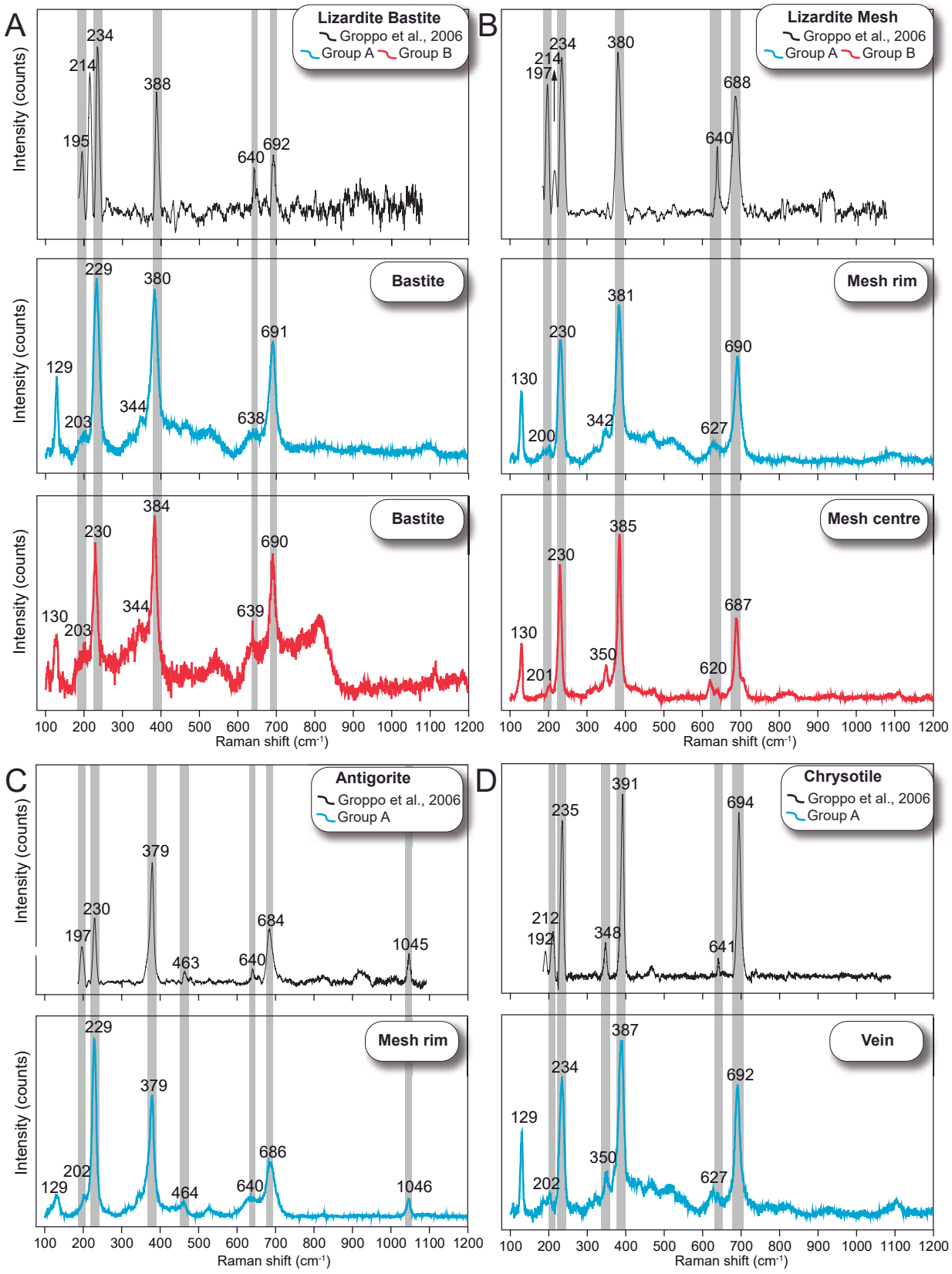

Figure. C4_10 *Micro-Raman spectra of serpentine in group A and B rocks from the serpentinitic matrix of VCSM. A) and B) Spectra of lizardite in bastite and mesh texture of group A and B rocks, respectively. C) and D) Antigorite and chrysotile spectra in group A rocks. Point analysis of Micro-Raman spectra in figures C4_3 and C4_4. Reference Raman spectra of lizardite from Groppo et al. (2006).*

4.3.5. Chlorite

Chlorite from both groups of rocks is clinochlore (29.37-34.66 wt.% SiO_2; 31.16-34.88 wt.% MgO and Mg#=0.92-0.95; Table C4_6).

Table C4_6. *Representative analyses of chlorite from serpentinitic matrix.*

Sample	08-SCB-127	LV-2	7-LV-19A	7-LV-19A
Rock type	Harzburgite	Serpentinite	Serpentinite	Serpentinite
Group	A	A	B	B
Mineral	Chlorite		Chlorite	
Major elements (wt%)				
SiO_2	33.24	30.60	32.50	34.66
TiO_2	b.d.l	0.04	b.d.l	b.d.l
Al_2O_3	17.02	20.75	18.14	15.97
Cr_2O_3	0.02	0.12	0.09	0.15
FeO*	3.32	4.21	4.09	4.18
MnO	b.d.l	0.04	0.05	0.05
MgO	34.33	32.14	33.16	33.93
NiO	0.07	0.08	0.19	0.30
CaO	0.03	0.00	0.02	0.02
Total	88.03	87.98	88.24	89.26
Formula based 28 oxygens				
Si	6.18	5.73	6.06	6.38
Ti	-	0.01	-	-
Al	3.73	4.58	3.98	3.46
Cr	0.00	0.02	0.01	0.02
Fe^{+2}	0.52	0.66	0.64	0.64
Mn	-	0.01	0.01	0.01
Mg	9.51	8.96	9.21	9.31
Ni	0.01	0.01	0.03	0.04
Ca	0.01	0.00	0.00	0.00
Mg#	0.95	0.93	0.94	0.94

*FeOT expressed as FeO, Mg#=Mg/(Mg+Fe2+); b.d.l: below detection limit.

4.4. Whole-rock composition

4.4.1. Major elements

The loss on ignition (LOI) values of serpentinized peridotites and serpentinites range from 11.72 wt% to 13.8 wt% in group A and 12.37 wt% to 16.4 wt% in group B, indicating high hydration up to fully serpentinized peridotite (see Table C4_7). For this reason, the major element compositions of studied samples are given below in an anhydrous basis. Major element concentrations of group A and B have a similar SiO_2/MgO ratio (c. 0.8-1; Fig. C4_11A) with variable contents of FeO_t and CaO (Fig. C4_11B and C4_11C). However, group A displays high contents in Al_2O_3 (1.48-3.66 wt% vs 0.28-1.75 wt% group B; Fig. C4_11A) and TiO_2 (0.04-0.1 wt% group A vs <0.03 wt% group B; Fig. C4_11D) with respect to group B samples.

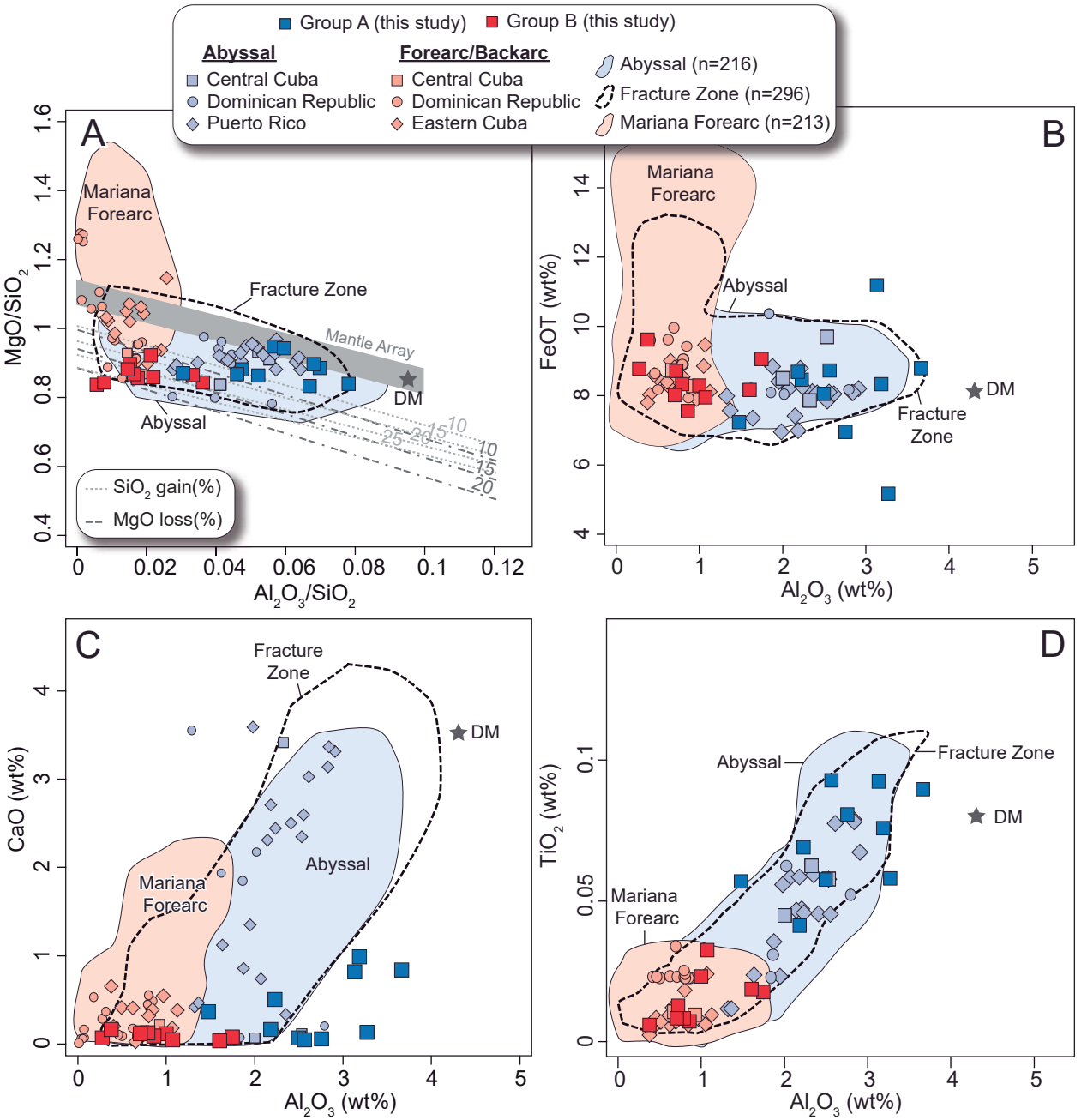

Figure. C4_11 *Whole-rock composition of serpentinized peridotites and serpentinites from serpentinitic matrix of the VCSM. A) MgO/SiO_2 vs. Al_2O_3/SiO_2. B) FeO_t wt% vs Al_2O_3wt%. C) CaO wt% vs Al_2O_3 wt%. D) TiO_2 wt% vs Al_2O_3 wt%. Other peridotites and serpentinites plotted for comparison: central Cuba (abyssal and forearc related serpentinites: Hattori and Guillot, 2007; Deschamps et al., 2012), eastern Cuba (backarc-related Moa-Baracoa, and forearc-related Mayarí-Cristal Massif, Marchesi et al., 2006); Dominican Republic (abyssal- and forearc-related peridotites from Loma Caribe, Camú and Septentrional fault zone, Puerto Plata and Rio San Juan: Saumur et al., 2010; Escuder et al., 2014; Marchesi et al., 2016), Puerto Rico (abyssal-related peridotites from Monte del Estado, Marchesi et al., 2011). Fields of abyssal (Mid Atlantic Ridge and Hess Deep: Kodolányi et al., 2012; Mid Atlantic Ridge: Paulick et al., 2006; Southwest Indian Ridge, American Antartic Ridge, Central Indian Ridge, Pacific Antartic Ridge: Niu, 2004), fracture zone (PetDB compilation, Lehnert et al., 2000) and Mariana forearc (Ishii et al., 1992; Savov et al., 2005; Kodolányi et al., 2012) are plotted for reference. Estimated composition of depleted mantle (DM) is from Salters and Stracke (2004). Dashed lines of SiO_2 gain and MgO loss by Malvoisin (2015). All data are presented on anhydrous basis.*

Table C4_7. *Whole-rock and trace element composition of samples from serpentinitic matrix of VCSM.*

Sample	LV-2	08-VC-78	08-VC-130B	09-LV-10	09-LV-12A	7-LV-18	08-SCB-51	08-SCB-123B	08-SCB-124
Latitude	22°27'10.55"N	22°22'34.80"N	22°19'25.00"N	22°23'6.70"N	22°19'56.69"N	22°21'4.85"N	22°21'43.20"N	22°20'51.25"N	22°20'54.74"N
Longitude	79°52'30.16"W	79°57'32.00"W	79°55'10.25"W	79°50'41.70"W	79°55'24.18"W	79°57'34.62"W	79°56'45.43"W	79°50'40.82"W	79°50'38.79"W
Group	A	A	A	A	A	A	A	A	A
Serpentinitzation*	72%	98%	100%	97%	100%	100%	100%	99%	100%
Major elements (wt%)									
SiO_2	38.84	41.62	39.07	40.96	40.13	40.87	40.44	40.97	40.67
TiO_2	0.08	0.05	0.08	0.06	0.07	0.07	0.04	0.05	0.05
Al_2O_3	2.71	2.17	2.21	1.94	2.39	2.73	1.86	1.25	2.77
Fe_2O_3T	10.77	7.78	8.35	8.19	6.7	7.95	8.22	6.79	4.87
MnO	0.14	0.1	0.14	0.16	0.15	0.09	0.13	0.11	0.15
MgO	34.4	35.94	37.05	36.13	37.82	34.05	35.09	35.64	36.5
CaO	0.71	0.06	0.04	0.44	0.05	0.85	0.14	0.31	0.11
Na_2O	b.d.l	b.d.l	b.d.l	b.d.l	b.d.l	0.01	b.d.l	b.d.l	b.d.l
K_2O	b.d.l	b.d.l	b.d.l	b.d.l	b.d.l	b.d.l	b.d.l	b.d.l	b.d.l
P_2O_5	0.01	0.01	0.01	0.01	0.01	b.d.l	0.01	b.d.l	0.01
LOI	11.72	12.07	12.39	11.86	12.44	12.6	13.1	13.7	13.8
Total	99.38	99.8	99.34	99.75	99.76	99.22	99.02	98.83	98.92
Trace elements (ppm)									
B	n.a	12.7	65.6	23.8	98.8	n.a	54.3	30.7	n.a
Li	0.63	4.83	0.278	0.295	0.337	1.982	1.377	0.344	0.262
Rb	0.551	0.493	0.499	0.222	0.344	0.328	0.279	0.264	0.204
Cs	0.026	0.321	0.013	0.015	0.032	0.013	0.204	0.014	0.031
Be	0.01	0.079	0.058	b.d.l	0.023	0.03	0.017	0.026	b.d.l
Sr	1.068	6.614	0.78	1.3	0.875	2.29	5.469	1.187	0.584
Ba	2.214	11.321	1.433	1.005	2.354	5.006	22.817	4.552	2.053
Sc	16.111	10.048	14.308	12.383	15.397	9.771	12.421	12.367	12.389
V	81.53	45.996	61.36	52.249	58.689	55.38	57.734	43.659	45.696
Cr	2934.584	2397.715	2544.501	3272.148	2582.558	2250.273	2564.806	3480.75	3231.766
Co	106.342	94.096	101.623	105.801	92.908	88.094	107.666	97.931	88.479
Ni	2699.659	1799.888	2222.073	2693.034	2133.204	1743.479	2241.475	3064.675	2495.87
Cu	23.942	2.168	12.881	26.246	34.942	25.408	22.259	11.823	22.143
Zn	47.702	48.144	54.618	58.23	61.803	32.09	37.37	37.576	64.383
Ga	2.005	2.148	2.053	2.018	1.957	2.679	2.092	1.518	1.762

Total Fe as Fe_2O_3T; b.d.l: below detection limit; *visual estimation

Table C4_7. *Continued.*

Sample	LV-2	08-VC-78	08-VC-130B	09-LV-10	09-LV-12A	7-LV-18	08-SCB-51	08-SCB-123B	08-SCB-124
Y	2.011	1.6	2.039	1.321	2.086	1.798	1.509	1.117	1.716
Nb	0.117	0.136	0.098	0.061	0.088	0.062	0.042	0.057	0.044
Zr	7.6	6.9	8.1	5.4	6.2	5	b.d.l	b.d.l	b.d.l
Mo	0.759	0.374	0.5	0.516	0.556	0.114	0.118	0.136	0.15
Sn	0.216	0.244	0.213	0.211	0.277	0.875	0.861	0.999	0.83
Tl	0.005	0.008	0.003	0.002	0.004	0.009	0.01	0.007	0.007
Pb	1.786	0.64	0.623	0.198	0.478	0.206	0.402	0.509	0.238
U	0.03	0.013	0.02	0.009	0.01	0.008	0.003	0.004	0.004
Th	0.153	0.073	0.1	0.018	0.036	0.03	0.011	0.014	0.009
La	0.045	0.094	0.05	0.026	0.082	0.161	0.025	0.038	0.031
Ce	0.123	0.269	0.155	0.064	0.16	0.136	0.052	0.066	0.074
Pr	0.026	0.041	0.03	0.018	0.022	0.05	0.009	0.011	0.025
Nd	0.178	0.254	0.217	0.093	0.136	0.28	0.065	0.088	0.164
Sm	0.118	0.084	0.108	0.063	0.078	0.111	0.057	0.075	0.107
Eu	0.041	0.047	0.035	0.021	0.027	0.056	0.031	0.05	0.028
Gd	0.186	0.153	0.176	0.117	0.154	0.185	0.126	0.107	0.185
Tb	0.038	0.027	0.037	0.02	0.041	0.038	0.027	0.017	0.034
Dy	0.273	0.224	0.275	0.16	0.265	0.288	0.213	0.153	0.234
Ho	0.068	0.053	0.066	0.037	0.066	0.066	0.056	0.031	0.07
Er	0.194	0.175	0.199	0.104	0.225	0.218	0.141	0.115	0.178
Tm	0.034	0.032	0.031	0.021	0.035	0.035	0.03	0.021	0.032
Yb	0.244	0.188	0.233	0.151	0.241	0.232	0.223	0.156	0.188
Lu	0.043	0.032	0.041	0.026	0.042	0.034	0.034	0.028	0.033
Hf	0.021	0.049	0.03	0.007	0.009	0.073	0.034	0.04	0.08
Os (ppb)	n.a	2	3	n.a	n.a	n.a	n.a	n.a	n.a
Ir	n.a	4	4	n.a	n.a	n.a	n.a	n.a	n.a
Ru	n.a	7	10	n.a	n.a	n.a	n.a	n.a	n.a
Rh	n.a	3	4	n.a	n.a	n.a	n.a	n.a	n.a
Pt	n.a	17	16	n.a	n.a	n.a	n.a	n.a	n.a
Pd	n.a	21	15	n.a	n.a	n.a	n.a	n.a	n.a
Au	n.a	3	3	n.a	n.a	n.a	n.a	n.a	n.a
Total PGE	n.a	54	52	n.a	n.a	n.a	n.a	n.a	n.a

Table C4_7. *Continued.*

Sample	08-SCB-127	09-LV-1A	09-LV-11B	7-LV-19A	7-LV-19C	08-SCB-40	08-SCB-127A	14-SC-1	14-SC-5	14-SC-6	14-SC-7
Latitude	22°21'12.14"N	22°27'15.70"N	22°23'42.36"N	22°21'2.06"N	22°21'0.50"N	22°29'14.38"N	22°32'3.67"N	22°22'26.58"N	22°19'50.35"N	22°19'51.25"N	22°19'50.08"N
Longitude	79°50'35.02"W	79°47'35.70"W	79°52'7.14"W	79°57'35.27"W	79°57'30.63"W	79°51'43.21"W	79°52'58.90"W	79°57'31.34"W	79°42'54.95"W	79°42'53.85"W	79°42'53.51"W
Group	A	B	B	B	B	B	B	B	B	B	B
Serpentinitzation*	64%	99%	98%	99%	99%	99%	99%	80%	98%	99%	98%
Major elements (wt%)											
SiO_2	40.31	40.63	42.63	42.02	41.26	41.2	40.8	41.05	40.41	40.91	40.79
TiO_2	0.08	0.02	b.d.l	0.03	0.02	0.02	0.01	0.01	0.01	0.01	0.01
Al_2O_3	3.15	0.86	0.24	0.92	1.5	1.37	0.62	0.32	0.71	0.67	0.59
Fe_2O_3T	8.39	7.95	8.43	7.6	8.61	7.74	8.3	9.02	6.89	7.81	7.51
MnO	0.13	0.06	0.11	0.08	0.12	0.11	0.07	0.11	0.09	0.1	0.11
MgO	33.86	37.47	35.71	36.08	34.8	35.63	36.6	34.64	34.58	35.52	35.98
CaO	0.72	0.1	0.06	0.04	0.07	0.03	0.11	0.14	0.07	0.11	0.1
Na_2O	0.03	b.d.l	b.d.l	0.01	b.d.l	b.d.l	0.01	b.d.l	0.02	b.d.l	b.d.l
K_2O	0.02	b.d.l	0.02	b.d.l	0.01	0.01	0.01	b.d.l	0.01	0.01	0.01
P_2O_5	0.01	0.01	0.01	0.01	0.01	0.01	b.d.l	0.01	0.01	b.d.l	0
LOI	12.4	12.37	12.38	12.4	12.8	13.1	12.7	13.9	16.4	14.1	14.1
Total	99.09	99.47	99.59	99.19	99.19	99.21	99.23	99.18	99.18	99.23	99.2
Trace elements (ppm)											
B	53.3	14.6	n.a	n.a	n.a	n.a	n.a	n.a	n.a	n.a	n.a
Li	0.846	0.109	0.224	0.139	0.333	0.127	0.111	0.303	1.327	2.501	1.336
Rb	0.395	0.254	0.191	0.313	0.214	0.199	0.364	0.301	0.311	0.19	0.231
Cs	0.356	0.015	0.007	0.014	0.015	0.017	0.014	0.01	0.013	0.017	0.014
Be	b.d.l	0.011	b.d.l	0.011	0.011	0.023	0.011	0.011	b.d.l	b.d.l	
Sr	2.272	2.91	1.789	0.748	1.528	0.925	1.441	1.063	1.322	1.712	2.043
Ba	7.318	4.119	1.013	2.615	2.981	5.273	4.007	0.843	1.02	5.752	7.69
Sc	9.932	8.656	3.487	7.601	5.797	8.464	4.199	4.607	5.709	6.183	7.099
V	59.638	37.305	17.134	44.435	38.532	41.194	32.495	25.578	33.046	37.196	29.373
Cr	2333.029	3881.678	2044.161	2440.099	2263.574	1866.21	1643.228	1577.826	2176.257	1904.416	1616.477
Co	82.373	86.677	117.836	95.953	94.731	91.301	88	90.916	98.103	93.732	97.396
Ni	1994.307	2192.165	2462.952	2356.173	2112.047	2085.591	2170.099	2057.509	2408.876	2182.513	2247.844
Cu	20.826	3.709	2.147	36.385	20.374	3.761	6.445	4.729	7.242	3.917	12.17
Zn	41.382	48.229	43.097	30.889	50.793	25.898	23.564	29.865	29.359	30.474	32.611
Ga	2.131	1.06	0.502	1.12	1.757	1.052	0.631	0.483	0.654	0.838	0.633

Table C4_7. *Continued.*

Sample	08-SCB-127	09-LV-1A	09-LV-11B	7-LV-19A	7-LV-19C	08-SCB-40	08-SCB-127A	14-SC-1	14-SC-5	14-SC-6	14-SC-7
Y	1.7	0.344	0.09	0.292	0.57	0.327	0.258	0.09	0.161	0.146	0.12
Nb	0.038	0.093	0.066	0.043	0.049	0.079	0.047	0.031	0.034	0.034	0.042
Zr	b.d.l	4.2	5	b.d.l	b.d.l	6	b.d.l	b.d.l	4	b.d.l	b.d.l
Mo	0.122	0.58	0.349	0.15	0.184	0.141	0.218	0.097	0.123	0.129	0.13
Sn	0.854	0.213	0.191	0.905	0.862	0.985	1.047	0.843	0.831	0.88	0.838
Tl	0.011	0.001	0.003	0.007	0.006	0.008	0.005	0.006	0.01	0.022	0.033
Pb	0.401	0.258	0.294	0.15	0.332	0.225	0.162	0.18	0.123	0.162	0.314
U	0.005	0.014	0.012	0.004	0.009	0.009	0.021	0.005	0.008	0.004	0.004
Th	0.007	0.027	0.009	0.013	0.013	0.041	0.018	0.008	0.01	0.005	0.008
La	0.052	0.021	0.036	0.021	0.099	0.152	0.062	0.042	0.035	0.185	0.034
Ce	0.041	0.062	0.11	0.026	0.113	0.351	0.096	0.06	0.041	0.032	0.056
Pr	0.016	0.011	0.007	0.006	0.024	0.037	0.016	0.009	0.009	0.03	0.01
Nd	0.155	0.058	0.022	0.036	0.149	0.153	0.088	0.025	0.037	0.121	0.042
Sm	0.096	0.016	0.005	0.015	0.039	0.03	0.021	0.008	0.006	0.019	0.012
Eu	0.043	0.008	0.001	0.009	0.009	0.018	0.01	0.002	0.002	0.004	0.003
Gd	0.181	0.019	0.006	0.026	0.059	0.026	0.016	0.008	0.008	0.018	0.011
Tb	0.035	0.003	b.d.l	0.005	0.008	0.005	0.003	0.002	0.001	0.003	0.002
Dy	0.248	0.017	0.005	0.038	0.064	0.038	0.024	0.007	0.008	0.017	0.015
Ho	0.063	0.008	0.002	0.01	0.018	0.011	0.009	0.002	0.004	0.004	0.004
Er	0.201	0.027	0.007	0.034	0.06	0.034	0.024	0.01	0.017	0.015	0.012
Tm	0.03	0.004	0.001	0.007	0.009	0.006	0.003	0.002	0.004	0.003	0.003
Yb	0.2	0.035	0.017	0.041	0.063	0.043	0.028	0.02	0.024	0.02	0.023
Lu	0.03	0.007	0.004	0.005	0.01	0.01	0.007	0.003	0.004	0.004	0.006
Hf	0.061	b.d.l	0.01	0.021	0.028	0.126	0.014	0.015	0.034	0.02	0.012
Os (ppb)	n.a	3	3	n.a	n.a	n.a	n.a	n.a	n.a	n.a	n.a
Ir	n.a	4	4	n.a	n.a	n.a	n.a	n.a	n.a	n.a	n.a
Ru	n.a	7	9	n.a	n.a	n.a	n.a	n.a	n.a	n.a	n.a
Rh	n.a	2	3	n.a	n.a	n.a	n.a	n.a	n.a	n.a	n.a
Pt	n.a	11	10	n.a	n.a	n.a	n.a	n.a	n.a	n.a	n.a
Pd	n.a	9	7	n.a	n.a	n.a	n.a	n.a	n.a	n.a	n.a
Au	n.a	2	10	n.a	n.a	n.a	n.a	n.a	n.a	n.a	n.a
Total PGE	n.a	36	36	n.a	n.a	n.a	n.a	n.a	n.a	n.a	n.a

4.4.2. Trace elements

C1 chondrite-normalized Rare Earth Element (REE) compositions of group A samples have lower contents of Light Rare Earth Elements (LREE) (La_N/Sm_N =0.13-0.94) relative to middle REE (MREE) and heavy REE (HREE) (Gd_N/Lu_N =0.40-0.75) and variable Eu anomaly ($(Eu/Eu^*)_N$ =0.61-1.70) (Fig. C4_12A). On the other hand, group B rocks are depleted in all REE (Fig. C4_12B), though LREE (La_N/Sm_N=0.82-6.08) and HREE (Gd_N/Lu_N= 0.19-0.73) are enriched relative to MREE, resulting in concave upwards U-shaped normalized patterns (Fig. C4_12B). The Eu anomaly in group B is variable from negative to positive ($(Eu/Eu^*)_N$ =0.56-1.96 (Fig. C4_12B).

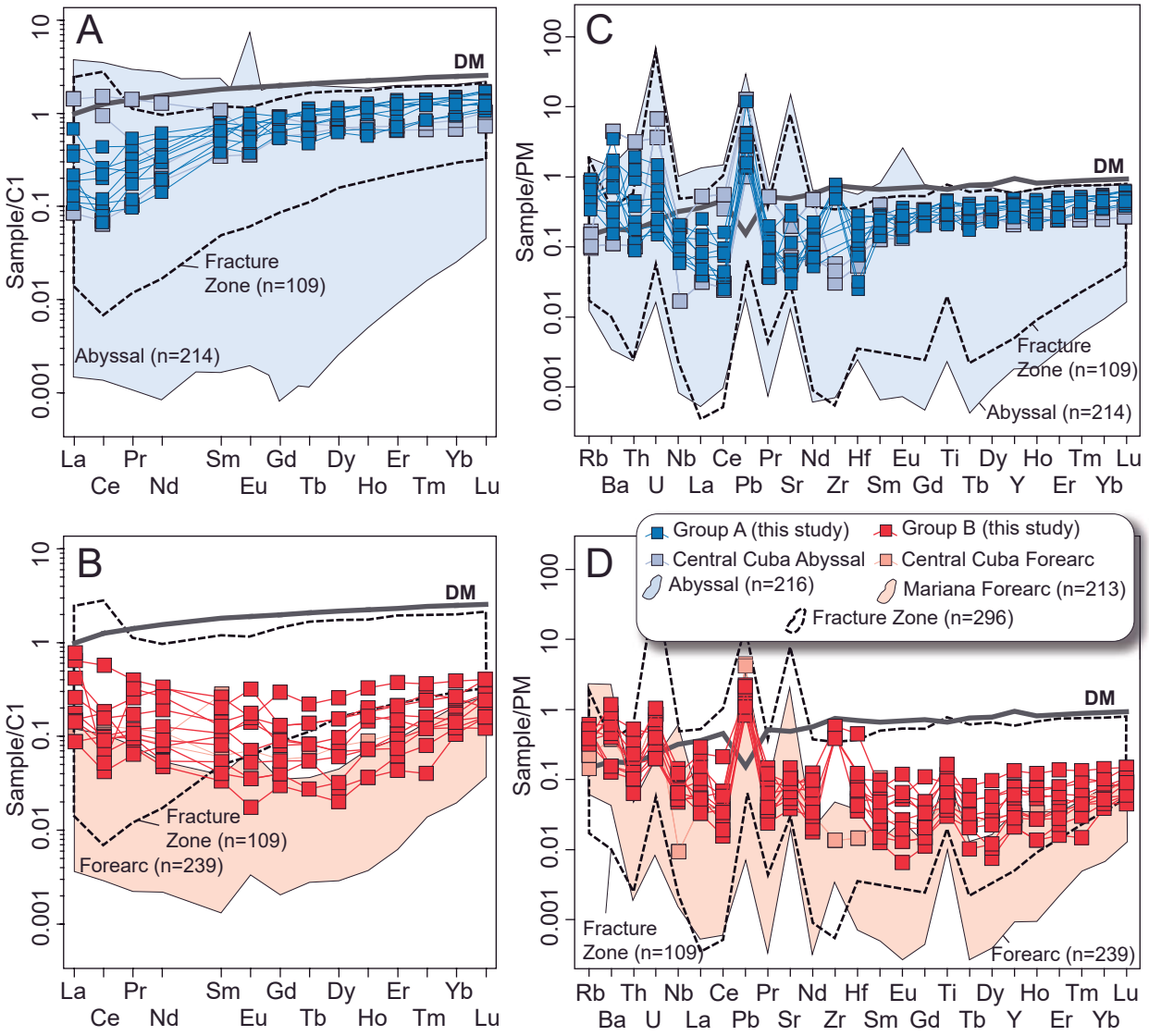

Figure. C4_12 *Normalized trace element composition from the serpentinitic matrix of the VCSM. A) and B) Chondrite-normalized whole-rock REE composition. C) and D) Primitive mantle-normalized whole-rock trace element composition. Chondrite (C1) and primitive mantle (PM) normalizing values are from McDonough and Sun (1995). Black line is depleted mantle (DM) composition from Salters and Stracke (2004). See references in Fig. C4_11 for central Cuba, abyssal, fracture zone and forearc peridotites.*

Large ion lithophile elements (LILE; Cs, Rb, Ba and U) in group A and B are enriched (Fig. C4_12C, C4_12D, C4_13A and C4_13B). Most notably, the High Field Strength Elements (HFSE) illustrate the contrasting nature of the two groups of rocks (Fig. C4_13C), group A having high contents of HFSE (e.g., Ti, Fig. C4_13C), whereas group B is depleted.

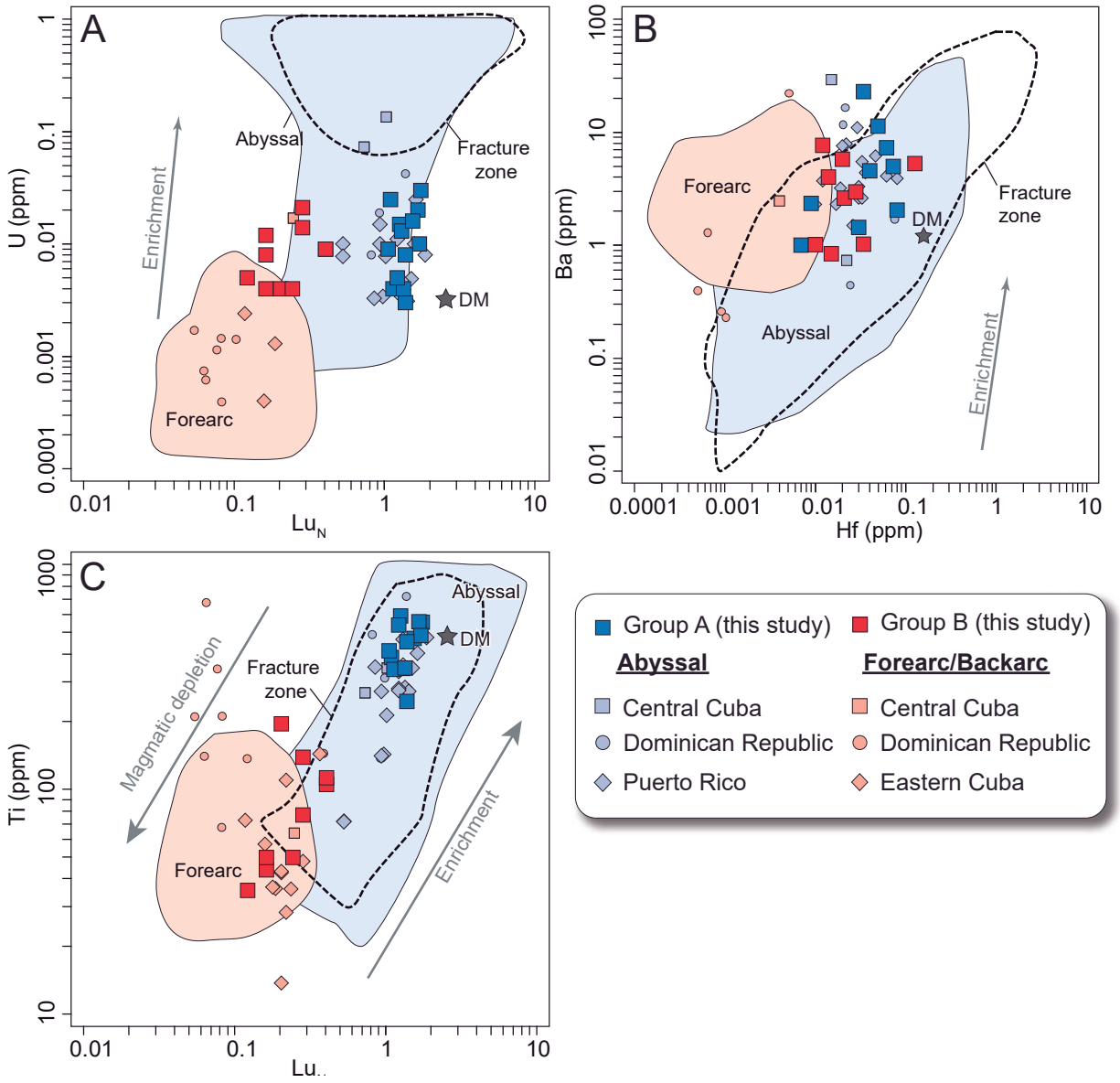

Figure. C4_13 *Whole-rock trace elements for group A and B rocks from the serpentinitic matrix of VCSM. A) U vs Lu_N. B) Ba vs Hf and C) Ti vs Lu_N. Depleted mantle (DM) composition from Salters and Stracke (2004). Lu is normalized to C1 chondrite composition of McDonough and Sun (1995). Fields of abyssal, fracture zone and forearc are plotted for reference (References as in Fig. C4_11).*

4.4.3. Platinum-group elements

The Platinum-group elements (PGE) have similar concentrations in both groups of rock: group A with 42 ppb and group B with 36 ppb (Table C4_7). The concentrations of Ir group elements (Ir, Os and Ru) are close to depleted mantle (Figs C4_14A and C4_14B), while Pd group elements (Rh, Pt and Pd) are slightly enriched relative to depleted mantle (Figs C4_14A and C4_14B).

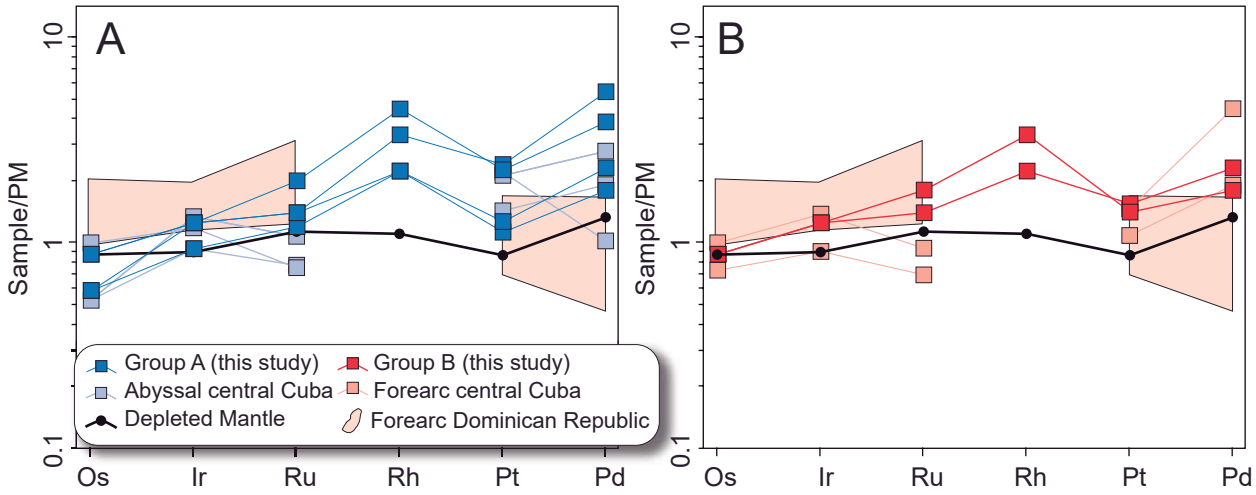

Figure. C4_14 *A) and B) PGE spider diagram of group A and B rocks from serpentinitic matrix of VCSM normalized to primitive mantle (PM). Plotted for comparison are forearc serpentinites from central Cuba (Hattori and Guillot, 2007); Dominican Republic (Saumur et al., 2009) and depleted mantle (black line, Salters and Stracke, 2004). Primitive mantle normalizing values are from McDonough and Sun (1995).*

4.4.4. Nd-Sr-Pb-B isotope systematics

The isotopic compositions of studied samples in both groups are similar with the exception of B isotopes (Table C4_8). Measured $^{87}Sr/^{86}Sr$ and $^{143}Nd/^{144}Nd$ ratios in group A rocks range 0.70492-0.70853 and 0.51247-0.51274, respectively, while measured $^{206}Pb/^{204}Pb$ (18.02-18.45), $^{207}Pb/^{204}Pb$ (15.56-15.62) and $^{208}Pb/^{204}Pb$ ratios (37.92-38.34) show restricted variation. Group B rocks have measured $^{87}Sr/^{86}Sr$ values of 0.70665-0.70776 and $^{143}Nd/^{144}Nd$ of 0.51249 (measurement was only possible in one sample; see Samples and Methods. Group B displays restricted measured $^{206}Pb/^{204}Pb$ (17.97-18.23), $^{207}Pb/^{204}Pb$ (15.48-15.63) and $^{208}Pb/^{204}Pb$ ratios (37.60-38.35). Group A rocks show a range of $\delta^{11}B$ of 1.43-11.10‰, whereas group B has higher values of $\delta^{11}B$ (18.23‰).

Table C4_8. *Isotopic composition of samples from the serpentinitic matrix of the VCSM*

Sample	08-VC-130B	09-LV-10	09-LV-12A	08-SCB-51	08-SCB-123B	08-SCB-127	09-LV-1A	09-LV-11B	08-SCB-40	08-SCB-127A	14-SC-1	14-SC-7
Group	A	A	A	A	A	A	B	B	B	B	B	B
B (ppm)	65.6	23.8	98.8	54.3	30.7	53.3	14.6	n.a	n.a	n.a	n.a	n.a
$d^{11}B$ (‰)	9.94	1.43	9.67	3.70	11.10	6.96	18.23	n.a	n.a	n.a	n.a	n.a
Sr (ppm)	0.78	1.3	0.875	5.469	1.187	2.272	2.91	1.789	0.925	1.441	1.063	2.043
Nd (ppm)	0.194	0.131	0.136	0.065	0.116	0.261	0.058	0.022	0.18	0.088	0.025	0.042
Pb (ppm)	0.623	0.198	0.478	0.402	0.509	0.401	0.258	0.294	0.225	0.162	0.18	0.314
$^{87}Sr/^{86}Sr$	0.70853	0.70774	0.70582	0.70492	0.70712	0.70790	0.70665	0.70776	0.70742	0.70754	0.70764	0.70735
$^{87}Sr/^{86}Sr$ error	0.0001	0.000009	0.00007	0.000007	0.0001	0.000024	0.000035	0.000062	0.000036	0.000028	0.000044	0.000019
$^{147}Sm/^{144}Nd$	0.3530	0.3180	b.d.l	b.d.l	0.4250	0.3370	b.d.l	b.d.l	0.1320	b.d.l	b.d.l	b.d.l
$^{143}Nd/^{144}Nd$	0.51251	0.51258	b.d.l	b.d.l	0.51247	0.51274	b.d.l	b.d.l	0.51249	b.d.l	b.d.l	b.d.l
$^{143}Nd/^{144}Nd$ error	0.009	0.008	b.d.l	b.d.l	0.008	0.003	b.d.l	b.d.l	0.008	b.d.l	b.d.l	b.d.l
$^{206}Pb/^{204}Pb$	18.35	18.02	18.45	18.39	18.29	18.31	18.18	17.97	18.21	18.22	18.23	18.01
$^{207}Pb/^{204}Pb$	15.62	15.58	15.58	15.56	15.58	15.57	15.49	15.48	15.58	15.60	15.63	15.58
$^{208}Pb/^{204}Pb$	38.34	37.92	38.21	38.19	38.28	38.23	37.79	37.60	38.31	38.25	38.35	37.95
$^{206}Pb/^{204}Pb_t$	18.31	17.97	18.42	18.38	18.28	18.29	18.11	17.92	18.16	18.06	18.20	17.99
$^{207}Pb/^{204}Pb_t$	15.61	15.58	15.58	15.56	15.58	15.57	15.49	15.48	15.58	15.59	15.63	15.58
$^{208}Pb/^{204}Pb_t$	38.27	37.89	38.18	38.18	38.27	38.22	37.75	37.59	38.24	38.21	38.33	37.94
$^{87}Sr/^{86}Sr_t$	0.7052	0.7069	0.7038	0.7047	0.7060	0.7070	0.7062	0.7072	0.7063	0.7062	0.7062	0.7068
$^{143}Nd/^{144}Nd_t$	0.51222	0.51232	b.d.l	b.d.l	0.51213	0.51246	-	-	0.51238	-	-	-

n.a: not analyzed; b.d.l: below detection limit;

T= 125Ma; Eclogitic metamorphic peak event in Santa Clara serpentinitic mélange that indicates pre-Aptian subduction (125Ma, García-Casco et al., 2002)

4.5. Discussion of serpentinitic matrix of the VCSM

4.5.1. Enrichment processes in the serpentinitic matrix of VCSM

Serpentinized peridotites and serpentinites from the matrix of the VCSM exhibit variable degrees of serpentinization (*c.* 45% to 100%; Table C4_7). In order to track the peridotite primary processes, first we focus on the effects of enrichment and element mobility. Group A and B rocks display low values of MgO/SiO_2 in comparison to the mantle array (Fig. C4_11A; Niu, 2004 and references therein). This is in agreement with a process of enrichment (melt/fluid) and magmatic depletion (e.g., Niu, 2004). Group A and B rocks underwent MgO loss and SiO_2 enrichment (*c.* 25% MgO loss and *c.* 15% SiO_2 gain, Fig. C4_11A; e.g. Malvoisin, 2015 and references therein). The MgO depletion may be a consequence of serpentinite formation after olivine and dissolution of brucite (e.g. Niu, 2004; see also mesh texture in supplementary material Figs. C4_3E and C4_4E). The enrichment in SiO_2 could be due to serpentinization. Fluids enriched in silica interact with peridotite at high fluid-rock interaction (e.g. Paulick et al., 2006; Boschi et al., 2008; Malvoisin, 2015). The CaO vs Al_2O_3 diagram shows poor correlations in group A and B rocks (Fig. C4_11C). Some authors suggest depletion of Ca is a result of serpentinitzation (e.g. Janecky and Seyfried, 1986; Palandri and Reed, 2004; Iyer et al., 2008). Notwithstanding, it is difficult to assess if such depletion is linked to depletion of the peridotitic protoliths (Deschamps et al., 2013). In addition, Al_2O_3, and TiO_2 are considered unchanged during serpentinization, as evidenced by their positive correlation (Fig. C4_11D; Niu, 2004 and references therein).

Group A and B rocks have a positive correlation with high field strength elements (HFSE) and MREE to HREE, which indicates behaviour was associated with magmatic process (Fig. C4_11C, C4_11D, C4_15A and C4_15B), like mantle partial melting (e.g. Niu, 2004; see below chapter 4.5.3). At low temperature conditions (< 400-500 ºC) the HFSE (e.g. Nb, Ti and Hf) behave as immobile elements (You et al., 1996; Kogiso et al., 1997). Both groups nevertheless show an enrichment in large ion lithophile elements (LILE; e.g. Cs, Rb, Ba and U), Pb and LREE (Fig. C4_15C). The high content in these elements could be associated with enrichment processes related to melt/fluid peridotite interactions (e.g. Niu, 2004; Paulick et al., 2006; Deschamps et al., 2013). LILE have been considered mobile in the presence of fluids, such as during serpentinization (e.g. Niu, 2004; Savov et al., 2005 and references therein), as evidenced by the poor correlation between LILE and HSFE (Fig. C4_13A and C4_13B). The REE patterns show a relative enrichment in LREE as opposed to HREE in group B rocks (Fig. C4_12, C4_15A to C4_15B). The LREE enrichment in serpentinines has been associated with melt/rock interaction (e.g., Bodinier et al., 1996; Niu, 2004). The post-melting refertilization best explains bulk-rock REE compositions. because LREE enrichments are mobilized by fluid/melts at high T, which fits in a context of subduction initiation where melts have formed due to mantle decompression. Such basaltic melts most likely interact with surrounding peridotites- giving rise to LREE-enriched compositions.

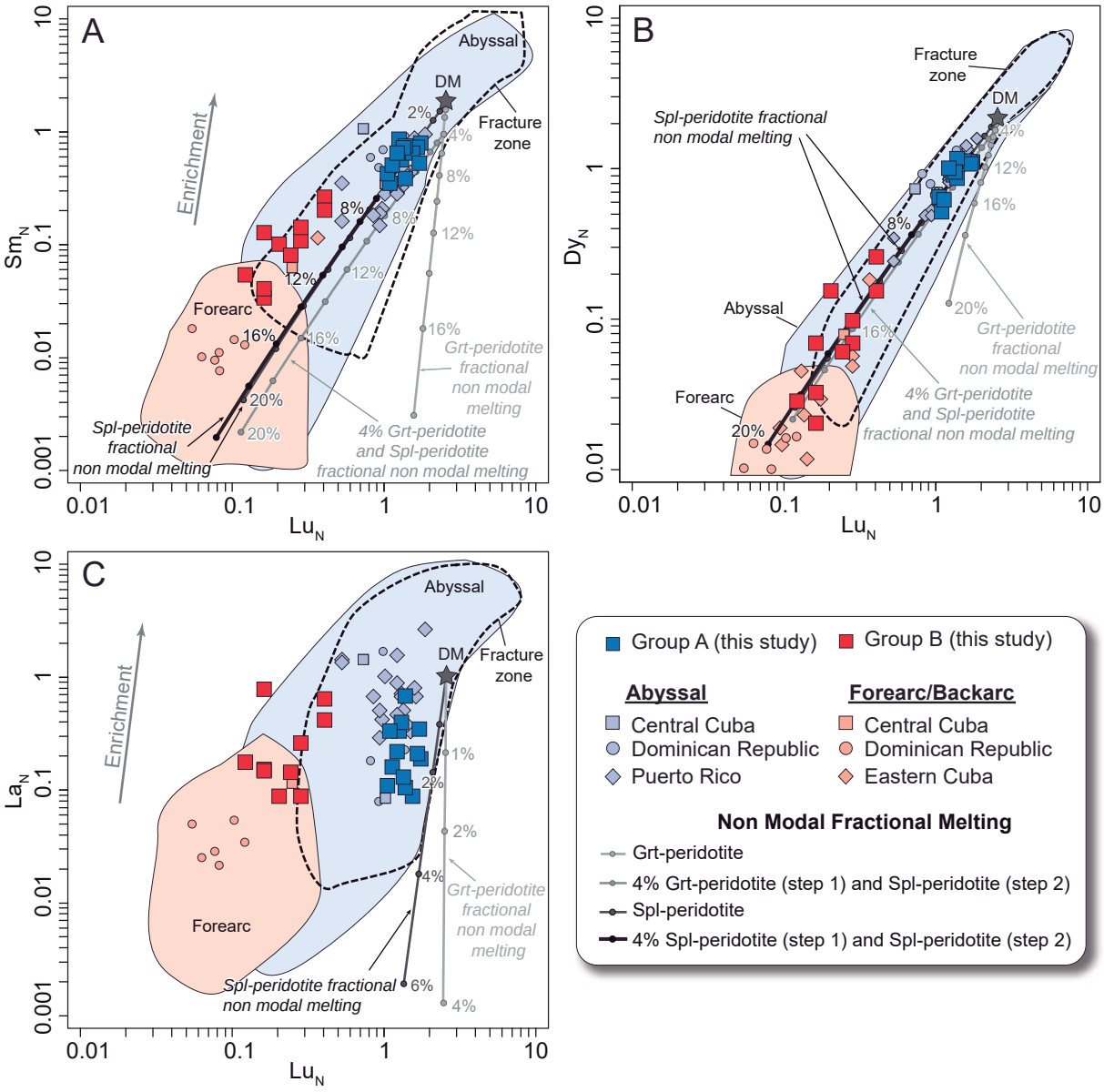

Figure. C4_15 *Melting models for group A and B rocks from the serpentinitic matrix of VCSM. A) Sm_N vs Lu_N. B) Dy_N vs Lu_N.C) La_N vs Lu_N plots. Spinel and garnet facies melting models are plotted for reference. Depleted mantle (DM) composition from Salters and Stracke (2004). The modelling was done following the equation of hydrous non-modal fractional melting (Johnson et al., 1990) in spinel and garnet peridotite facies. Source and melting modes and partition coefficients are reported in chapter 3.9 and Table C3_2. Percentages indicate degrees of melting. Fields of abyssal, fracture zone and forearc are plotted for comparison (references as in Fig. C4_11).*

We consider that the enrichment process of VSCM serpentinites was controlled by fluids/melts in a context of abyssal and/or subduction zone setting. Late serpentinization can be related to a seawater alteration of oceanic lithosphere (e.g., Boschi et al., 2008; Delacour et al., 2008) and/or be produced by fluid release from slab devolatilization in the context of a subduction setting (e.g., Spandler and Pirard, 2013; Baitsch-Ghirardello et al., 2014; Ribeiro et al., 2015; Cannaó et al., 2016). Major and trace elements of A and B serpentinized peridotites and serpentinites from VCSM show contrasted compositional features of abyssal and mantle wedge serpentinites, respectively (Fig. C4_11, C4_12, C4_13 and C4_15). Thus, the key is to assess the contribution of the seawater/slab devolatilization in the serpentinization process.

4.5.2. Role of serpentinization and fluid reservoirs in a subduction context

The isotopic signature of group A and B rocks is quite similar, and far from the typical depleted mantle isotopic signature of unaltered peridotites (Figs. C4_16 and C4_17; Rehkämper and Hofmann, 1997). In addition, similar contents in LILE and LREE in both rock groups are in line with similar isotopic signatures, pointing to the same process of enrichment, i.e., serpentinization (Figs C4_16 and C4_17). The Nd, Sr and B isotopic signatures of A and B rocks do not show the typical $^{143}Nd/^{144}Nd$ depletion, $\delta^{11}B$ enrichment and high $^{87}Sr/^{86}Sr$ values related to seawater (Figs C4_16 and C4_17), the alteration of peridotite in mid-ocean ridge and fracture zone setting (e.g., Snow et al., 1994; Hart et al., 1999; Delacour et al., 2008; Kodolányi et al., 2012). Therefore, the isotopic signature of group A and B rocks cannot be explained merely by seawater alteration.

The VCSM serpentinized peridotites and serpentinites were, at some point, related to a subduction setting. The potential reservoirs may therefore be related to such a geodynamic setting. Many serpentinitic mélanges form along the subduction channel in the slab-mantle interface (e.g. Shervais et al., 2011), where different types of fluids evolving from the slab are available for metasomatic alteration of surrounding mantle (e.g., Scambelluri et al., 2004a; King et al., 2006; Angiboust et al., 2012; Spandler and Pirard, 2013; Baitsch-Ghirardello et al., 2014). Serpentinized peridotite (SPER; peridotite serpentinized by seawater), altered oceanic crust-derived fluid (Staudigel et al., 1995; Kelley et al., 2003) and global subducting sediment-derived fluid (Johnson and Plank, 1999; Plank, 2014) are the most important sources.

Among these, we consider potential isotopic reservoirs, taking into account the subduction setting of the Proto-Caribbean plate at *c.* 125 Ma (Rojas-Agramonte et al., 2012). In this context, we evoke: 1) peridotite partly serpentinized by seawater (SPER, Figs C4_16 and C4_17), as expected in a slow spreading ridge (Cannat, 1993); and 2) fluid derived from altered oceanic crust reservoir (AOCF; Kelley et al., 2003), calculated according to the partition coefficients of Johnson and Plank (1999) and Tonarini et al. (2007). Finally, 3) fluid derived from global subducting sediment reservoir (GLOSSF; Plank, 2014), calculated using the average composition of subducting sediments found in deep sea trenches around the world (see Plank, 2014; Fig. C4_16) and partition coefficients of Johnson and Plank (1999) and Tonarini et al. (2007) (see chapter 3.10 and Table C3_3 for further explanation of endmembers).

The contribution of a mixture of AOCF and GLOSSF with serpentinized peridotite (SPER) explains the isotopic composition of Nd, Sr and B isotopes in the serpentinized peridotites and serpentinites of VCSM (Figs. C4_16 and C4_17). Yet the Pb isotopic ratios of A and B rocks cannot be explained by a mixture of AOCF-GLOSSF with the serpentinized peridotite endmember. Moreover, serpentinites from VCSM have low radiogenic $^{206}Pb/^{204}Pb$ and $^{208}Pb/^{204}Pb$, evidencing a third endmember with high $^{87}Sr/^{86}Sr$ (*c.* 0.710) and low $^{143}Nd/^{144}Nd$ (*c.* 0.5120), $\delta^{11}B$ (*c.* -4), $^{206}Pb/^{204}Pb$ (*c.* 18) and $^{208}Pb/^{204}Pb$ (*c.* 38). Such an endmember is identified as a terrigenous reservoir (TER) (unaltered crustal sediments: Poli and Schmidt, 2002; Rudnick

and Gao, 2003) containing sediments derived from the basement of Southern Mexico and the Colombian Andes (NW Gondwana; Fig. C4_16), which represents the most probable type of sediments entering the subduction channel at *c.* 125 Ma (see chapter 7; e.g. Rojas-Agramonte et al., 2016 and references therein). The basement rocks of Southern Mexico and the Colombian Andes were generated at *c.* 1.1- 1.4 Ga, as evidenced by granulites and migmatites (Ruiz et al., 1999; Weber et al., 2010). Pre-magmatic zircons of gneiss, migmatite and volcanic rocks (250- 1100 Ma) with Hf model ages close to *c.* 1.1-1.4 Ga point to the same event of basement formation (Weber et al., 2010; Rojas-Agramonte et al., 2016). In addition, lead isotopes in juvenile magmas from Cuba and Hispaniola display the Pb signature of ancient basement (likely Gondwana-related, Kamenov et al., 2011). Therefore, we calculated the isotopic evolution of the basement reservoir of Rudnick and Gao (2003) at *c.* 1.2 Ga following Stracke et al. (2003a) and Willbold and Stracke (2006), with the partition coefficients of Johnson and Plank (1999) and Tonarini et al. (2007) for the fluid (terrigenous fluid: TERF).

The isotopic signature of the slab fluid is calculated using variable proportions of AOCF, GLOSSF and TERF endmembers. Depending on the endmember proportions used for slab fluid, the mixing line between slab fluid and serpentinized peridotite will vary, according to their own compositions (Figs. C4_16 and C4_17). Hence, mixing proportions of different fluid endmembers (termed here slab fluid) with serpentinized peridotites are only guidelines for the more probable reservoirs of fluid that interacted with peridotites of the VCSM. We selected the slab-fluid composition with a high contribution of AOCF to assess the effect of AOCF, slab-fluids 1 to 3 (Figs. C4_16 and C4_17; e.g. Hauff et al., 2003 and references therein). The effect of sedimentary contribution (GLOSSF and TERF) is evaluated by means of slab fluids 4 and 5 (Figs. C4_16 and C4_17). The slab fluid that best describes the composition of group A and B rocks contains TERF in higher amounts than GLOSSF. When GLOSSF is the main component, the resulting mixing line (slab fluids 3 and 4) shows high values of $^{206}Pb/^{204}Pb$, $^{207}Pb/^{204}Pb$ and $^{208}Pb/^{204}Pb$, which are not consistent with group A and B rocks. Therefore, slab fluids that better explain the isotopic signature of rocks of the VCSM are those with high contents of AOCF and TERF. When the fluid mixtures here considered (SPER-Slab fluids 1, 2, 3, 4 and 5) interact with a serpentinized peridotite (see mixing lines, Figs. C4_16 and C4_17), only *c.* 2% of slab fluid is needed to explain the variability of group A and B rocks.

Nevertheless, B isotopes overestimate the amount of slab fluid (10%-40%; Fig. C4_17). This can be traced to the fractioning effect of B (c.f. Bonatti et al., 1984; Scambelluri et al., 2004b; Vils et al., 2008 and 2009). The B content of SPER is typical of seawater serpentinization (Vils et al., 2008 and 2009), which differs by two orders of magnitude from the slab fluid endmember. Such differences in B content cause a higher percentage of slab fluid to move towards the SPER endmember (due to lower B content), thereby leading to an overestimation of the slab fluid contribution of groups A and B.

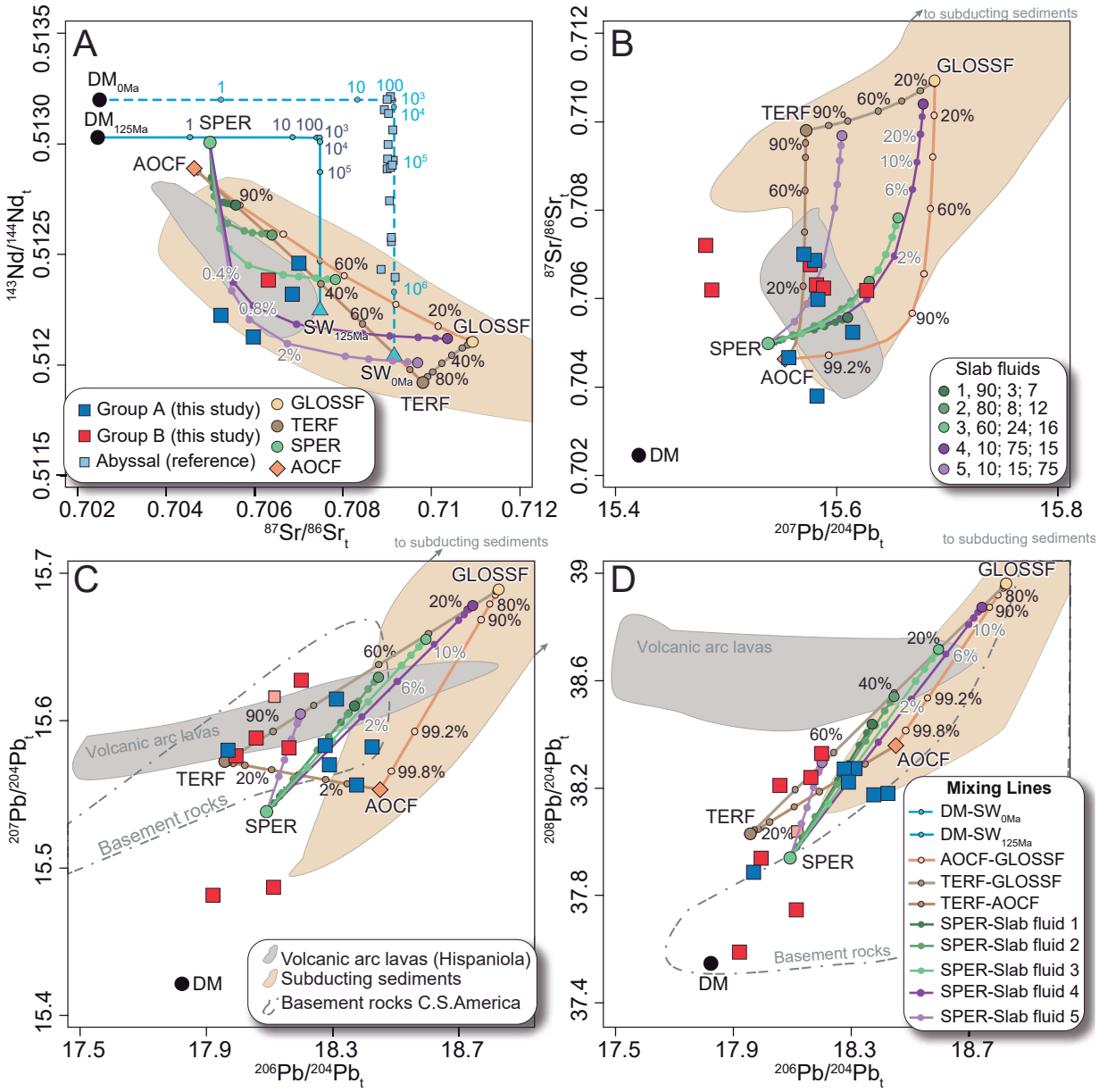

Figure. C4_16 *Nd, Sr and Pb isotopes of serpentinitic matrix rocks from VCSM. A) $^{143}Nd/^{144}Nd_t$ vs $^{87}Sr/^{86}Sr_t$. B) $^{87}Sr/^{86}Sr_t$ vs $^{207}Pb/^{204}Pb_t$. C) $^{207}Pb/^{204}Pb_t$ vs $^{206}Pb/^{204}Pb_t$. D)$^{208}Pb/^{204}Pb_t$ vs $^{206}Pb/^{204}Pb_t$ diagrams. Field outlines are composed of subducting sediments found in deep sea trenches around the world (orange field; Plank, 2014), basement rocks of Southern México and Colombian Andes (dashed line, Ruiz et al., 1999) and Neogene volcanic arc lavas from Hispaniola (grey field; Kamenov et al., 2011). DM (Depleted Mantle), AOCF (altered oceanic crust fluid), GLOSSF (global subducting sediment fluid), TERF (terrigenous fluid), SW (seawater) and SPER (serpentinized peridotite) are isotopic reservoir endmembers. More information on endmember sources in chapter 3.10 and Table C3_3. Seawater-DM mixing line was calculated following the equations of McCulloch et al. (1981). AOCF-GLOSSF, TERF-GLOSSF, TERF-AOCF and SPER-Slab fluids 1 to 5 were calculated using the equation of isotopic mixture from Faure and Mensing (2005). The proportions of AOCF: GLOSSF: TERF in all slab fluids are shown in the legend. All mixing lines, endmembers and samples were age corrected at c. 125Ma to the eclogitic metamorphic peak event in VCSM that indicates pre-Aptian subduction (Garcia-Casco et al., 2002). The actual seawater and its mixing line, as well as reference abyssal samples (Delacour et al., 2008), were not recalculated to 125 Ma.*

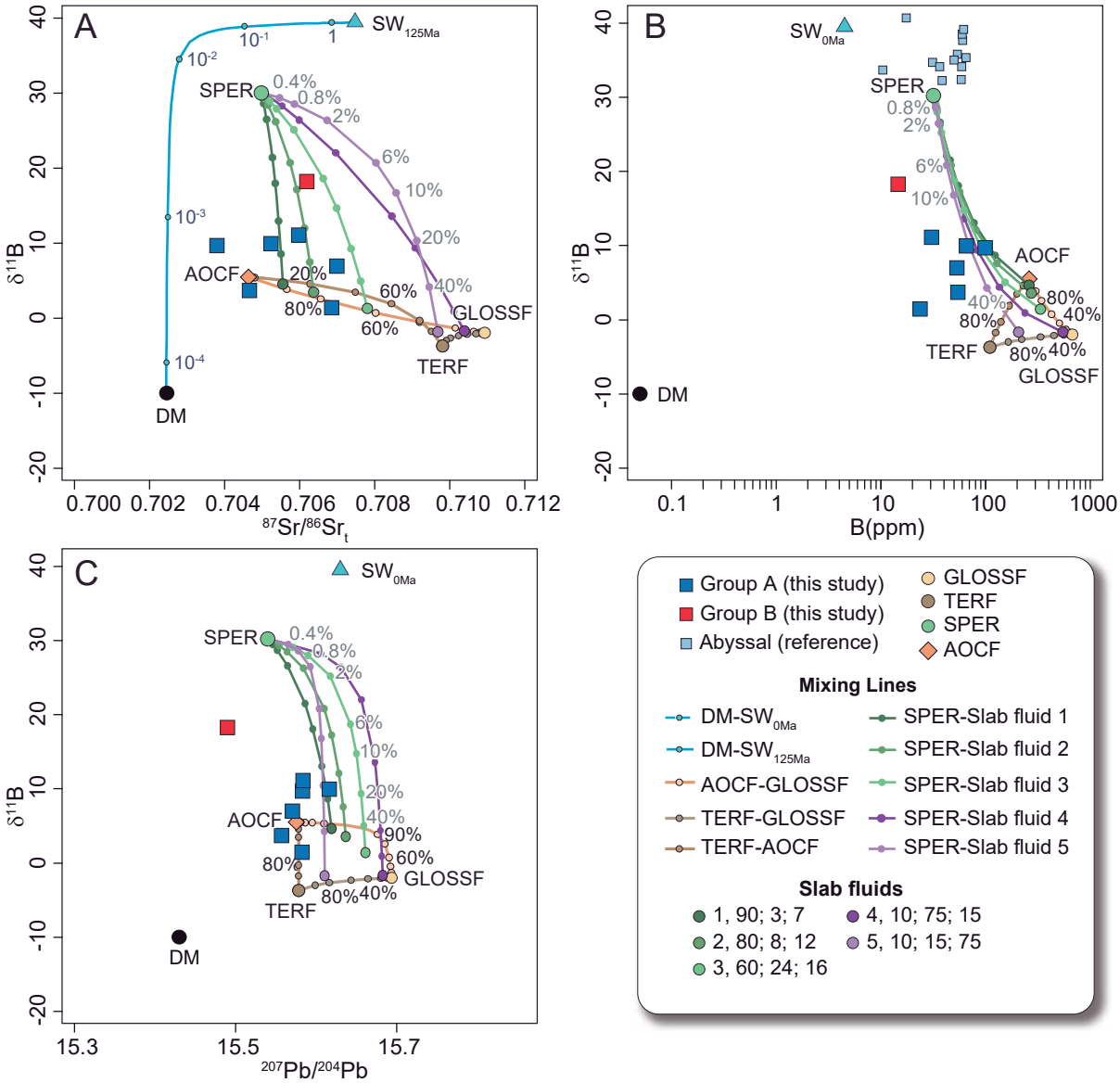

Figure. C4_17 *Boron isotopic composition from serpentinitic matrix rocks of VCSM. A) $\delta^{11}B$ vs $^{87}Sr/^{86}Sr_t$. B) $\delta^{11}B$ vs B. C) $\delta^{11}B$ vs $^{207}Pb/^{204}Pb$ diagrams. Abyssal serpentinites altered by seawater are plotted for reference (Vils et al., 2008 and 2009). Mixing endmembers, mixing line percentages are as in Fig. C4_16. For more details see chapter 3.10 and Table C3_3.*

Our findings suggest that a small input of slab fluid is enough to reset the primary signature of seawater alteration (e.g. Cannaó et al., 2016 and references therein). The combination of enriched fluids such as AOCF, GLOSSF and TERF is the most feasible cause of element enrichment. In fact, Deschamps et al. (2012) and Hattori et al. (2007) propose heterogeneous sedimentary fluid sources for Cuban serpentinites to explain their Sr and Pb isotopic signatures. Geochemical thermo-mechanical numerical modelling (Gerya et al., 2002; Baitsch-Ghirardello et al., 2014) carried out using Pb isotopes at subduction settings supports the idea of self-organized of flow patterns that favour physical and geochemical mixture of slab fluids (subducting sediments and oceanic crust) in the subduction channel. Bebout and Penniston-Dorland (2016) use field evidence to show how subducting fluids from different sources are capable of moving through subduction channel mélanges that act as a conduit for fluids (see chapter 7).

4.5.3. Geochemical fingerprints of mantle source and partial melting processes

The petrogenetic evolution of group A and B rocks is preserved in relict phases (Cr-spinel, olivine, orthopyroxene and clinopyroxene) and whole-rock major and trace element composition.

Group A serpentinized peridotites and serpentinites have olivine - Cr-spinel pairs that plot in the olivine-spinel mantle array (OSMA) with low Cr# in Cr-spinel, and forsterite content in olivine of 90% to 92% (Fig. C4_7). These rocks moreover contain Al-rich ortho- and clinopyroxenes (Fig. C4_8). Such mineralogical features are typical of fertile MORB-like mantle (abyssal peridotites) that underwent a low degree of partial melting (Figs. C4_6 and C4_8; Choi et al., 2008 and references therein). Major and trace elements also underline the fertile character of group A rocks, with high contents in Al_2O_3 and TiO_2 (Fig. C4_11D). The C1-normalized REE patterns of these rocks resemble those of a depleted mantle that underwent low melt extraction (Fig. C4_12A; e.g., Niu, 2004).

Group B rocks have olivine-Cr-spinel pairs that fall in the OSMA array, but with high Cr# in Cr-spinel and forsterite content of 91%-93% (Fig. C4_7). Orthopyroxenes from these rocks are Al-poor (Fig. C4_8). These mineralogical characteristics suggest a refractory character associated with high degrees of partial melting (e.g. Parkinson and Pearce., 1988; Parkinson et al, 1992; Pearce et al., 2000; Choi et al., 2008; Saka et al., 2014; Cao et al., 2016). It is further evidenced by lower CaO, Al_2O_3 and TiO_2 contents (Fig. C4_11), as well as by depletion in HFSE and REE in comparison to depleted mantle (Figs. C4_12 and C4_13). The normalized REE pattern displays low MREE and slightly enriched HREE, showing a “U” shaped pattern (Fig. C4_12B). The progressive depletion in LREE and enrichment of MREE to HREE would indicate a high extent of partial melting (e.g, Savov et al., 2005; Deschamps et al., 2013; Cao et al., 2016).

Such contrasted mineralogical and geochemical characteristics indicate that the VCSM serpentinized peridotites and serpentinites represent different mantle domains. In order to constrain the melting process of ultramafic rocks in the VCSM, we model hydrous fractional non-modal melting of depleted mantle (see chapter 3.9 and Table C3_2 for procedure). We use fractional melting modelling because it is the closest approximation to peridotite formation in oceanic lithospheric mantle (cf., Dick, 1989; Johnson et al., 1990; Johnson and Dick, 1992; Seyler et al., 2001).

The melting modelling was carried out considering two cases for each group of peridotites: Case X) melting in garnet facies and case Y) melting in spinel facies of a depleted mantle (DM), with one- and two-step melting for both cases.

The modelling results of group A peridotites are displayed in figures C4_15 and C4_18. Case X, with one-step melting in the garnet facies modellization, results in steep slopes, an image which does not fit with the compositions of group A rocks (Fig. C4_18A). Case X with two-step melting was carried out by first melting in garnet facies at 4% followed by a second step under the spinel facies conditions (Fig.

C4_18B). The better fit of group A rock compositions would correspond to 4% to 8 % melting in the spinel facies (Figs. C4_18C and C4_18D). Case Y with one-step melting in the spinel facies shows a good fit with group A rocks that experienced 4%-6% of melting (Fig. C4_18C). Two-step melting of the order of 4% (first step) and 2% to 4% (second step) results in compositions similar to those found for group A rocks (Fig. C4_18D).

To sum up, the modelling results that best fit group A rocks is case Y, indicative of low degrees of partial melting (c. 4% to 6% of one-step melting in spl-peridotite and 2% to 4% of two-step melting, Fig. C4_18), which confirms their fertile character.

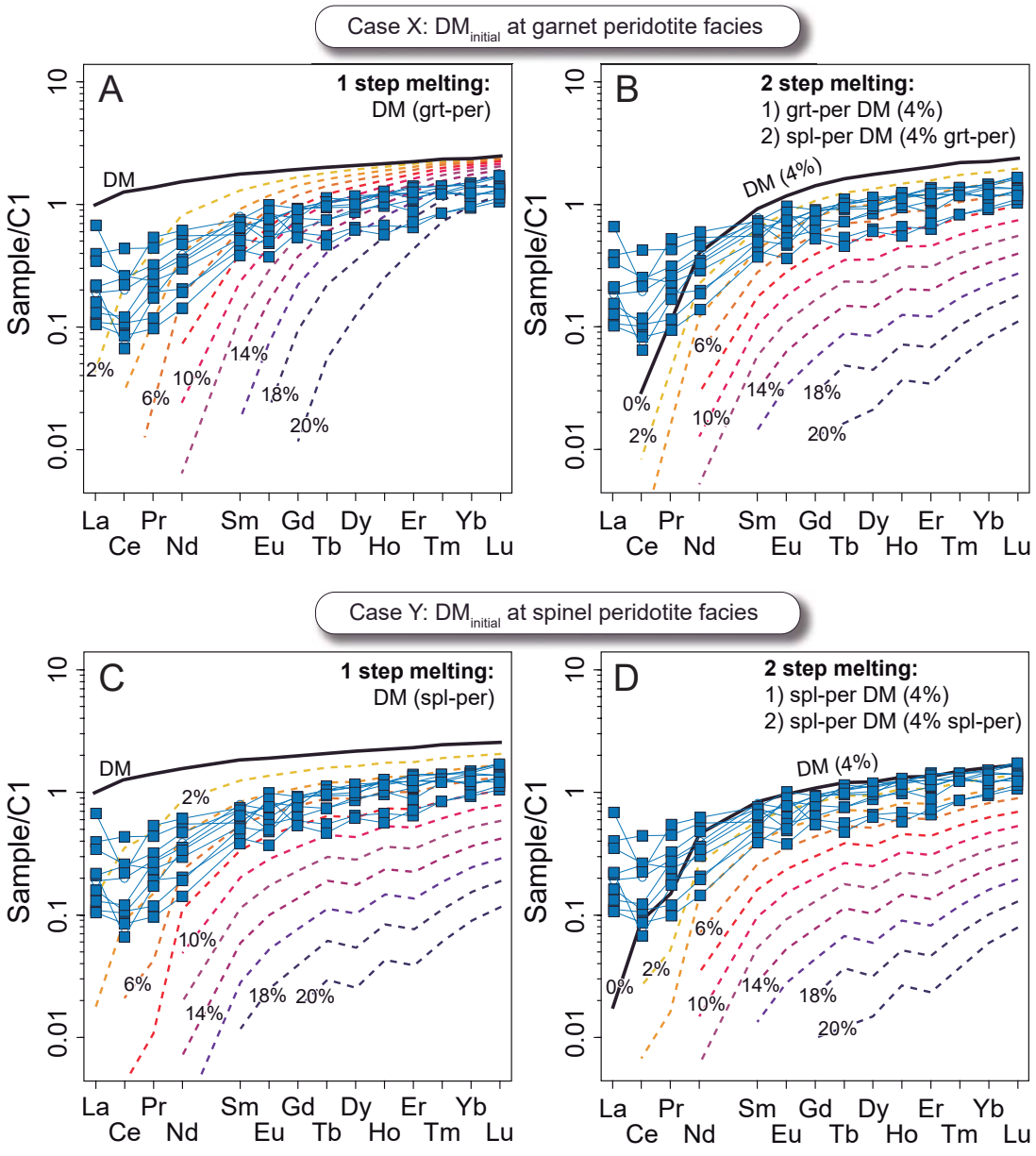

Figure. C4_18 *Non-modal fractional melting modelling of studied group A peridotites from the serpentinitic matrix of VCSM. A) and B) case X modelling for melting at the garnet peridotite facies. A) One simple batch of melt (dashed lines); B) Two batches of melting (second in the spinel facies). C) and D) case Y modelling at spinel peridotite facies. C) One-step melting; D) Two-step melting. Melting models calculated using equation of Shaw (2000). Depleted mantle (DM) composition is from Salters and Stracke (2004). See chapter 3.9 and Table C3_2 for details. Percentages indicate degree of melting.*

The melting modelling of group B rocks is shown in figures C4_15 and C4_19. Case X, with one-step melting at the garnet facies, do not fit group B compositions (melting curves are highly enriched in HREE, Fig. C4_19A). Two-step melting of 4% grt-peridotite first with a second spl-peridotite would fit group B rocks for 14% to 20% melting (Fig. C4_19B). Case Y (spinel-peridotite facies) melting modelling curves also fit with group B compositions for 14% to 20% at one step (Fig. C4_19C), or 10% to 18 % melting in two steps (Fig. C4_19D). All modellings except case X with one step melting —that is, case X two-step and case Y one- and two-step melting— predict high degrees of partial melting for group B peridotites. This process can explain the depletion of REE and demonstrates the strong residual character of group B.

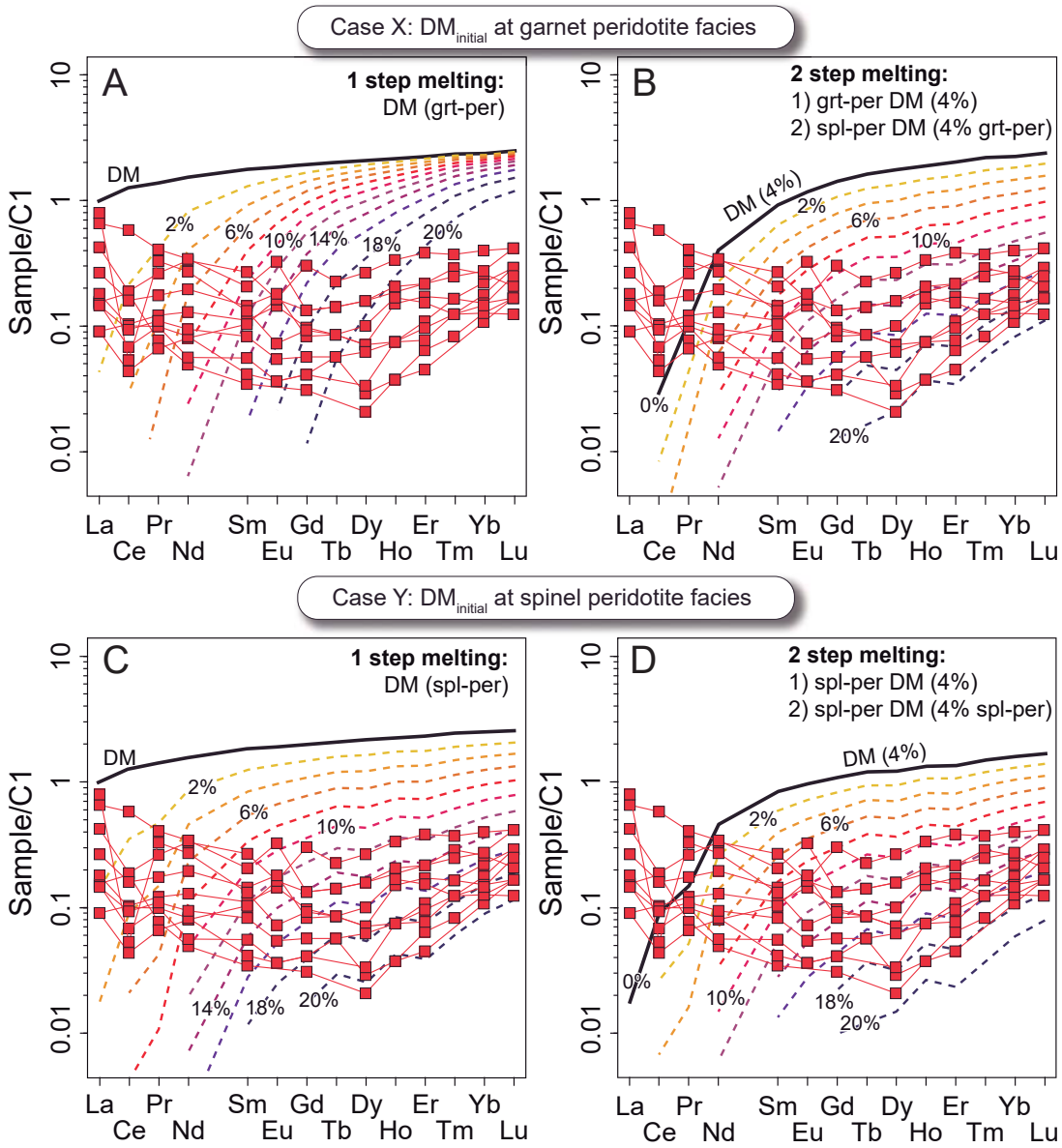

Figure. C4_19 *Non-modal fractional melting modelling of studied group B peridotites from the serpentinitic matrix of the VCSM. A) and B) case X modelling for melting at garnet peridotite facies. A) One simple batch of melt (dashed lines); B) Two batches of melting (second in spinel facies). C) and D) case Y modelling at spinel peridotite facies. C) One step-melting; D) Two-step melting. Melting models calculated using equation of Shaw (2000). Depleted mantle (DM) composition is from Salters and Stracke (2004). See chapter 3.9 and Table C3_2 for details. Percentages indicate degree of melting.*

The modelling results of group A and B peridotites agree with those obtained using compositions of spinel, olivine and pyroxene compositions modelled by Choi et al. (2008) and Dupuis et al. (2005), which predict 3% to 10% of partial melting for group A and 17%-30% for group B (Figs. 6C and 6D).

The two groups of rocks crop out close to each other in the field (Fig. C4_1), suggesting that they are genetically related, forming part of the same lithosphere. The contrasted partial melting degrees can only be explained if group B rocks are the result of melting group A peridotite (Fig. C4_20A and C4_20B). Case X (grt-peridotite facies Fig. C4_20) cannot explain group A compositions in a first step of melting; a second step is needed. As a consequence, group B should be the result of a third step melting (Fig. C4_20A). This possibility would favour case Y (spl-peridotite facies; Fig. C4_20B). Because case X of step 1 melting cannot explain group A compositions, a second step must account for their compositions (step 1 in grt-peridotite, step 2 in spl-peridotite, Fig. C4_20A). Hence, a third step of melting is needed to explain group B compositions (Fig. C4_20A). On the other hand, case Y could easily explain groups A (one step) and B (two step) compositions for spinel facies (Fig. C4_20B), although in chapter 7 extensive discussion addresses this possibility.

Serpentinized peridotites and serpentinites of group A have mineral and whole-rock compositions that correspond to abyssal/fracture zone peridotites (Figs. C4_6 to C4_13 and C4_15). Melting modelling supports this evidence, because low degrees of partial melting are expected in abyssal/fracture zone settings (Fig. C4_15, Warren, 2016 and references therein). In contrast, group B rocks have refractory mineral, whole-rock compositions, and higher degrees of partial melting (c. 14-30%), typical of forearc settings (Figs. C4_6 to C4_13 and C4_15; Savov et al., 2005). The compositional features of ultramafic rocks in VCSM are similar to other ophiolitic peridotites around the Caribbean realm. The Sierra del Convento and La Corea mélanges (eastern Cuba mélanges [Blanco-Quintero et al., 2011a; Cárdenas-Párraga et al., 2017], Puerto Plata, Rio San Juan Dominican Republic; Saumur et al., 2010; Deschamps et al., 2012; Escuder et al., 2014) and Monte del Estado complexes (Puerto Rico; Marchesi et al., 2011) represent abyssal peridotites formed in a mid-ocean ridge spreading centre (Figs. C4_11 and C4_12) having compositions similar to group A rocks from this study. In contrast, ophiolitic peridotites in Mayarí-Cristal, Moa Baracoa (eastern Cuba; Marchesi et al., 2006) and Camú and Septentrional fault zones (Dominican Republic; Saumur et al., 2010; Escuder et al., 2014) display compositions that are associated with backarc and forearc settings (Figs. C4_11 and C4_12). The Loma Caribe peridotite (Cordillera Central, Dominican Republic; Marchesi et al., 2016) displays two main compositions interpreted as a combination of abyssal and forearc settings. The combinations of both tectonic settings explain the assemblage of group A and B rocks in the VCSM. Group A and B ultramafic rocks are found close to each other at the outcrop scale. Thus, the key issue is addressing the geodynamic setting that could explain the presence of these heterogeneous rocks in the same subduction environment.

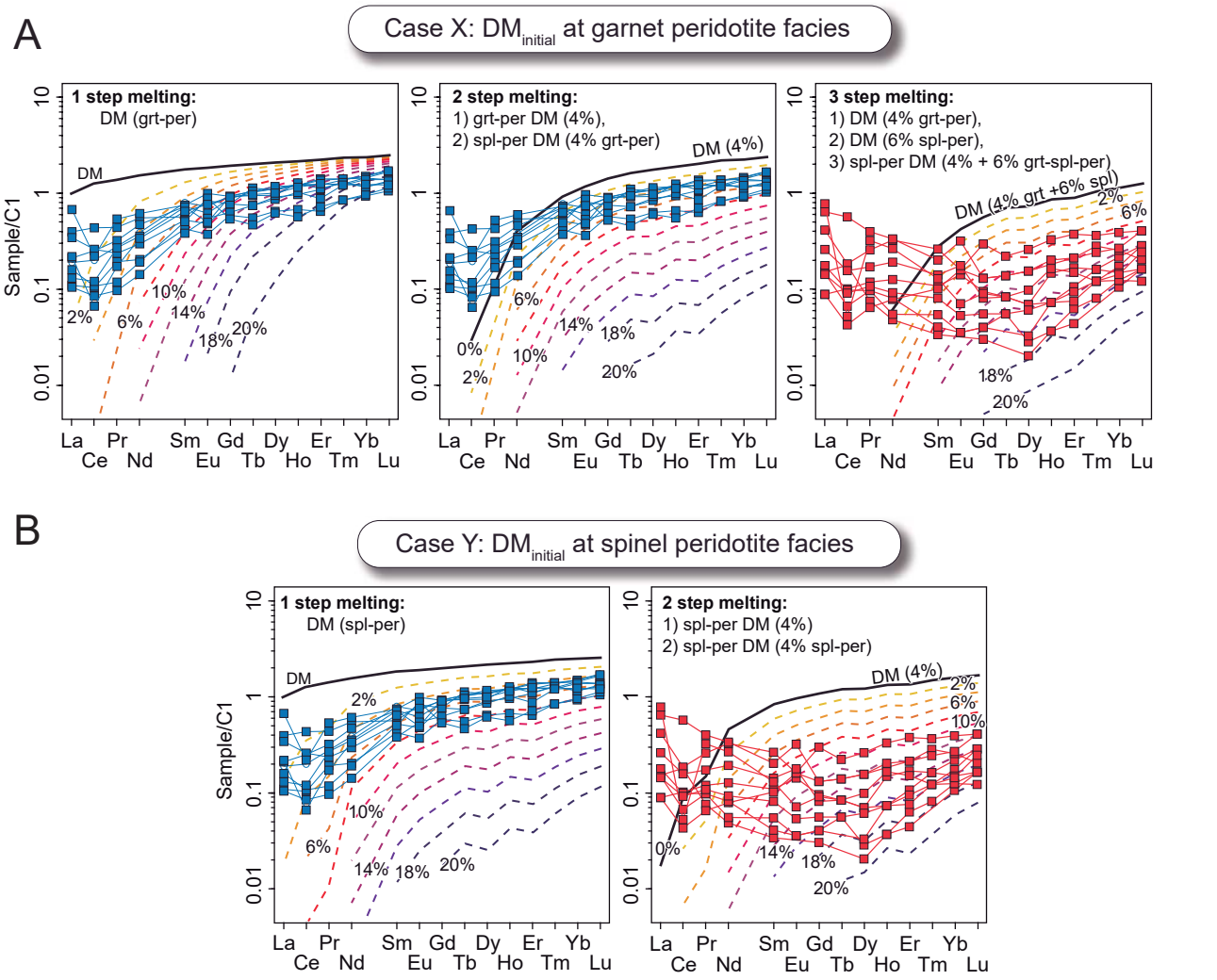

Figure. C4_20 *Contrasted melting modellings for group A and B peridotites from the serpentinitic matrix of the VCSM. A) Initial melting at garnet facies. B) Initial melting at spinel facies. Case X has a first step melting at garnet-peridotite facies, a second step at spinel facies of an already depleted mantle source (4% in grt-peridotite), and a third step at spinel facies conditions of a depleted mantle source (4% at grt-peridotite facies and 6% at spl-peridotite facies). Case Y has first and second step meltings at spinel-peridotite facies. The second is at 4% of depleted mante source. Melting models calculated using equation of Shaw (2000). Depleted mantle (DM) composition from Salters and Stracke (2004). See chapter 3.9 and Table C3_2 for details. Percentages indicate degree of melting.*

Chapter 5

Mafic crust of VCSM

5.1. Field relations

5.2. Sub-volcanic unit: diabase and microgabbro

5.3. Plutonic unit: layered gabbros and ol-gabbros

5.4. Discussion of mafic crust of the VCSM

5. The mafic crust of the Villa Clara serpentinitic mélange

5.1. Field relations

The mafic crust of the Villa Clara serpentinitic mélange (VCSM) occurs as dismembered tectonic blocks included in serpentinite. The absence of a continuous foliation within blocks and serpentinite matrix, as well as the absence of contact metamorphism, evidence a tectonic boundary between serpentinite and blocks (Kanchev et al., 1978 and references therein). The tectonic blocks follow the main tectonic structures and show irregular shape with metric to kilometric size (up to *c.* 10 km; Fig. C5_1).

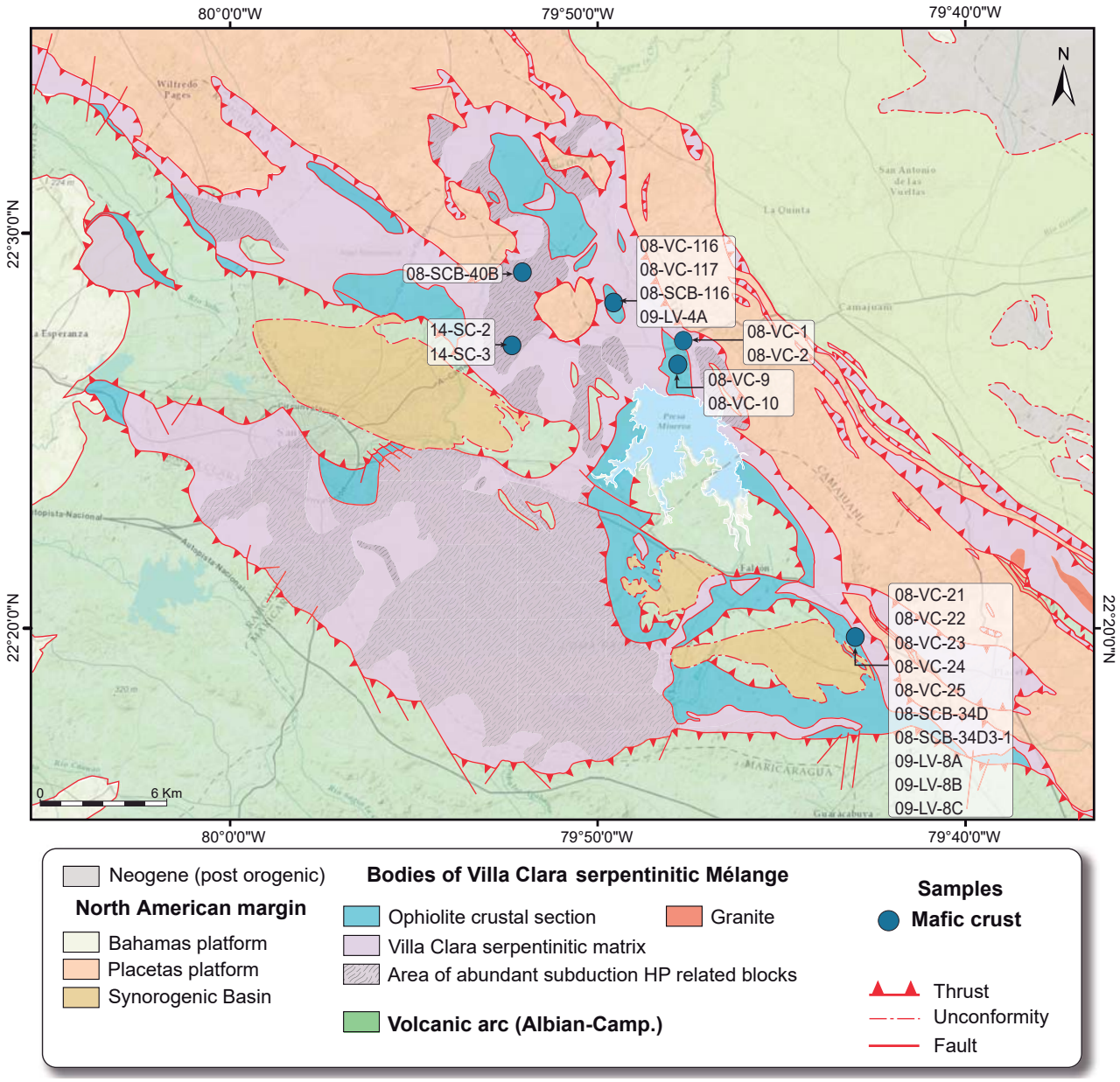

Figure. C5_1. *Geological map of Las Villas 1:100000, indicating the main geologic features and sample locations of the mafic crust of the VCSM (modified from Kanchev et al., 1978; Álvarez et al., 1991 and García et al., 1998).*

The blocks of the mafic crust of the VCSM were described for the first time by Rutten et al. (1938) and Kanchev et al. (1978), and were included in the Tobas Formation. This formation includes blocks of diabase, microgabbro, layered gabbro, volcanic arc rocks, tuff and radiolarite of diverse origin (ophiolite and volcanic arc). Other authors (Zelepuguin et al., 1982; Puscharovsky et al., 1989; Iturralde-Vinent, 1996c) have distinguished diabase and microgabbro as the crustal section of the ophiolite, the Sagua la Chica Formation. Paleontologic data of radiolarites interspersed with basalts yield an Early Cretaceous age (Rutten et al., 1938; Llanes et al., 1998). In order to simplify the terminology, we refer to the mafic crust of the Villa Clara serpentinitic mélange (VCSM).

In the outcrop, we distinguish two rock units in terms of appearance and rock textures: i) Sub-volcanic: diabase and microgabbro; and ii) Plutonic: layered gabbro (Fig. C5_2).

The sub-volcanic unit occurs as discontinuous blocks, metres to decametres in length, within the serpentinitic matrix (Fig. C5_2A to C5_2C). It is composed of breccified and massive bodies of diabase and microgabbro (Fig. C5_2A and C5_2B). They show fine inequigranular porphyritic and typical ophitic textures, and contain plagioclase, clinopyroxene and magnetite. Nevertheless, they display metamorphic mineral assemblages with amphibole, epidote, chlorite and prehnite, which attest to the green-schist and amphibolite facies assemblages.

The plutonic unit is discontinuous and decametric in length (Fig. C5_2D). It is composed of layered gabbro, at decametric and hand sample scales (Fig. C5_2E). The layers exhibit coarse grain size and an orientation of minerals that indicates a cumulate character (Fig. C5_2E). Layered gabbros contain plagioclase, clinopyroxene, orthopyroxene and olivine. In some areas, they display metamorphic mineral assemblages with amphibole, serpentine, epidote, chlorite and prehnite. Locally, the blocks of layered gabbros appear in contact with diabase, and microgabbro by tectonic faults (Fig. C5_2F).

Figure. C5_2. *Field relations of mafic rocks in Villa Clara serpentinitic mélange. A) General view of diabase and microgabbro. B) Detail of diabase and microgabbro showing brecciated structures. C) Diabase blocks within the serpentinitic matrix and a hand sample. D) Layered gabbro, diabase and microgabbro. Dotted lines indicate layers. E) Detail of layered structures in cumulate gabbro showing massive structure. F) Detail of tectonic contact between diabase/microgabbro and layered gabbros.*

5.2. Sub-volcanic unit: diabase and microgabbro

The diabase and microgabbro of this unit show plagioclase and clinopyroxene in the magmatic assemblage. They can be discerned as two groups in terms of secondary mineral assemblages that replace the magmatic assemblage. Group 1 consists of 10 samples (08-VC-1, 08-VC-2, 08-VC-9, 08-VC-10, 08-VC-116, 08-VC-117, 08-SCB-40B, 08-SCB-116; 09-LV-4A, 14-SC-2) that do not contain quartz and alkali feldspar in their secondary assemblage, whereas group 2 contains, in addition, these minerals (4 samples: 08-VC-21, 08-VC-22, 08-SCB-34D, 09-LV-8C).

5.2.1. Petrography

Diabase and microgabbro of groups 1 and 2 display plagioclase, clinopyroxene and accessory apatite, magnetite and ilmenite as the primary assemblage. Amphibole, epidote, chlorite and prehnite are metamorphic minerals present in both groups. Quartz and alkali feldspar occur in group 2.

These rocks have inequigranular, subophitic textures evidenced by euhedral crystals of plagioclase (Figs. C5_3A and C5_3B). Clinopyroxene is located in the mesostasis where it partially includes plagioclase crystals. Subophitic textures appear pseudomorphized due to the alteration of clinopyroxene by amphibole (Fig. C5_3B).

Plagioclase is the most abundant mineral (*c.* 60 % vol.). It shows normal zoning as well as simple and polysynthetic twins (Fig. C5_3B). In some samples plagioclase is deformed, as attested to by disruption of the polysynthetic twins. Samples with fine-grained matrix have disoriented microliths of plagioclase, *c.* 100 µm in size, that are more abundant than plagioclase phenocrysts (*c.* 500 µm). In medium-grained samples the plagioclase grains are 400 µm in size. Clinopyroxene, *c.* 30-40 % vol., is usually found as subhedral micro phenocrysts (*c.* 400 µm in size) in fine grain samples (Figs. C5_3C and C5_3D). But in medium-grained samples clinopyroxene reach up to 1 mm size. These rocks show a gradual decrease of phenocryst grain size that signals a diabase to microgabbro texture. In the less altered samples, clinopyroxene shows oriented exolutions of orthopyroxene (*c.* 10 µm, Fig. C5_3E). Clinopyroxene is generally replaced by amphibole (Fig. C5_3E). Magnetite and ilmenite (*c.* 5 % vol.) have euhedral to subhedral shape and appear in contact with clinopyroxene and plagioclase, and locally, included by amphibole. Apatite (1 % vol.) reflects a euhedral habit, locally included by amphibole.

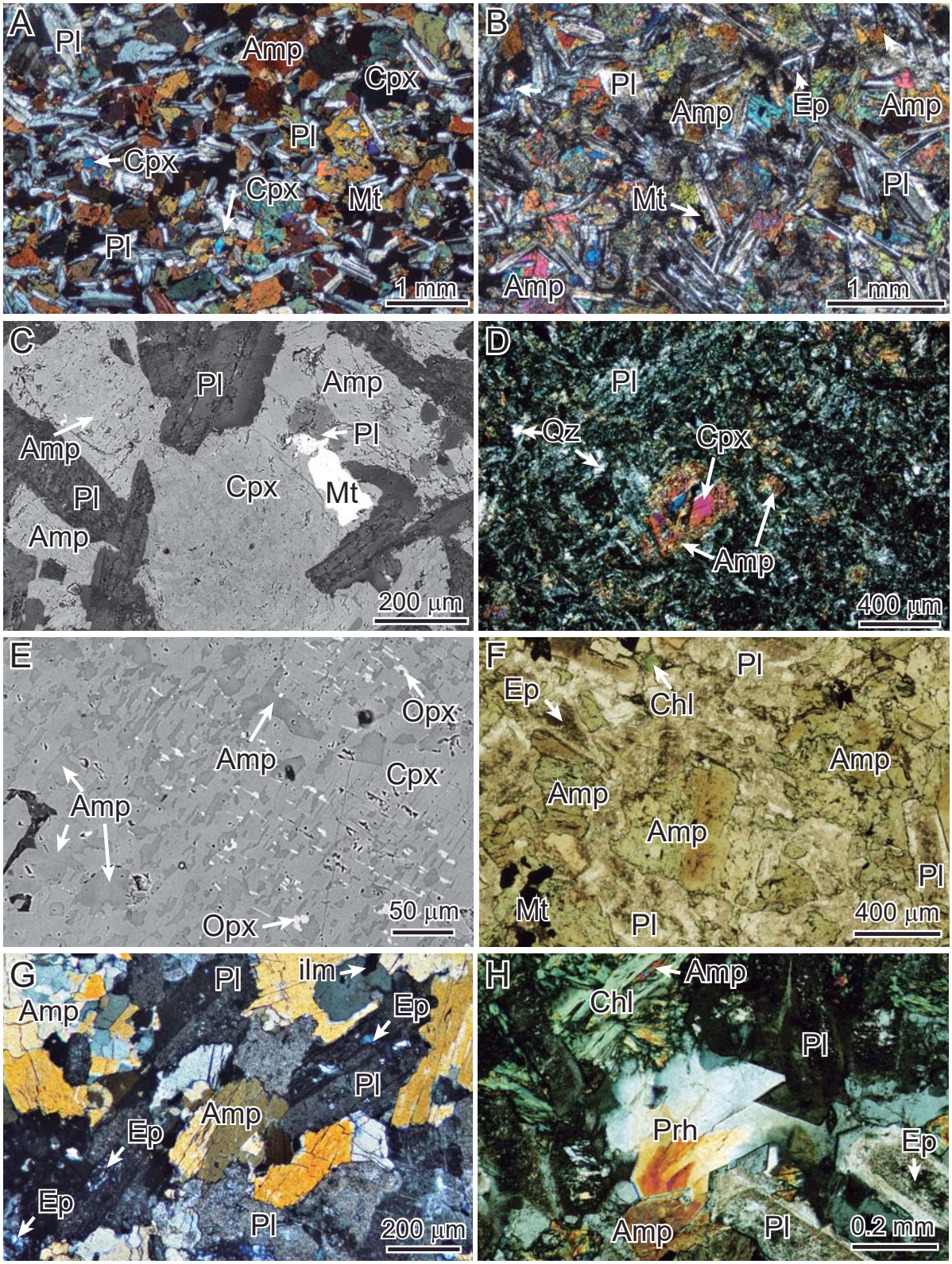

Figure. C5_3. *Optical photographs and back-scatter electron images (BSE) of diabase and microgabbro blocks of the mafic crust of the VCSM. A) Microgabbro with subophitic textures. Euhedral plagioclase with simple and polysynthetic twins. Clinopyroxene partially replaced by amphibole. B) Typical pseudomorphosed subophitic texture of diabase. Amphibole in the mesostasis replacing clinopyroxene. C) BSE image of plagioclase with normal zoning; clinopyroxene displays patchy texture. D) Clinopyroxene replaced by amphibole and decusate microliths of plagioclase. E) Detail of image C) Showing clinopyroxene with oriented orthopyroxene exolutions and replacement by amphibole. F) Zoned amphibole and chlorite replacing amphibole. Epidote replaces plagioclase. G) Aggregates of amphibole and epidote replacing plagioclase core. H) Prehnite after plagioclase and epidote replacing plagioclase core.*

In the more intensely metamorphosed samples, amphibole with subhedral shape is the main secondary mineral (*c.* 40 % vol.). It appears as large crystals (*c.* 500 µm) and shows zoning with brown cores and marked pleochroism to green-pale green rims (Fig. C5_3F). Samples where clinopyroxene has been completely replaced by amphibole display aggregates of amphibole that pseudomorphize clinopyroxene (Fig. C5_3B). Amphibole is replaced by chlorite (Fig. C5_3F). Plagioclase displays replacement textures attested by sericite, prehnite and epidote in the core and late rims of albite (Figs. C5_3G and C5_3H). In group 2 samples, the cores of plagioclase grains were altered by alkali feldspar and epidote. In some samples prehnite appears as late veins that crosscut primary assemblages and amphibole.

The order of magmatic crystallization was: apatite, magnetite-ilmenite, plagioclase, clinopyroxene. Secondary assemblages started with formation of brown amphibole that replaced clinopyroxene, followed by green amphibole (rim of brown amphibole and amphibole aggregates) and chlorite. Plagioclase was altered to albite (plagioclase rim; Fig. C5_3F) followed by a later alteration of epidote, alkali feldspar and, finally, replaced by sericite.

5.2.2. Mineral chemistry

The compositions of primary and secondary mineral assemblages are displayed below. The mineral formula of feldspar was normalized to 8 oxygens, pyroxene to 6 oxygens, magnetite to 4 oxygens, ilmenite to 3 oxygens, amphibole to 23 oxygens, epidote to 12.5 oxygens, prehnite to 11 oxygens and chlorite to 28 oxygens (more details in chapter 3).

5.2.2.1. Minerals of magmatic assemblage

Plagioclase is the most abundant mineral in diabase and microgabbro in group 1 and 2 rocks. In group 1 its compositions range from bytownite (An_{81}) to Albite (An_{2}) (Fig. C5_4). As described above, plagioclase is zoned with bytownite-labradorite composition in the core that changes progressively to albite towards the rim (Fig. C5_4A, Table C5_1). Group 2 compositions of magmatic plagioclase are not preserved, displaying compositions from oligoclase (An_{26}) to albite (An_{0}; Fig. C5_4A, Table C5_1). Group 2 rocks bear alkali feldspar (Or_{92-97}) replacing plagioclase.

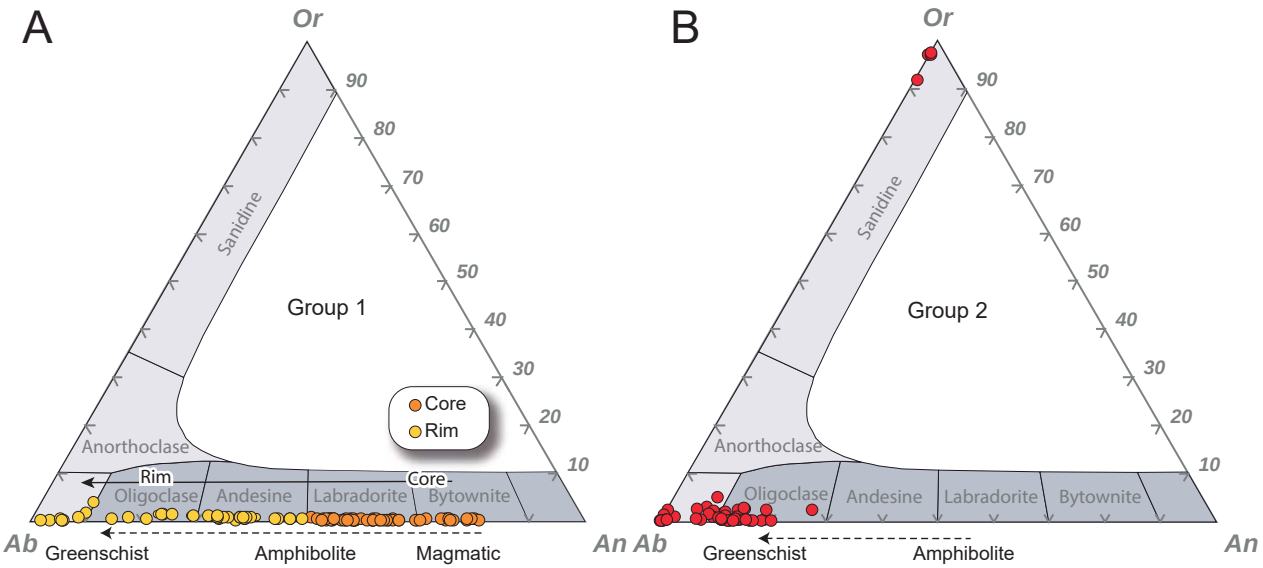

Figure. C5_4 *Classification of feldspars of diabase and microgabbro in the An-Ab-Or diagram. A) Group 1. B) Group 2. Ab: Albite; Or: Ortose; An: Anorthite.*

Table C5_1. *Representative analyses of feldspars of the sub-volcanic unit.*

Sample	08-VC-10	08-VC-117	14-SC-2	09-LV-4A	09-LV-4A	08-VC-21	08-VC-21	08-VC-22	09-LV-8C
Rock type	Diabase	Mirogabbro				Microgabbro			
Unit	Sub-volcanic								
Group	1	1	1	1	1	2	2	2	2
Textural position	Core	Rim	Rim	Core	Rim	Core	Core	Core	Core
Mineral	Bytownite	Albite	Andesine	Labradorite	Oligoclase	Oligoclase	Albite	Oligoclase	Albite
Major elements (wt%)									
SiO_2	49.78	67.30	60.95	53.50	61.25	66.10	67.32	65.62	69.18
TiO_2	0.05	b.d.l	b.d.l	0.02	b.d.l	b.d.l	b.d.l	0.01	b.d.l
Al_2O_3	30.97	19.61	25.02	28.66	23.24	21.21	20.37	21.74	19.94
FeOT*	0.50	0.01	0.11	0.13	0.31	0.20	0.31	0.07	0.06
MnO	0.01	0.02	b.d.l	b.d.l	0.03	0.01	0.03	0.02	b.d.l
MgO	0.03	b.d.l	b.d.l	0.04	0.04	0.01	0.00	0.01	0.02
CaO	14.83	0.42	6.54	11.29	4.73	2.43	1.20	2.64	0.49
SrO	n.a.	n.a.	n.a.	0.05	0.05	n.a.	n.a.	n.a.	n.a.
BaO	n.a.	n.a.	n.a.	0.03	0.14	n.a.	n.a.	n.a.	n.a.
Na_2O	3.44	11.84	7.63	5.20	9.00	10.86	11.00	10.80	11.11
K_2O	0.02	0.03	0.14	0.07	0.21	0.12	0.46	0.07	0.16
Total	99.63	99.23	100.40	99.00	99.00	100.94	100.69	100.98	100.96
Formula based 8 oxygens									
Si	2.28	2.97	2.70	2.44	2.75	2.89	2.94	2.87	2.99
Ti	0.00	-	-	0.00	-	-	-	0.00	-
Al	1.68	1.02	1.30	1.54	1.23	1.09	1.05	1.12	1.02
Fe^{+3}	0.02	0.00	0.00	0.01	0.01	0.01	0.01	0.00	0.00
Mg	0.00	-	-	0.00	0.00	0.00	0.00	0.00	0.00
Na	0.31	1.01	0.65	0.46	0.78	0.92	0.93	0.91	0.93
K	0.00	0.00	0.01	0.00	0.01	0.01	0.03	0.00	0.01
Ca	0.73	0.02	0.31	0.55	0.23	0.11	0.06	0.12	0.02
Ba	-	-	-	0.00	0.00	-	-	-	-
Sr	-	-	-	0.00	0.00	-	-	-	-
Or %	0.11	0.14	0.84	0.41	1.19	0.64	2.53	0.37	0.92
Ab %	29.53	97.95	67.29	45.27	76.57	88.42	91.93	87.77	96.73
An %	70.35	1.91	31.87	54.32	22.24	10.93	5.54	11.86	2.36

*FeOT expressed as FeO; b.d.l: below detection limit; n.a: not analyzed

Clinopyroxene is common in diabase and microgabbro of groups 1 and 2, while orthopyroxene appears only in group 1 rocks, as exolutions within clinopyroxene. In the classification diagram of Morimoto et al. (1988), clinopyroxene and orthopyroxene plot in the quadrangular field that represents calcic-ferro-magnesian pyroxenes (Fig. C5_5A; Table C5_2). Group 1 clinopyroxenes are diopside (Wo_{45-48} En_{36-44} Fs_{8-18}); orthopyroxene exolutions are enstatite (Wo_{2-5} En_{53-55} Fs_{42-43}) (Fig. C5_5B). On the other hand, group 2 clinopyroxenes are augite (Wo_{34-45} En_{39-47} Fs_{10-23}) (Fig. C5_5C). Group 1 clinopyroxenes display lower contents of Al_2O_3 (0.5 to 1.34 wt% Al_2O_3) in comparison to group 2 (1.76 to 5.17 wt% Al_2O_3), whereas in Mg# = 100*[Mg/(Mg+Fe^{2+})] is similar in both groups (68-85 in group 1 and 66-83 in group 2). Figures C5_5B and C5_5C display isotherms of pyroxene solvus indicating that group 1 pyroxenes display exolutions due to cooling to 500 ºC, hence a metamorphic composition. In turn, group 2 pyroxenes have compositions that agree with high temperatures (Fig. C5_5C) indicative of magmatic compositions (1000-800 ºC).

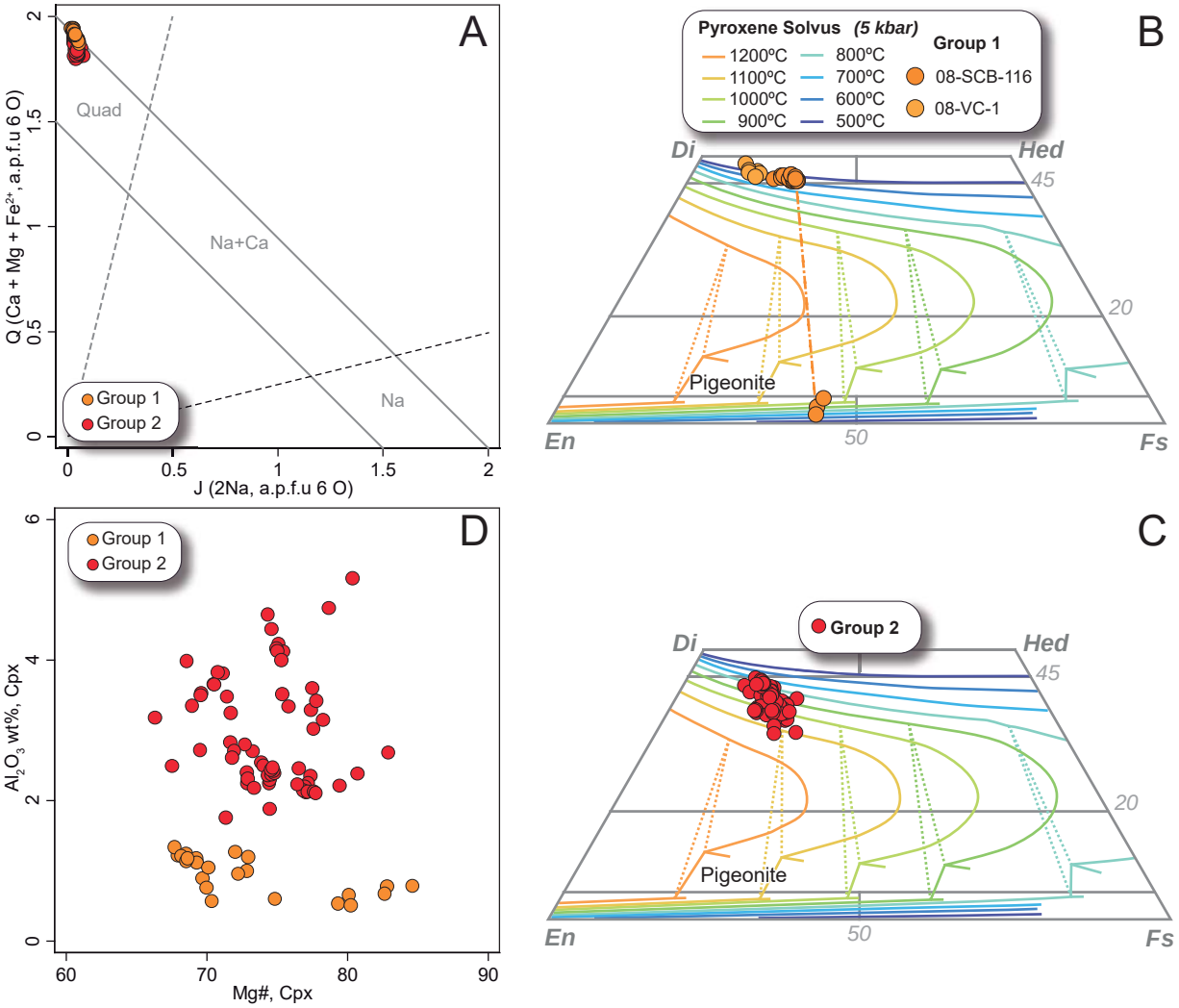

Figure. C5_5 *Pyroxene composition of the sub-volcanic unit. A) Classification diagram of Morimoto et al. (1988). B) Quadrangular pyroxene classification diagram of group 1. C) Quadrangular pyroxene classification diagram of group 2. D) Al_2O_3 wt% vs Mg# in clinopyroxene. En: Enstatite; Wo: Wollastonite; Fs: Ferrosilite. Isotherms of pyroxene solvus at 5 kbar from Lindsley (1983).*

Table C5_2. *Representative analyses of pyroxenes of the sub-volcanic unit.*

Sample	08-VC-1	08-SCB-116	08-SCB-116	08-SCB-116	08-VC-21	08-VC-22	09-LV-8C
Rock type	Diabase		Microgabbro				
Unit	Sub-volcanic						
Group	1	1	1	1	2	2	2
Mineral	Clinopyroxene		Orthopyroxene		Clinopyroxene		
Classification	Diopside		Enstatite		Augite		
Major elements (wt%)							
SiO_2	53.17	51.88	51.55	51.10	51.72	50.16	51.79
TiO_2	0.01	0.24	0.12	0.20	0.57	0.73	0.43
Al_2O_3	0.67	1.20	0.41	0.50	2.54	3.83	3.52
Cr_2O_3	0.02	0.04	b.d.l	b.d.l	b.d.l	b.d.l	0.03
V_2O_3	0.01	0.03	b.d.l	0.01	0.10	0.07	0.10
FeOT*	6.62	8.94	25.47	25.85	9.59	11.09	8.97
MnO	0.26	0.41	1.05	1.04	0.27	0.34	0.27
MgO	14.96	13.52	18.40	19.47	15.21	15.07	15.40
CaO	23.22	22.52	2.21	0.83	20.48	19.17	20.12
Na_2O	0.20	0.24	0.07	0.06	0.31	0.33	0.26
Total	99.15	99.02	99.27	99.06	100.79	100.80	100.90
Formula based 6 oxygens							
Si	1.98	1.96	1.98	1.96	1.90	1.85	1.90
Al	0.03	0.05	0.02	0.02	0.11	0.17	0.15
Fe^{3+}	0.02	0.04	0.02	0.06	0.07	0.12	0.04
Ti	0.00	0.01	0.00	0.01	0.02	0.02	0.01
Cr	0.00	0.00	-	-	-	-	0.00
V	0.00	0.00	-	0.00	0.00	0.00	0.00
Mg	0.83	0.76	1.05	1.11	0.83	0.83	0.84
Mn	0.01	0.01	0.03	0.03	0.01	0.01	0.01
Fe^{2+}	0.19	0.25	0.79	0.77	0.22	0.23	0.23
Ca	0.93	0.91	0.09	0.03	0.81	0.76	0.79
Na	0.01	0.02	0.01	0.00	0.02	0.02	0.02
Wo %	46.99	46.30	4.55	1.70	41.51	39.07	41.26
En %	42.14	38.67	52.77	55.36	42.89	42.74	43.94
Fs %	10.88	15.02	42.68	42.94	15.60	18.19	14.80

*FeOT expressed as FeO; b.d.l: below detection limit; n.a: not analyzed

The Fe-Ti oxides present in group 1 of sub-volcanic unit are magnetite and ilmenite (Fig. C5_6). The magnetite is homogeneous in composition and shows low TiO_2 (c. 0.08 wt%) and Al_2O_3 (<0.01 wt%), with high Fe^{3+} (*c.* 2 cations p.f.u) and Fe^{2+} (*c.* 1 cations p.f.u). Ilmenite displays 47 to 49 wt% TiO_2 with low Fe^{3+} (*c.* <0.14 cations p.f.u) and high Fe^{2+}(*c.* <0.90 cations p.f.u; Fig. C5_6 and Table C5_3).

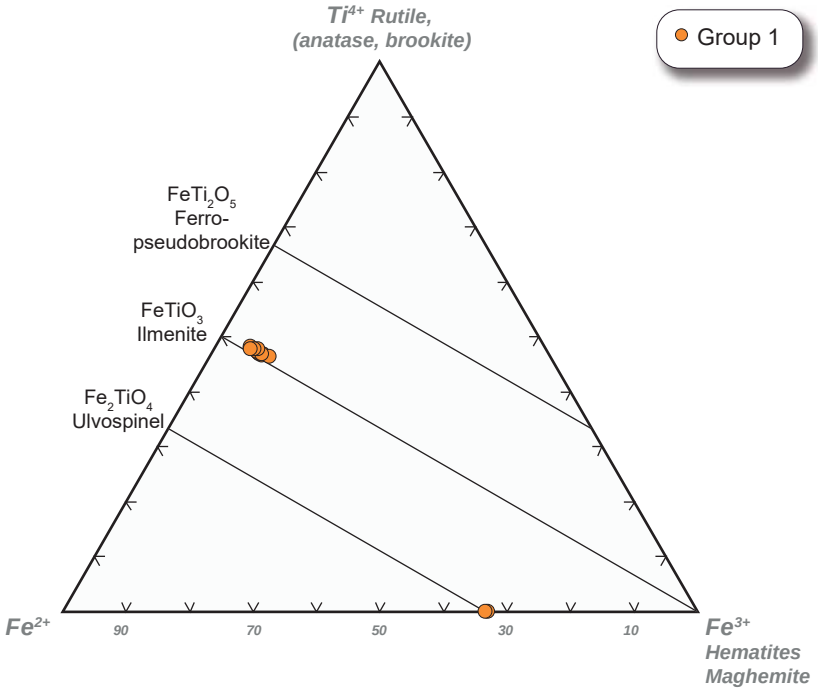

Figure. C5_6. *Fe-Ti oxide classification based on Ti^{4+}-Fe^{2+}-Fe^{3+} (atoms per formula unit) of the sub-volcanic unit.*

Table C5_3. *Representative analyses of Fe-Ti oxides of the sub-volcanic unit.*

Sample	09-LV-4A	09-LV-4A	08-VC-117	08-VC-1	08-SCB-116	08-SCB-116
Rock type	Microgabro	Microgabro	Mirogabbro	Diabase	Microgabbro	Microgabbro
Unit	Sub-volcanic					
Group	1	1	1	1	1	1
Mineral	Ilmenite				Magnetite	
SiO_2	0.04	0.00	0.01	0.01	b.d.l	0.07
TiO_2	48.22	48.45	49.30	48.99	0.09	0.09
Al_2O_3	0.02	0.02	0.02	0.01	0.01	b.d.l
Cr_2O_3	0.04	0.06	b.d.l	b.d.l	0.02	b.d.l
V_2O_3	b.d.l	b.d.l	0.44	0.40	0.01	b.d.l
FeOT*	49.86	49.59	47.87	47.18	98.96	98.93
MnO	1.04	1.06	1.27	1.06	0.01	0.02
ZnO	b.d.l	b.d.l	b.d.l	b.d.l	b.d.l	0.02
MgO	0.00	0.06	b.d.l	0.37	b.d.l	b.d.l
NiO	b.d.l	b.d.l	0.00	0.01	0.02	0.05
Co	n.a	n.a	n.a	n.a	n.a	n.a
Total	99.22	99.25	98.91	98.03	99.11	99.19
Formula based 3 oxygens (ilmenite) and 4 oxygens (magnetite)						
Si	0.00	0.00	0.00	0.00	-	0.00
Ti	0.92	0.92	0.94	0.94	0.00	0.00
Al	0.00	0.00	0.00	0.00	0.00	-
Cr	0.00	0.00	-	-	0.00	-
Fe^{3+}	0.16	0.16	0.11	0.11	2.00	1.99
Fe^{2+}	0.89	0.88	0.91	0.90	0.98	0.99
V	-	-	0.01	0.01	0.00	-
Mn	0.02	0.02	0.03	0.02	0.00	0.00
Mg	0.00	0.00	-	0.01	-	-
Zn	-	-	-	-	-	0.00
Ni	-	-	0.00	0.00	0.00	0.00
Cr#	54.42	69.05	-	-	0.50	-
Mg#	0.02	0.27	-	1.55	-	-
Fe^{3+} #	99.20	98.87	99.34	99.61	99.95	-

*FeOT expressed as FeO; b.d.l: below detection limit; n.a: not analyzed

5.2.2.2. Minerals of the metamorphic assemblage

Amphibole is the most abundant mineral in the metamorphic assemblage in all types of rock. In both groups amphibole displays calcic compositions that range from pargasite, magnesio-hornblende to tremolite (Fig. C5_7 amphibole nomenclature after Hawthorne et al., 2012). Textural observations indicate two types of amphibole: i) Amphibole 1: zoned amphibole (brown core and green to pale green rim) not showing direct replacement after clinopyroxene; in group 2 this amphibole does not show zonation; and ii) Amphibole 2 (green amphibole), which replaces clinopyroxene.

Both types of amphibole formed at low pressure conditions. The amphibole formula was based on 23 oxygens. In rocks of group 1, amphibole shows low Ti^{C} a.p.f.u (0.01-0.30 amphibole 1 and 0.06-0.24 amphibole 2) and Na^{B} (<0.17 amphibole 1 and <0.12 amphibole 2). High Al^{IV} in amphibole 1 (core of 1.08 to 1.74 a.p.f.u and rim of 0.21 to 1.22 a.p.f.u) and amphibole 2 (0.72 to 1.39 a.p.f.u) indicate low pressure conditions for both amphiboles (Figs. C5_7B, C5_7C and Table C5_4; Laird and Albee, 1981; Laird et al., 1984; Spear, 1993). The alkali occupancy $(Na+K)_{A}$ in amphibole 1 is higher in the core (0.18-0.55 a.p.f.u) than in the rim (0.04-0.25 a.p.f.u). All the observations suggest a decrease in temperature from core to rim.

In rocks of group 2, amphibole has low Ti^{C} (0.10-0.24 and 0.04-0.13 a.p.f.u in amphibole 1 and 2, respectively) and high Al^{IV} (1.15-1.51 and 0.51-1.23 a.p.f.u, amphibole 1 and 2, respectively), but higher Na^{B} (0.07-0.26 a.p.f.u in both amphiboles; Fig. C5_7C and Table C5_4) as opposed to amphiboles of group 1 rocks, suggesting somewhat higher pressure for group 2 rocks. The $(Na+K)_{A}$ contents are high in amphibole 1 (0.43-0.54 a.p.f.u) and low in amphibole 2 (0.12-0.35 a.p.f.u), indicating decreasing temperature for the group 1 rocks.

Some authors (e.g., Vanko, 1986; Kendrick et al., 2015 and references therein) have correlated Cl with $Al^{VI}+Fe^{3+}+Ti^{C}$ a.p.f.u in an attempt to track changes in temperature during fluid infiltration. In group 1 rocks, amphibole 1 displays slightly higher chlorine content (Fig. C5_7D, 0.02-0.07 Cl a.p.f.u) in comparison to group 2 amphiboles (0.01-0.05 Cl a.p.f.u). Group 2 rocks display the same correlations, with high Cl content in amphibole 1 and low in amphibole 2 (0.05-0.07 to <0.03, respectively; Fig. C5_7D). The chlorine in amphibole correlates positively with $Al + Fe^{3+} + Ti$ (Fig. C5_7D), supporting decreasing temperature during amphibole growth. The presence of fluid, most likely seawater, is needed to produce the amphibolisation. Nevertheless, we could not appraise the amount of fluid responsible for amphibolisation.

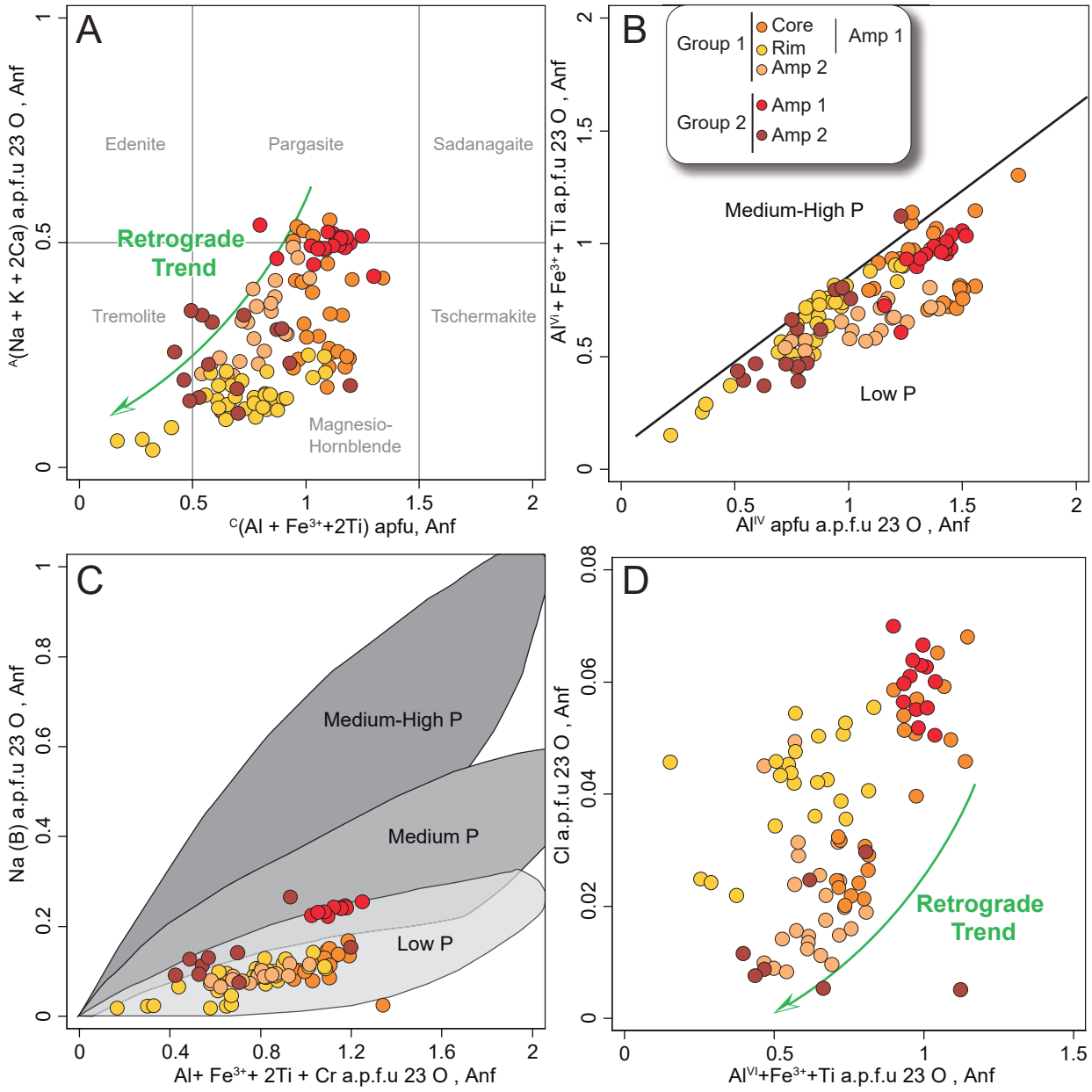

Figure. C5_7. *Group 1 and 2 amphibole composition of the sub-volcanic unit. A) Classification diagram of calcic amphiboles by Hawthorne et al. (2012). B) $Al^{VI}+Fe^{3+}+Ti$ a.p.f.u vs Al^{IV} a.p.f.u. C) Na^{B} a.p.f.u vs $Al^{VI}+Fe^{3+}+2{\cdot}Ti$ +Cr a.p.f.u. D) Cl a.p.f.u vs $Al^{VI}+Fe^{3+}+Ti$ a.p.f.u. Fields of medium-high, medium, and low pressure from Laird and Albee (1981) and Laird et al. (1984).*

Table C5_4. *Representative analyses of amphiboles of the sub-volcanic unit.*

Sample	09-LV-4A	08-SCB-116	08-VC-1	08-VC-1	08-SCB-116
Rock type	Microgabbro		Diabase		Microgabbro
Unit	Sub-volcanic				
Group	1	1	1	1	1
Amphibole Type	Amp 1	Amp 1	Amp 1	Amp 1	Amp 2
Textural position	Core		Rim		Cpx replacement
Classification	Mg-Hbl	Pg	Tr	Mg-Hbl	Mg-Hbl
Major elements (wt%)					
SiO_2	45.39	43.45	52.60	49.90	47.74
TiO_2	1.67	2.40	0.27	0.85	1.38
Al_2O_3	7.50	9.27	3.32	4.53	6.32
Cr_2O_3	0.02	0.03	0.33	b.d.l	0.17
V_2O_3	b.d.l	0.09	0.04	0.08	0.09
FeOT*	18.82	16.59	10.03	14.14	13.59
MnO	0.39	0.23	0.18	0.25	0.30
ZnO	b.d.l	b.d.l	b.d.l	0.02	0.02
MgO	11.60	11.41	17.35	14.97	14.32
NiO	0.01	0.04	0.01	b.d.l	0.03
CaO	10.32	11.55	12.16	11.32	11.66
Na_2O	1.27	1.96	0.48	0.69	1.30
K_2O	0.10	0.13	0.12	0.17	0.04
Cl	b.d.l	0.09	0.09	0.18	0.06
Total	97.09	97.22	96.99	97.10	97.03
Formula based 23 oxygens					
Si_T	6.75	6.50	7.52	7.27	6.99
Al_T	1.25	1.50	0.48	0.73	1.01
Al_C	0.07	0.14	0.08	0.05	0.08
Ti_C	0.19	0.27	0.03	0.09	0.15
Cr_C	0.00	0.00	0.04	-	0.02
$Fe^{3+}{}_C$	0.67	0.35	0.26	0.42	0.39
Mg_C	2.57	2.55	3.70	3.25	3.12
Ni_C	0.00	0.00	0.00	-	0.00
Zn_C	-	-	-	0.00	0.00
$Fe^{2+}{}_C$	1.50	1.69	0.89	1.19	1.23
$Fe^{2+}{}_B$	0.18	0.04	0.05	0.12	0.04
Mn_B	0.05	0.03	0.02	0.03	0.04
Ca_B	1.65	1.85	1.86	1.77	1.83
Na_B	0.13	0.08	0.07	0.09	0.09
Na_A	0.24	0.49	0.07	0.11	0.28
K_A	0.02	0.02	0.02	0.03	0.01
A-vacancy	0.74	0.49	0.91	0.86	0.71
Cl	-	0.02	0.02	0.04	0.01
$(Na+K)^A$	0.26	0.51	0.09	0.14	0.29

*FeOT expressed as FeO; b.d.l: below detection limit; n.a: not analyzed

Table C5_4. *Continued.*

Sample	08-VC-22	08-VC-22	08-VC-22	08-VC-22
Rock type	Diabase		Diabase	
Unit	Sub-volcanic			
Group	2	2	2	2
Amphibole Type	Amp 1	Amp 1	Amp 2	Amp 2
Textural position			Cpx replacement	
Classification	Pg	Mg-Hbl	Mg-Hbl	Tr
Major elements (wt%)				
SiO_2	42.22	43.51	47.52	50.48
TiO_2	1.81	1.07	0.92	0.58
Al_2O_3	9.34	8.15	5.39	3.36
Cr_2O_3	0.01	0.01	0.00	0.00
V_2O_3	b.d.l	b.d.l	b.d.l	b.d.l
FeOT*	23.35	23.58	19.01	16.76
MnO	0.44	0.45	0.40	0.45
ZnO	b.d.l	b.d.l	b.d.l	b.d.l
MgO	7.60	7.68	11.24	13.23
NiO	b.d.l	b.d.l	b.d.l	b.d.l
CaO	9.46	9.72	10.48	10.85
Na_2O	2.26	2.05	1.49	0.94
K_2O	0.49	0.53	0.50	0.25
F	0.40	0.47	0.55	0.42
Cl	0.19	0.27	0.10	0.05
Total	97.56	97.48	97.59	97.37
Formula based 23 oxygens				
Si_T	6.49	6.70	7.13	7.46
Al_T	1.51	1.30	0.87	0.54
Al_C	0.18	0.18	0.08	0.05
Ti_C	0.21	0.12	0.10	0.06
Cr_C	0.00	0.00	0.00	0.00
$Fe^{3+}{}_C$	0.65	0.59	0.44	0.28
Mg_C	1.74	1.76	2.51	2.92
Ni_C	0.00	0.00	0.00	0.00
Zn_C	-	-	-	-
$Fe^{2+}{}_C$	2.22	2.34	1.87	1.69
$Fe^{2+}{}_B$	0.13	0.11	0.08	0.10
Mn_B	0.06	0.06	0.05	0.06
Ca_B	1.56	1.61	1.68	1.72
Na_B	0.25	0.22	0.19	0.12
Na_A	0.42	0.39	0.24	0.15
K_A	0.10	0.10	0.10	0.05
A-vacancy	0.49	0.51	0.66	0.81
Cl	0.05	0.07	0.02	0.01
F	0.19	0.23	0.26	0.20
$(Na+K)^A$	0.51	0.49	0.34	0.19

*FeOT expressed as FeO; b.d.l: below detection limit

Prehnite shows minimal substitution of Fe^{3+} and Al (<0.01 of Fe#, Table C5_5). Epidote replaces plagioclase cores in group 1 and 2 diabase and microgabbro rocks. Epidote has compositions of clinozoizite with low Fe# = [$Fe^{3+}/(Fe^{3+}+Al^{3+})$] <0.09 in group 1, whereas in group 2 it bears higher values (c. 0.20, Table C5_6). Chlorite from group 1 rocks displays low Mg (0.95 to 1.12 a.p.f.u) and high Fe (7.97 to 8.27 a.p.f.u), whereas in group 2 rocks it shows higher Mg (2.81 to 3.81 a.p.f.u) and lower Fe (5.49 to 6.68 a.p.f.u). Al^{VI} is slightly higher in group 1 (2.57-2.73 a.p.f.u) than in group 2 rocks (2.06-2.78 a.p.f.u). The composition of chlorites of group 1 and 2 rocks belongs to the clinochlore-chamosite series (see Table C5_7).

Table C5_6. *Representative analyses of prehnite from sub-volcanic unit.*

Sample	09-LV-4A	09-LV-4A	09-LV-4A	09-LV-4A	09-LV-4A	08-VC-1	08-VC-1
Rock type	Microgabro					Diabase	
Unit	Sub-volcanic						
Group	1	1	1	1	1	1	1
Mineral	Prehnite						
Major elements (wt%)							
SiO_2	43.67	44.12	43.93	44.22	44.31	44.03	43.84
TiO_2	0.01	b.d.l	b.d.l	0.08	0.02	0.05	b.d.l
Al_2O_3	23.97	23.99	24.14	23.54	23.85	23.62	23.85
FeOT*	0.11	0.14	0.11	0.28	0.18	0.33	0.25
MnO	b.d.l	b.d.l	0.02	0.04	0.02	0.07	0.06
MgO	b.d.l	0.01	0.02	b.d.l	b.d.l	n.a	n.a
CaO	26.99	26.35	26.33	26.44	26.19	26.65	26.72
Na_2O	0.05	0.09	0.16	0.16	0.16	0.08	0.09
K_2O	b.d.l	0.02	0.01	0.02	0.03	0.00	0.01
Total	94.82	94.71	94.72	94.77	94.76	94.82	94.82
Formula based 11 oxygens							
Si_T	3.02	3.05	3.04	3.06	3.06	3.05	3.03
Al_T	0.98	0.95	0.96	0.94	0.94	0.95	0.97
Al_M	0.98	1.00	1.00	0.98	1.00	0.97	0.98
Fe^{3+}_M	0.01	0.01	0.01	0.02	0.01	0.02	0.01
Mn_A	-	-	0.00	0.00	0.00	0.00	0.00
Mg_A	-	0.00	0.00	-	-	-	-
Ca_A	2.00	1.95	1.95	1.96	1.94	1.97	1.98
Na_A	0.01	0.01	0.02	0.02	0.02	0.01	0.01
K_A	0.00	0.00	0.00	0.00	0.00	0.00	0.00
Fe#	0.00	0.00	0.00	0.01	0.01	0.01	0.01

*FeOT expressed as FeO; b.d.l: below detection limit; n.a: not analyzed

Table C5_6. *Representative analyses of epidote from sub-volcanic unit.*

Sample	08-VC-117	08-VC-117	08-VC-22	08-VC-22
Rock type	Microgabbro			
Unit	Sub-volcanic			
Group	1	1	2	2
Mineral	Epidote			
Major elements (wt%)				
SiO_2	38.72	39.10	39.02	38.84
TiO_2	b.d.l	0.06	0.03	0.03
Al_2O_3	30.03	30.34	23.90	24.24
Cr_2O_3	0.03	b.d.l	b.d.l	b.d.l
V_2O_3	b.d.l	b.d.l	0.28	0.25
FeOT*	3.76	3.08	8.25	8.20
MnO	0.03	0.05	0.07	0.13
ZnO	0.02	n.a	0.05	0.02
MgO	0.00	0.03	1.53	1.48
NiO	n.a	0.01	b.d.l	b.d.l
CaO	24.52	24.48	24.02	24.11
SrO	n.a	n.a	b.d.l	b.d.l
BaO	n.a	n.a	b.d.l	b.d.l
Na_2O	0.02	0.01	0.06	b.d.l
K_2O	0.00	n.a	b.d.l	b.d.l
Total	97.13	97.16	97.22	97.30
Formula based	12.5 oxygens			
Si_T	2.99	3.01	3.06	3.05
Al_T	0.01	-	-	-
Al_{M1}	1.00	1.00	1.00	1.00
Al_{M2}	1.00	1.00	1.00	1.00
Al_{M3}	0.73	0.76	0.21	0.24
Fe^{3+}_{M3}	0.24	0.20	0.54	0.54
Mn_{M3}	0.00	0.00	0.00	0.01
Fe^{2+}_{M3}	0.00	0.00	0.00	0.00
Cr_{M3}	0.00	-	0.00	0.00
V_{M3}	-	-	0.02	0.02
Zn_{M3}	0.00	-	0.00	0.00
Mg_{M3}	0.00	0.00	0.18	0.17
Ti_{M3}	-	0.00	0.00	0.00
Ca_{A1}	1.00	1.00	1.00	1.00
Ca_{A2}	1.00	1.00	1.00	1.00
Sr_{A2}	-	-	-	-
Ba_{A2}	-	-	-	-
Na_{A2}	-	-	-	-
K_{A2}	-	-	-	-
Fe#	0.08	0.07	0.20	0.19

*FeOT expressed as FeO; b.d.l: below detection limit; n.a: not analyzed

Table C5_7. *Representative analyses of chlorite from sub-volcanic unit.*

Sample	14-SC-2	14-SC-2	08-VC-21	08-VC-22	08-VC-22
Rock type	Microgabbro				Diabase
Unit	Sub-volcanic				
Group	1	1	2	2	2
Mineral	Chlorite		Chlorite		
Major elements (wt%)					
SiO_2	24.10	22.79	27.29	26.24	27.53
TiO_2	0.16	0.05	0.10	b.d.l	0.45
Al_2O_3	19.87	19.46	18.31	20.24	16.81
Cr_2O_3	0.04	b.d.l	0.03	0.01	0.06
V_2O_3	0.31	0.03	0.04	0.06	b.d.l
FeOT*	42.19	42.80	31.72	33.36	30.04
MnO	0.23	0.39	0.38	0.51	0.30
ZnO	0.00	0.03	0.04	0.09	b.d.l
MgO	2.81	3.24	11.49	9.65	12.12
NiO	0.05	0.03	0.02	0.02	0.00
CaO	0.22	0.06	0.19	0.18	0.15
F	b.d.l	b.d.l	b.d.l	b.d.l	0.19
Total	90.01	88.89	89.76	90.36	87.72
Formula based 28 oxygens					
Si_T	5.44	5.27	5.81	5.59	5.97
Al_T	2.56	2.73	2.19	2.41	2.03
Al_M	2.74	2.57	2.41	2.69	2.26
Cr_M	0.01	-	0.01	0.00	0.01
Mg_M	0.95	1.12	3.65	3.07	3.92
Fe^{2+}_M	7.97	8.27	5.65	5.95	5.44
Mn_M	0.04	0.08	0.07	0.09	0.05
Ni_M	0.01	0.01	0.00	0.00	0.00
Ca_M	0.05	0.02	0.04	0.04	0.04
F	-	-	-	-	0.13
Mg#	0.11	0.12	0.39	0.34	0.42

*FeOT expressed as FeO; b.d.l: below detection limit. Mg#=(Fe/Fe+Mg)

5.2.3. Whole-rock chemistry

Whole-rock compositions and isotopic data can be found in Table C5_8 and Table C5_9.

5.2.3.1. Major elements

Whole-rock major element composition allows for discriminating two groups in the sub-volcanic unit. Group 1 displays high Mg# = [100·MgO_{mol}/(MgO_{mol}+0.9·$FeO_{T\ mol}$)] compositions (*c.* 54 to 69) and CaO (*c.* 7 to 13 wt%), and low SiO_2 (*c.* 48 to 54 wt%) and K_2O (*c.* <0.31 wt%), all in anhydrous basis (Fig. C5_8).

However, group 2 rocks have lower Mg# (*c.* 41 to 43) and CaO (*c.* 6 to 7 wt%) and higher SiO_2 (c. 56 wt%), K_2O (*c.* 1.3 wt%) and Na_2O (*c.* 4wt%). This variability points to a magmatic differentiation of group 1 from 2 (Fig. C5_8). Notwithstanding, enrichment processes during metamorphic transformation modified the amount of alkali elements (Na_2O and K_2O) of the whole rock.

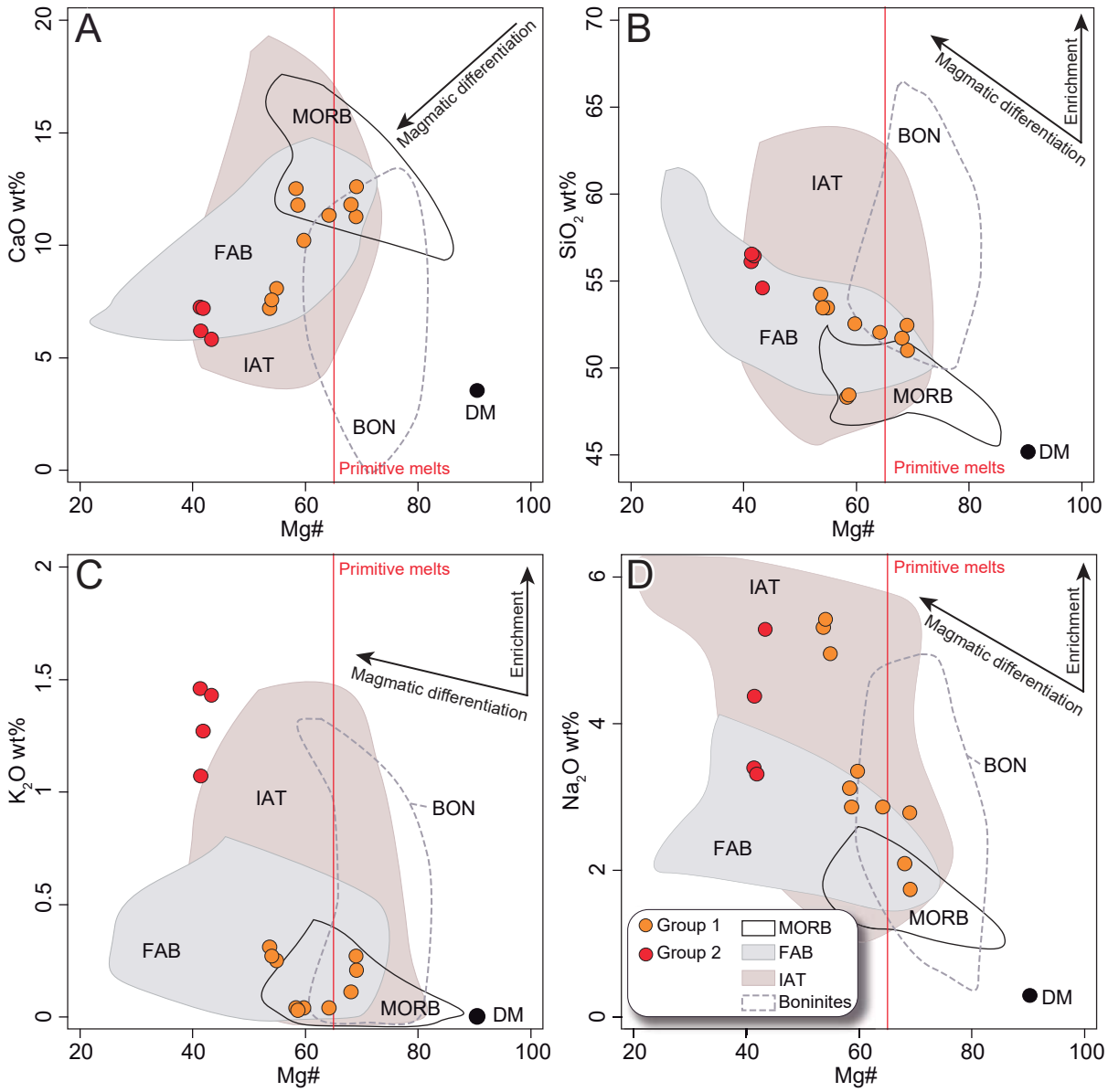

Figure. C5_8 *Whole-rock compositions of the sub-volcanic rocks. A) CaO wt% vs Mg#. B) SiO_2 wt% vs Mg#. C) K_2O wt% vs Mg#. D) Na_2O wt% vs Mg#. Mg# was calculated using molar proportions of MgO and FeOtotal and 10% Fe_2O_3 (Gill, 2010). Primitive melts considered bear >65 Mg# (Gill, 2010 and references therein). All oxides calculated in anhydrous basis. Fields of mid-ocean ridge basalts (MORB) from Gurenko and Chaussidon (1997), compilation of Stracke et al. (2003a) and (2003b); Forearc basalt (FAB) from Reagan et al. (2010) and Ishizuka et al. (2011); Island arc toleiites (IAT) from Marchesi et al. (2007), Escuder et al. (2007) and (2011); and Boninites from Pearce et al. (1992), Marchesi et al. (2007), Bonev and Stampli (2008), Reagan et al. (2010) and Escuder et al. (2011). Depleted mantle (DM) is plotted as a reference from Salters and Stracke (2004).*

Table C5_8. *Whole-rock composition of samples of the sub-volcanic unit from the mafic crust in the VCSM.*

Sample	08-VC-2	08-VC-10	09-LV-4A	08-VC-1	08-VC-117	08-SCB-116	08-SCB-40B
Latitude	22°27'5.70"N	22°26'35.60"N	22°28'2.90"N	22°27'5.70"N	22°28'2.90"N	22°28'0.66"N	22°29'14.38"N
Longitude	79°47'35.70"W	79°48'14.80"W	79°49'28.50"W	79°47'35.70"W	79°49'28.50"W	79°49'27.42"W	79°51'43.21"W
Unit	Sub-volcanic						
Group	1	1	1	1	1	1	1
Rock type	Diabase	Diabase	Microgabbro	Diabase	Microgabbro	Diabase	Diabase
Major elements (wt%)							
SiO_2	49.26	50.83	50.52	50.65	52.24	46.68	50.62
TiO_2	0.54	0.91	1.17	0.64	1.17	1.33	0.86
Al_2O_3	16.28	15.83	15.77	15.82	16.14	16.03	16.28
Fe_2O_3T	8.49	10.01	9.79	8.09	9.94	11.20	9.01
MnO	0.13	0.18	0.16	0.14	0.16	0.18	0.16
MgO	8.62	6.76	5.42	8.20	5.22	7.11	7.33
CaO	12.16	9.89	7.63	10.88	6.94	12.08	11.02
Na_2O	1.68	3.24	4.68	2.69	5.12	3.02	2.78
K_2O	0.20	0.04	0.24	0.26	0.30	0.04	0.04
P_2O_5	0.05	0.07	0.12	0.05	0.12	0.12	0.09
LOI	2.19	1.87	4.04	1.96	2.41	2.02	1.66
Total	99.60	99.63	99.54	99.38	99.76	99.81	99.85
Trace elements (ppm)							
Li	1.377	0.532	1.923	1.240	1.624	2.350	0.432
Rb	2.807	0.545	3.421	4.267	5.335	0.775	0.433
Cs	0.291	0.027	0.622	0.168	0.798	0.116	0.054
Be	0.048	0.261	0.417	0.214	0.410	0.309	0.325
Sr	183.240	222.382	1327.299	197.607	433.962	447.412	153.016
Ba	75.382	39.618	120.562	114.593	116.610	122.178	26.932
Sc	18.056	40.901	33.241	39.390	34.235	43.868	36.673
V	236.460	288.613	280.548	230.118	287.050	347.578	214.598
Cr	301.717	54.340	34.998	276.512	39.356	77.876	201.724
Co	41.536	50.780	39.448	48.751	49.924	69.753	58.023
Ni	90.655	45.237	27.059	88.103	27.694	49.021	80.539
Cu	19.050	81.081	60.649	71.759	120.720	80.288	27.755
Zn	30.490	48.901	57.095	49.991	140.200	80.993	62.520
Ga	12.610	15.029	15.689	12.524	15.967	15.362	14.505

Total Fe as Fe_2O_3T

n.a: not analyzed; b.d.l: below detection limit

Table C5_8. *Continued.*

Sample	08-VC-2	08-VC-10	09-LV-4A	08-VC-1	08-VC-117	08-SCB-116	08-SCB-40B
Trace elements (ppm)							
Y	13.503	21.078	27.229	15.583	27.259	31.285	22.326
Nb	0.767	0.549	1.095	0.486	1.047	1	0.85
Zr	30.9	41.2	76.8	32.8	70.1	41	53.6
Mo	1.033	1.847	1.287	1.661	2.129	3.565	3.095
Sn	0.514	0.459	0.612	0.153	1.511	0.82	0.725
Tl	0.016	0.004	0.005	0.007	0.006	0.003	0.002
Pb	0.449	0.318	0.32	0.557	8.619	0.36	0.341
U	0.047	0.041	0.048	0.037	0.051	0.025	0.042
Th	0.217	0.137	0.164	0.108	0.145	0.036	0.117
La	1.329	1.772	3.296	1.674	3.157	2.182	2.841
Ce	3.579	5.37	9.649	4.76	9.275	7.919	7.765
Pr	0.614	0.971	1.639	0.806	1.574	1.531	1.282
Nd	3.116	5.556	9.082	4.481	8.124	8.633	6.600
Sm	1.166	2.152	3.171	1.625	2.804	3.151	2.235
Eu	0.36	0.874	1.142	0.633	1.123	1.337	0.936
Gd	1.507	2.864	3.899	2.081	3.746	4.386	3.025
Tb	0.288	0.514	0.674	0.371	0.649	0.743	0.525
Dy	2.044	3.472	4.475	2.557	4.373	5.054	3.509
Ho	0.486	0.78	1.008	0.578	0.988	1.134	0.802
Er	1.372	2.137	2.761	1.575	2.685	3.102	2.194
Tm	0.232	0.346	0.441	0.248	0.441	0.499	0.357
Yb	1.441	2.119	2.712	1.566	2.703	2.981	2.185
Lu	0.208	0.326	0.413	0.244	0.405	0.453	0.337
Hf	0.647	0.521	1.099	0.514	0.828	0.899	0.742

Table C5_8. *Continued.*

Sample	14-SC-2	08-VC-9	08-VC-116	08-VC-21	08-VC-22	09-LV-8C	08-SCB-34D
Latitude	22°27'9.60"N	22°27'16.90"N	22°28'24.80"N	22°19'44.20"N	22°19'44.20"N	22°19'44.20"N	22°19'44.20"N
Longitude	79°52'22.20"W	79°47'44.20"W	79°49'34.10"W	79°42'53.10"W	79°42'53.10"W	79°42'53.10"W	79°42'53.10"W
Unit	Sub-volcanic						
Group	1	1	1	2	2	2	2
Rock type	Microgabbro	Microgabbro	Diabase	Diabase	Diabase	Diabase	Diabase
Major elements (wt%)							
SiO_2	51.32	50.04	46.09	54.03	54.17	54.68	52.75
TiO_2	1.24	0.80	1.32	1.05	1.05	1.08	1.23
Al_2O_3	16.12	16.19	17.28	16.21	16.27	16.18	16.79
Fe_2O_3T	9.99	8.55	10.49	10.55	10.35	10.65	10.56
MnO	0.17	0.15	0.15	0.20	0.20	0.20	0.21
MgO	5.35	8.30	6.76	3.38	3.38	3.42	3.68
CaO	7.25	11.42	11.22	6.97	6.90	5.99	5.61
Na_2O	5.20	2.02	2.72	3.26	3.18	4.23	5.10
K_2O	0.26	0.11	0.03	1.41	1.22	1.03	1.38
P_2O_5	0.12	0.07	0.13	0.30	0.30	0.32	0.36
LOI	2.80	2.07	3.44	1.81	2.07	1.92	2.21
Total	99.82	99.72	99.63	99.17	99.08	99.70	99.88
Trace elements (ppm)							
Li	1.569	0.477	5.584	8.263	5.807	11.886	13.647
Rb	4.920	0.597	1.539	24.498	23.446	19.584	22.213
Cs	0.794	0.324	0.302	0.503	0.609	0.283	0.608
Be	0.443	b.d.l	0.542	0.513	0.396	0.953	0.981
Sr	637.225	178.597	735.895	376.518	381.718	362.188	263.706
Ba	136.831	44.891	35.655	429.250	424.925	366.869	515.322
Sc	35.031	14.275	41.057	11.680	10.296	31.158	38.085
V	292.276	206.721	322.489	237.216	223.795	251.987	356.174
Cr	36.402	155.299	60.061	26.890	56.285	18.219	25.803
Co	42.472	76.062	51.538	32.630	66.036	54.667	47.746
Ni	27.396	111.554	49.759	8.693	10.214	8.475	17.769
Cu	67.158	10.318	9.561	182.602	184.238	149.612	144.184
Zn	57.057	15.945	56.713	76.270	59.698	90.284	107.679
Ga	16.347	11.127	16.450	17.265	15.854	17.799	18.895

Total Fe as Fe_2O_3T; b.d.l: below detection limit

Table C5_8. *Continued.*

Sample	14-SC-2	08-VC-9	08-VC-116	08-VC-21	08-VC-22	09-LV-8C	08-SCB-34D
Trace elements (ppm)							
Y	27.762	17.449	29.82	27.172	26.414	29.536	34.085
Nb	0.981	0.667	1.46	2.475	2.304	2.539	2.816
Zr	75.5	44.9	82	108.3	109.6	111.4	107
Mo	1.481	5.107	1.763	1.846	7.295	3.482	2.655
Sn	1.248	0.742	1.098	1.519	1.618	1.816	1.54
Tl	0.003	0.002	0.007	0.092	0.09	0.078	0.064
Pb	0.892	b.d.l	1.697	1.442	0.96	1.429	1.908
U	0.038	0.042	0.061	0.572	0.655	0.736	0.599
Th	0.127	0.134	0.274	1.328	1.381	1.411	1.224
La	3.14	1.786	3.82	11.95	12.983	12.498	13.728
Ce	9.202	5.291	11.252	28.563	30.67	28.667	32.089
Pr	1.556	0.916	1.897	4.182	4.539	4.185	4.822
Nd	8.118	5.034	10.366	19.277	20.676	18.981	20.151
Sm	2.786	1.837	3.577	4.947	5.343	4.835	5.160
Eu	1.156	0.718	1.239	1.368	1.504	1.551	1.744
Gd	3.801	2.638	4.412	4.913	5.379	5.027	5.85
Tb	0.658	0.475	0.755	0.798	0.865	0.783	0.91
Dy	4.398	3.15	5.009	4.39	5.162	4.868	5.74
Ho	0.992	0.685	1.104	0.999	1.063	1.044	1.248
Er	2.791	1.975	3.067	2.626	2.895	2.913	3.373
Tm	0.448	0.302	0.445	0.413	0.465	0.461	0.542
Yb	2.739	1.854	2.827	2.544	2.814	2.899	3.31
Lu	0.423	0.271	0.425	0.366	0.43	0.464	0.508
Hf	1.07	0.818	1.147	2.418	2.809	2.6	2.307

Whole-rock major element compositions of the sub-volcanic unit were classified using TAS, AFM and K_2O vs SiO_2 diagrams (Fig. C5_9). Group 1 rocks are basalt, basaltic andesite to andesite with a tholeiitic to low K calc-alkaline signature (Fig. C5_9A to C5_9C). Group 2 are basaltic andesite to andesite with a medium K calc-alkaline signature. Nevertheless, these classification diagrams (Figs. C5_9A to C5_9C) overestimate the alkali component due to major alteration of the unit (loss-on-ignition, LOI, 1.7 to 4.04 of groups 1 and 2). In order to avoid overestimation of alkalis, we use immobile trace element ratios Zr/Ti and Nb/Y (Fig. C5_9D, Winchester and Floyd, 1977). This diagram classifies group 1 as basalt, whereas group 2 is of basaltic andesite composition.

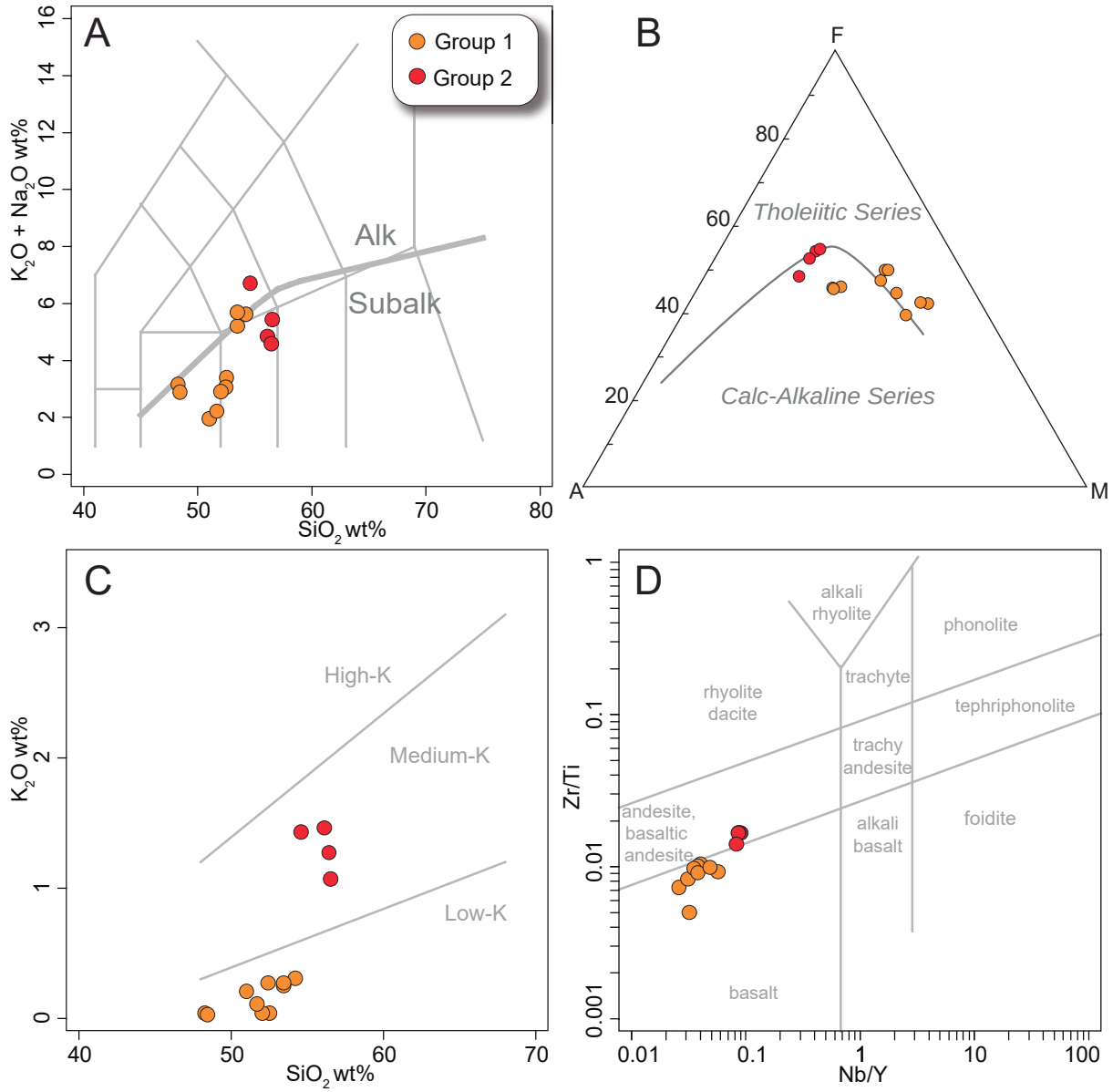

Figure. C5_9 *Classification diagrams of the sub-volcanic unit. A) Total alkali vs. silica (TAS, Le Maître, 2002). B) (Na_2O+K_2O)- FeO_T- MgO (AFM), fields of Irvine and Baragar (1971). C) K_2O wt% vs SiO_2 wt% fields of Rickwood (1989). D) Zr/Ti vs. Nb/Y diagram with fields of Winchester and Floyd (1977).*

5.2.3.2. Trace elements

The chondrite normalized (CI) REE patterns of group 1 rocks of the sub-volcanic unit (Fig. C5_10A) display depletion in light REE (LREE, $La/Sm_{N\ CI95}$ =0.43-0.79; normalized to C1 chondrite from McDonough and Sun, 1995) with nearly flat ($Sm/Lu_{N\ CI95}$ =0.93-1.39) middle REE (MREE) to heavy REE (HREE) that resemble normal mid-ocean ridge basalt (N-MORB) patterns. Six samples display a moderate positive Eu anomaly ($Eu/Eu^{*}=[Eu_{N\ C195}/(Sm_{N\ CI95} \cdot Gd_{N\ CI95})^{1/2}]$=1.07 average); another five samples show no Eu anomaly or a slightly negative anomaly (Eu/Eu^{*}=0.83 to 0.99). N-MORB normalized patterns (Fig. C5_10B) show a positive Th anomaly, negative Nb anomaly and nearly flat trace patterns from La to Yb ($La/Yb_{N\ N\text{-}MORB89}$=0.89 to 1.65). Group 2 shows LREE enrichment ($La/Sm_{N\ CI95}$ =1.51-1.66) with high MREE to HREE ($Sm/Lu_{N\ CI95}$ =1.68-2.25) and a negative Eu anomaly (Eu/Eu^{*}=0.85-0.97, Fig. C5_10C). N-MORB

normalized patterns of group 2 rocks show high values from La to low Yb ($La/Yb_{N\ N\text{-}MORB89}$=5.06 to5.73; normalized to N-MORB from Sun and McDonough, 1989), and a characteristic positive Th anomaly ($Th_{N\ N\text{-}MORB89}$=10.2-11.6) higher than in group 1 rocks, with negative Nb and Ti anomalies ($Nb/La_{N\ N\text{-}MORB89}$=0.19 to 0.22 and $Ti/Gd_{N\ N\text{-}MORB89}$=0.59-0.64, respectively, Fig. C5_10D).

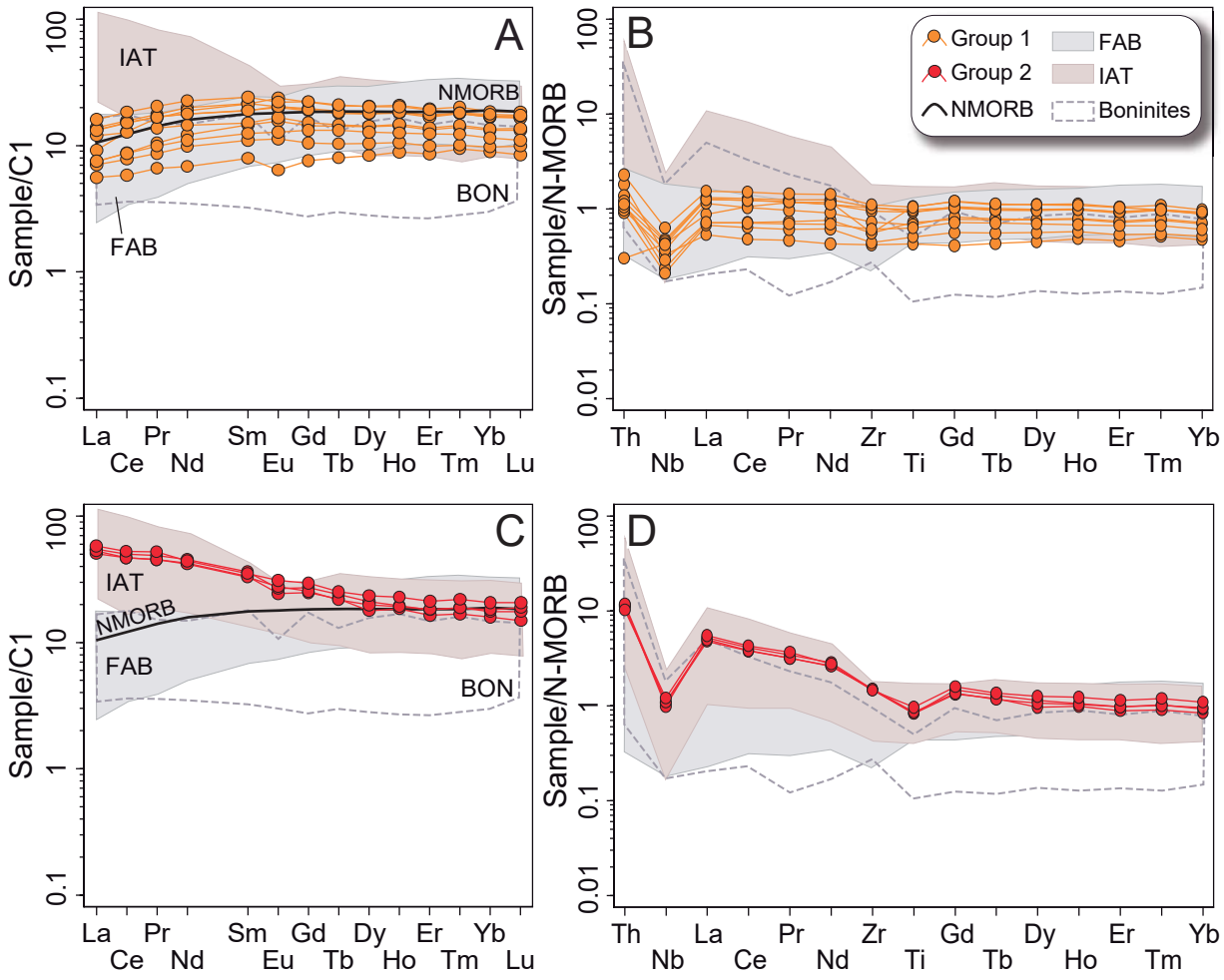

Figure. C5_10 *Normalized trace element composition of sub-volcanic rocks. A) and C) Chondrite-normalized whole-rock REE. B) and D) N-MORB normalized whole-rock trace element composition. CI chondrite-normalizing values were from McDonough and Sun (1995) and N-MORB normalisation values from Sun and McDonough (1989). Fields of forearc basalt (FAB) are from Reagan et al. (2010) and Ishizuka et al.(2011); Island arc toleiites (IAT) from Marchesi et al. (2007), Escuder et al. (2007) and (2011); and Boninites from Pearce et al. (1992), Bonev and Stampli (2008) and Reagan et al. (2010).*

5.2.3.1 *5.2.3.3. Nd-Sr isotope systematics*

The isotopic compositions of sub-volcanic rocks are similar for both groups. Measured $^{87}Sr/^{86}Sr$ and $^{143}Nd/^{144}Nd$ ratios in group 1 rocks range 0.70352-0.70578 and 0.51302-0.51318 (Table C5_9). Group 2 rocks gave $^{87}Sr/^{86}Sr$ values of 0.70342-0.70377 and $^{143}Nd/^{144}Nd$ of 0.51299-0.51301.

Table C5_9. *Isotopic composition of samples of the sub-volcanic unit from the mafic crust in the VCSM.*

Sample	08-VC-2	08-VC-117	08-SCB-116	08-SCB-40B	14-SC-2	08-VC-9	08-VC-22	09-LV-8C	08-SCB-34D
Unit	Sub-volcanic								
Group	1	1	1	1	1	1	2	2	2
Sr (ppm)	173.470	433.869	447.268	152.959	637.131	163.221	418.282	362.051	263.615
Nd (ppm)	3.179	8.124	8.633	6.600	8.118	4.716	18.682	18.981	20.151
$^{87}Sr/^{86}Sr$	0.70412	0.70511	0.70400	0.70352	0.70578	0.70362	0.70344	0.70342	0.70377
$^{87}Sr/^{86}Sr$ error	0.0020	0.0020	0.0020	0.0020	0.0030	0.0030	0.0020	0.0020	0.0020
$^{147}Sm/^{144}Nd$	0.2165	0.2087	0.2207	0.2047	0.2075	0.2208	0.1544	0.1540	0.1548
$^{143}Nd/^{144}Nd$	0.51311	0.51305	0.51315	0.51318	0.51302	0.51309	0.51301	0.51299	0.51297
$^{143}Nd/^{144}Nd$ error	0.0020	0.0020	0.0020	0.0030	0.0020	0.0020	0.0020	0.0020	0.0020
$^{87}Sr/^{86}Sr_t$	0.70403	0.70505	0.70399	0.70351	0.70574	0.70359	0.70313	0.70315	0.70334
$^{143}Nd/^{144}Nd_t$	0.51293	0.51288	0.51297	0.51302	0.51285	0.51291	0.51288	0.51286	0.51284

T= 125Ma; Eclogitic metamorphic peak event in Santa Clara serpentinitic mélange that indicates pre-Aptian subduction (125Ma, García-Casco et al., 2002)

5.3. Plutonic unit: layered Gabbros and Ol-Gabbros

The plutonic unit is composed of accumulated gabbro (3 samples: 08-VC-23, 08-VC-25, and 14-SC-3) and cumulate olivine gabbro (4 samples: 08-VC-24, 09-LV-8A, 09-LV-8B and 08-SCB-34-D3-1). The terminology of cumulate gabbro and cumulate ol-gabbros was based on the USGS classification (Le Maître, 2002). The plutonic unit shows plagioclase, clinopyroxene, orthopyroxene and olivine in the magmatic assemblage

5.3.1. Petrography

The cumulate gabbros and ol-gabbros contain variable proportions of plagioclase, clinopyroxene, orthopyroxene, olivine and magnetite as accessory phases. Amphibole, serpentine, epidote, chlorite and prehnite are also present as metamorphic minerals. Clinopyroxene, orthopyroxene and olivine constitute main mafic minerals in cumulate gabbros and ol-gabbros.

These rocks have equigranular and adcumulate textures marked by plagioclase and clinopyroxene orientation (Fig. C5_2E, C5_11A and C5_11B). The cumulus phases include plagioclase, clinopyroxene, orthopyroxene and olivine. The intercumulus phases are Fe-Ti oxides. Plagioclase (*c.* 1 mm) with euhedral to subhedral shape is the most abundant phase, *c.* 60-50 % vol., with normal and polysynthetic twins (Fig. C5_11A and C5_11B). Clinopyroxene (*c.* 1-0.5 mm), *c.* 30-48 % vol., has a subhedral shape with twins. In some samples it is poikilitic, including crystals of plagioclase. Olivine (*c.* < 1 mm, c. 15-20 % vol.), is not present in all samples. It has xenomorphic textures, locally including plagioclase (Fig C5_11C). Olivine is generally altered by serpentine and magnetite along partition planes, resulting in mesh rim textures (Fig C5_11C). Orthopyroxene with subhedral shape (*c.* 0.5 mm), 10-1 % vol., is the least abundant phase.

Some samples display metamorphic assemblages. The smaller crystals of clinopyroxene (*c.* 50 µm) are replaced by amphibole, which is zoned with pale green (core) to colourless (rim) in large crystals (*c.* 1 mm); prismatic colourless amphiboles are also present in the most altered samples. Amphibole has euhedral to

subhedral shape. Pseudomorphs of amphibole after clinopyroxene are common (Fig C5_11D). Amphibole is also altered to chlorite. Serpentine after olivine is common (Fig. C5_11C). Plagioclase is transformed to prehnite and epidote. During the retrograde path, the rock prehnite show altered plagioclase and form veins that crosscut primary and metamorphic assemblages of amphibolite facies (Fig C5_11D).

The apparent order of magmatic crystallization is: plagioclase, olivine, clinopyroxene, orthopyroxene. The metamorphic assemblage indicates low temperature.

Figure. C5_11 *Crossed polar optical photographs of gabbro and Ol-gabbro from the VCSM. A) Layered gabbro with adcumulate texture; note the preferred orientation of plagioclase and clinopyroxene. B) Ol-gabbro showing cumulus phases (plagioclase, clinopyroxene, orthopyroxene and olivine). C) Replacement of serpentine after olivine. Note plagioclase included in olivine. D) Pseudomorphs of amphibole after clinopyroxene and prehnite vein.*

5.3.2. Mineral chemistry

Mineral compositions of the plutonic unit are offered below. The mineral formula of feldspar was normalized to 8 oxygens, pyroxene to 6 oxygens, olivine and magnetite to 4 oxygens, amphibole to 23 oxygens, epidote to 12.5 oxygens, chlorite to 28 oxygens and prehnite to 11 oxygens (more details in chapter 3).

5.3.2.1. Minerals of the magmatic assemblage

Plagioclase does not display zonation. It has a restricted composition of bytownite (An_{80-90}; Fig. C5_12, Table C5_10).

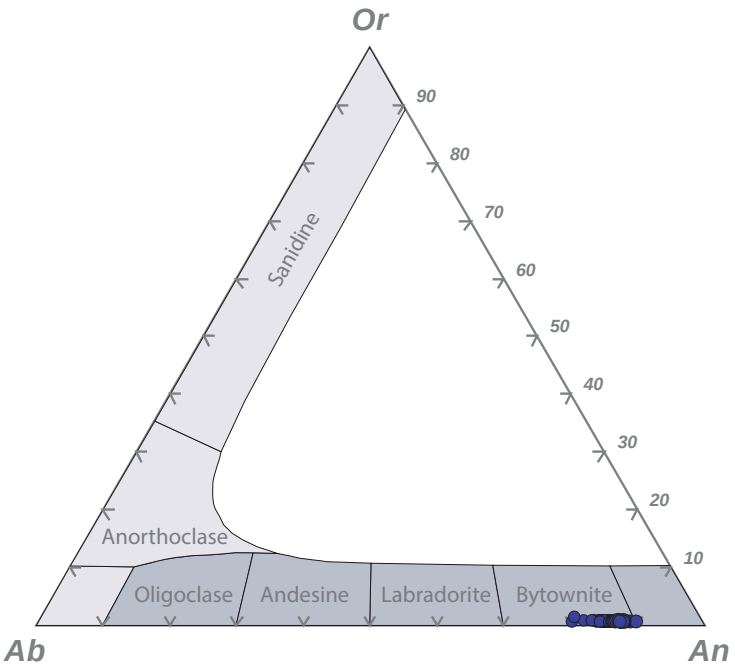

Figure. C5_12 *Classification of feldspars of the plutonic unit in the An-Ab-Or diagram.*

Table C5_10. *Representative analyses of feldspars of the plutonic unit.*

Sample	08-VC-23	08-VC-25	08-VC-24	09-LV-8B	09-LV-8A	08-SCB-34-D3-1
Rock type	Cumulated gabbro			Ol-gabbro		
Unit			Plutonic			
Mineral	Bytownite	Bytownite	Bytownite	Bytownite	Bytownite	Bytownite
Major elements (wt%)						
SiO_2	46.83	46.41	46.57	47.30	46.89	45.70
TiO_2	0.01	0.01	0.01	0.02	0.05	0.03
Al_2O_3	33.63	33.78	33.58	33.70	33.44	33.54
FeOT*	0.54	0.51	0.53	0.49	0.48	0.49
MnO	b.d.l	0.01	0.01	0.02	0.01	b.d.l
MgO	0.08	0.05	0.05	b.d.l	0.06	0.12
CaO	17.50	17.69	17.88	17.43	17.39	17.86
Na_2O	1.72	1.73	1.76	1.74	1.58	1.57
K_2O	0.01	0.03	0.02	0.01	b.d.l	0.02
Total	100.32	100.22	100.41	100.75	99.89	99.34
Formula Based 8 oxygens						
Si	2.15	2.13	2.14	2.16	2.16	2.12
Ti	0.00	0.00	0.00	0.00	0.00	0.00
Al	1.82	1.83	1.82	1.81	1.81	1.84
Fe^{+3}	0.02	0.02	0.02	0.02	0.02	0.02
Mg	0.01	0.00	0.00	0.00	0.00	0.01
Na	0.15	0.15	0.16	0.15	0.14	0.14
K	0.00	-	0.00	0.00	0.00	0.00
Ca	0.86	0.87	0.88	0.85	0.86	0.89
Or %	0.06	0.17	0.11	0.06	-	0.12
Ab %	15.09	15.01	15.10	15.29	14.12	13.68
An %	84.85	84.82	84.78	84.65	85.88	86.20

*FeOT expressed as FeO; b.d.l: below detection limit

Pyroxenes were classified using the diagram of Morimoto et al. (1988) (Fig. C5_13A). All pyroxenes plot in the quadrangular field that represents calcic-ferro-magnesian pyroxenes (Fig. C5_13B). Clinopyroxene has diopside and augite compositions (Wo_{37-49} En_{45-53} Fs_{6-12}) and orthopyroxene is enstatite (Wo_{2-3} En_{78-79} Fs_{18-20}). Clinopyroxene compositions indicate primary clinopyroxene (augite, 1000-800ºC; Fig. C5_13B) and metamorphic compositions (diopside, 500-600ºC, Fig. C5_13B). Orthopyroxene composition is magmatic in the same temperature range as magmatic clinopyroxene.

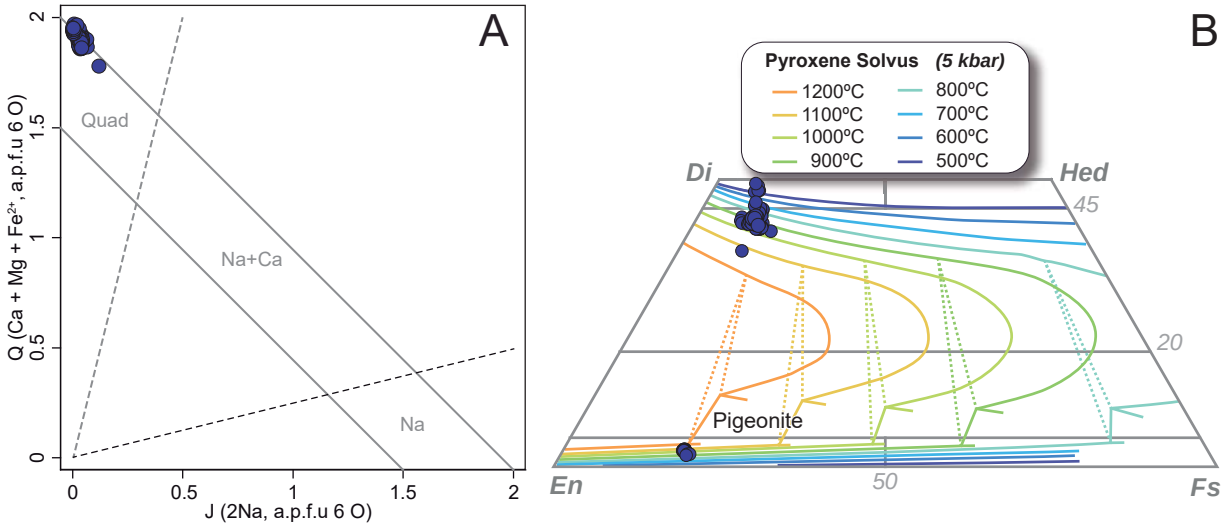

Figure. C5_13 *Pyroxene composition of the plutonic unit. A) Classification diagram of Morimoto et al. (1988). B) Quadrangular pyroxene classification diagram. En: Enstatite; Wo: Wollastonite; Fs: Ferrosilite. Isotherms of pyroxene solvus at 5 kbar from Lindsley (1983).*

Table C5_11. *Representative analyses of pyroxene from plutonic unit.*

Sample	08-VC-23	08-VC-24	09-LV-8B	09-LV-8A	09-LV-8A	09-LV-8B	09-LV-8B
Rock type	Cumulate gabbro			Cumulate Ol-gabbro			
Unit	Plutonic						
Mineral	Clinopyroxene					Orthopyroxene	
Classification	Augite			Diopside		Enstatite	
Major elements (wt%)							
SiO_2	52.41	52.87	53.14	54.90	54.83	55.29	55.47
TiO_2	0.56	0.33	0.35	0.19	0.11	0.23	0.22
Al_2O_3	2.36	2.15	2.28	1.08	0.66	1.36	1.40
Cr_2O_3	0.18	0.12	0.22	0.28	0.26	0.13	0.15
V_2O_3	0.03	0.04	0.07	0.05	0.03	0.04	0.05
FeOT*	5.58	6.75	5.88	4.05	4.38	12.34	12.20
MnO	0.19	0.15	0.21	0.15	0.12	0.28	0.30
MgO	16.99	17.65	17.07	16.46	16.43	30.10	29.84
CaO	21.70	21.04	20.88	23.94	24.24	1.51	1.47
Na_2O	0.26	0.19	0.21	0.18	0.22	0.03	b.d.l
Total	100.28	101.30	100.33	101.30	101.34	101.33	101.14
Formula based 6 oxygens							
Si	1.91	1.91	1.94	1.98	1.98	1.93	1.95
Al	0.10	0.09	0.10	0.05	0.03	0.06	0.06
Fe^{3+}	0.06	0.08	0.01	0.00	0.01	0.06	0.03
Ti	0.02	0.01	0.01	0.01	0.00	0.01	0.01
Cr	0.01	0.00	0.01	0.01	0.01	0.00	0.00
V	0.00	0.00	0.00	0.00	0.00	0.00	0.00
Mg	0.92	0.95	0.93	0.89	0.89	1.57	1.56
Mn	0.01	0.00	0.01	0.00	0.00	0.01	0.01
Fe^{2+}	0.11	0.12	0.17	0.12	0.12	0.30	0.32
Ca	0.85	0.81	0.82	0.93	0.94	0.06	0.06
Na	0.02	0.01	0.01	0.01	0.02	0.00	-
Wo %	43.53	41.27	42.28	47.76	47.89	2.84	2.79
En %	47.43	48.17	48.09	45.69	45.17	78.66	78.72
Fs %	9.04	10.57	9.63	6.55	6.94	18.50	18.50

*FeOT expressed as FeO; b.d.l: below detection limit

Olivine exhibit a forsterite (Fo) content of *c.* 0.82 with variable 0.08 to 0.17 wt% NiO (Table C5_12). The oxides present in the plutonic unit are magnetite (Figure C5_14; Table C5_13).

Table C5_12. *Representative analyses of olivine of the plutonic unit.*

Sample	08-SCB-34-D3-1	08-SCB-34-D3-1	08-SCB-34-D3-1	08-SCB-34-D3-1	08-SCB-34-D3-1
Rock type	Cumulate Ol-gabbro				
Unit	Plutonic				
Mineral	Olivine				
Major elements (wt%)					
SiO_2	38.77	38.71	39.64	39.51	39.45
TiO_2	0.09	0.02	b.d.l	b.d.l	0.01
Al_2O_3	b.d.l	0.03	b.d.l	0.01	0.01
Cr_2O_3	b.d.l	0.06	0.01	0.01	b.d.l
V_2O_3	b.d.l	b.d.l	b.d.l	0.02	b.d.l
FeO*	17.40	17.40	16.94	17.19	17.28
MnO	0.26	0.24	0.27	0.23	0.26
ZnO	0.04	b.d.l	b.d.l	0.01	b.d.l
MgO	42.23	42.30	43.12	43.44	44.25
NiO	0.08	0.14	0.15	0.15	0.16
CaO	0.12	0.11	b.d.l	b.d.l	b.d.l
Total	99.00	99.01	100.13	100.57	101.41
Formula based 4 oxygens					
Si	0.99	0.99	1.00	1.00	0.98
Ti	0.00	0.00	-	-	0.00
Al	-	0.00	-	0.00	-
Cr	-	-	-	0.00	-
V	-	-	-	0.00	-
Fe^{+3}	0.01	0.01	0.00	0.01	0.03
Fe^{+2}	0.36	0.36	0.36	0.36	0.33
Mn	0.01	0.01	0.01	0.00	0.01
Zn	0.00	-	-	0.00	-
Mg	1.62	1.62	1.63	1.63	1.65
Ni	0.00	0.00	0.00	0.00	0.00
Ca	0.00	0.00	-	-	-
Fo	0.82	0.82	0.82	0.82	0.83

*FeOT expressed as FeO, Fo=Mg/(Mg+Fe+2); b.d.l: below detection limit.

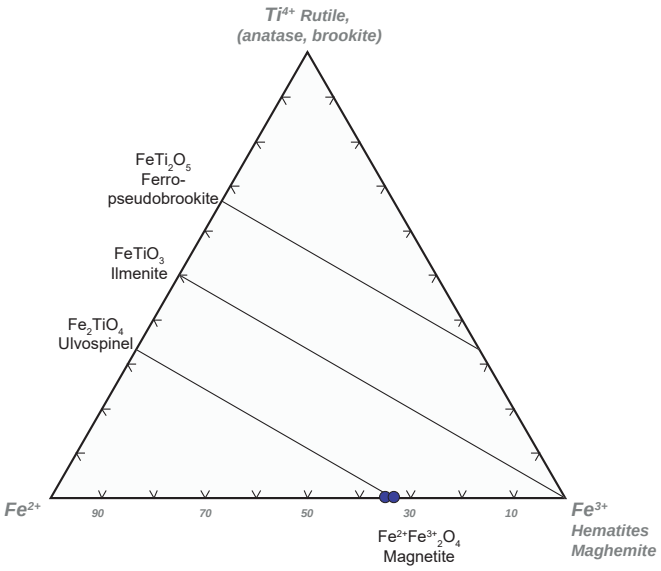

Figure. C5_14 *Fe-Ti oxide classification based on Ti^{4+}-Fe^{2+}-Fe^{3+} calculated by atoms per formula unit (a.p.f.u) of plutonic unit.*

Table C5_13. *Representative analyses of magnetite of the plutonic unit.*

Sample	08-SCB-34-D3-1		
Rock type	Cumulate Ol-gabbro		
Unit	Plutonic		
Mineral	Magnetite		
SiO_2	0.79	2.08	1.60
TiO_2	b.d.l	0.00	b.d.l
Al_2O_3	b.d.l	b.d.l	0.01
Cr_2O_3	b.d.l	0.01	0.02
V_2O_3	b.d.l	b.d.l	b.d.l
FeOT*	96.70	96.33	96.78
MnO	0.01	0.01	0.01
ZnO	0.02	0.01	0.04
MgO	1.80	1.56	2.27
NiO	0.02	0.01	0.03
Co	0.18	0.15	0.15
Total	99.52	100.16	100.91
Formula based 3 c	Formula based 4 oxygens		
Si	0.03	0.07	0.06
Ti	-	0.00	-
Al	0.00	-	0.00
Cr	0.00	0.00	0.00
Fe^{3+}	1.94	1.85	1.89
Fe^{2+}	0.93	0.99	0.93
V	-	-	-
Mn	0.00	0.00	0.00
Mg	0.10	0.08	0.12
Zn	0.00	0.00	0.00
Ni	0.00	0.00	0.00
Cr#	0.49	1.00	0.50
Mg#	0.09	0.08	0.11
Fe^{3+} #	1.00	1.00	1.00

*FeOT expressed as FeO; b.d.l: below detection limit

5.3.2.2. Minerals of the metamorphic assemblage

Amphibole displays large crystals whith easily discernible core and rim, and replacements after clinopyroxene in pseudomorphic textures that show no zoning. Colourless prismatic crystals of amphiboles are also present. Thus, three types of amphibole can be distinguished in terms of petrography. Amphibole 1, with green to colourless large crystals, is pargasite to magnesio-hornblende (Fig. C5_15; Table C5_14). Pale green to colourless amphibole 2 replacing clinopyroxene is magnesio-hornblende. Amphibole 3 appearing in the matrix as colourless prismatic crystals is magnesio-hornblende to tremolite (Fig. C5_15).

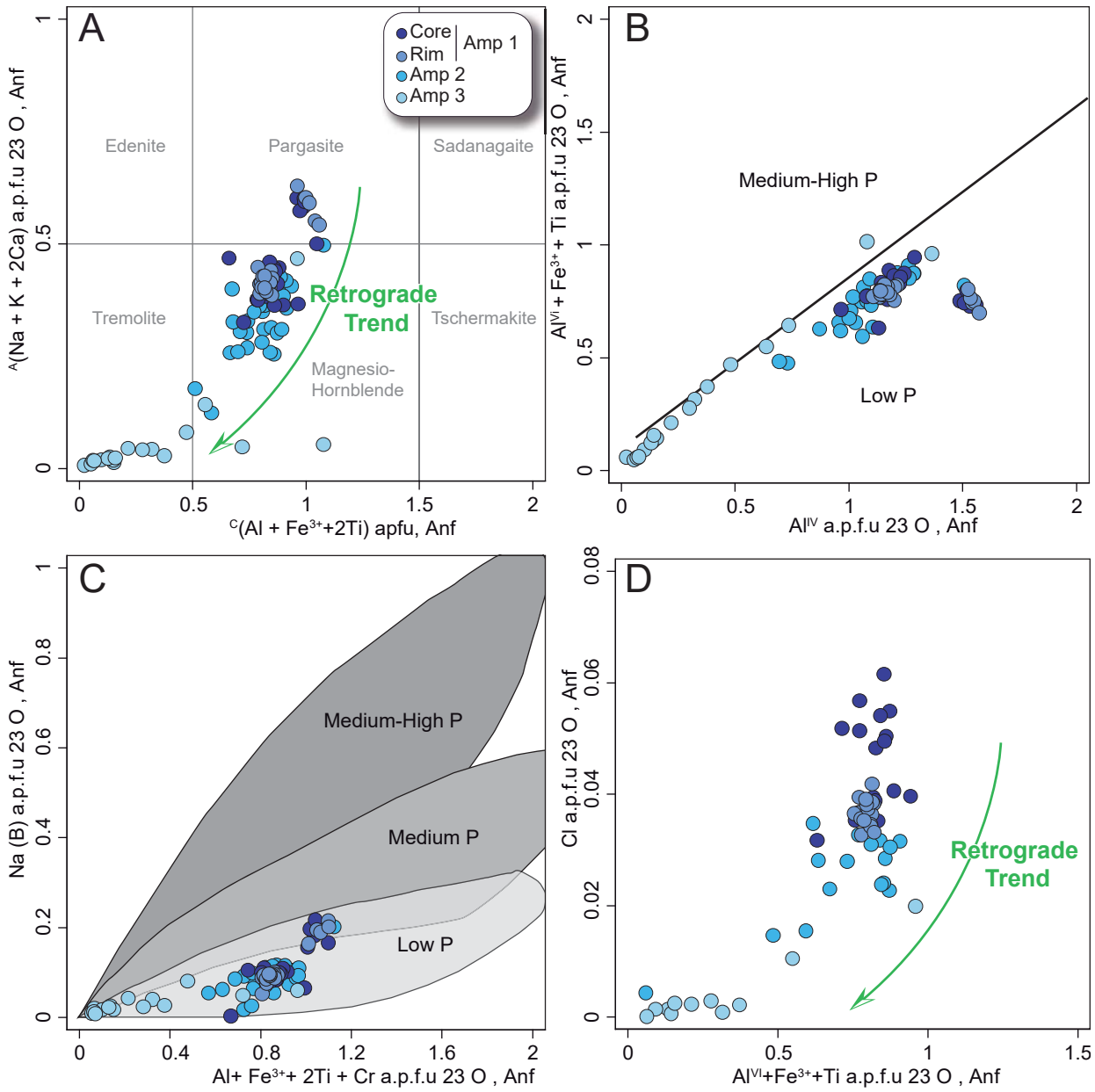

Figure. C5_15 *Amphibole composition of cumulate gabbro and ol-gabbro. A) Classification diagram of calcic amphiboles by Hawthorne et al. (2012). B) $Al^{VI}+Fe^{3+}+Ti$ a.p.f.u vs Al^{IV} a.p.f.u. C) Na^{B} a.p.f.u vs $Al^{VI}+Fe^{3+}+2{\cdot}Ti$ +Cr a.p.f.u. D) Cl a.p.f.u vs $Al^{VI}+Fe^{3+}+Ti$ a.p.f.u. Fields of medium-high, medium, and low pressure from Laird and Albee (1981) and Laird et al. (1984).*

Amphiboles in cumulate gabbro and ol-gabbro appear to have formed at low to medium pressure conditions. Ti in site C has low values in amphibole 1 (0.01-0.28 a.p.f.u), 2 (<0.25 a.p.f.u) and 3 (<0.07 a.p.f.u), indicating low temperature conditions (Spear, 1993). The high Al^{IV} content in amphibole 1 (0.97-1.56 to 1.11-1.58 a.p.f.u, core and rim, respectively; Table C5_14) to low Al^{IV} in amphibole 2 (0.07-1.51 a.p.f.u) and amphibole 3 (0.02-1.36 a.p.f.u) indicates a change in pressure conditions (Fig. C5_15B). Contents of Na in site B indicate medium-low pressure for amphibole 1 (0.05-0.22 a.p.f.u), while amphibole 2 (0.01-0.20) and 3 (<0.08) most likely formed at lower pressure (Figs. C5_15B and 15C; Laird and Albee, 1981; Laird et al., 1984). The temperature conditions can be estimated by $(Na+K)_A$ and Ti^C site (Spear, 1993). Amphibole 1 bears similar $(Na+K)_A$ core and rim (0.32-0.60 and 0.39-0.63,

respectively), whereas $(Na+K)_A$ in amphiboles 2 (0.02-0.49 a.p.f.u) and 3 (<0.46) indicates decreasing temperature conditions.

The correlation of Cl with $Al^{VI}+Fe^{3+}+Ti^{C}$ (a.p.f.u) may be attributed to changing pressure/temperature conditions during fluid infiltration (Fig. C5_15D; e.g., Vanko, 1986; Kendrick et al., 2015 and references therein). The Cl content in the core of amphibole 1 is higher than in the rim, which indicates a higher temperature amphibole in the former. Late amphiboles 2 and 3 display low chlorine content, confirming decreasing temperature conditions.

Table C5_14. *Representative analyses of amphibole of the plutonic unit.*

Sample	09-LV-8B	09-LV-8B	09-LV-8B	09-LV-8B	09-LV-8A	09-LV-8A	09-LV-8A
Rock type	Cumulate Ol-gabbro						
Unit	Plutonic						
Amphibole Type	Amp 1	Amp 1	Amp 1	Amp 1	Amp 2	Amp 3	Amp 3
Textural position	Core		Rim		Cpx replacement	Matrix	
Classification	Pg	Mg-Hbl	Pg	Mg-Hbl	Mg-Hbl	Tr	Mg-Hbl
Major elements (wt%)							
SiO_2	45.71	45.45	45.52	45.75	50.20	57.49	52.79
TiO_2	2.07	2.33	2.38	2.41	0.80	0.01	0.05
Al_2O_3	10.16	10.15	10.46	10.40	7.79	0.50	4.30
Cr_2O_3	0.39	0.45	0.38	0.42	0.31	0.02	0.00
V_2O_3	0.27	0.26	0.25	0.27	0.10	b.d.l	b.d.l
FeOT*	9.34	9.45	9.24	9.30	7.39	2.80	5.70
MnO	0.15	0.11	0.10	0.12	0.10	0.09	0.09
ZnO	0.03	0.05	0.01	0.00	0.05	b.d.l	b.d.l
MgO	16.35	16.31	16.28	16.28	18.50	22.98	20.96
NiO	0.05	0.07	0.04	0.03	0.03	0.07	0.02
CaO	11.23	11.33	11.20	11.21	12.44	13.03	12.25
Na_2O	2.58	2.18	2.49	2.31	1.42	0.09	0.73
K_2O	0.31	0.34	0.31	0.34	0.00	0.01	0.04
F	0.00	0.19	0.10	0.12	0.00	0.03	0.13
Cl	b.d.l	b.d.l	b.d.l	b.d.l	b.d.l	0.00	0.04
Total	98.64	98.67	98.76	98.96	99.12	97.10	97.09
Formula based 23 oxygens							
Si_T	6.51	6.48	6.47	6.49	6.97	7.92	7.36
Al_T	1.49	1.52	1.53	1.51	1.03	0.08	0.64
Al_C	0.21	0.18	0.23	0.23	0.25	0.00	0.07
Ti_C	0.22	0.25	0.25	0.26	0.08	0.00	0.01
Cr_C	0.04	0.05	0.04	0.05	0.03	0.00	0.00
$Fe^{3+}{}_C$	0.32	0.36	0.32	0.33	0.33	0.06	0.48
Mg_C	3.47	3.47	3.45	3.44	3.83	4.72	4.36
Ni_C	0.01	0.01	0.00	0.00	0.00	0.01	0.00
Zn_C	0.00	0.01	0.00	0.00	0.01	-	-
$Fe^{2+}{}_C$	0.72	0.67	0.70	0.69	0.47	0.21	0.09
$Fe^{2+}{}_B$	0.07	0.09	0.08	0.08	0.06	0.06	0.10
Mn_B	0.02	0.01	0.01	0.01	0.01	0.01	0.01
Ca_B	1.71	1.73	1.71	1.70	1.85	1.92	1.83
Na_B	0.20	0.17	0.20	0.20	0.08	0.01	0.06
Na_A	0.52	0.44	0.49	0.43	0.30	0.01	0.14
K_A	0.06	0.06	0.06	0.06	0.00	0.00	0.01
A-vacancy	0.43	0.50	0.46	0.50	0.70	0.98	0.86

*FeOT expressed as FeO; b.d.l: below detection limit

Chlorite displays high Mg (7.94 to 8.25 a.p.f.u) and low Fe (1.08 to 1.22 a.p.f.u.) with compositions of clinochlore-chamosite series (see Table C5_15).

Table C5_15. *Representative analyses of chlorite of the plutonic unit.*

Sample	09-LV-8A	09-LV-8A	09-LV-8A	09-LV-8A
Rock type	Cumulate gabbro			
Unit	Plutonic			
Mineral	Chlorite			
Major elements (wt%)				
SiO_2	34.48	29.46	29.92	29.85
TiO_2	b.d.l	b.d.l	0.01	b.d.l
Al_2O_3	16.25	22.12	21.08	21.40
Cr_2O_3	0.01	b.d.l	b.d.l	0.02
FeOT*	7.69	6.97	6.98	6.78
MnO	0.12	0.06	0.05	0.02
MgO	27.90	28.07	28.72	28.98
NiO	0.22	0.08	0.08	0.08
CaO	0.49	0.02	0.02	0.06
F	0.05	0.09	0.07	0.05
Total	87.22	86.85	86.92	87.25
Formula based 28 oxygens				
Si_T	6.59	5.66	5.74	5.70
Al_T	1.41	2.34	2.26	2.30
Al_M	2.24	2.66	2.51	2.52
Ti_M	-	-	0.00	-
Cr_M	0.00	-	-	0.00
Mg_M	7.94	8.03	8.22	8.25
$Fe^{2+}{}_M$	1.23	1.12	1.12	1.08
Mn_M	0.02	0.01	0.01	0.00
Ni_M	0.03	0.01	0.01	0.01
Ca_M	0.10	0.00	0.00	0.01
F	0.03	0.05	0.04	0.03
Mg#	0.87	0.88	0.88	0.88

*FeOT expressed as FeO; b.d.l: below detection limit; Mg#=(Fe/Fe+Mg)

Serpentine has low Al (<0.11 a.p.f.u) and Fe^{2+} (0.13-0.41 a.p.f.u; Table C5_16). Epidote replacing plagioclase has a composition of clinozoizite with low Fe# (<0.12; Table C5_17). Prehnite shows minor substitution of Fe^{3+}- Al (<0.01 of Fe#= [Fe^{3+}/(Fe^{3+}+Al^{3+})]; Table C5_18).

Table C5_16. *Representative analyses of serpentine of the plutonic unit.*

Sample	08-SCB-34-D3-1	08-SCB-34-D3-1	08-SCB-34-D3-1	08-SCB-34-D3-1
Rock type	Cumulate Ol-Gabbro			
Unit	Plutonic			
Mineral	Serpentine			
Major elements (wt%)				
SiO_2	43.14	42.98	41.40	43.44
TiO_2	0.01	b.d.l	0.01	0.00
Al_2O_3	0.02	0.28	0.97	0.04
Cr_2O_3	0.01	0.01	0.01	0.02
V_2O_3	b.d.l	b.d.l	b.d.l	b.d.l
FeO*	3.45	2.46	5.25	1.65
MnO	0.03	0.01	0.03	0.01
ZnO	b.d.l	b.d.l	b.d.l	b.d.l
MgO	39.46	40.53	39.97	40.96
NiO	0.01	0.02	0.02	0.04
CaO	0.03	0.02	0.03	0.01
Na_2O	0.01	0.01	0.02	0.01
K_2O	0.03	0.02	0.02	0.01
Cl	0.16	0.12	0.12	0.07
Total	86.37	86.46	87.83	86.28
Formula based 14 oxygens				
Si	4.08	4.04	3.90	4.07
Ti	0.00	0.00	0.00	0.00
Al	0.00	0.03	0.11	0.00
Cr	0.00	0.00	0.00	0.00
V	-	-	-	-
Fe^{+2}	0.27	0.19	0.41	0.13
Mn	0.00	0.00	0.00	0.00
Zn	-	-	-	-
Mg	5.56	5.68	5.61	5.72
Ni	0.00	0.00	0.00	0.00
Ca	0.00	0.00	0.00	0.00
Na	0.00	0.00	0.00	0.00
K	0.00	0.00	0.00	0.00
Cl	0.03	0.02	0.02	0.01
Mg#	0.95	0.97	0.93	0.98
Mg+Fe+Mn+Ni	5.83	5.87	6.03	5.85

*FeOT expressed as FeO, Mg#=Mg/(Mg+Fe2+); b.d.l: below detection limit.

Table C5_17. *Representative analyses of epidote of the plutonic unit.*

Sample	09-LV-8B	09-LV-8B	09-LV-8B
Rock type	Cumulate Ol-gabbro		
Unit	Plutonic		
Mineral	Epidote		
Major elements (wt%)			
SiO_2	39.63	40.83	40.25
TiO_2	0.05	0.01	b.d.l
Al_2O_3	29.71	33.06	32.27
Cr_2O_3	0.00	b.d.l	b.d.l
V_2O_3	b.d.l	0.03	0.03
FeOT*	4.75	0.32	1.80
MnO	0.04	0.03	0.05
ZnO	0.01	b.d.l	b.d.l
MgO	b.d.l	0.03	b.d.l
NiO	0.02	0.00	b.d.l
CaO	23.89	24.08	24.10
SrO	0.09	b.d.l	0.07
BaO	b.d.l	0.02	b.d.l
Na_2O	0.02	0.19	0.01
K_2O	b.d.l	b.d.l	b.d.l
Total	98.20	98.60	98.58
Formula based 12.5 oxygens			
Si_T	3.03	3.06	3.04
Al_T	-	-	-
Al_{M1}	1.00	1.00	1.00
Al_{M2}	1.00	1.00	1.00
Al_{M3}	0.68	0.92	0.87
Fe^{3+}_{M3}	0.30	0.02	0.11
Mn_{M3}	0.00	0.00	0.00
Fe^{2+}_{M3}	0.00	0.00	0.00
Cr_{M3}	0.00	0.00	0.00
V_{M3}	0.00	0.00	0.00
Zn_{M3}	0.00	0.00	0.00
Mg_{M3}	0.00	0.00	0.00
Ti_{M3}	0.00	0.00	0.00
Ca_{A1}	1.00	1.00	1.00
Ca_{A2}	0.96	0.94	0.95
Sr_{A2}	0.00	0.00	0.00
Ba_{A2}	0.00	0.00	0.00
Na_{A2}	0.00	0.03	0.00
K_{A2}	0.00	0.00	0.00

*FeOT expressed as FeO; b.d.l: below detection limit; n.a: not analyzed

Table C5_18. *Representative analyses of prehnite of the plutonic unit.*

Sample	09-LV-8A	09-LV-8A	09-LV-8A	09-LV-8A	09-LV-8A
Rock type	Cumulated Ol-gabbro				
Unit	Plutonic				
Mineral	Prehnite				
Major elements (wt%)					
SiO_2	44.56	44.27	44.45	44.44	44.29
TiO_2	b.d.l	0.03	0.05	0.01	0.03
Al_2O_3	24.17	24.27	23.97	23.93	24.46
FeOT*	0.09	0.09	0.11	0.18	0.09
MnO	0.01	b.d.l	0.01	0.02	b.d.l
MgO	b.d.l	b.d.l	b.d.l	b.d.l	0.03
CaO	26.80	26.66	26.47	26.83	26.88
Na_2O	0.04	0.01	0.10	0.04	0.04
K_2O	0.01	b.d.l	0.01	b.d.l	0.01
Total	95.68	95.33	95.17	95.45	95.82
Formula based 11 oxygens					
Si_T	3.05	3.04	3.06	3.05	3.03
Al_T	0.95	0.96	0.94	0.95	0.97
Al_M	1.00	1.00	1.00	0.99	1.00
$Fe^{3+}{}_M$	0.01	0.01	0.01	0.01	0.00
Mn_A	0.00	-	0.00	0.00	-
Mg_A	-	-	-	-	0.00
Ca_A	1.96	1.96	1.95	1.97	1.97
Na_A	0.01	0.00	0.01	0.01	0.00
K_A	0.00	-	0.00	-	0.00

*FeOT expressed as FeO; b.d.l: below detection limit

5.3.3. Whole-rock chemistry

Major, trace element data, and isotopic data of rocks of the plutonic unit are given in Table C5_19 and Table C5_20.

5.2.3.1. Major elements

Rocks of the plutonic unit display high Mg# (c. 80 %) and CaO wt% (*c.* >12 wt%, anhydrous basis) with low TiO_2 (*c.* <0.23 wt%). High Mg# and CaO contents indicate accumulation of ferromagnesian minerals (clinopyroxene, orthopyroxene and olivine) and plagioclase (high CaO, (Fig. C5_16). The presence of clinopyroxene, orthopyroxene and olivine indicates quartz-normative affinity.

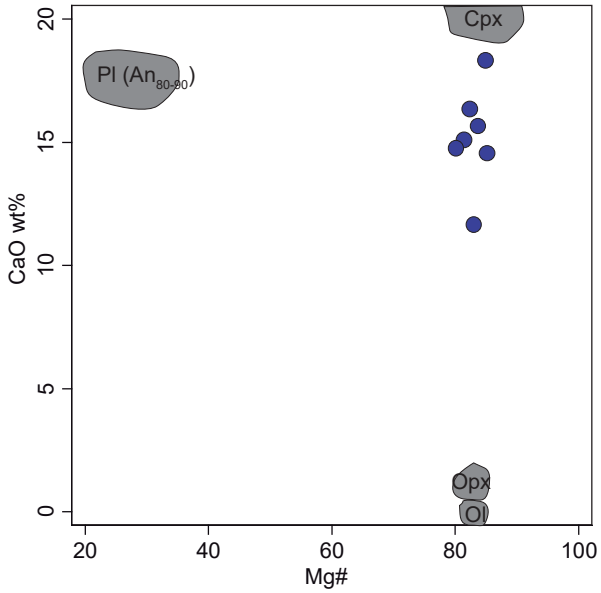

Figure. C5_16 *CaO vs Mg# diagram for whole-rock and mineral composition of the magmatic assemblage of the plutonic unit. The spread of whole-rock data of cumulate gabbros and ol-gabbros show a spreading in CaO composition which can be attributed to the fractionation effect of pyroxene, olivine and plagioclase. Mg# was calculated using molar proportions of MgO and FeOtotal, considering 90 % FeO and 10 % Fe_2O_3 (Gill, 2010).*

Table C5_19. *Whole-rock and trace element composition of samples of the plutonic unit of the mafic crust in the VCSM.*

Sample	08-VC-23	08-VC-25	14-SC-3	08-VC-24	09-LV-8A	09-LV-8B	08-SCB-34-D3-1
Latitude	22°19'44.20"N	22°19'44.20"N	22°27'9.60"N	22°19'44.20"N	22°19'44.20"N	22°19'44.20"N	22°19'44.20"N
Longitude	78°17'6.90"W	78°17'6.90"W	79°52'22.20"W	78°17'6.90"W	79°42'53.10"W	79°42'53.10"W	79°42'53.10"W
Unit	Plutonic						
Rock type	Cumulate Gabbro			Cumulate Ol-Gabbro			
Major elements (wt%)							
SiO_2	43.04	47.03	47.46	43.83	43.89	46.85	45.85
TiO_2	0.08	0.15	0.12	0.08	0.13	0.22	0.11
Al_2O_3	19.97	20.56	21.56	24.11	16.01	6.92	16.43
Fe_2O_3T	6.01	4.42	2.83	2.77	5.65	9.78	5.98
MnO	0.09	0.09	0.06	0.07	0.10	0.16	0.11
MgO	13.38	8.80	7.25	5.89	14.74	17.92	14.01
CaO	10.95	14.59	17.98	15.31	13.72	14.07	15.31
Na_2O	0.94	0.75	1.09	1.32	0.63	0.27	0.64
K_2O	0.08	0.67	b.d.l	0.46	b.d.l	b.d.l	b.d.l
P_2O_5	0.01	0.01	0.01	0.01	0.01	0.02	0.01
LOI	5.45	2.41	1.54	5.35	4.69	3.42	1.44
Total	100.00	99.48	99.90	99.20	99.57	99.63	99.89
Trace elements (ppm)							
Li	1.669	12.352	0.383	11.906	6.205	3.552	0.929
Rb	2.224	16.800	0.324	10.671	0.320	0.791	0.277
Cs	0.791	2.415	0.044	1.930	0.091	0.084	0.063
Be	b.d.l	0.111	0.039	b.d.l	0.039	0.039	0.032
Sr	237.936	198.067	135.964	572.508	153.449	45.037	102.482
Ba	20.330	54.921	9.102	75.281	13.918	9.046	5.726
Sc	5.431	23.040	41.676	9.001	33.782	62.613	37.635
V	46.822	123.255	117.963	54.880	90.438	181.809	103.637
Cr	149.517	145.941	461.915	119.587	847.186	1556.888	787.055
Co	64.934	49.881	68.067	23.812	52.440	92.645	56.703
Ni	210.678	87.292	86.276	61.097	310.828	318.168	278.937
Cu	8.987	92.922	29.549	21.757	122.234	124.267	68.335
Zn	0.000	11.789	19.091	0.000	29.411	51.471	33.343
Ga	9.466	12.219	10.938	11.332	7.889	6.191	9.007

Total Fe as Fe_2O_3T; b.d.l: below detection limit

Table C5_19. *Continued.*

Sample	08-VC-23	08-VC-24	08-VC-25B	09-LV-8A	09-LV-8B	08-SCB-34-D3-1	14-SC-3
Trace elements (ppm)							
Y	1.892	1.968	4.628	3.659	6.957	3.779	3.872
Nb	0.108	0.054	0.196	0.101	0.386	0.076	0.137
Zr	5.5	2.6	7.7	2.072	3	1.943	1.6
Mo	3.263	1.372	3.265	2.227	3.049	1.812	4.919
Sn	0.295	0.193	0.226	0.333	0.406	0.312	0.326
Tl	b.d.l	0.016	0.018	0.008	0.02	0.002	0.001
Pb	b.d.l	b.d.l	b.d.l	0.233	0.43	0.23	0.387
U	0.005	0.005	0.003	0.01	0.024	0.013	0.021
Th	0.024	0.012	0.03	0.008	0.175	0.01	0.008
La	0.262	0.223	0.211	0.155	0.289	0.152	0.166
Ce	0.482	0.379	0.641	0.507	0.886	0.43	0.477
Pr	0.112	0.099	0.128	0.096	0.178	0.09	0.096
Nd	0.579	0.499	0.833	0.644	1.115	0.561	0.591
Sm	0.236	0.223	0.388	0.317	0.536	0.276	0.280
Eu	0.189	0.198	0.233	0.233	0.261	0.21	0.223
Gd	0.343	0.362	0.597	0.487	0.887	0.486	0.496
Tb	0.05	0.056	0.112	0.086	0.163	0.089	0.091
Dy	0.362	0.388	0.788	0.581	1.111	0.607	0.609
Ho	0.087	0.083	0.167	0.134	0.253	0.14	0.143
Er	0.226	0.217	0.472	0.36	0.698	0.369	0.393
Tm	0.032	0.034	0.068	0.056	0.109	0.059	0.062
Yb	0.211	0.218	0.379	0.329	0.656	0.341	0.363
Lu	0.032	0.03	0.053	0.05	0.098	0.053	0.056
Hf	0.089	0.08	0.182	0.01	0.05	0.01	0.01

5.2.3.2. Trace elements

Trace element compositions of the plutonic unit samples display depletion in LREE ($La/Sm_{N\ CI95}$=0.31-0.69), with nearly flat MREE to HREE ($Sm/Lu_{N\ CI95}$ =0.83-1.24) in the chondrite-normalized REE pattern (Fig. C5_17A). The marked positive Eu anomaly (Eu/Eu^{*}=1.15 to 2.12) is characteristic of cumulate gabbros and ol-gabbros. The N-MORB normalized patterns are depleted relative to N-MORB (Fig. C5_17B), with marked negative anomalies in Nb ($Nb/La_{N\ N\text{-}MORB89}$=0.26 to 0.89, with the exception of two samples (08-VC-25B and 09-LV-8B) and Zr ($Zr/Nd_{N\ N\text{-}MORB89}$=0.26 to 0.94). Th is enriched in comparison to other trace elements.

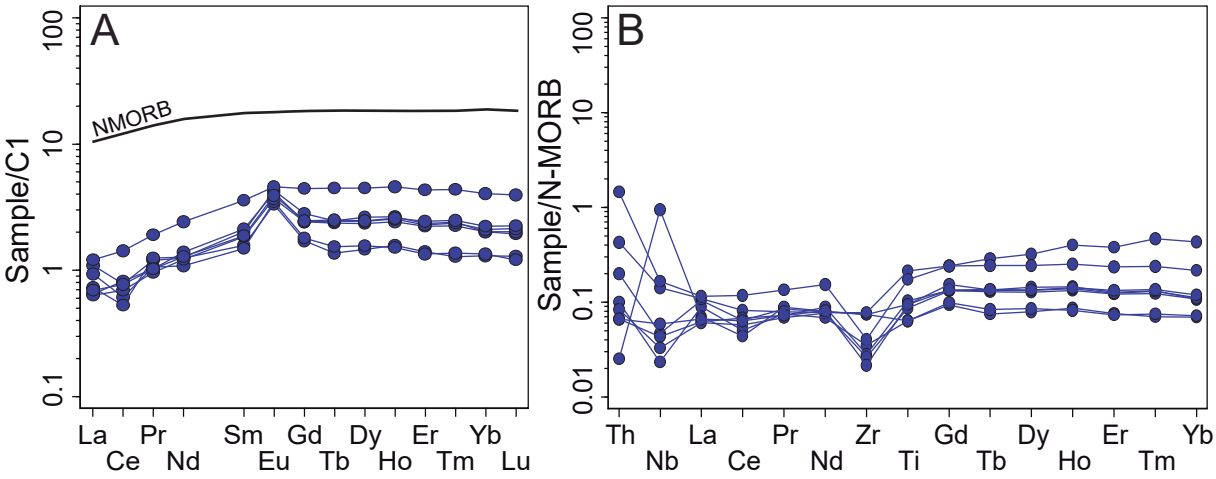

Figure. C5_17 *Normalized trace element composition of the plutonic unit. A) Chondrite-normalized whole-rock REE. B) N-MORB-normalized whole-rock trace element composition. Chondrite- and N-MORB-normalization values are from McDonough and Sun (1995) for CI chondrite and Sun and McDonough (1989) for N-MORB.*

5.2.3.4. Nd-Sr isotope systematics

The Sr and Nd isotopic compositions of the plutonic unit are measured $^{87}Sr/^{86}Sr$ ratio range 0.70303-0.70346 and $^{143}Nd/^{144}Nd$ ratio range of 0.51277-0.51300 (see Table C5_20).

Table C5_20. *Isotopic composition of samples of the plutonic unit of the mafic crust from the VCSM.*

Sample	08-VC-25	09-LV-8B	08-SCB-34-D3-1	14-SC-3
Unit	Plutonic			
Sr (ppm)	223.340	45.020	102.439	135.910
Nd (ppm)	0.553	1.115	0.561	0.591
$^{87}Sr/^{86}Sr$	0.70346	0.70337	0.70303	0.70330
$^{87}Sr/^{86}Sr$ error	0.0040	0.0020	0.0030	0.0010
$^{147}Sm/^{144}Nd$	0.2927	0.2904	0.2975	0.2863
$^{143}Nd/^{144}Nd$	0.51277	0.51300	0.51293	0.51290
$^{143}Nd/^{144}Nd$ error	0.0050	0.0040	0.0060	0.0040
$^{87}Sr/^{86}Sr_t$	0.70334	0.70328	0.70301	0.70328
$^{143}Nd/^{144}Nd_t$	0.51253	0.51276	0.51268	0.51266

T= 125Ma; Eclogitic metamorphic peak event in Santa Clara serpentinitic mélange that indicates pre-Aptian subduction (125Ma, García-Casco et al., 2002)

5.4. Discussion of mafic crust of the VCSM

The mafic crust of the Villa Clara serpentinitic mélange comprises sub-volcanic and plutonic units. This discussion is divided in two parts: sub-volcanic unit and plutonic unit.

5.4.1. Sub-volcanic unit of the VCSM

5.4.1.1. Element behaviour and metamorphism of the sub-volcanic unit

The diabase and microgabbro underwent low pressure metamorphism that has partly to completely transformed the primary mineral assemblages. The effect of metamorphism is evidenced by petrography (presence of amphibole, epidote and prehnite) and mineral and whole-rock chemistry. The LOI values (1.66 to 4.04 wt%), major elements (such as Si, K and Na) and LILE attest to protolith alteration (e.g., Kelley et al., 2003; Ribeiro et al., 2013; Hirahara et al., 2015).

The alkali elements were used as tracers of alteration (Fig. C5_18A, Miyashiro, 1975). In figure C5_18A, group 1 rocks fit with weakly to strongly altered, whereas group 2 appear to be weakly altered. Large ion lithophile elements (LILE, Rb, Sr, Ba) were plotted against an immobile element (Yb) in order to track element mobility (Fig. C5_18B to C5_18D). Enriched compositions in groups 1 and 2 indicate post magmatic processes that mobilize such elements (e.g. seawater alteration, Pearce, 1982; Delacour et al., 2008; Ribeiro et al., 2013; Hirahara et al., 2015). Therefore, the mobile character of alkali elements and LILE cannot be used to track magmatic processes that would allow one to characterize the protolith and its provenance.

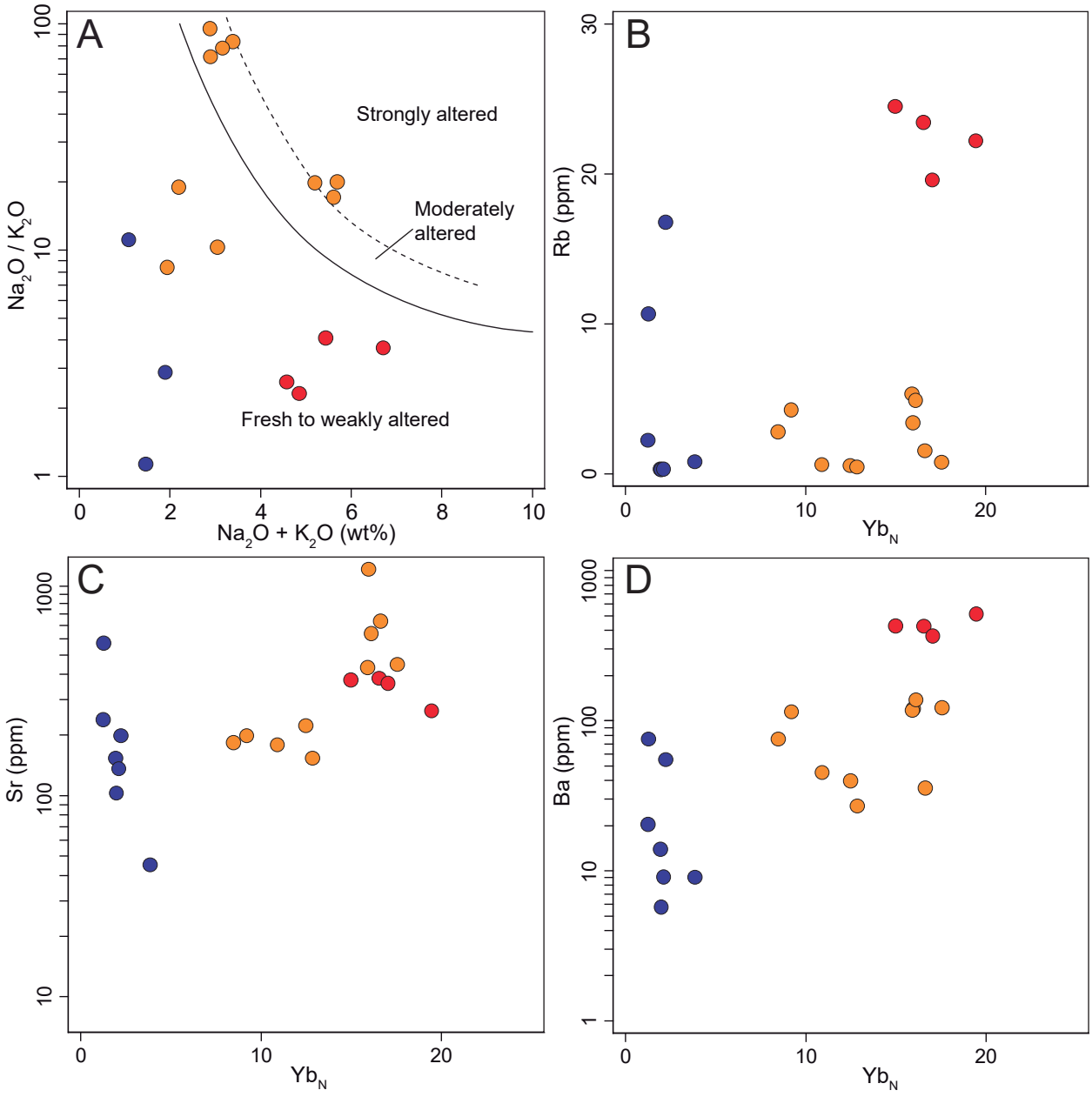

Figure. C5_18 *Major and trace element diagrams for the mafic crust of the VCSM. A) Na_2O/K_2O vs $Na_2O+ K_2O$ (wt%) anhydrous. Lines and fields from Miyashiro (1975). B) Rb vs Yb_N. C) Sr vs Yb_N. D) Ba vs Yb_N. Yb normalized to chondrite after McDonough and Sun (1995).*

The study of isotopic systems (Nd and Sr) sheds light on which isotopic reservoirs are associated with element enrichment during metamorphism. We recalculated isotopic ratios of samples and endmember reservoirs to the timing of subduction initiation of the Proto-Caribbean plate at *c.* 125 Ma (Garcia-Casco et al., 2002). The sub-volcanic unit displays similar Nd and Sr compositions, showing $^{143}Nd/^{144}Nd$ depletion and high values of $^{87}Sr/^{86}Sr$, with a trend that fits the mixing line of depleted mantle - Cretaceous seawater (with low W/R ratio= <1-10), according to oceanic crust alteration (e.g. Hart et al., 1999; Kelley et al., 2003; Boschi et al., 2008; Delacour et al., 2008; Vils et al., 2008 and 2009; Fig. C5_19).

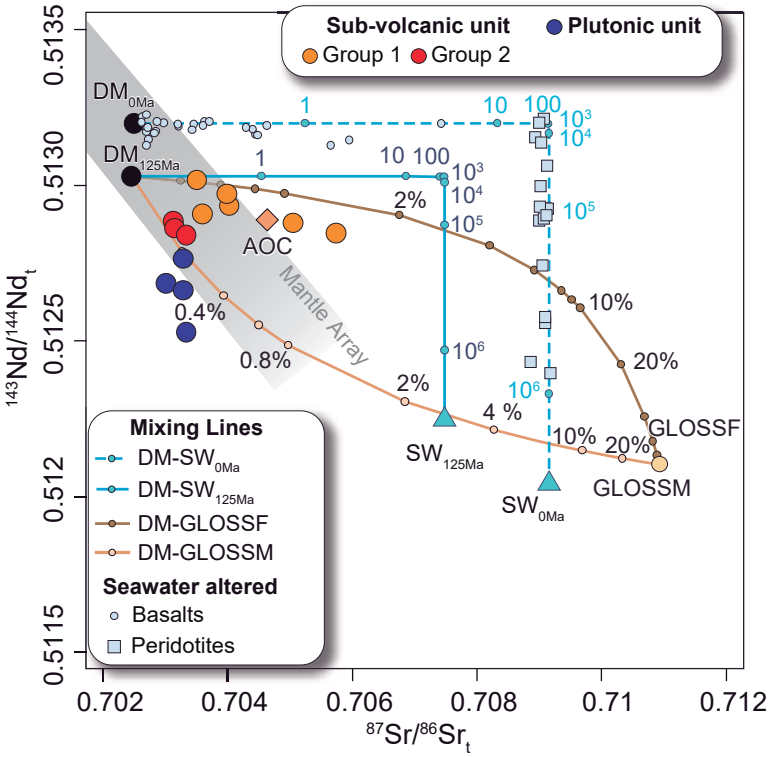

Figure. C5_19 *$^{143}Nd/^{144}Nd_t$ vs $^{87}Sr/^{86}Sr_t$ isotope systematics of the mafic crust of the VCSM. Mantle array of samples compiled from Stracke et al. (2003a) and (2003b), depleted mantle (DM from Rehkämper and Hofmann, 1997), and global subducting sediment fluid/melt (GLOSSF and GLOSSM: Plank, 2014; Johnson and Plank, 1999). Seawater-DM mixing lines were calculated following the equations of McCulloch et al. (1981). DM-GLOSSF and DM-GLOSSM were calculated using the equation of isotopic mixture from Faure and Mensing (2005). All mixing lines, endmembers and samples were age-corrected at c. 125 Ma (Garcia-Casco et al., 2002), with the exception of actual seawater and altered abyssal samples (Boschi et al., 2008; Delacour et al., 2008; Vils et al., 2008 and 2009). More information on endmembers and mixing lines in chapter 3.10.*

The metamorphic mineral assemblages (diopside + plagioclase + amphibole: pargasite to tremolite + epidote + prehnite) indicate low pressure/low-medium temperature metamorphism. The low pressure metamorphism is evidenced by low Ti^C, Na^B and high Al^{IV} (Fig. C5_7). The relatively constant values of Na^B in core and rim indicate rim growth at constant pressure. The high values of $(Na+K)_A$ in amphibole cores, which decrease progressively to the rims (Fig. C5_7A), indicate retrograde zoning that took place during cooling. The high chlorine content in high temperature amphiboles is comparable to amphiboles found in present-day oceanic environments, offering additional evidence of ocean floor metamorphism (Fig. C5_7D; e.g., Laird and Albee, 1981; Laird et al., 1984; Vanko, 1986; Kendrick et al., 2015 and references therein).

5.4.1.2. Petrogenesis of sub-volcanic unit of the VCSM

Hereinafter, immobile elements are used to characterize magmatic processes of the sub-volcanic unit. We use high field strength elements (HFSE, Hf, Zr, Ti, Nb), rare earth elements (REE) and some transitional elements (i.e., V) that are considered immobile (e.g., Pearce and Cann, 1971; Shervais, 1982; Pearce et al., 2014; Saccani et al., 2015 and references therein). The HFSE/HREE ratios (e.g., Th/Yb,

Nb/Yb) were used to track magma provenance and subduction-derived fluid interactions (e.g., Pearce, 2008 and 2014). Different element behaviours point to the processes behind enrichment/depletion. As Zr concentrations are useful to track magma differentiation (Duggen et al., 2008) in metamorphosed rocks, Zr and TiO_2 contents are plotted in Figure C5_20. Group 1 rocks are depleted in HFSE (Zr=31 to 82 ppm), whereas group 2 is seen to have higher concentrations (Zr= 107 to 111 ppm; Fig. C5_20). Such enrichment in Zr in group 2 rocks indicates that these rocks are differentiated magmas.

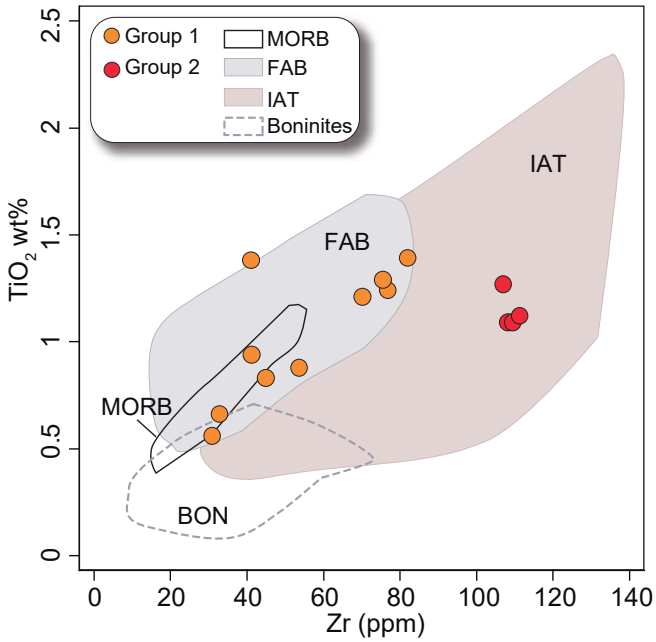

Figure. C5_20 *TiO_2 wt% anhydrous vs Zr (ppm) of sub-volcanic rocks of the VCSM. Fields of forearc basalt (FAB) are from Reagan et al. (2010) and Ishizuka et al. (2011); Island arc tholeiites (IAT) from Kerr et al. (1999), Jolly et al. (2002), Díaz de Villalvila et al. (2003), Escuder et al. (2006, 2007, 2011, 2014), Marchesi et al. (2007), Lidiak et al. (2011) and Cintron Franqui et al. (2017). Boninites from Pearce et al. (1992), Bonev and Stampli (2008) and Reagan et al. (2010).*

Group 1 of the sub-volcanic unit shows REE and N-MORB normalized patterns similar to tholeiitic mid-ocean ridge basalts (MORB), while group 2 shows more enriched compositions (Fig. C5_10). However, all types of sub-volcanic rocks display positive Th and negative Nb anomalies in comparison to N-MORB compositions (Fig. C5_10B and C5_10D), and both display high Th/Nb ratios and low to medium Ti/V ratios (low Ti/V ratios for group 1 and medium Ti/V ratio group 2; Fig. C5_21). Furthermore, their compositions do not fall in the MORB-OIB mantle array, and they appear to have a subduction-related imprint (Fig. C5_21A). The compositions of group 1 rocks, plotted in figures C5_10, C5_20 and C5_21, resemble those of forearc basalts (FAB) from Izu Bonin (Reagan et al., 2010 and Ishizuka et al., 2011); group 2 displays compositions of island arc tholeiites (IAT) that crop out along the Caribbean realm (Kerr et al.,1999; Jolly et al., 2002; Díaz de Villalvila et al., 2003; Escuder et al., 2006, 2007, 2011, 2014; Proenza et al., 2006; Marchesi et al.,2007; Lidiak et al., 2011; Cintron Franqui et al., 2017; Torró et al., 2017). Both groups of the sub-volcanic unit are related to a suprasubduction zone setting, where group 1, with FAB affinity, may be the first melts produced once subduction started, as suggested by Reagan

et al. (2010). Group 2, having IAT affinity, is expected to have formed after group 1, since it represents more differentiated melts.

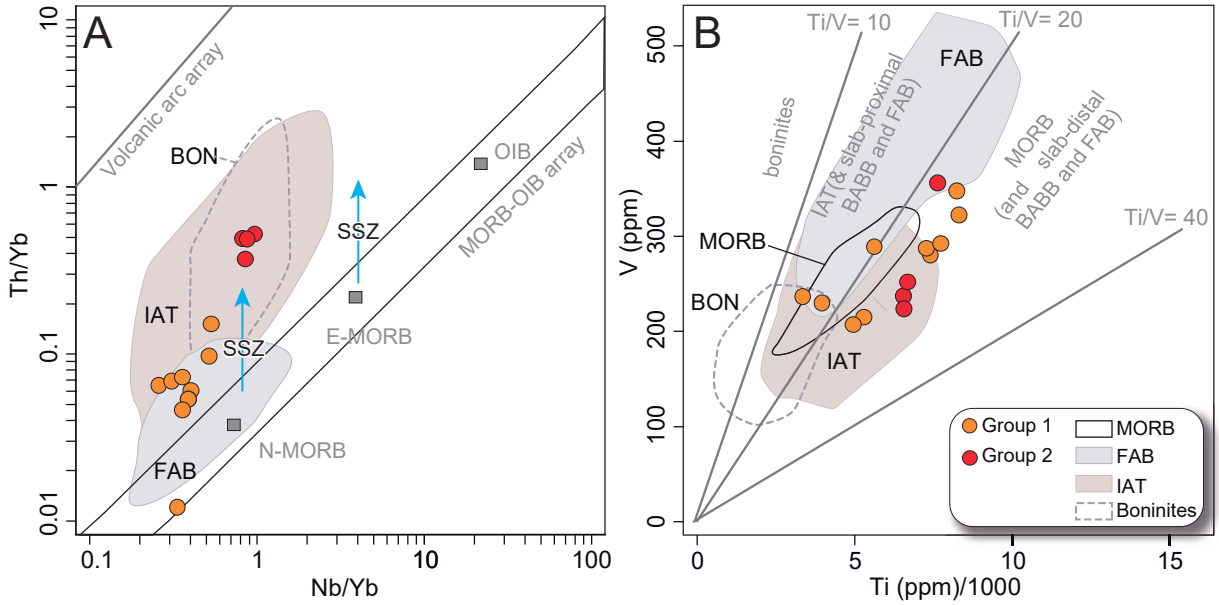

Figure. C5_21 *A) Th/Yb vs Nb/Yb and B) V vs Ti (ppm)/1000 from Pearce (2008) and Shervais (1982). Fields of forearc basalt (FAB) are from Reagan et al. (2010) and Ishizuka et al. (2011) and Island arc tholeiites (IAT) from Kerr et al. (1999), Jolly et al. (2002), Díaz de Villalvila et al. (2003), Escuder et al. (2006, 2007, 2011, 2014), Marchesi et al. (2007), Lidiak et al. (2011) and Cintron Franqui et al. (2017). Boninites are from Pearce et al. (1992), Bonev and Stampli (2008) and Reagan et al. (2010). N-MORB, E-MORB and OIB from Sun and McDonough (1989) are plotted for reference. Suprasubduction zone enrichment is indicated as SSZ in the diagrams.*

Positive Th and negative Nb anomalies, as well as low to medium Ti/V ratios, attest to a mantle source that has an additional subduction-related component (e.g., Kelemen et al., 2003; Reagan et al., 2010; Stern et al., 2012). The most incompatible elements (LILE; Fig.C5_18) appear enriched in both groups 1 and 2. It is generally accepted (e.g. Schmidt and Jagoutz, 2017 and references therein) that LILE derive from the slab, which is in line with HFSE and REE.

Here, we use Nd and Sr isotopes to identify possible mantle reservoirs, due to the fact that radiogenic isotopes do not fraction during magmatic differentiation. Sub-volcanic rocks show comparable isotopic composition, indicating the same mantle source. The mantle source may have experienced a small slab input (<2%; Fig.C5_19, DM-GLOSSF and DM-GLOSSM mixing lines; global subducting sediment fluid/melt, GLOSSF and GLOSSM, respectively), which decreased the $^{143}Nd/^{144}Nd$ ratio to less radiogenic Nd. Unfortunately, the $^{87}Sr/^{86}Sr$ ratio was modified by seawater infiltration; the more radiogenic Sr fits with seawater mixing line (Fig.C5_19).

To sum up, group 1 sub-volcanic unit rocks display compositions of forearc basalts, and group 2 of island arc tholeiite affinity, with more differentiated compositions. The presence of a small subduction-related signature may be explained by slab fluids/melts (GLOSSF/GLOSSM). All these evidences point to a subduction zone geodynamic setting.

5.4.1.3. Melting modelling of sub volcanic unit of the VCSM and their link with peridotites of VCSM

The scientific community agrees that basalts, diabases and microgabbros in abyssal/suprasubduction zone setting have most likely have undergone some degree of fractional crystallization during their ascent (e.g., Sobolev and Chaussidon, 1996; Allan et al., 1999; Reagan et al., 2017; Schmidt and Jagoutz, 2017). Therefore, in order to avoid effects of magmatic differentiation, we consider only primitive melt compositions using Mg# (definition: magma that has undergone minimal magmatic differentiation; e.g. Sobolev and Chaussidon, 1996; Gill, 2010 and references therein). Primitive melts display Mg# > 65% (e.g. Gill, 2010 and references therein), only three samples of group 1 meeting this requirement. In addition, it is important to take into account processes such as fractional crystallization of plagioclase, which could yield positive or negative Eu anomalies. We only use samples that show slight deviations from Eu/Eu^{*}= 1. Two samples of group 1 (samples 08-VC-1 and 08-VC-9) were selected as potentially representative of primary melt.

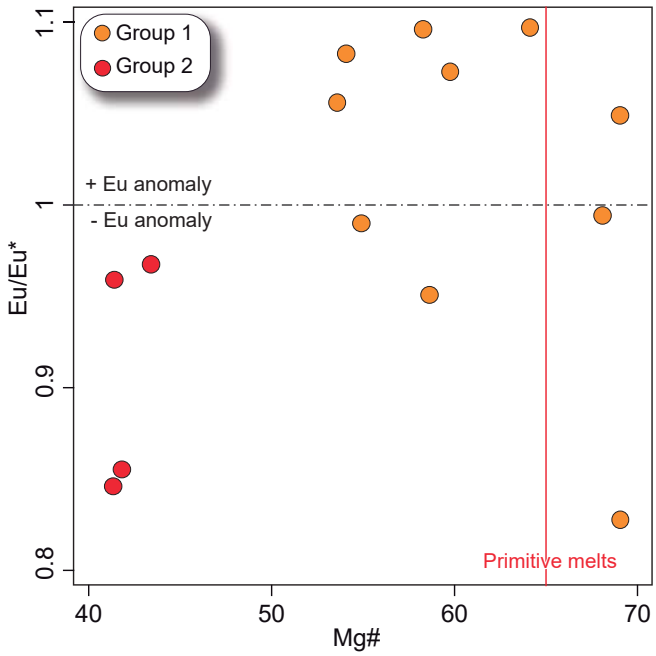

Figure. C5_22 *Eu/Eu* vs Mg# values of samples from the sub-volcanic in rocks of the VCSM. See text for explanations.*

The primary melts of the sub-volcanic unit were modelled using hydrous fractional non-modal melting of depleted mantle (see chapter 3.9 and table C3_2 for procedure). Here, we use the same parameters (partition coefficients, mineral source modes, mineral melt modes, degree of melting and source rock composition) and the non-modal fractional melting equation of Shaw (2000) applied in modelling peridotite melting in the VCSM (chapter 4.5.3).

The melting modelling considers two possibilities: Case X) First batch of melt from a depleted mantle at the garnet-peridotite facies, and case Y) first batch of melt from a depleted mantle at the spinel-peridotite facies. Both cases consider diverse options in terms of one step melting (Figs. C5_23A.1 and

C5_23B.1), two step melting (Figs. C5_23A.2 and C5_23B.2) and Case X that have three step melting (case X only; Fig. C5_23A.3).

The one step melting curves of case X modelling (Fig. C5_23A.1) do not fit with sub-volcanic group 1 rock compositions, as there is a change of slope from low to high melting degrees (high LREE to low HREE at small melting degrees vs. low LREE to high HREE). This effect is produced by garnet, which retains HREE. The two step melting with a first 4% melting at garnet-peridotite facies and a second step in the spinel-peridotite facies could not account for the sub-volcanic rock compositions, owing to the higher HREE compositions of the melting curves (Fig. C5_23A.2). The three step melting (4% melting of DM grt-peridotite, followed by 6% melting of DM spl-peridotite and melting of DM in the spl-peridotite facies) likewise cannot explain sub-volcanic rock composition (Fig. C5_23A.3), in this case because of the low MREE and HREE composition of the melting curves.

Meanwhile, case Y (at spinel-peridotite facies, Fig. C5_23B), entailing one and two steps, reproduces the compositions of the sub-volcanic rocks. For one step melting the sub-volcanic unit may have been produced after c. 6-8% melting of DM (Fig. C5_23B.1), whereas *c.* 8-10 % applies to two-step melting (Fig. C5_23B.2). Two step melting considers a depleted mantle source that underwent a first step of melting (*c.* 4% DM) and a second step of melting of *c.* 4% to 6%. Both options are feasible. Yet considering that group 1 of the sub-volcanic unit is constituted by forearc basalts, they should have formed after melting of an already depleted mantle source that re-melts in a second step. The two step modelling in the spinel peridotite field is consistent with the geochemistry of the sub-volcanic unit and subduction initiation geodynamic setting envisaged for the Caribbean realm at 125 Ma.

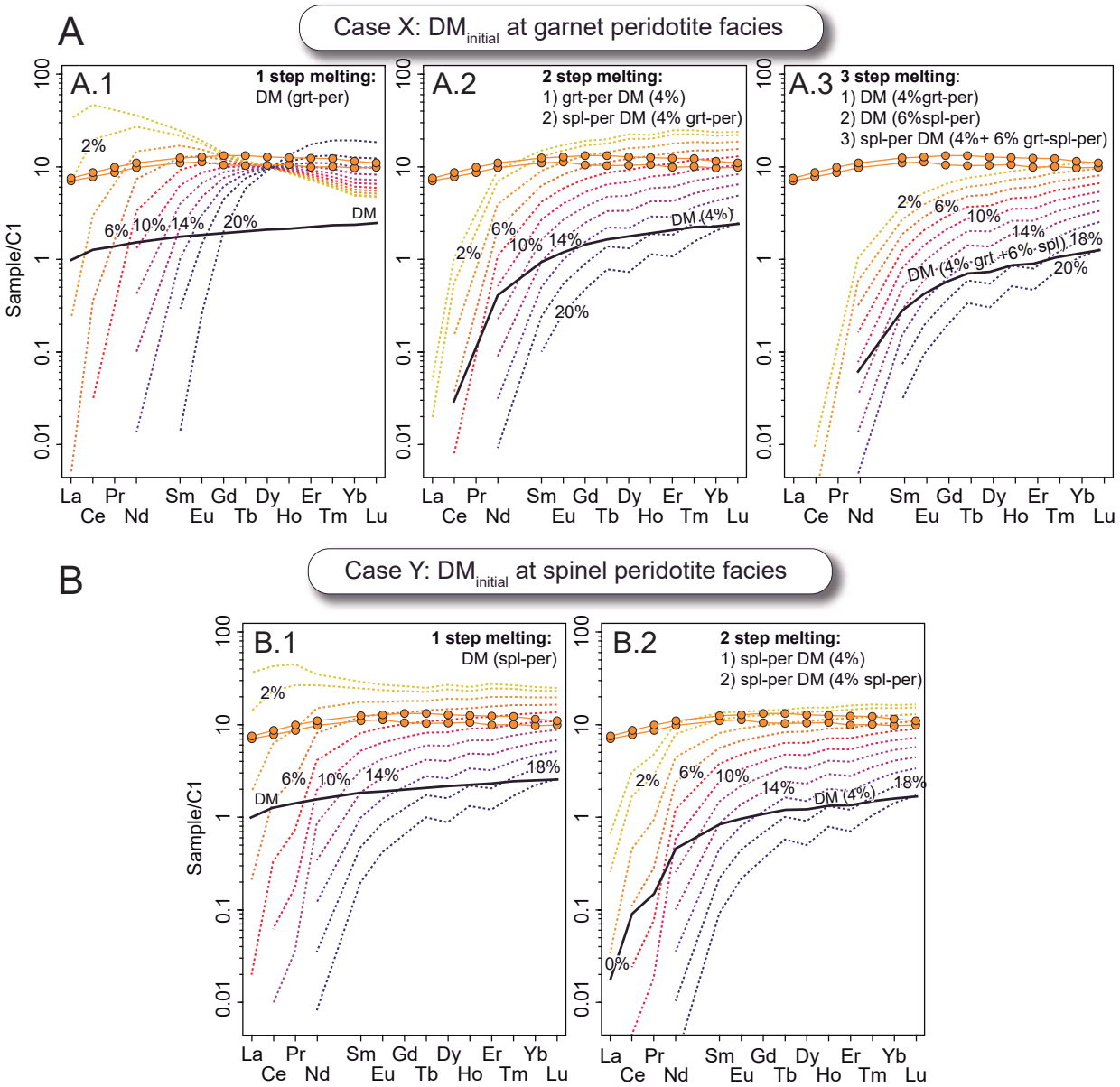

Figure. C5_23 *Non-modal fractional melting modelling of group 1 (FAB-like) of the sub-volcanic unit. Chondrite-normalized REE patterns. A) Initial melting at the garnet facies (case X). B) Initial melting at the spinel facies (case Y). A.1) One step melting at garnet-peridotite facies, A.2) Two step melting, first 4% DM at garnet-peridotite (grt-per) facies and second at the spinel-peridotite facies, A.3) Three step melting, first at 4% DM (grt-per), second at 6% DM (spl-per) and third step melting at spinel-peridotite facies. B.1) One step melting at spinel-peridotite facies (spl-per), B.2) Two step melting, first at 4% DM (spl-per) facies and second at spinel-peridotite facies. Dashed lines are calculated melt composition. Source of melting is depleted mantle (DM) composition, from Salters and Stracke (2004). Melting modelling calculated using equation of Shaw (2000). Source and melting modes and partition coefficients are indicated in chapter 3.9 and Table C3_2. Percentages indicate degree of melting.*

5.4.1.4. Correlations of sub-volcanic unit of the VCSM with other crustal sections of the Caribbean.

In the previous chapters we characterize the sub-volcanic unit in terms of its composition, origin, associated processes of enrichment and geodynamic setting of formation. In this chapter we aim to place the sub-volcanic unit of VCSM in the geodynamic setting of the Caribbean realm. The sub-volcanic unit is part of the Early Cretaceous Caribbean Island arc, which can be tracked along Cuba, Dominican Republic, Puerto Rico and Virgin Islands. Here, we understand the Early Cretaceous Caribbean Island Arc as the volcanic and sub-volcanic rocks that have been classified as part of an ophiolite section formed during the first stages of subduction and onset of arc formation. Some ophiolite classification schemes distinguish subduction-related and subduction-unrelated ophiolites (e.g. Dilek and Furnes, 2011; 2014; Furnes and Dilek, 2017 and references therein). This classification is based on complexes of ultramafic to felsic rocks that are temporally and spatially associated, and that may have undergone melting and magmatic differentiation in an oceanic context (Dilek and Furnes, 2011). This means that the creation of oceanic crust in a supra-subduction setting is nowadays considered as typical of ophiolites. In the Caribbean realm, many sections of supra subduction zone ophiolites occur.

The generation of oceanic crust in the Caribbean realm was continuous from Early Cretaceous to Tertiary (e.g. Lidiak et al., 2015 and references therein). The tectonics of the Caribbean realm started with the breakup of Pangea and creation of the Inter-American transform, which allowed for the drift of North America and favoured opening of the Proto-Caribbean oceanic basin at Jurassic times (of Atlantic lithosphere origin, e.g. Pindell et al., 2012; Rojas-Agramonte et al., 2016). At this stage, creation of the Proto-Caribbean oceanic crust resulted in geochemical compositions of typical mid-ocean ridge basalts (e.g. Stracke et al., 2003a; 2003b and references therein). Remnants of such lithosphere can be found in amphibolites and basalts of Sierra Bermeja and Water Island formations, respectively in Puerto Rico and Virgin Islands (Jolly et al., 2002, 2007; Jolly and Lidiak et al., 2006; Lidiak et al., 2011; Cintron Franqui et al., 2017; Fig. C5_24). The Early Cretaceous convergence of the Proto-Caribbean and Caribbean plates entailed westward subduction of the Proto-Caribbean basin below the Pacific plate (Boschman et al., 2014 and references therein). Subduction inception can be tracked along the Caribbean realm by the presence of forearc basalts (FAB). Evidence of subduction initiation is presented here by the group 1 sub-volcanic unit of VCSM in Central Cuba, which displays FAB signatures. Other studies in Eastern Cuba (La Tinta mélange; Lázaro et al., 2016), Dominican Republic (Maimón formation; Torró et al., 2017) and Puerto Rico (Rio Majada and Lower Cajul formations; Jolly et al., 2002; Lidiak et al., 2011) describe forearc basalts (Fig. C5_24). This implies that subduction initiation can be tracked over more than 1600 km, along Cuba, Dominican Republic and Puerto Rico. Forearc basalts were defined by Reagan et al. (2010) as basalts generated by mantle decompression at a trench-related spreading center. Their compositions are similar to MORB (see Fig. C5_24), but they may display a small or no slab imput. The slab input is reflected by a characteristic Nb negative anomaly and Th enrichment (e.g. Kelemen

et al., 2003) in comparison to normal MORB compositions. In some cases, subsequent melting of a more depleted mantle source with more subducted components due to subduction progression creates melts of boninitic affinity (high MgO, low alkalis and TiO_2; Kelemen et al., 2003; Pearce, 2014). Such compositions have been found in Cuba (La Havana, Holguín and Mayarí Cristal complexes; Kerr et al., 1999; Proenza et al., 2006; Marchesi et al., 2007), Dominican Republic (Rio San Juan and Puerto Plata complexes, Maimón and Los Ranchos formation; Escuder et al., 2006, 2011 and 2014; Torró et al., 2017) and Virgin Islands (Water Island formation; Jolly and Lidiak, 2006). As subduction evolved, island arc tholeiites (IAT) were formed, displaying a marked subduction-related signature such as enrichment in LREE with positive Th and negative Nb anomalies, and LILE enriched compositions. Group 2 of the sub-volcanic unit of the VCSM displays such compositions, more evolved than group 1 of FAB affinity (see Fig. C5_24). In Central and Eastern Cuba (Central: Sagua la Chica and Los Pasos formations; Kerr et al., 1999; Díaz de Villalvila et al., 2003; Eastern Cuba: Guamuta, Loma de la Bandera, Téneme, Quiviján and Estrella de Mayarí formations; Kerr et al., 1999; Proenza et al., 2006; Marchesi et al., 2007), primitive island arc tholeiites of Early Cretaceous record SW subduction of the Proto-Caribbean basin, as well as in Puerto Rico (Lower Cajul and Rio Majada formation; Jolly et al., 2002; Lidiak et al., 2011; Cintron Franqui et al., 2017). During the Late Cretaceous to Tertiary, active subduction created volcanic arc (IAT and calcalkaline basalts; Kerr et al., 1999; Jolly et al., 2002; Díaz de Villalvila et al., 2003; Lidiak et al., 2011; Lidiak and Anderson, 2015; Cintron Franqui et al., 2017 and references therein), backarc (Fig. C5_24; Marchesi et al., 2007) and forearc basalts (Kerr et al., 1999; Díaz de Villalvila et al., 2003; Escuder et al., 2014; Lázaro et al., 2016; Torró et al., 2017) in the Caribbean plate.

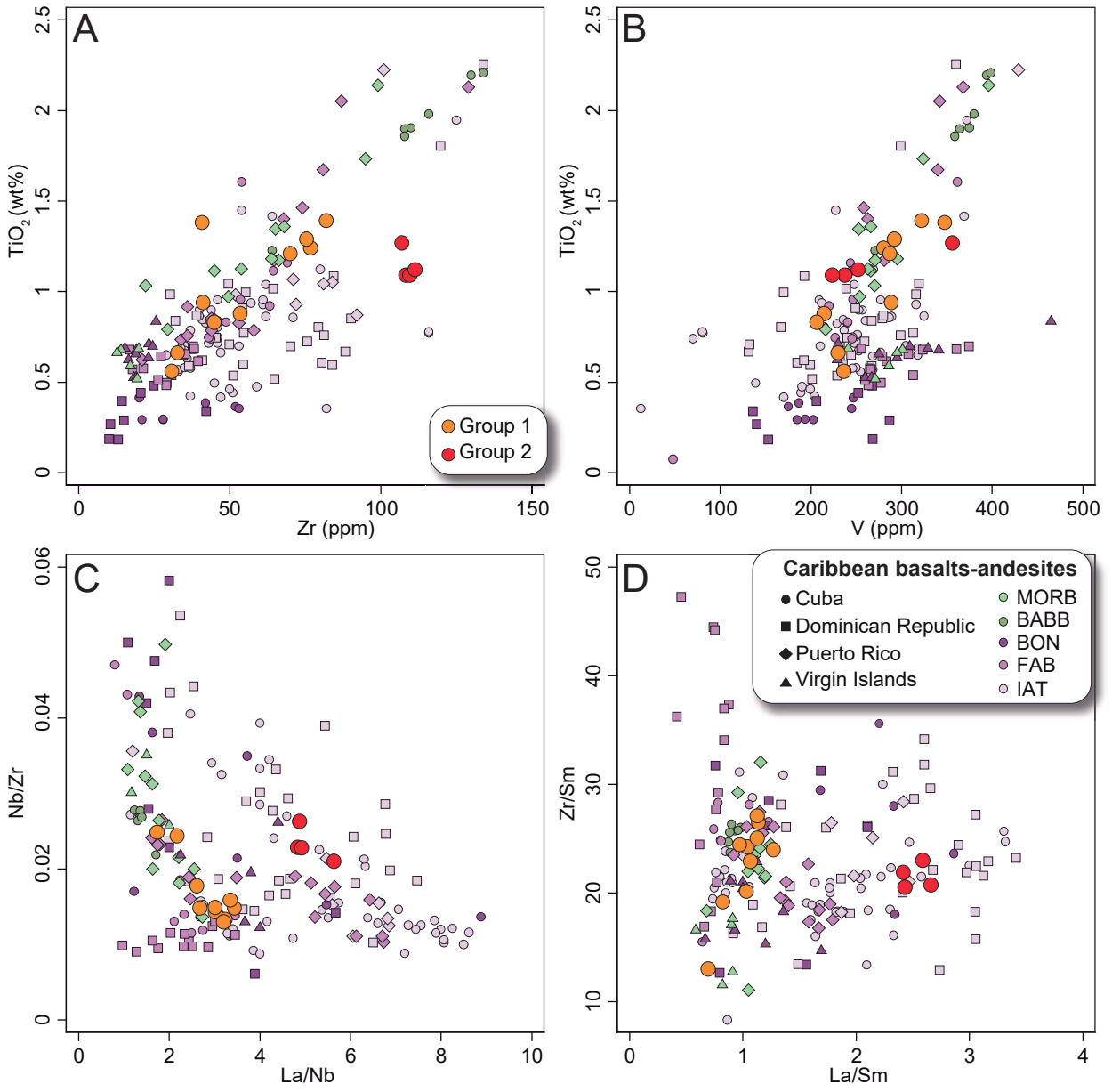

Figure. C5_24 *Trace element diagrams of Early Cretaceous Caribbean Island Arc. A) TiO_2 (wt%) vs Zr (ppm). B) TiO_2 (wt%) vs V (ppm). C) Nb/Zr vs La/Nb. D) Zr/Sm vs La/Sm. Plotted samples of Cuba (Kerr et al., 1999; Díaz de Villalvila et al., 2003; Marchesi et al., 2007; Lázaro et al., 2016), Dominican Republic (Escuder et al., 2006, 2007, 2011 and 2014; Torró et al., 2017), Puerto Rico (Jolly et al., 2002, 2007; Lidiak et al., 2011; Cintron Franqui et al., 2017) and Virgin Islands (Jolly and Lidiak et al., 2006).*

5.4.2. Plutonic unit of the VCSM

The plutonic unit is composed of rocks with variable proportions of plagioclase, clinopyroxene, orthopyroxene and olivine. These proportions and adcumulate textures indicate that the plutonic unit is constituted by cumulate gabbro and ol-gabbro. The preferential orientation of plagioclase and clinopyroxene evidence accumulation (Fig. C5_2). The whole-rock composition of major elements shows high Mg# with a progressive increase of CaO, which depend on preferential mineral proportions due to accumulation processes (Fig. C5_16). Trace element compositions are depleted with respect to N-MORB

compositions with LREE-depleted and positive Eu anomalies and variable HREE. The REE patterns and Eu anomaly (Fig. C5_17) indicate that the plutonic unit was the result of crystal fractionation, not allowing the petrogenesis of the corresponding magmas to be constrained.

In the previous work of Rutten et al. (1938), Kanchev et al. (1978), Álvarez et al. (1991) and García et al. (1998), the plutonic unit appears in contact with the sub-volcanic unit. Due to tropical weathering, it is difficult to determine if there is a genetic contact between the two units. In the map by García et al. (1998), a tectonic contact between them is depicted.

The isotopic composition may help to understand if there is a genetic relationship between the mantle source that originated sub-volcanic and plutonic units. The isotopic signatures of the sub-volcanic and plutonic units are slightly different, with high depletion of $^{143}Nd/^{144}Nd$ in the plutonic unit (Fig. C5_19; 0.51252 to 0.51276 at *c.* 125Ma). This indicates a heterogeneous mantle source. As argued above, the mantle source of the sub-volcanic unit is affected by a small slab signature (see chapter 5.4.1.2). Together with the low $^{143}Nd/^{144}Nd$ of the plutonic unit, this would indicate a clear slab signature most likely related to global subducting sediment melt (*c.* 0.8 % of GLOSSM, Fig. C5_19), after melting of slab sediments in a context of subduction initiation. The different slab input may result in a heterogeneous enrichment of the magma source, perhaps giving rise to the sub-volcanic and plutonic unit in the VCSM.

The isotopic Nd and Sr signature of the plutonic unit does not record high values of $^{87}Sr/^{86}Sr$. Nevertheless, the plutonic unit bears evidence of ocean floor metamorphism (e.g. Kelley et al., 2003; Ribeiro et al., 2013; Hirahara et al., 2015), although it is not generalized.

Chapter 6

Exotic ultramafic block in the VCSM

6.1. Field relations

6.2. Petrography

6.3. Mineral chemistry

6.4. Whole-rock chemistry

6.5. P-T Conditions

6.6. Discussion of exotic ultramafic block of the VCSM

6. An exotic ultramafic block in the Villa Clara serpentintic mélange

6.1. Field relations

The Villa Clara serpentinitic mélange includes exotic blocks of eclogite, garnet-amphibolite, blueschist facies rocks and antigorite-serpentinite (Atg-serpentinite; Fig. C6_1). Here we focus on Atg-serpentinite, well exposed in the Pelo Malo megablock, to the East of Santa Clara city (Fig. C6_1).

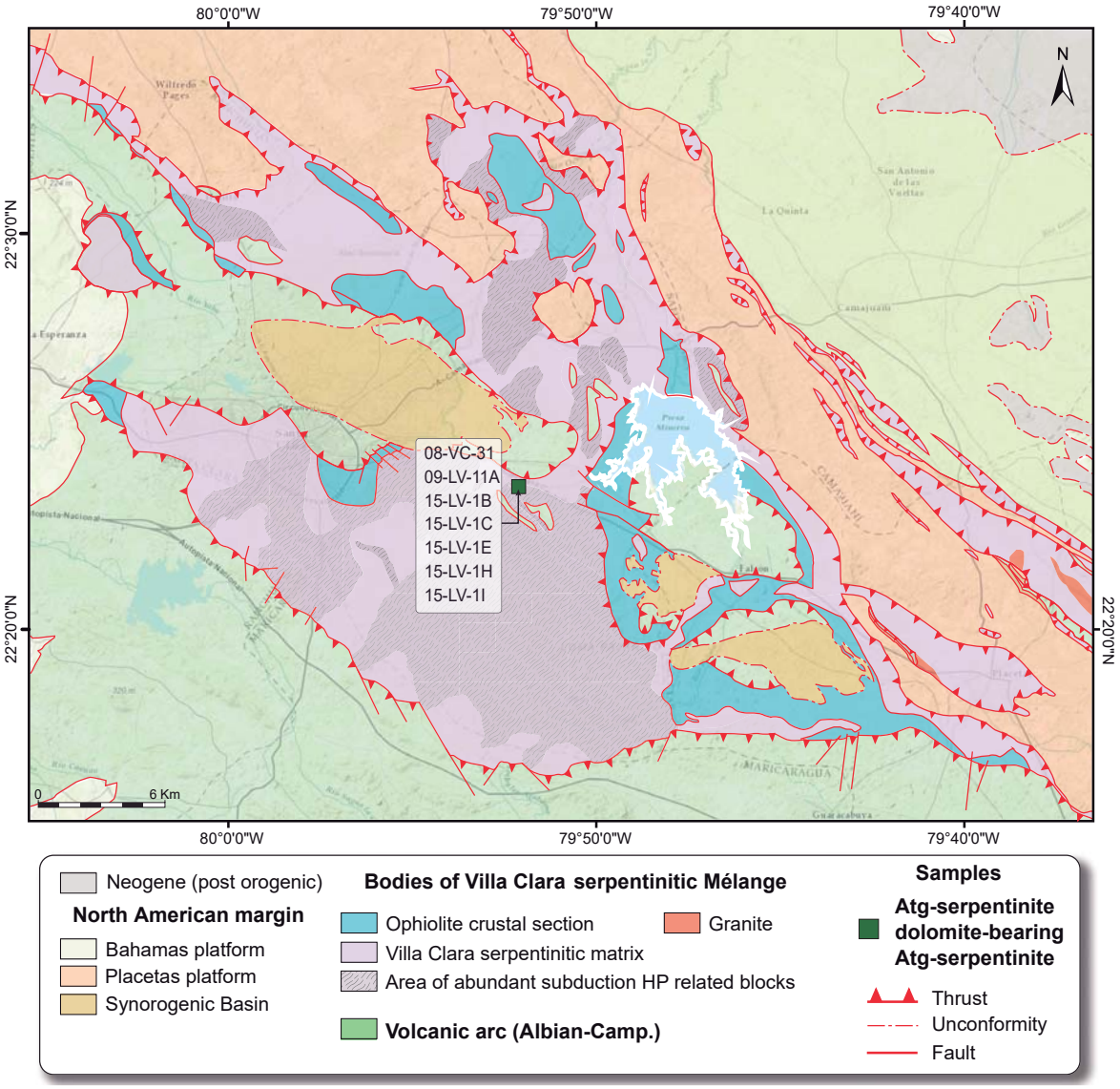

Figure. C6_1 *Geological map of Las Villas 1:100000, with the main geologic features and sample location of Atg-serpentinite Pelo Malo block from VCSM (modified from Kanchev et al., 1978; Álvarez et al., 1991 and García et al., 1998).*

The surface area of the megablock is 55150 m^2 and consists of bluish to greenish massive and strongly foliated Atg-serpentinite (Figs. C6_2A and C6_2B). The surrounding rocks, enclosing the megablock, consist of low-T brecciated serpentinite that constitute much of the serpentinite matrix of the mélange (see chapter 4 for further details; cf. Kanchev et al., 1978). Locally, centimetre-scale tremolite veins (2 cm to 15 cm width) occur within Atg-serpentinite, and zoned blackwalls occur at the vein-rock contact (Figs. C6_2C to C6_2F).

The whole vein-wall rock structure can be described as formed by four domains: i) Atg-serpentinite host rock, ii) antigorite + chlorite + tremolite (Atg + Chl + Tr) blackwall outer band; iii) chlorite + tremolite (Chl + Tr) blackwall inner band; and iv) tremolite vein (Tr-vein) (Figs. C6_2E and C6_2F). Notably, similar veins are absent in nearby low-T brecciated serpentinite rock surrounding the Pelo Malo megablock, attesting to its tectonic nature.

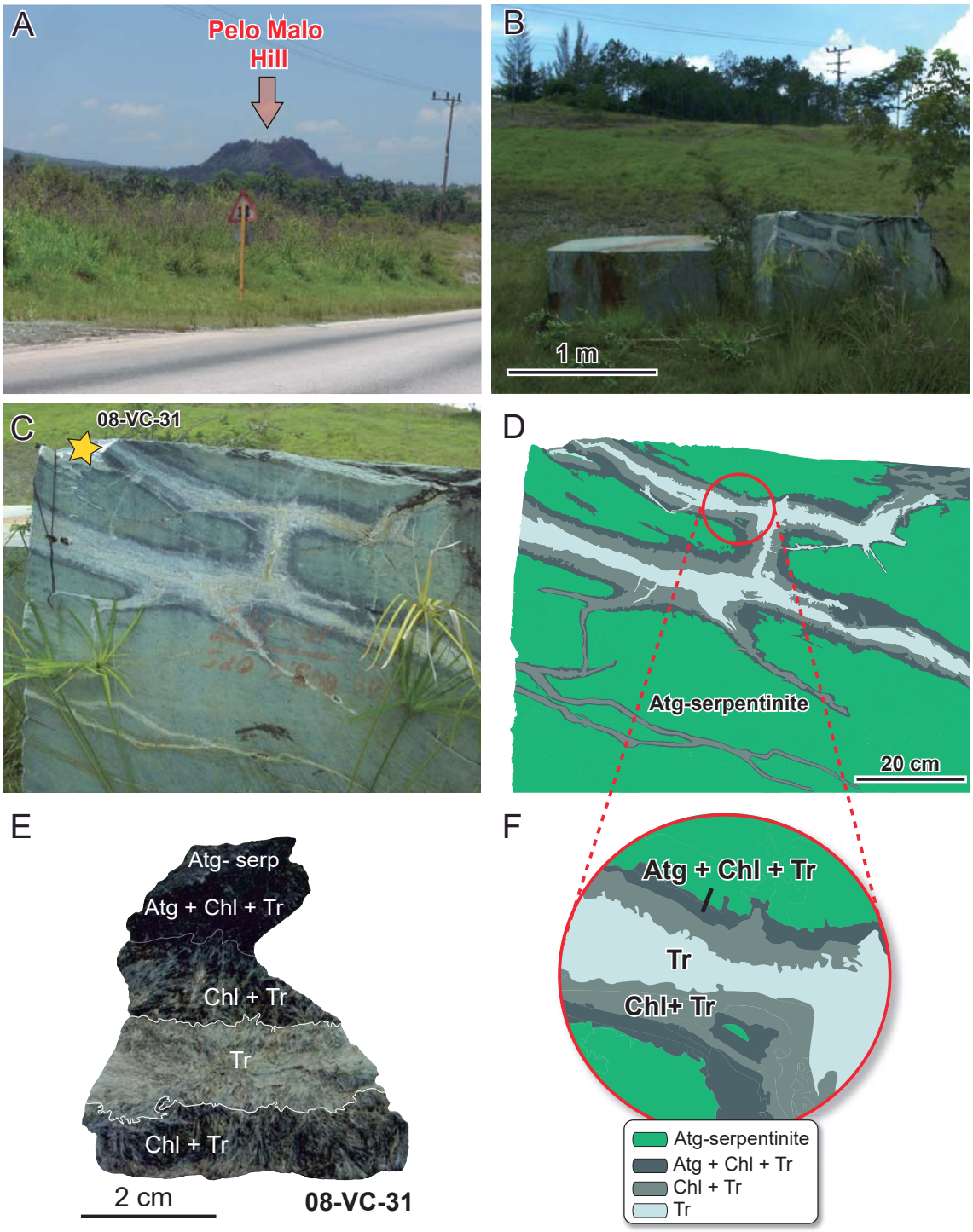

Figure. C6_2 *A) Field view of the Pelo Malo serpentinite megablock. B) Quarry pieces of Pelo Malo serpentinite. C) Detail of vein structure within Atg-serpentinite; sample 08-VC-31 was taken from this piece. D) Schematic drawing of the vein structure. Zoom inside the vein structure showing different domains: Atg + Chl + Tr zone, Chl + Tr zone and tremolite vein. E) Hand-specimen view of the vein and domains; note the sharp contact between the tremolite vein and the inner chlorite + tremolite domain.*

6.2. Petrography

The Pelo Malo Atg-serpentinite has a massive structure and strongly foliated fabric denoting significant strain during and after serpentinization. Atg-serpentinites can be divided in two groups depending on dolomite content (Fig. C6_3A and C6_3B). Dolomite-bearing Atg-serpentinites have antigorite and minor dolomite, chlorite and ferrian chromite, magnetite, with occasional ilmenite and Fe-Ni sulphide. Antigorite and dolomite appear intergrown in replacement textures of former chromian spinel (Fig. C6_3A), indicating infiltration of a CO_2-H_2O fluid during serpentinization. On the other hand, Atg-serpentinites bear antigorite, plus chlorite, magnetite and ferrian chromite as transformation products of former chromian spinel. Relicts of high-T olivine, pyroxenes and spinel are lacking.

The antigorite is the most abundant mineral in dolomite-bearing Atg-serpentinites and Atg-serpentinites. Both rock types have non-pseudomorphic interpenetrating texture (c.f. O'Hanley, 1996). Antigorite blades have variable size, from 1 mm to 20 µm in length (Fig. C6_3B). Neither lizardite nor chrysotile was found in Raman spectra (Fig. C6_3C). Chromian spinel was completely transformed into ferrian chromite, magnetite and chlorite. Chlorite also appears dispersed in the matrix.

The outer Atg + Chl + Tr blackwall domain is characterized by unoriented blades of antigorite (0.1 to 0.5 mm in length) intergrown with chlorite and dispersed euhedral crystals of tremolite that are 0.5 to 1 mm in length (Fig. C6_4). The abundance of antigorite decreases towards the Chl + Tr domain (it appears as small blades of 0.05-0.2 mm; Fig. C6_4), while tremolite abundance increases. The interface between the Chl + Tr blackwall domain and the Tr-vein is sharp, denoting that the latter corresponds to the locus of direct crystallization from fluid in an open fracture (Figs. C6_2, C6_3 and C6_4). The Tr-vein domain has dispersed euhedral shaped tremolite (c. 0.5-0.8mm) within fibrous aggregates arranged in areas of variable orientation (Fig. C6_3F). Common textures include fan-shaped tremolite clusters (1 mm to up to 1 cm in length; Fig. C6_3E). The tremolite changes in orientation (Figs. C6_3E and C6_3F) indicate that the vein and the adjacent Chl + Tr domain are deformed, though deformation is concentrated in the vein, suggesting shear deformation during and after fluid infiltration and crystallization. Dispersed chlorite-rich clusters within the vein are interpreted as mechanically detached fragments of the Chl + Tr domain.

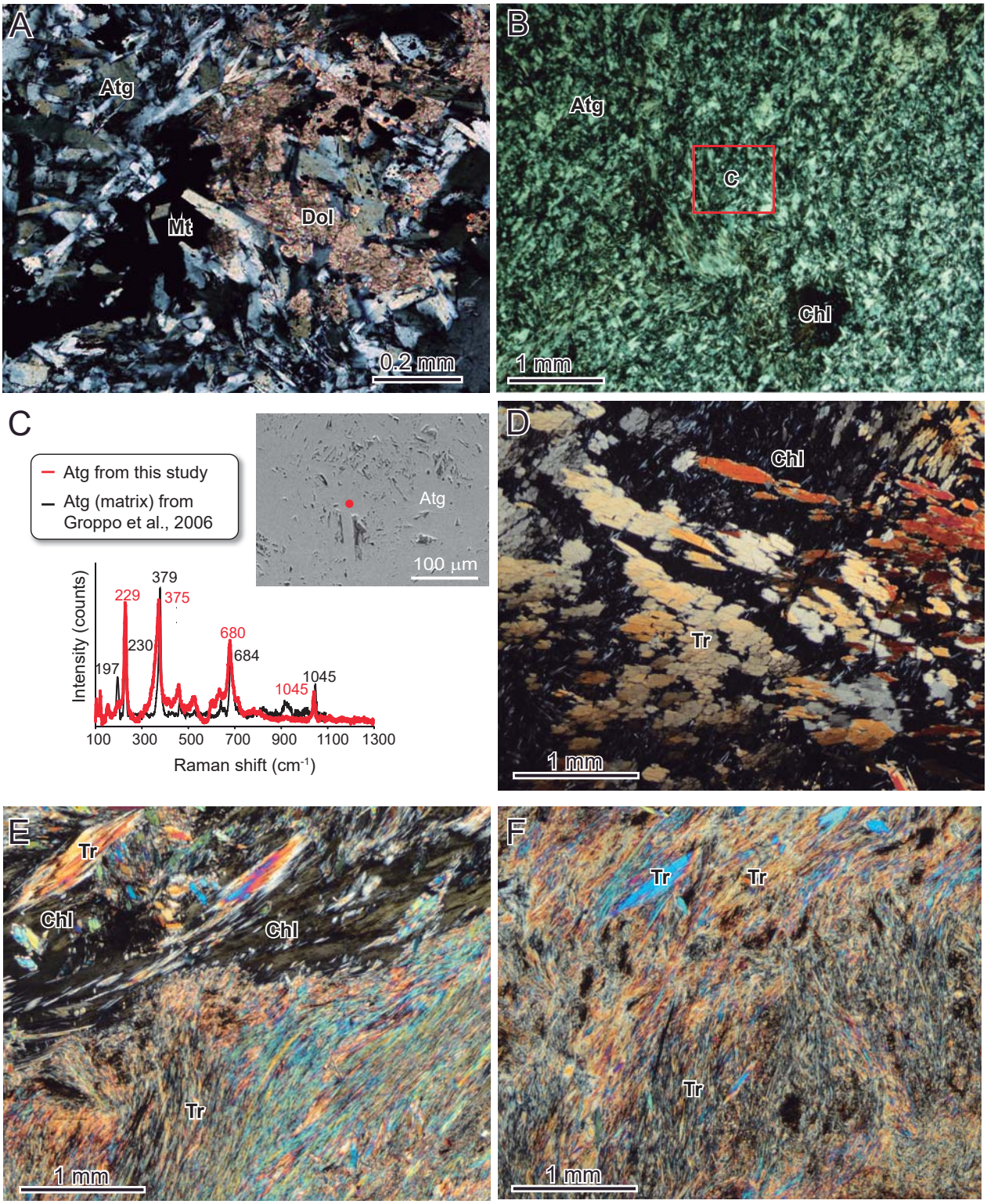

Figure. C6_3. *Cross-polarized light photomicrographs and BSE image of Atg-serpentinite and vein domains. A) Dolomite-bearing Atg-serpentinite showing antigorite-dolomite intergrowths; B) Atg-serpentinite showing interpenetrating texture and chlorite blasts; C) Backscattered electron image of the area indicated in A showing blades of antigorite. The point indicates the area analyzed with micro-Raman spectroscopy. The Raman spectrum shows the characteristic peaks of antigorite (e.g., Groppo et al., 2006, for comparison). D) Chlorite + tremolite domain with abundant euhedral crystals of tremolite in a matrix of chlorite. E) Sharp contact between chlorite + tremolite domain and tremolite vein; note intense deformation. F) Tremolite vein showing deformed fibrous crystals of tremolite with variable crystal orientation and local euhedral crystals of greater size.*

6.3. Mineral chemistry

Representative mineral compositions of spinel group minerals, serpentine group minerals, chlorite, amphibole and carbonates are displayed below. The mineral formula was normalized to certain oxygens depending on each mineral as elements per formula unit (p.f.u.): spinel group minerals (4 oxygens), serpentine (14 oxygens), chlorite (28 oxygens), amphibole (23 oxygens) and carbonates (2 cations p.f.u) (more details in chapter 3).

Antigorite from dolomite-bearing Atg-serpentinite has Mg ≈ 5.37-5.58 and Al ≈ 0.08-0.25 a.p.f.u. and Mg#≈[Mg/(Mg+Fe^{2+})] ≈ 0.96-0.97 (see Table C6_1). Textural relations and antigorite composition change along the cross-section from the Atg + Chl + Tr to the Chl + Tr domains, as illustrated in the X-ray images of Fig. C6_4. They show an increase of Al in antigorite across the Atg + Chl + Tr domain and a corresponding decrease in Fe, Mg and Si, denoting the tschermak exchange vector (Si(Mg, Fe)Al_{-2}) (Fig. C6_4). In this domain, antigorite has Mg ≈ 4.93-5.26 and Al ≈ 0.04-0.44 a.p.f.u (Figs. C6_5A to C6_5C). Antigorite from the Atg + Chl +Tr and scarce relicts within the Chl + Tr domains show negative Fe-Mg correlation, with higher Fe and lower Mg# (0.90-0.92) towards the vein, indicating FeMg-1 exchange (Fig. C6_5C). The distribution of Cr is irregular and related to the replacement of chromian spinel (top right of the Cr image, Fig. C6_4).

Table C6_1. *Representative analyses of antigorite from exotic ultramafic block of the VCSM.*

Sample	09-LV-11A		08-VC-31		08-VC-31	
Rock type	dolomite-bearing Atg-serpentinite		Atg-serpentinite			
Vein domains	None		Atg + Chl + Tr		Chl + Tr	
Mineral	Serpentine		Serpentine		Serpentine	
Major elements (wt%)						
SiO_2	42.44	43.75	42.62	42.49	43.26	43.07
TiO_2	0.02	b.d.l	b.d.l	b.d.l	b.d.l	0.02
Al_2O_3	2.25	1.17	2.19	1.53	0.53	0.89
Cr_2O_3	0.89	0.16	0.50	0.42	0.14	0.22
FeO_T^*	2.74	2.07	7.05	6.59	6.17	6.14
MnO	0.06	0.09	0.15	0.21	0.11	0.08
MgO	38.65	39.65	35.65	35.77	36.63	36.46
NiO	0.20	0.19	0.25	0.31	0.19	0.19
CaO	b.d.l	b.d.l	0.01	b.d.l	b.d.l	0.01
Na_2O	0.03	b.d.l	b.d.l	0.03	b.d.l	b.d.l
K_2O	b.d.l	b.d.l	0.01	b.d.l	0.01	0.01
Total	87.28	87.08	88.43	87.35	87.04	87.09
Formula based 14 oxygens						
Si	3.96	4.06	4.00	4.03	4.10	4.08
Ti	0.00	-	-	-	-	0.00
Al	0.25	0.13	0.24	0.17	0.06	0.10
Cr	0.07	0.01	0.04	0.03	0.01	0.02
Fe^{2+}	0.21	0.16	0.55	0.52	0.49	0.49
Mn	0.00	0.01	0.01	0.02	0.01	0.01
Mg	5.37	5.49	4.99	5.06	5.18	5.15
Ni	0.02	0.01	0.02	0.02	0.01	0.01
Ca	-	-	0.00	-	-	0.00
Na	0.01	-	-	0.01	-	-
K	-	-	0.00	-	0.00	0.00
Mg#**	0.96	0.97	0.90	0.91	0.91	0.91
Mg+Fe+Mn+Ni	5.61	5.67	5.57	5.63	5.69	5.66

b.d.l= below detection limit. *FeOT= total iron as FeO. **Mg#= [Mg/(Mg+Fe^{2+})]

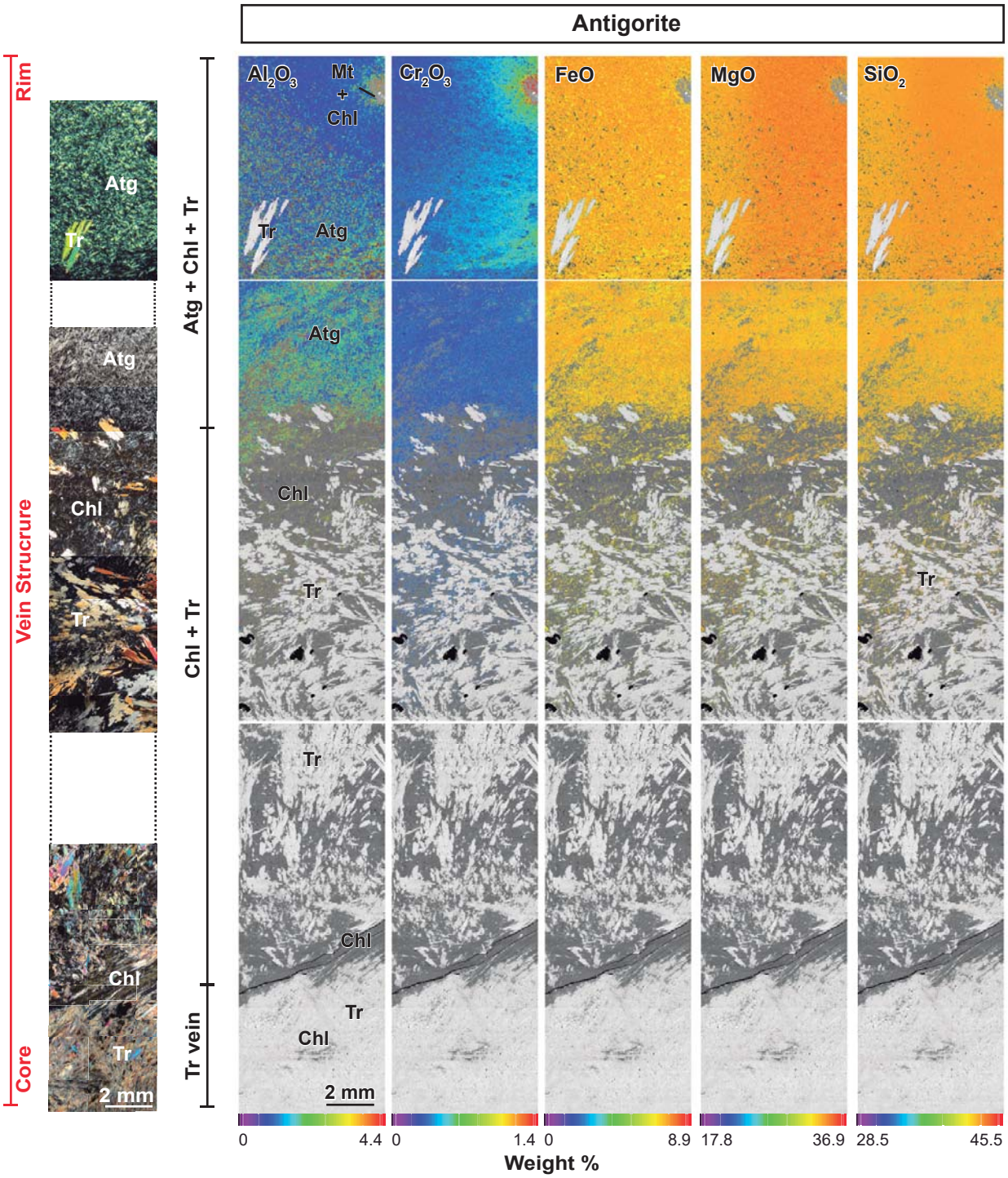

Figure C6_4. *Composite X-ray images corresponding to a cross-section across the vein structure (top is wallrock and bottom is the centre of the vein). The images were processed to show Al_2O_3, Cr_2O_3, FeO, MgO and CaO wt% (see chapter 3.3), and masked to show antigorite only, set on top of backscattered electron images that show the basic textural features across the vein structure. Left side images correspond to optical photomicrographs (crossed polars) of the scanned vein domains. Labels as in Fig. C6_3.*

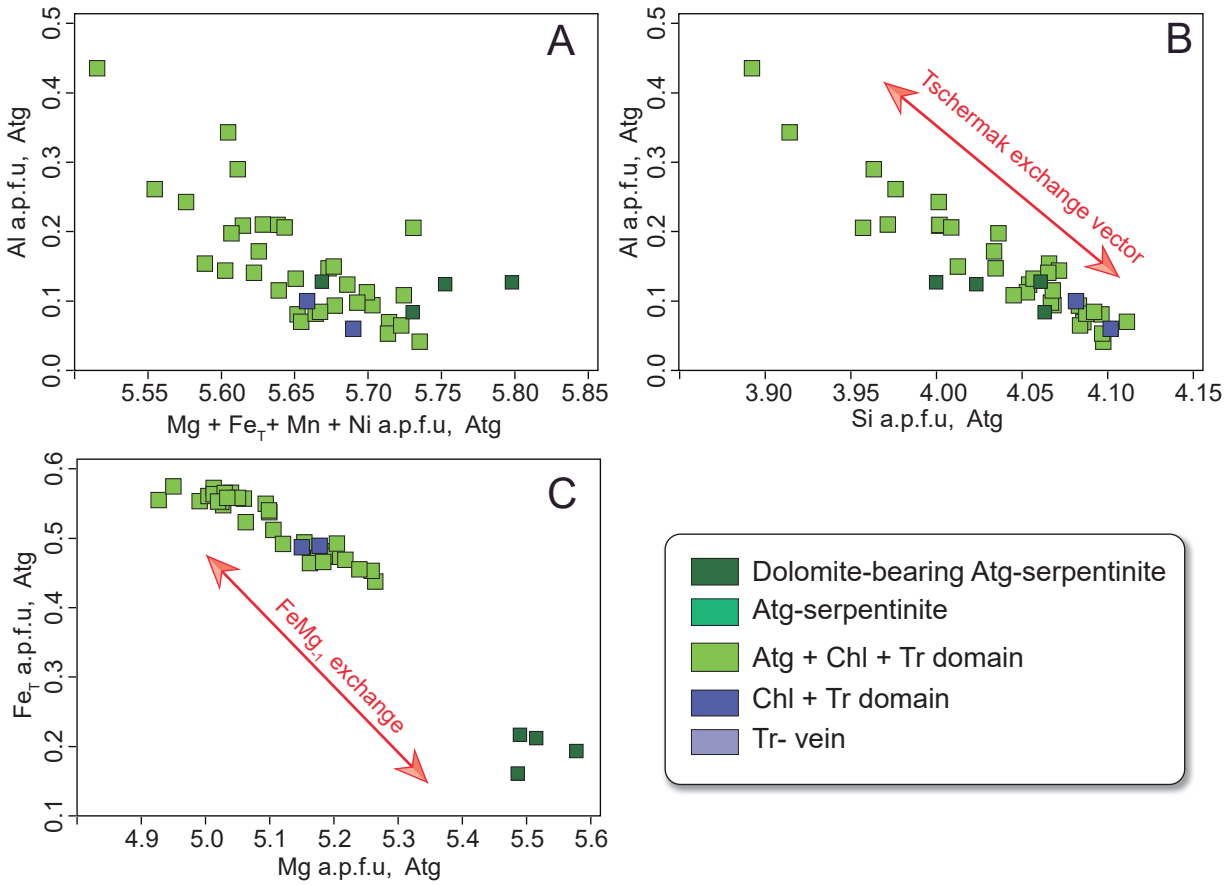

Figure C6_5. *Composition of antigorite in dolomite-bearing Atg-serpentinite and Atg-serpentinite. Colours of symbols represent vein domains.*

The chlorite appears in blackwall domains and in serpentinites as mantles surrounding magnetite crystals. Chlorite in Atg-serpentinite, blackwall domains and vein has Si ranging 6.32 - 6.64, Mg ≈ 8.83 - 9.44 a.p.f.u and Mg# ≈ 0.90 - 0.91 (Figs. C6_6A to C6_6C and Table C6_2), typical of clinochlore. Two contrasted chemical compositions are observed on the basis of textural position. In the Atg + Chl + Tr and Chl + Tr domains, chlorite is poorer in Cr (0.02-0.15 a.p.f.u) than chlorite with high Cr (0.19-0.62 a.p.f.u) related to small crystals of magnetite which evidence the former local presence of chromian spinel (Fig. C6_7). In the Atg + Chl + Tr domain chlorite has lower Al content (3.09-3.18 a.p.f.u) than in the Chl + Tr domain (up to 3.30 a.p.f.u, Fig. C6_6B). In all domains Al and Cr show a negative correlation (Fig. C6_7).

Table C6_2. *Representative analyses of chlorite from exotic ultramafic block of VCSM.*

Sample	08-VC-31		08-VC-31		08-VC-31		08-VC-31	
Rock type	Atg-Serpentinite							
Vein domains	None		Atg + Chl + Tr		Chl + Tr		Tr-Vein	
Mineral	Chlorite		Chlorite		Chlorite		Chlorite	
Major elements (wt%)								
SiO_2	33.67	33.37	34.61	34.63	33.98	34.58	33.43	34.03
TiO_2	b.d.l	b.d.l	0.01	0.04	b.d.l	b.d.l	b.d.l	b.d.l
Al_2O_3	11.67	11.67	14.14	14.11	14.32	14.39	13.92	13.77
Cr_2O_3	4.66	4.85	0.40	0.98	0.28	0.45	0.40	0.31
FeO_T^*	5.83	5.78	6.11	6.14	6.02	5.97	5.97	5.88
MnO	0.07	0.04	0.06	0.05	0.05	0.09	0.03	0.06
MgO	32.25	32.56	32.69	32.77	33.50	33.51	31.59	31.28
NiO	0.22	0.28	0.35	0.31	0.32	0.34	0.26	0.28
CaO	b.d.l	0.01	0.02	0.02	0.01	0.04	0.03	0.22
Na_2O	b.d.l	b.d.l	0.01	0.02	0.05	0.02	0.01	0.02
K_2O	b.d.l	b.d.l	b.d.l	b.d.l	b.d.l	b.d.l	0.01	0.02
Total	88.37	88.56	88.40	89.07	88.53	89.39	85.64	85.86
Formula based on 28 oxygens								
Si	6.43	6.37	6.51	6.47	6.39	6.43	6.49	6.58
Ti	-	-	0.00	0.01	-	-	-	-
Al	2.63	2.62	3.13	3.11	3.17	3.16	3.18	3.14
Cr	0.70	0.73	0.06	0.15	0.04	0.07	0.06	0.05
Fe^{2+}	0.93	0.92	0.96	0.96	0.95	0.93	0.97	0.95
Mn	0.01	0.01	0.01	0.01	0.01	0.01	0.00	0.01
Mg	9.18	9.26	9.16	9.13	9.39	9.29	9.14	9.01
Ni	0.03	0.04	0.05	0.05	0.05	0.05	0.04	0.04
Ca	-	0.00	0.00	0.00	0.00	0.01	0.01	0.05
Na	-	-	0.00	0.01	0.02	0.01	0.01	0.01
K	-	-	-	-	-	-	0.00	0.00
Mg#**	0.91	0.91	0.91	0.90	0.91	0.91	0.90	0.90

b.d.l= below detection limit. *FeOT= total iron as FeO. **Mg#= [$Mg/(Mg+Fe^{2+})$]

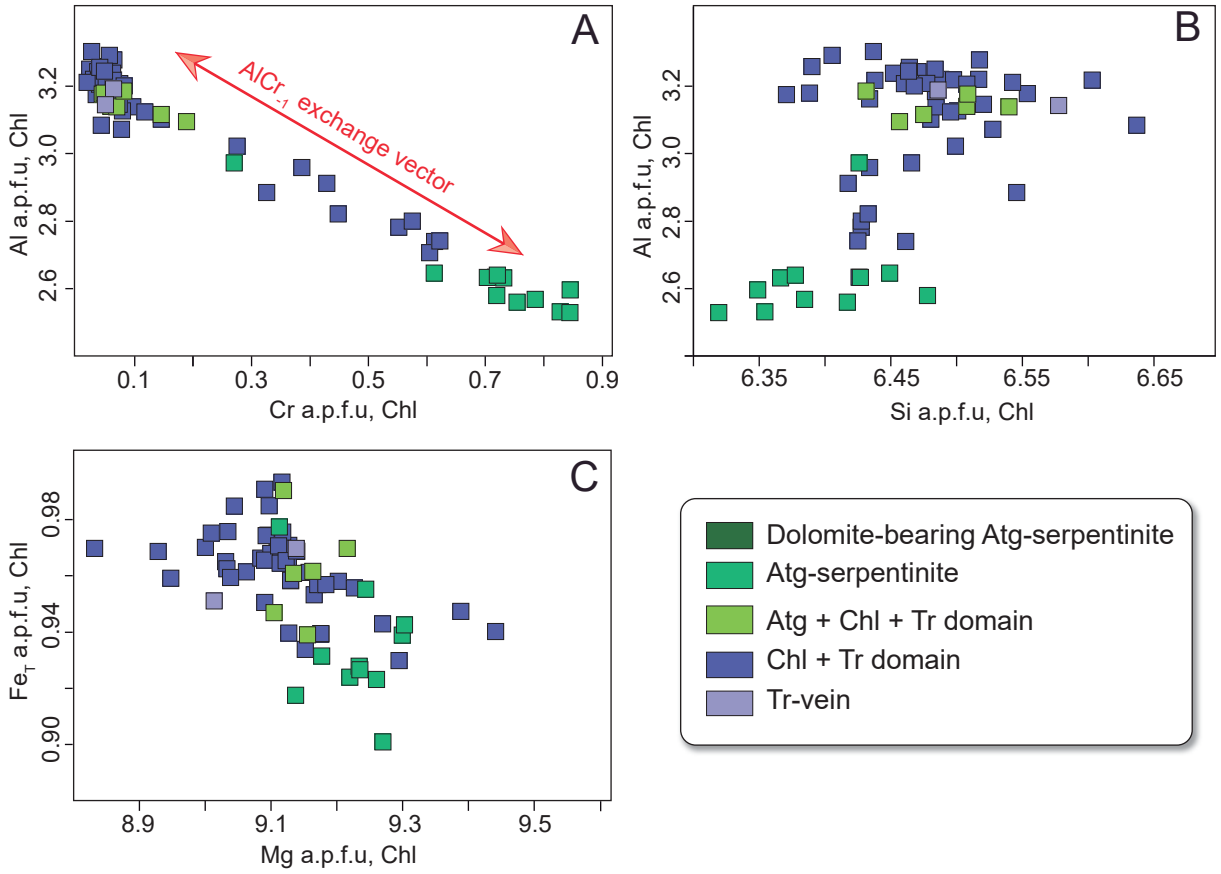

Figure C6_6 *Composition of chlorite in dolomite-bearing Atg-serpentinite and Atg-serpentinite. Colours of symbols represent vein domains.*

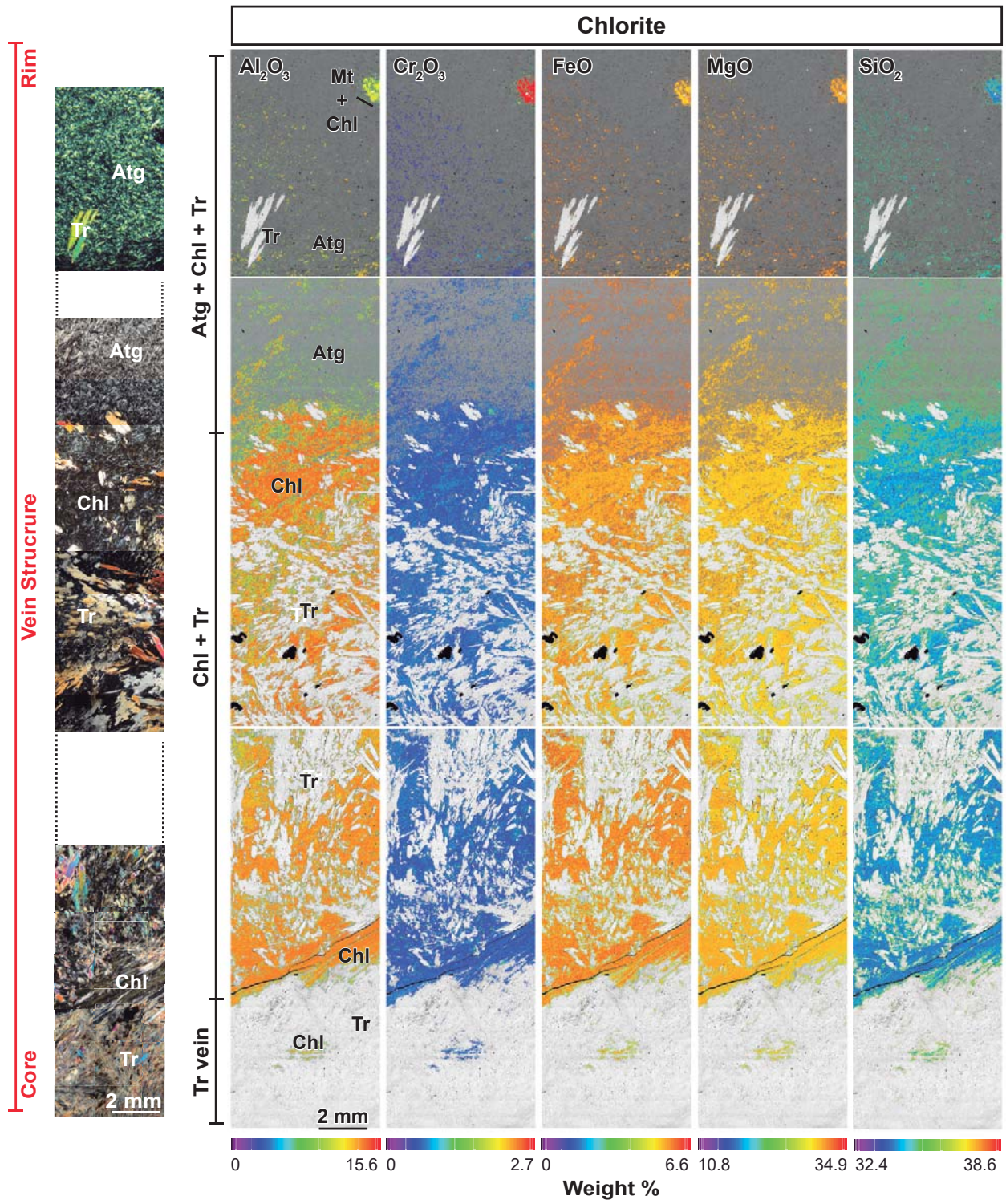

Figure C6_7 *Composite X-ray images corresponding to a cross-section across the vein structure (top is wallrock and bottom is the centre of the vein). The images were processed to show Al_2O_3, Cr_2O_3, FeO, MgO and CaO wt % (see chapter 3.3), and masked to show chlorite only, set on top of the backscattered electron images that show the basic textural features across the vein structure. Left side images correspond to optical photomicrographs (crossed polars) of the scanned vein domains. Labels as in Fig. C6_3.*

The amphibole appears in the vein structure displays a calcic composition typical of tremolite (Fig. C6_8). Tremolite in all domains and vein has a similar composition, with Si ranging from 7.97 to 8.00 a.p.f.u and Mg# ≈ 0.90 - 0.94 (see Table C6_3). In addition, tremolite has minor amounts of Na^B (<0.19 a.p.f.u) and $(Na+K)_A$ ≈ 0.03 to 0.22 a.p.f.u. A subtle zoning, with slightly Al-enriched and Fe-poorer cores, is seen in the corresponding X-ray images (Fig. C6_9).

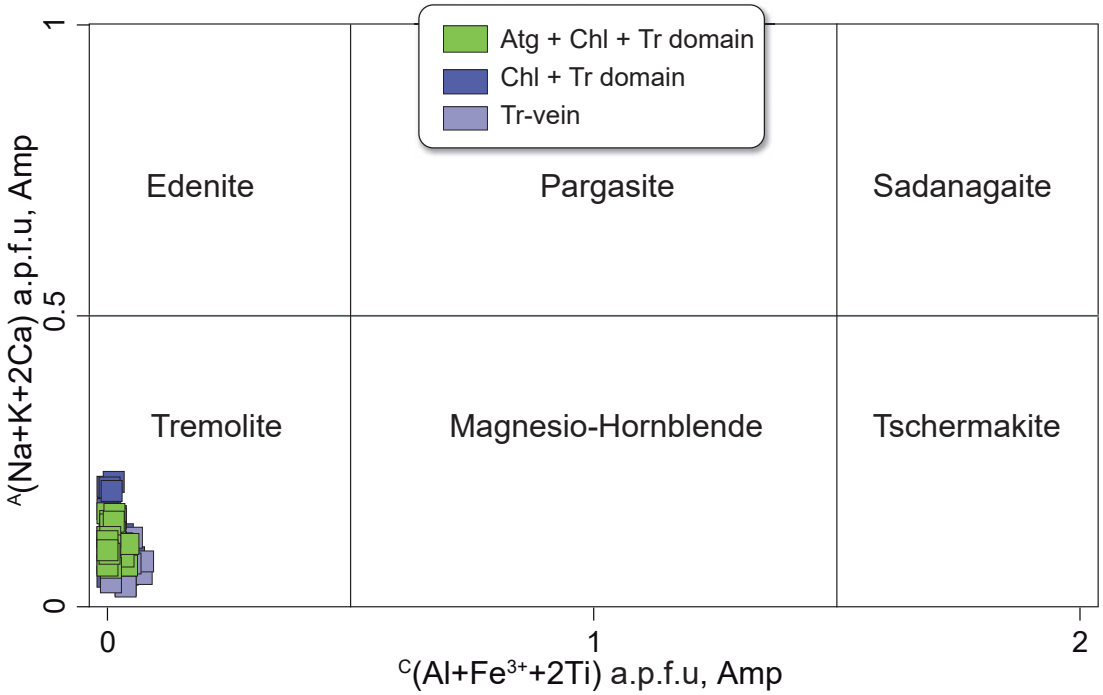

Figure C6_8 *Classification of calcic amphiboles after Hawthorne et al. (2012). Colour symbols show different vein domains.*

Table C6_3. *Representative analyses of amphibole from exotic ultramafic block of VCSM.*

Sample	08-VC-31					
Rock type	Atg-serpentinite					
Vein domains	Atg + Chl + Tr		Chl + Tr		Tr-vein	
Mineral	Tremolite		Tremolite		Tremolite	
Major elements (wt%)						
SiO_2	58.27	57.55	58.64	57.55	56.15	57.88
TiO_2	0.03	0.03	0.03	0.03	0.03	b.d.l
Al_2O_3	0.09	0.14	0.12	0.18	0.37	0.05
Cr_2O_3	0.03	0.01	0.01	0.10	0.55	0.02
FeO_T^*	2.88	2.98	2.80	3.17	3.84	2.61
MnO	0.09	0.09	0.11	0.11	0.16	0.08
MgO	22.80	22.44	23.44	22.31	21.21	22.64
NiO	0.06	0.10	0.10	0.10	0.07	0.09
CaO	12.83	12.72	13.14	12.62	12.24	13.19
Na_2O	0.66	0.72	0.37	0.70	0.86	0.30
K_2O	0.08	0.16	0.03	0.12	0.13	0.05
Sum	97.82	97.03	98.79	97.14	95.72	96.99
Formula based 23 oxygens						
Si_T	7.99	7.98	7.96	7.97	7.94	8.00
Al_T	0.01	0.02	0.02	0.03	0.06	0.00
Al_C	0.00	0.00	0.00	0.00	0.00	0.01
Ti_C	0.00	0.00	0.00	0.00	0.00	-
Cr_C	0.00	0.00	0.00	0.01	0.06	0.00
$Fe^{3+}{}_C$	0.01	0.00	0.00	0.02	0.00	0.00
Mg_C	4.66	4.64	4.74	4.61	4.47	4.66
Ni_C	0.01	0.01	0.01	0.01	0.01	0.01
$Fe^{2+}{}_C$	0.31	0.35	0.24	0.35	0.45	0.30
Mn_C	0.00	0.00	0.00	0.00	0.00	0.01
$Fe^{2+}{}_B$	0.00	0.00	0.08	0.00	0.00	0.00
Mn_B	0.01	0.01	0.01	0.01	0.02	0.00
Ca_B	1.88	1.89	1.91	1.87	1.85	1.95
Na_B	0.10	0.10	0.00	0.11	0.13	0.05
Ca_A	0.00	0.00	0.00	0.00	0.00	0.00
Na_A	0.07	0.09	0.10	0.08	0.10	0.03
K_A	0.01	0.03	0.01	0.02	0.02	0.01

b.d.l= below detection limit. *FeOT= total iron as FeO.

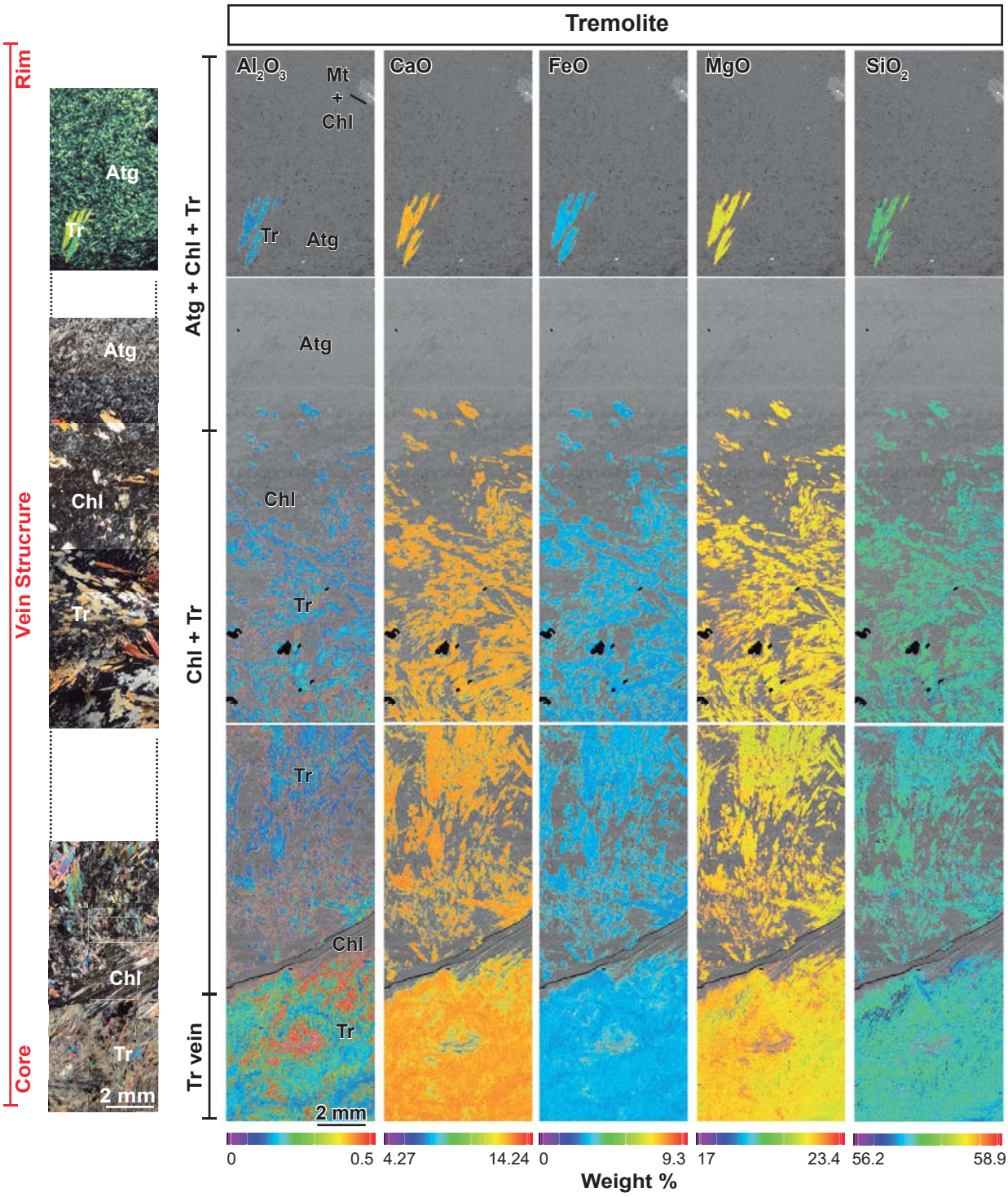

Figure C6_9 *Composite X-ray images corresponding to a cross-section across the vein structure. The images were processed to show Al_2O_3, Cr_2O_3, FeO, MgO and CaO wt% (see chapter 3.3), and masked to show amphibole only, set on top of backscattered electron images that show the basic textural features across the vein structure. Left side images correspond to optical photomicrographs (crossed polars) of the scanned vein domains. Labels as in Fig. C6_3.*

The spinel group minerals are composed of magnetite and ferrian chromite. Magnetite has Cr ≈ 0.02 - 0.03 a.p.f.u., Ti ≈ 0.01 a.p.f.u and Ni ≈ 0.02 - 0.03 a.p.f.u (Fig. C6_10A and Table C6_4). Ferrian chromite has Cr ≈ 1.24 - 1.73 a.p.f.u, Ti ≈ 0.01 - 0.10 a.p.f.u and Fe^{3+}# ≈ 0.11 - 0.34, and small amount of Al ≈ 0.01 - 0.02 a.p.f.u (Fig. C6_10B). The alteration trend shows the progressive enrichment in Fe^{3+} and strong depletion in Al and Mg that characterize ferrian chromite (Fig. C6_10B). High values of Cr# and Fe^{3+}# and Ti indicate that spinel is strongly transformed to ferrian chromite and magnetite (e.g. Colás et al., 2014). Its composition does not correspond to primary spinel, making it useless for deciphering the plate tectonic setting of the ultramafic protolith of the studied rocks (e.g. Parkinson and Pearce., 1988; Parkinson et al., 1992; Pearce et al., 2000; Proenza et al., 2004; Choi et al., 2008; Saka et al., 2014; Cao et al., 2016).

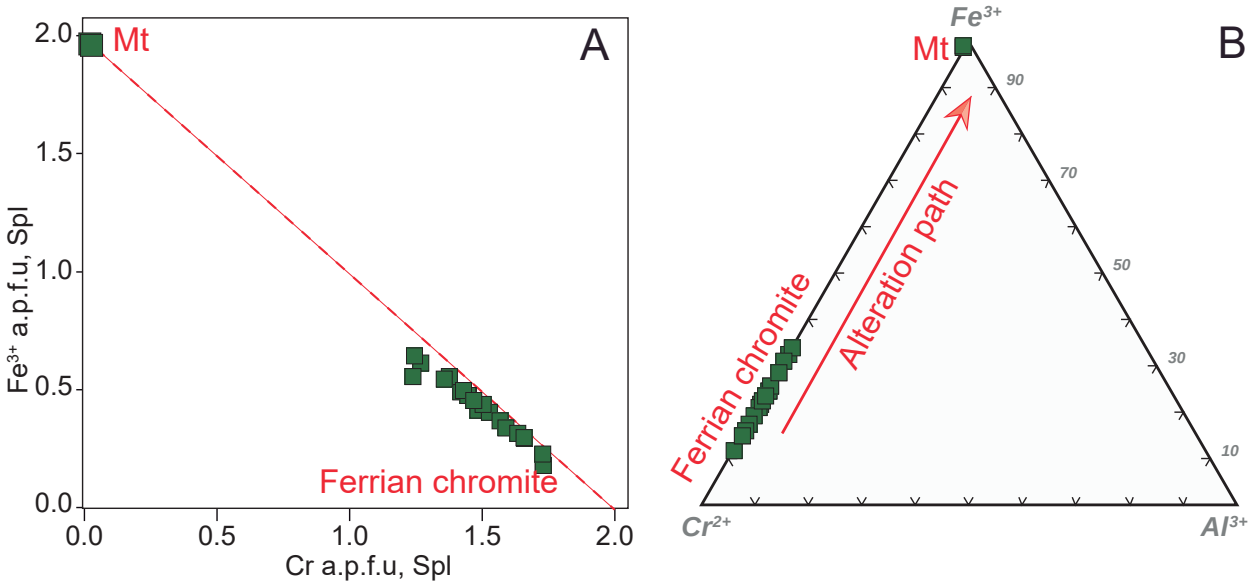

Figure C6_10 *Mineral composition of spinel group minerals in dolomite-bearing Atg-serpentinites.*

Table C6_4. *Representative analyses of spinel group from exotic ultramafic block of VCSM.*

Sample	09-LV-11A			08-VC-31		
Rock type	dolomite-bearing Atg-serpentinite			Atg-serpentinite		
Vein domains	None			Atg + Chl + Tr		
Mineral	Magnetite			Ferrian-chromite		
Major elements (wt%)						
SiO_2	b.d.l	b.d.l	0.04	0.28	0.03	0.06
TiO_2	0.20	0.20	0.15	1.15	0.90	1.82
Al_2O_3	-	-	-	0.32	0.34	0.20
Cr_2O_3	0.76	0.95	0.88	48.50	50.43	41.71
V_2O_3	0.06	0.06	0.06	-	-	-
FeO_T	90.47	88.83	89.95	41.68	40.95	47.98
MnO	0.21	0.30	0.10	2.02	2.36	2.59
ZnO	0.11	0.06	0.05	-	-	-
MgO	0.71	0.76	0.35	0.61	0.61	0.53
NiO	0.85	0.90	0.69	0.09	0.08	0.13
CaO	b.d.l	b.d.l	b.d.l	0.01	b.d.l	b.d.l
Total	93.37	92.06	92.27	94.67	95.70	95.02
Formula based 4 oxygens						
Si	0.00	0.00	0.00	0.01	0.00	0.00
Ti	0.01	0.01	0.00	0.03	0.03	0.05
Al	-	-	-	0.01	0.02	0.01
Cr	0.02	0.03	0.03	1.49	1.53	1.27
V	0.00	0.00	0.00	-	-	-
Mn	0.01	0.01	0.00	0.07	0.08	0.08
Zn	0.00	0.00	0.00	-	-	-
Mg	0.04	0.04	0.02	0.04	0.04	0.03
Ni	0.03	0.03	0.02	0.00	0.00	0.00
Fe^{3+}	1.96	1.96	1.96	0.41	0.40	0.61
Fe^{2+}	0.93	0.92	0.96	0.94	0.91	0.94
Mg#	0.04	0.05	0.02	0.04	0.04	0.03
Cr#	-	-	-	0.99	0.99	0.99
Fe^{3+}#	-	-	-	0.21	0.21	0.32

FeO_T= total iron as FeO. Mg#= [Mg/ (Mg + Fe^{2+})]. Cr#= [Cr/ (Cr + Al)]. Fe^{3+}#= [Fe^{3+}/ (Fe^{3+} + Cr + Al)]. b.d.l= below detection limit.

Dolomite has Ca ranging from 0.99 to 1.13 a.p.f.u and Mg ≈ 0.86 - 0.96 a.p.f.u (Table C6_5). Other carbonate species were not detected by means of EMPA.

Table C6_5. *Representative analyses of carbonates from exotic ultramafic block of VCSM.*

Sample	09-LV-11A				
Rock type	dolomite-bearing Atg-serpentinite				
Mineral	Dolomite				
Major elements (wt%)					
FeO_T	0.22	1.14	1.25	0.60	0.91
MnO	0.16	0.95	1.07	0.54	0.83
MgO	18.53	18.76	19.06	18.62	19.24
CaO	33.98	31.82	31.58	32.61	31.12
SrO	0.12	0.03	b.d.l.	0.08	0.03
Na_2O	0.01	0.01	b.d.l.	0.05	0.03
C	12.88	12.76	12.83	12.74	12.80
Total	100.22	99.45	99.99	99.19	99.06
Formula based 2 cations					
Mn	0.00	0.03	0.03	0.01	0.02
Mg	0.86	0.88	0.89	0.87	0.89
Ca	1.13	1.07	1.05	1.10	1.06
Sr	0.00	0.00	-	0.00	0.00
Na	0.00	0.00	-	0.00	0.00
C	2.00	2.00	2.00	2.00	2.00
Fe^{3+}	0.01	0.03	0.03	0.02	0.02

FeO_T= total iron as FeO. All Fe cation calculated as Fe^{3+}. b.d.l.= below detection limit.

6.4. Whole-rock chemistry

6.4.1. Major elements

Major element composition makes it possible to discriminate between dolomite-bearing Atg-serpentinite and Atg-serpentinite (Figs. C6_11A to C6_11D and Table C6_6). Dolomite-bearing Atg-serpentinite has SiO_2 = 45.44- 46.47, Al_2O_3 ≈1.20- 2.04, CaO ≈ 0.57- 1.05 and TiO_2 ≈ 0.03- 0.05 wt% (anhydrous basis; Fig. C6_11). In addition, MgO/SiO_2 and Al_2O_3/SiO_2 range from 0.92 to 0.95 and from 0.03 to 0.05, respectively (Fig. C6_11B). In contrast, Atg-serpentinite has a higher concentration in SiO_2 (47.44- 49.69 wt%) and a lower proportion of MgO (41.74- 42.46 wt%), with lower MgO/SiO_2 (0.85-0.88) and CaO (0.01-0.03 wt%).

The major element composition of blackwall domains and Tr-vein are relatively rich in SiO_2 (51.23-59.63 wt%) and CaO (4.81-12.31 wt%), but lower in MgO/SiO_2 (0.39-0.68) than the host rock Atg-serpentinites (Figs. C6_11B and C6_11C). The Al_2O_3 content in the blackwall is higher in Atg + Chl + Tr and Chl + Tr domains than the Tr-vein.

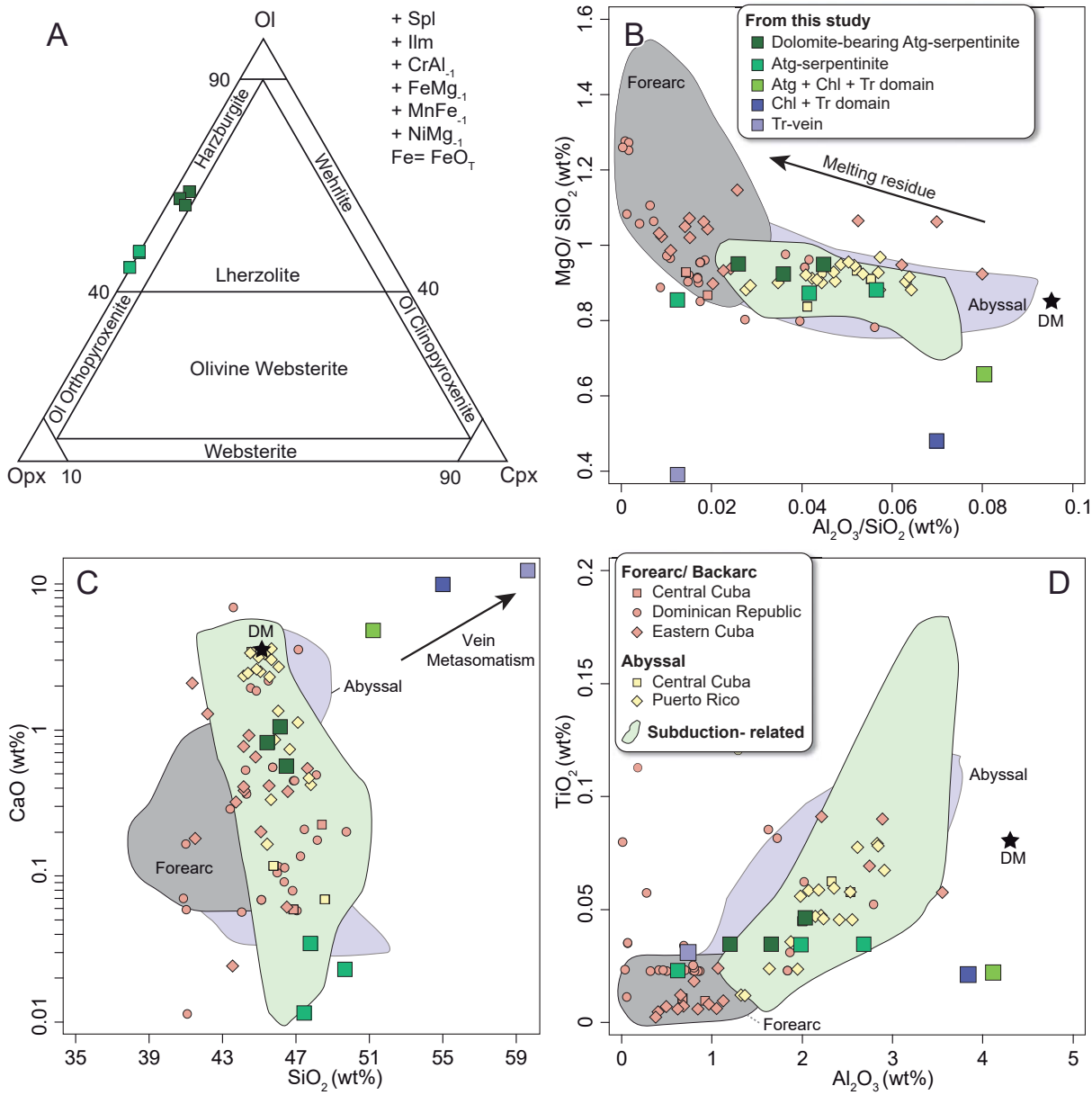

Figure. C6_11 *Whole-rock composition of dolomite-bearing Atg-serpentinite and Atg-serpentinite from the VCSM. A) Oxi-equivalent Ol-Cpx-Opx diagram. Note that dolomite-bearing Atg-serpentinite samples fall away from the Ol-Opx tie-line due to the presence of dolomite. B) MgO/SiO_2 vs. Al_2O_3/SiO_2 wt%. C) CaO wt% vs SiO_2 wt%. D) TiO_2 wt% vs. Al_2O_3 wt%. Pelo Malo serpentinites (samples from this study and Kanchev et al., 1978). Other peridotites and serpentinites for comparision: central Cuba (abyssal and forearc-related serpentinites from VCSM: Hattori and Guillot, 2007; Deschamps et al., 2012), eastern Cuba (backarc-related, Moa-Baracoa and forearc-related Mayarí-Cristal Massif, Marchesi et al., 2006; subduction-related serpentinites of Sierra del Convento and La Corea mélanges, Blanco et al., 2011c). Dominican Republic peridotites and serpentinites (forearc-related from Loma Caribe, Camú fault zone and Septentrional fault zone; subduction-related from Puerto Plata and Rio San Juan; Saumur et al., 2010; Escuder et al., 2014; Marchesi et al., 2016), Puerto Rico (abyssal-related from Monte del Estado, Marchesi et al., 2011), Alps (subduction-related from Erro Tobbio-Voltri Massif, Scambelluri and Tonarini, 2012; Cannaò et al., 2016), mid-ocean ridge (abyssal-related in solid line, Mid Atlantic Ridge and Hess Deep: Kodolányi et al., 2012; Mid Atlantic Ridge, Paulick et al., 2006; Southwest Indian Ridge, American Antartic Ridge, Central Indian Ridge, Pacific Antartic Ridge, Niu, 2004) and Mariana forearc (forearc-related in dotted line, Ishii et al., 1992; Savov et al., 2005; Kodolányi et al., 2012). Subduction-related rocks are in green fields. The composition of depleted mantle (DM) is from Salters and Stracke (2004). All data are in an anhydrous basis. Oxi-equivalent Ol-Cpx-Opx diagrams performed with CSpace software (Torres-Roldán et al., 2000).*

Table C6_6. *Whole-rock, trace element and isotopic composition of dolomite-bearing Atg-serpentinites and Atg-serpentinites of the VCSM.*

Sample	09-LV-11A	15-LV-1I	15-LV-1C	15-LV-1B	15-LV-1E	15-LV-1H	08-VC-31		
Rock type	Dolomite-bearing Atg-serpentinite			Atg-serpentinite			Atg + Chl + Tr	Chl + Tr	Tr vein
Major elements (wt%)									
SiO_2	39.28	40.21	39.89	43.26	41.6	41.21	46.42	51.97	57.65
TiO_2	0.04	0.03	0.03	0.02	0.03	0.03	0.02	0.02	0.03
Al_2O_3	1.76	1.04	1.43	0.54	1.73	2.33	3.73	3.63	0.72
Fe_2O_{3T}*	8.02	7.11	7.96	6.79	7.98	7.6	6.02	4.19	3.44
MnO	0.12	0.109	0.132	0.125	0.121	0.115	0.12	0.1	0.1
MgO	37.31	38.24	36.87	36.97	36.32	36.32	30.52	24.99	22.54
CaO	0.71	0.49	0.91	0.02	0.03	0.01	4.36	9.33	11.9
Na_2O	b.d.l	b.d.l	b.d.l	b.d.l	b.d.l	b.d.l	b.d.l	0.51	0.48
K_2O	b.d.l	b.d.l	b.d.l	b.d.l	b.d.l	b.d.l	0.02	0.14	0.15
P_2O_5	0.01	0.01	0.01	0.02	0.01	0.01	0.01	0.01	0.01
LOI	12.16	12.09	12.01	11.58	11.45	11.71	8.09	4.63	2.44
Total	99.41	99.33	99.24	99.33	99.27	99.34	99.31	99.52	99.46
Trace elements (ppm)									
Li	0.07	0.044	0.074	0.647	0.105	0.133	0.16	0.11	0.16
Be	0.03	0.016	0.023	0.015	0.019	0.02	0.69	1.11	2.46
Co	95.2	67.9	96.5	89.9	78.0	80.2	72.4	59.8	40.9
Ni	1887	1433	2037	1927	2033	2361	1489	1389	813
Zn	29.6	40.2	40.9	34.8	55.4	61.3	44.8	29.3	21.2
Cr	1946	2532	2259	1477	2371	2733	1610	1170	715
Cu	8.01	11.93	28.38	68.87	14.68	12.62	2.42	72.30	7.38
Rb	0.15	0.57	0.36	1.08	0.43	0.40	0.71	0.91	3.22
Sr	47.72	6.65	11.30	85.18	0.79	1.00	20.49	35.45	39.53
Y	0.83	0.43	0.93	2.00	0.73	0.73	1.37	1.32	4.32
Zr§	6.8	b.d.l	b.d.l	b.d.l	b.d.l	b.d.l	5.1	3.6	3.7
Nb	0.06	0.10	0.07	0.06	0.07	0.10	0.04	0.08	0.34
Cs	0.01	0.02	0.02	0.03	0.03	0.03	0.03	0.06	0.02
Ba	10.83	1.10	4.21	4.45	1.19	1.03	2.07	2.22	1.37
La	0.026	0.067	0.048	0.435	0.267	0.237	0.037	0.050	0.149
Ce	0.072	0.103	0.082	0.381	0.361	0.381	0.112	0.193	0.499
Pr	0.012	0.014	0.011	0.077	0.064	0.064	0.034	0.047	0.119
Nd	0.061	0.069	0.055	0.312	0.302	0.299	0.211	0.386	0.745
Sm	0.025	0.024	0.036	0.099	0.084	0.085	0.085	0.154	0.301
Eu	0.012	0.006	0.011	0.041	0.024	0.026	0.015	0.022	0.074
Gd	0.074	0.035	0.073	0.144	0.106	0.107	0.134	0.152	0.413
Tb	0.013	0.007	0.015	0.029	0.019	0.019	0.024	0.031	0.076
Dy	0.118	0.058	0.128	0.226	0.130	0.132	0.166	0.198	0.539
Ho	0.030	0.015	0.035	0.058	0.029	0.029	0.043	0.044	0.135
Er	0.095	0.043	0.105	0.177	0.082	0.085	0.118	0.119	0.417
Tm	0.018	0.008	0.020	0.029	0.015	0.015	0.024	0.023	0.083
Yb	0.102	0.057	0.150	0.195	0.105	0.100	0.124	0.131	0.555
Lu	0.017	0.011	0.026	0.029	0.019	0.020	0.021	0.022	0.108
Hf	0.010	0.148	0.129	0.045	0.114	0.187	b.d.l	0.059	0.121
Pb	0.328	0.733	0.603	2.364	0.721	0.423	0.248	0.502	0.473

*Fe_2O_{3T}= total iron as Fe_2O_3.

§Zr= Zr is analyzed by FRX.

b.d.l.=below detection limit.

Table C6_6. *Continued.*

Sample	09-LV-11A	15-LV-1I	15-LV-1C	15-LV-1B	15-LV-1E	15-LV-1H	08-VC-31		
Rock type	Dolomite-bearing Atg-serpentinite			Atg-serpentinite			Atg + Chl + Tr	Chl + Tr	Tr vein
Th	0.013	0.036	0.029	0.029	0.037	0.044	0.011	0.093	0.479
U	0.013	0.008	0.005	0.085	0.013	0.009	0.008	0.011	0.024
V	41.2	32.8	52.1	15.8	53.9	50.6	32.1	34.7	22.1
Ga	1.533	1.643	1.696	1.070	1.916	2.329	4.246	4.719	0.703
Mo	1.09	0.06	0.11	0.49	0.35	0.08	0.10	0.08	0.10
Sc	9.25	7.24	10.35	2.76	12.73	12.31	3.29	2.38	3.50
Sn	0.22	b.d.l	0.01	0.82	b.d.l	b.d.l	0.65	0.42	0.64
Tl	b.d.l	0.004	0.004	0.005	0.003	0.004	b.d.l	0.005	0.007
$^{87}Sr/^{86}Sr$	0.70456	-	-	-	-	-	-	0.70507	0.70502
$^{87}Sr/^{86}Sr$ (2s int. Error %)	0.002	-	-	-	-	-	-	0.003	0.002
$^{87}Sr/^{86}Sr_t$	0.70448	-	-	-	-	-	-	0.70494	0.70460
$^{147}Sm/^{144}Nd$	0.2601	-	-	-	-	-	-	0.2402	0.2445
$^{143}Nd/^{144}Nd$	0.51267	-	-	-	-	-	-	0.51262	0.51262
$^{143}Nd/^{144}Nd$ (2s int. Error %)	0.005	-	-	-	-	-	-	0.004	0.003
$^{143}Nd/^{144}Nd_t$	0.51246	-	-	-	-	-	-	0.51242	0.51240

Sr and Nd isotopic ratios are age corrected in all samples to eclogitic peak event in serpentinitic mélange in central Cuba, that indicates subduction at c. 125Ma (Garcia-Casco et al., 2002, 2006).

6.4.2. Trace elements and Nd-Sr isotope systematics

Chondrite-normalized Rare Earth Element (REE) patterns of dolomite-bearing Atg-serpentinites are depleted in light-REE (LREE) and progressively enriched in heavy-REE (HREE), with $La_N/Sm_N \approx 0.64$- 1.74 and $Sm_N/Lu_N \approx 0.23$- 0.36 (Fig. C6_12A). A negative Eu-anomaly is characteristic of dolomite-bearing Atg-serpentinite ($Eu/Eu^* \approx 0.63$- 0.85) (Fig. C6_12A). On the other hand, Atg-serpentinite is enriched in LREE ($La_N/Sm_N \approx 1.74$- 2.74; Fig. C6_12A) relative to dolomite bearing Atg-serpentinite. Atg-serpentinite has flat patterns and shows slightly negative to absent Eu-anomaly ($Eu/Eu^* \approx 0.78$-1.04). Blackwall domains Atg + Chl + Tr and Chl + Tr and the Tr-vein are depleted in LREE and enriched in MREE and HREE ($La_N/Sm_N \approx 0.26$; $Sm/Lu \approx 0.76$) with a marked negative Eu anomaly ($Eu/Eu^* \approx 0.50$; Fig. C6_12B).

In the silicate Earth-normalized diagram, the patterns of dolomite-bearing Atg-serpentinites, Atg-serpentinites and vein domains are similar, with positive anomalies in Cs, Th, U, Pb and Ti, and negative anomalies in Nb, Ce and Sm (Figs. C6_12C and C6_12D). Large Ion Litophile Elements (LILE) are highly enriched in blackwall domains and vein, in particular Cs and Rb, while Pb is almost constant in all samples (Fig. C6_12D). High Field Strength Elements (HFSE), such as Zr, Nb and Ti, have a narrow range of compositions in all rock types. Notably, Th, U, Nb, Ce and HREE concentrations decrease from the Tr-vein through the blackwall domains to the Atg-serpentinite host-rock. Serpeninites have restricted composition in HFSE elements with high contents of Ti and Yb comparable to abyssal and subducted serpentinites (Fig. C6_12E). The same relations appear in the La/Sm vs Lu diagram (Fig. C6_12F).

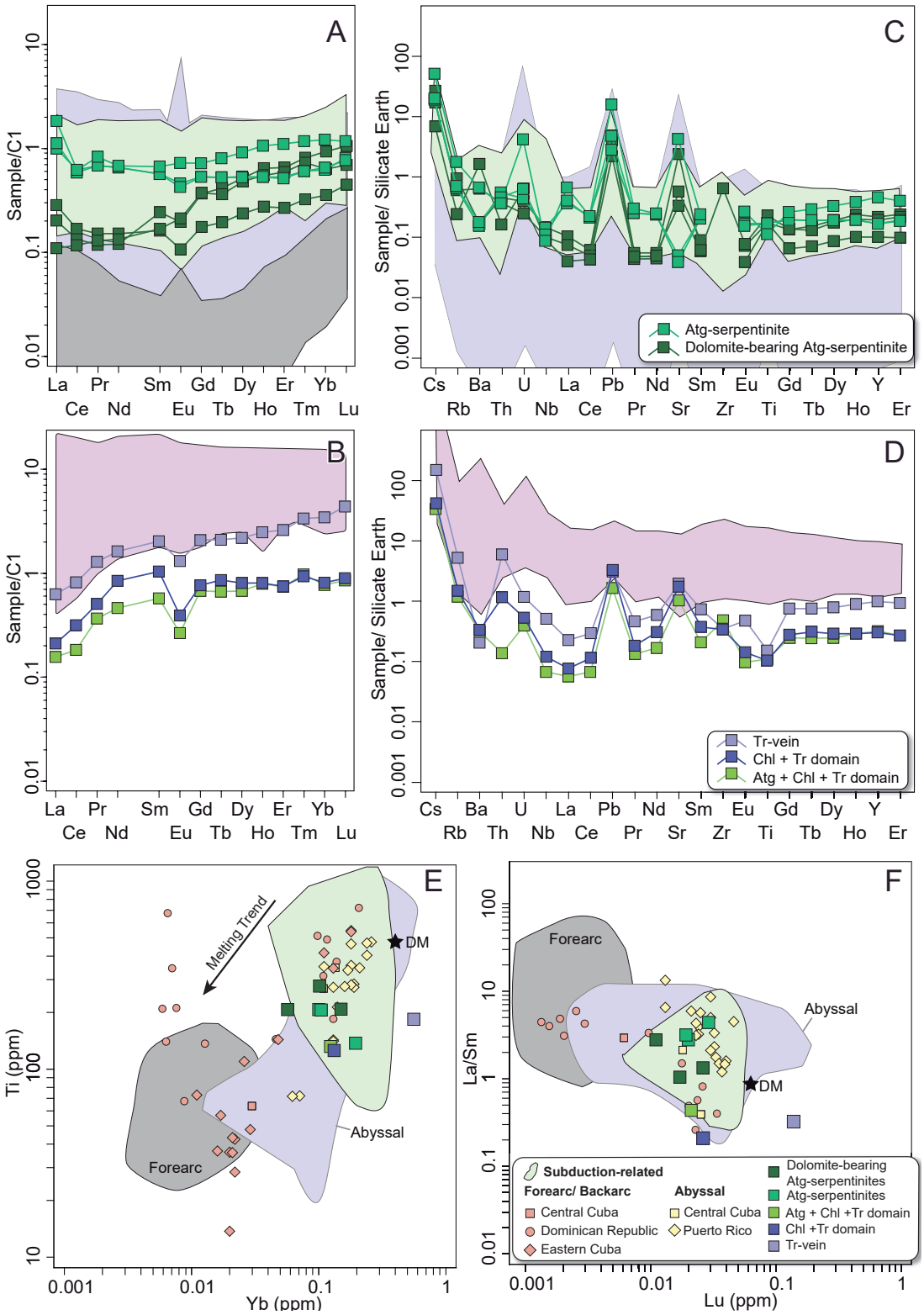

Figure. C6_12 *Trace element composition of dolomite-bearing Atg-serpentinite and Atg-serpentinite of the VCSM. A) and C) Chondrite-normalized REE patterns. B) and D) Trace element patterns normalized to silicate earth. E) Ti vs Yb diagram. F) La/Sm vs Lu diagram. Pale grey area/solid line, dark grey area/dotted line and green area define fields of abyssal, forearc and subduction-related peridotites and serpentinites, respectively (data sources as in Fig. C6_11). REE and trace element composition of metasomatic rinds are from Samaná Peninsula (Dominican Republic, Sorensen et al., 1997), Alps (Angiboust et al., 2014), Santa Catalina Island (Sorensen, 1988; Sorensen and Grossman, 1989; Penniston-Dorland et al., 2014), Franciscan Complex (Sorensen et al., 1997; Saha et al., 2005; Ukar and Cloos, 2013) and New Caledonia (Taetz et al., 2016). Bulk-Earth and CI-Chondrite normalizing values are after McDonough and Sun (1995).*

The Nd and Sr isotope systematic of dolomite-bearing Atg-serpentinite, blackwall domains and vein show quite restricted ranges of $^{143}Nd/^{144}Nd$ (0.51262-0.51267) and $^{87}Sr/^{86}Sr$ (0.70456-0.70507) compositions (Fig. C6_13 and Table C6_6). The low contents of Sr and Nd in these serpentinites make it difficult to obtain Nd and Sr isotopic ratios.

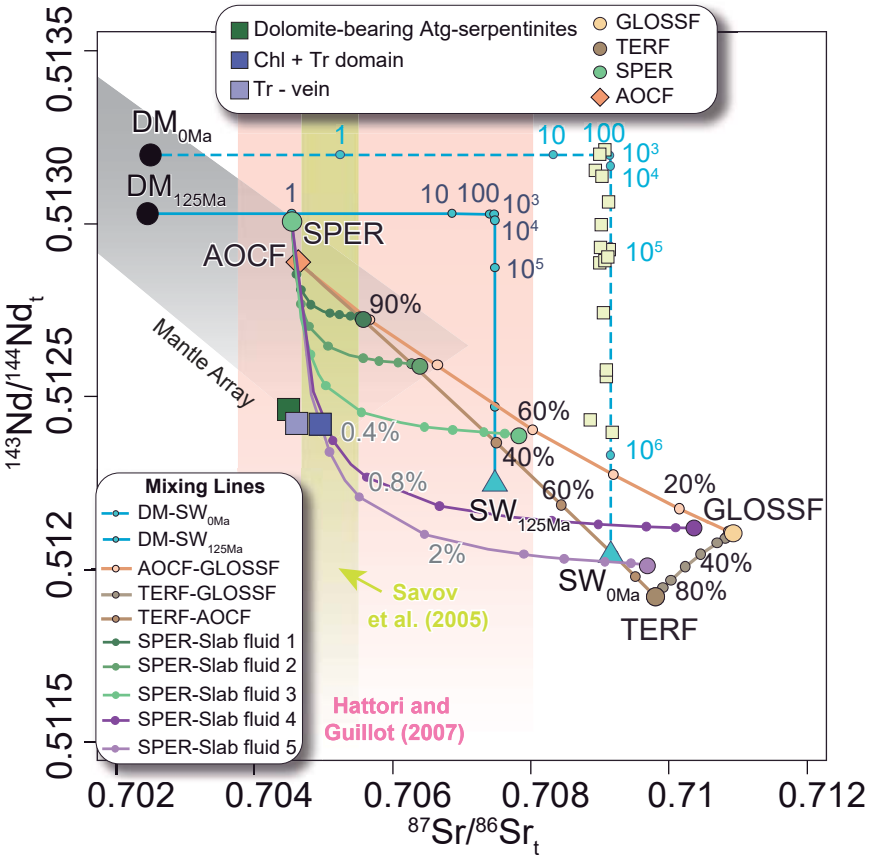

Figure. C6_13 *$^{143}Nd/^{144}Nd$ vs $^{87}Sr/^{86}Sr$ of dolomite-bearing Atg-serpentinite, Chl + Tr domain and Tr-vein. The endmember compositions used for the isotopic mixing line modelling are DM (Depleted Mantle), AOCF (altered oceanic crust fluid), GLOSSF (global subducting sediment fluid), TERF (terrigenous fluid), SW (seawater) and SPER (serpentinized peridotite). More information on endmembers source in chapter 3.10 and Table C3_3. Seawater-DM mixing line was calculated following the equations of McCulloch et al. (1981) at 125Ma and 0 Ma (actual seawater). AOCF-GLOSSF, TERF-GLOSSF, TERF-AOCF and SPER-slab fluid 1 to 5 were calculated using the equation of isotopic mixture from Faure and Mensing (2005). The endmember proportions of slab fluids are slab fluid 1: 90% AOCF, 3% GLOSSF, 7% TERF; slab fluid 2: 80% AOCF, 8% GLOSSF, 12% TERF; slab fluid 3: 60% AOCF, 24% GLOSSF, 16% TERF; slab fluid 4: 10% AOCF, 75% GLOSSF, 15% TERF; and slab fluid 5: 10% AOCF, 15% GLOSSF, 75% TERF. All mixing lines, endmembers and samples were age-corrected at c. 125 Ma eclogitic metamorphic peak event in VCSM that indicates pre-Aptian subduction (Garcia-Casco et al., 2002), with the exception of abyssal samples (small yellow squares by Delacour et al., 2008) and actual seawater endmember. Also indicated are the interval of $^{87}Sr/^{86}Sr$ in abyssal serpentinites from central Cuba (data after Hattori and Guillot, 2007) and the field of Mariana forearc serpentinites (from Savov et al., 2005). Note that samples from this study fall in the field of Hattori and Guillot (2007).*

6.5. P-T Conditions

Due to the lack of suitable thermobarometric equilibria in the serpentinites, metamorphic conditions were constrained by means of pseudosection approach, with the system CFMASH, using the calculated bulk composition of the Atg + Chl + Tr blackwall domain (see chapter 3.8). The selection of this blackwall domain for thermodynamic modelling is based on its lower thermodynamic variance, as compared to other types of rock studied. In an open system, the larger number of coexisting phases warrants a lesser number of freely variable chemical potentials at constant P-T (Korzhinskii, 1959); hence, the selected domain offers the possibility to constrain P-T conditions with higher precision (more details in chapter 3.8). In addition, this procedure is correct only if the Atg + Chl + Tr domain reached local equilibrium upon development, a scenario that may apply only to the final stage of development of the blackwall upon arrest of fluid infiltration. For all these reasons, the results should be considered approximate. The calculated isopleths corresponding to the observed Mg# in Tr and Chl do not crosscut in the P-T field of the corresponding assemblage, a likely consequence of unconstrained chemical potentials of components, variable fluid composition, the lack of equilibrium, the limitations of the solution models of minerals considered and/or the simple system considered (lacking Fe^{3+}, for example). However, it is possible to tentatively propose P-T conditions of vein formation. We used the subducting oceanic crust geotherm and P-T path of associated eclogite blocks (*c.* 20 kbar and c. 570ºC; Garcia-Casco et al., 2002) surrounded by Atg-serpentinite mantles (Auzende et al., 2002) in the VCSM, as well as pseudosection modelling of Atg + Chl + Tr domain as guides for P-T conditions. This results on vein structure formation at *c.* 450ºC and *c.* 10 kbar (Fig. C6_14).

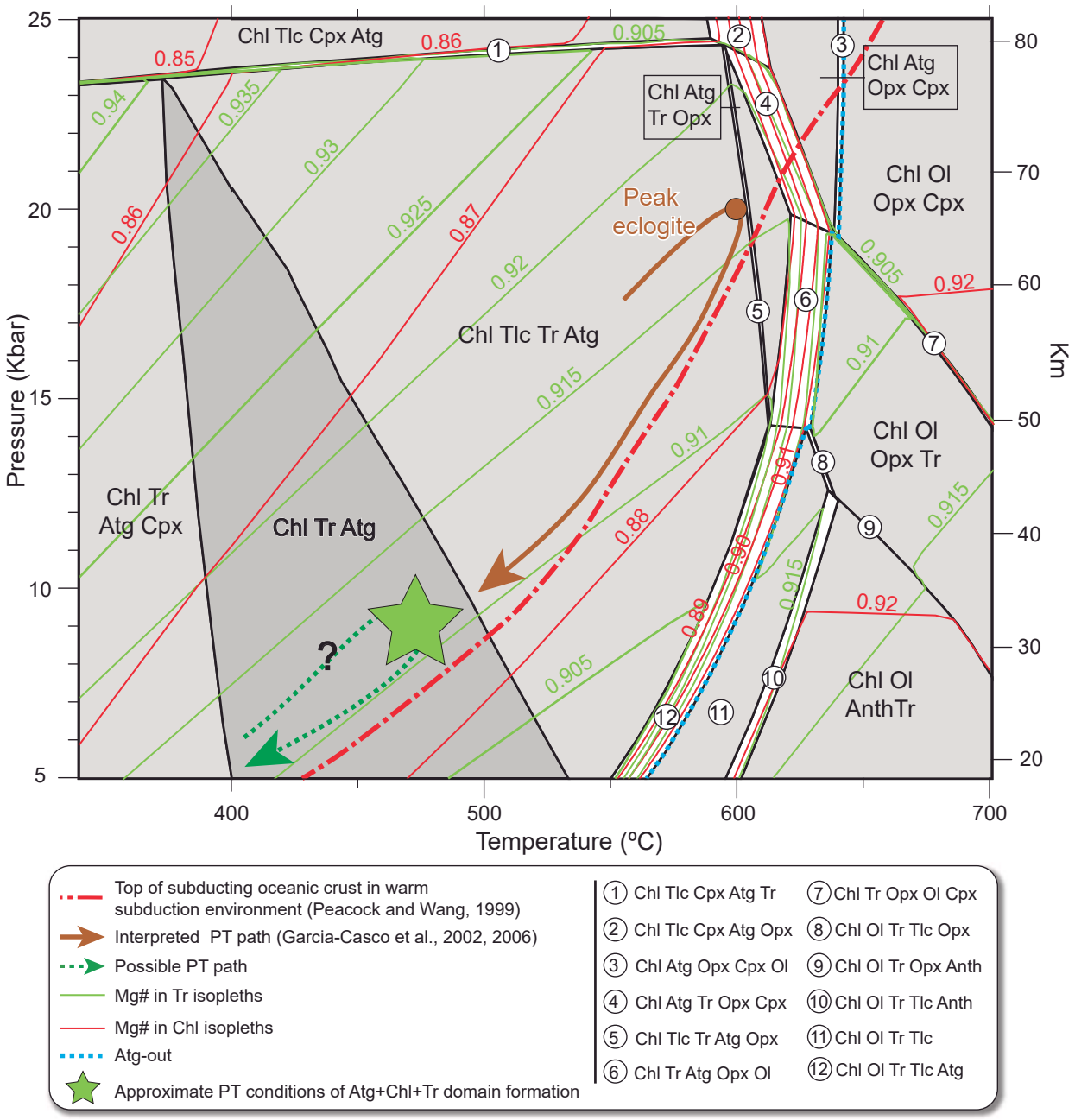

Figure. C6_14 *Calculated P-T equilibrium phase diagram (pseudosection) for the Atg + Chl + Tr metasomatic domain in the system CFMASH (4.13 CaO wt%, 5.49 FeO wt%, 29.13 MgO wt%, 9.31 Al_2O_3 wt%, 41.00 SiO_2 wt%, H_2O in excess). Brown solid line represents P-T path of an eclogite block from the VCSM (Garcia-Casco et al., 2002; 2006); small brown spot represents peak conditions. Red dashed red line represents the top of subducting oceanic crust in a warm subduction environment (Peacock and Wang, 1999). Blue dotted line indicates limit of antigorite stability field. Green star is the approximate PT conditions of Atg + Chl + Tr. Phases: Chl, Chlorite; Atg, Antigorite; Tr, Tremolite; Tlc, Talc; Ol, Olivine; Cpx, Clinopyroxene; Opx, Orthopyroxene; Anth, Anthophyllite. The highest variance (F= 4) is represented by the darkest grey field assemblages and the lowest variance (F=2) by white fields. More details in chapter 3.8.*

6.6. Discussion of exotic ultramafic block of theVCSM

6.6.1. Nature of the dolomite-bearing Atg-serpentinite and Atg-serpentinite protolith

The dolomite-bearing Atg-serpentinites and Atg-serpentinites are completely serpentinized (100% antigorite). Hence, element enrichment/depletion is related to alteration/refertilization processes that modify the protolith composition. Major element compositions in dolomite-bearing and Atg-serpentinites may have been mobilized by late serpentinitzation processes such as MgO loss and/or SiO_2 enrichment in an abyssal/subduction zone setting (e.g. Niu, 2004; Malvoisin, 2015). The CaO enrichment in the dolomite-bearing Atg-serpentinites may be traced to two possibilities: A) former presence of clinopyroxene in the primary mineral assemblage; B) CaO + H_2O-CO_2 enriched fluid that interacted with the peridotite. The interpenetrating textures between dolomite and antigorite demonstrate that dolomite and antigorite were formed during serpentinization (Fig. C6_3A; see Martin et al., 2016). The coexistence of antigorite + dolomite constrains the composition of the infiltrating fluid to $X_{CO2} < 0.2$; higher values of X_{CO2} would have formed talc/olivine-magnesite assemblages (cf., Trommsdorff and Evans, 1997). Thus, fluid slightly enriched in CO_2 was present during serpentinization. However, Atg-serpentinites do not display dolomite/calcite. Therefore, if such serpentinizing fluid carried Ca, the Atg-serpentinites should contain dolomite in their mineral assemblage (note that they crop out in the same area as dolomite-bearing Atg-serpentinites). As a result, the most likely option is to assume a difference in the primary mineral assemblage: clinopyroxene absent and clinopyroxene-bearing protoliths that were transformed into dolomite-bearing rocks after reaction with an infiltrating H_2O-CO_2 fluid. Unfortunately, it is not possible to estimate the amount of clinopyroxene of the peridotite protolith due to the uncertain CO_2 amount added to the dolomite-bearing Atg-serpentinites.

The fluid mobile elements (such as Cs, Ba, Pb, U and Sr; except two samples depleted in Ba and Sr) evidence positive anomalies in dolomite-bearing and Atg-serpentinites which indicate the presence of a fluid-enriched protolith (Fig. C6_12C). Because HFSE and REE are considered immobile, they are used to track magmatic processes (You et al., 1996; Kogiso et al., 1997). In figures C6_12E and C6_12F, dolomite-bearing Atg-serpentinites and Atg-serpentinites display compositions that plot in the abyssal and subduction-related field, having fertile compositions. Deschamps et al. (2013) used the term subduction-related serpentinites to encompass serpentinites formed in a subduction zone and exhumed in accretionary complexes or suture zones. This group of serpentinites include protoliths of subducted oceanic peridotites of abyssal origin and extended continental margin peridotites exhumed and hydrated during rifting. Significantly, the Pelo Malo Atg-serpentinites have major and trace element compositions similar to this group of serpentinites (Figs. C6_11 and C6_12; note high Al_2O_3/SiO_2 and TiO_2 and HREE, HFSE and LILE patterns). The LREE enrichment compositions displayed in Atg-serpentinites may be attributed to post melting refertilization of basaltic melts (as described by other authors, e.g. Niu, 2004; Marchesi et al., 2016 and references therein).

In view of the above, we propose that the Pelo Malo Atg-serpentinite megablock formed after serpentinization of subducted peridotite. This is in agreement with calculated pressures of *c.* 10 kbar for blackwall formation (Fig. C6_14) and the facts that: a) serpentinites are strongly sheared, b) the tremolite vein and blackwalls crosscut the Atg-serpentinite foliation, and c) the veins are not present in nearby low-T brecciated serpentinite that envelopes the Pelo Malo megablock. In this context, infiltration of a H_2O-CO_2 fluid during subduction into peridotite protoliths with relatively higher amounts of CaO triggered the formation of dolomite-bearing Atg-serpentinites, while Atg-serpentinites formed from CaO-poor protoliths. The temperature of transformation was *c.* 450 ºC (at *c.* 10 kbar; Fig. C6_14), and any case higher than 350 ºC, which marks the consumption of lizardite (Evans, 2004). Indeed, similar rocks occur in high pressure subduction-related mélanges and tectonic units from the Caribbean region (Cuba and Dominican Republic, Saumur et al., 2010; Escuder et al., 2014; Cuba, Blanco-Quintero et al., 2011d; Cárdenas-Párraga et al., 2017) and the Alps (e.g. Scambelluri et al., 2001a and 2001b; Scambelluri and Tonarini, 2012; Cannaò et al., 2016). Yet, serpentinization previous to subduction in the oceanic environment is also a potential process that may have affected the Pelo Malo protoliths.

6.6.2. Origin of the serpentinizing- and vein-forming fluid

Pelo Malo protolith has been modified by serpentinization processes that could have taken place in abyssal and subduction zone settings. Here we evaluate both possibilities.

Seawater penetrates into the thin oceanic crust along transform and normal faults, promoting serpentinization in the oceanic environment (Cannat, 1993; Miranda and Dilek, 2010). The effects of seawater infiltration during abyssal serpentinization drastically change Sr and, to a lesser extent, Nd isotopic composition as a function of the water/rock ratio (cf. McCulloch et al., 1981), as is commonly observed in mid-ocean ridge peridotites (e.g., Delacour et al., 2008; see Fig. C6_13). The Nd and Sr isotopic compositions of the vein, metasomatic domains and dolomite-bearing Atg-serpentinite from Pelo Malo megablock display the same isotopic signature (Fig. C6_13), implying that the same type of fluid reservoir interacted with all types of rock. Their composition does not correspond to the isotopic composition of depleted mantle (Fig. C6_13), nor does the seawater serpentinization account for the observed depletion of $^{143}Nd/^{144}Nd$ and $^{87}Sr/^{86}Sr$ enrichment. Note that, because of the high Sr content in seawater and the relatively high mobility of Sr in rocks, even quite a limited interaction with seawater is enough to reset the Sr isotope value to that of seawater. Thus, given that the Nd isotopic ratio of the Pelo Malo serpentinite, blackwall and tremolite vein are well below 125 Ma seawater values, seawater is not the main agent associated with serpentinization of the studied samples (Fig. C6_13). It does, nonetheless, indicate a contribution of different isotopic reservoirs. Fluids evolved from subducted sediment, altered oceanic crust and likely seawater serpentinized mantle, or a mixture thereof, are feasible agents of serpentinization/carbonation (c.f. Bebout, 1991, 2007, 2014; Bebout and Barton, 2002; King et al., 2006 and 2007; Penniston-Dorland et al., 2012; Bebout and Penniston-Dorland, 2016). Actual examples

of serpentinites affected by subduction-derived fluids are located in the Mariana forearc (yellow field by Savov et al., 2005; Fig. C6_13). The $^{87}Sr/^{86}Sr$ compositions of Mariana forearc serpentinites display compositions similar to the dolomite-bearing Atg-serpentinites and vein domains, thereby pointing to interaction with the slab-derived fluid.

Three fluid endmembers were selected for isotopic modeling (Fig. C6_13): altered oceanic crust fluid (AOCF; Kelley et al., 2003), global subducting sediment (GLOSSF; Plank, 2014) and terrigenous fluid (TERF; unaltered crustal sediments from Poli and Schmidt, 2002 and Rudnick and Gao, 2003; see chapter 3.10 for supplementary information on elemental and isotopic ratios of these reservoirs). A more extensive discussion of endmember reservoirs can be found in chapter 4.5.2 regarding the serpentinitic matrix of the VCSM. The slab fluid is made up of different proportions of AOCF, GLOSSF and TERF (Fig. C6_13). The different slab fluids may interact with a previous seawater serpentinized peridotite (SPER; Fig. C6_13). The peridotite may be completely or partially serpentinized, with a wide range of water/rock ratios (in this case the $^{87}Sr/^{86}Sr$ ratio was selected for a water/rock ratio close to 1). Slab fluids that contain a high component of AOCF and TERF describe the isotopic signature of these rocks and vein domains better (slab fluid 3 and 5 in Fig. C6_13). Only a small input of slab fluid (*c.* 0.4 %) is needed to account for the isotopic composition of dolomite-bearing Atg-serpentinites and vein domains. Some authors (e.g. Cannaó et al., 2016 and references therein) evidence the effect of slab fluid masking the primary isotopic signature of seawater serpentinized peridotite/depleted mantle source.

Given the mixed isotopic nature of the slab fluid, we conclude that Pelo Malo serpentinites formed by infiltration of fluids evolved from the slab as a combination of AOCF, GLOSSF and TERF. Furthermore, similar isotopic and trace element composition (Figs. C6_12 and C6_13) of vein domains, Tr-vein and dolomite-bearing Atg-serpentinites suggest that a very similar fluid formed the vein, most likely during the same infiltration event. We envisage a LILE-enriched slab fluid produced by slab devolatilization (c.f. Bebout and Penniston-Dorland, 2016 and references therein) at depth in the subduction environment, liberated in the subduction channel/slab and transferred upwards along the channel/slab.

Our proposal of a subduction zone slab derived fluid fluxing through subducted Pelo Malo peridotite comes to complement the proposition by Hattori and Guillot (2007) of merely sedimentary contribution to lizardite-antigorite-bearing serpentinites from the central Cuba mélange (based on elemental and Sr isotope systematics). The presence of vein structure in high temperature Atg-serpentinites evidences a path for fluids in a subduction channel mélange acting as a fluid channelway (e.g., Zack and John, 2007; Angiboust et al., 2012 and 2014; Bebout and Penniston-Dorland, 2016).

6.6.3. Blackwall formation model

Deformation of Pelo Malo peridotite during serpentinization most likely favoured a porous flow of fluid that was locally channelled along fractures (c.f. Plümper et al., 2017). The chemical and isotopic composition of the Tr-vein and associated blackwall offer insight into the nature of the infiltrating fluids. The fluid contained dissolved Si, Ca, Al, Mg and Fe, for all these elements form part of the tremolite vein and adjacent blackwall. The reaction of such a fluid with the Ca-poor (dolomite-free) Atg-serpentinite wallrock formed two distinct metasomatic domains at the blackwall. The mineral assemblages and composition of antigorite and chlorite (with progressive compositional changes across the composite vein structure, Figs. C6_2, C6_4 to C6_7 and C6_15) of these two domains clearly point to changes in bulk rock composition of the wallrock upon the progress of metasomatic reactions. A model of domain formation in the CaO-FeO-MgO-Al_2O_3-SiO_2-H_2O system is illustrated in the MASH phase-diagram of Fig. C6_15A. This diagram is constructed in molar proportions of the indicated species after projection from tremolite (average) and exchange vectors as indicated in the figure. Note that this projection implies that all the depicted phase assemblages contain tremolite. The projection is therefore not valid for the Atg-serpentinite wallrock, but this is only a minor violation of thermodynamic rules compared with unconstrained complexities of the natural process. Among these, the unknown composition of the fluid is the most important. Henceforth, the phase relations involving the Si-Al-Mg-Fe-Ca fluid illustrated in Fig. C6_15A are only schematic.

We first consider a “static” model for blackwall formation in which the composition of the Si-Al-Mg-Fe-Ca fluid is constant upon reaction progress. In the MASH diagram of Fig. C6_15A, this scenario is illustrated by the line that joins the bulk composition of Atg-serpentinite (in the Atg-Chl tie-line, close to Atg) with the external Si-Al-Mg-Fe-Ca fluid. The topology illustrated in the diagram shows that along this line, i.e., as a function of rock/fluid ratio, two assemblages are possible — Chl + Tr + Fluid and Atg + Chl +Tr + Fluid, respectively at lower and higher rock/fluid ratios. This conceptual model fits with observations, as both theoretical assemblages correspond to the observed metasomatic domains, Chl + Tr adjacent to the vein and Atg + Chl + Tr closer to the wallrock. Furthermore, for mass-balance (i.e., reaction progress consumes fluid) and geometrical (distance from fluid source) reasons, lower rock/fluid ratios are expected in the former. In other words, metasomatic zones may form as a function of the amount of infiltrated fluid by means of a reaction of the form:

Antigorite + Fluid → Chlorite + Tremolite

with the inner zone extensively infiltrated up to the point of reaching total consumption of antigorite, as observed (except for some relic grains; Fig. C6_4). Even if this “static” model of a fluid of constant composition qualitatively describes the formation of two metasomatic zones adjacent to the vein, it is probably not correct because the progress of metasomatic reactions should change fluid composition.

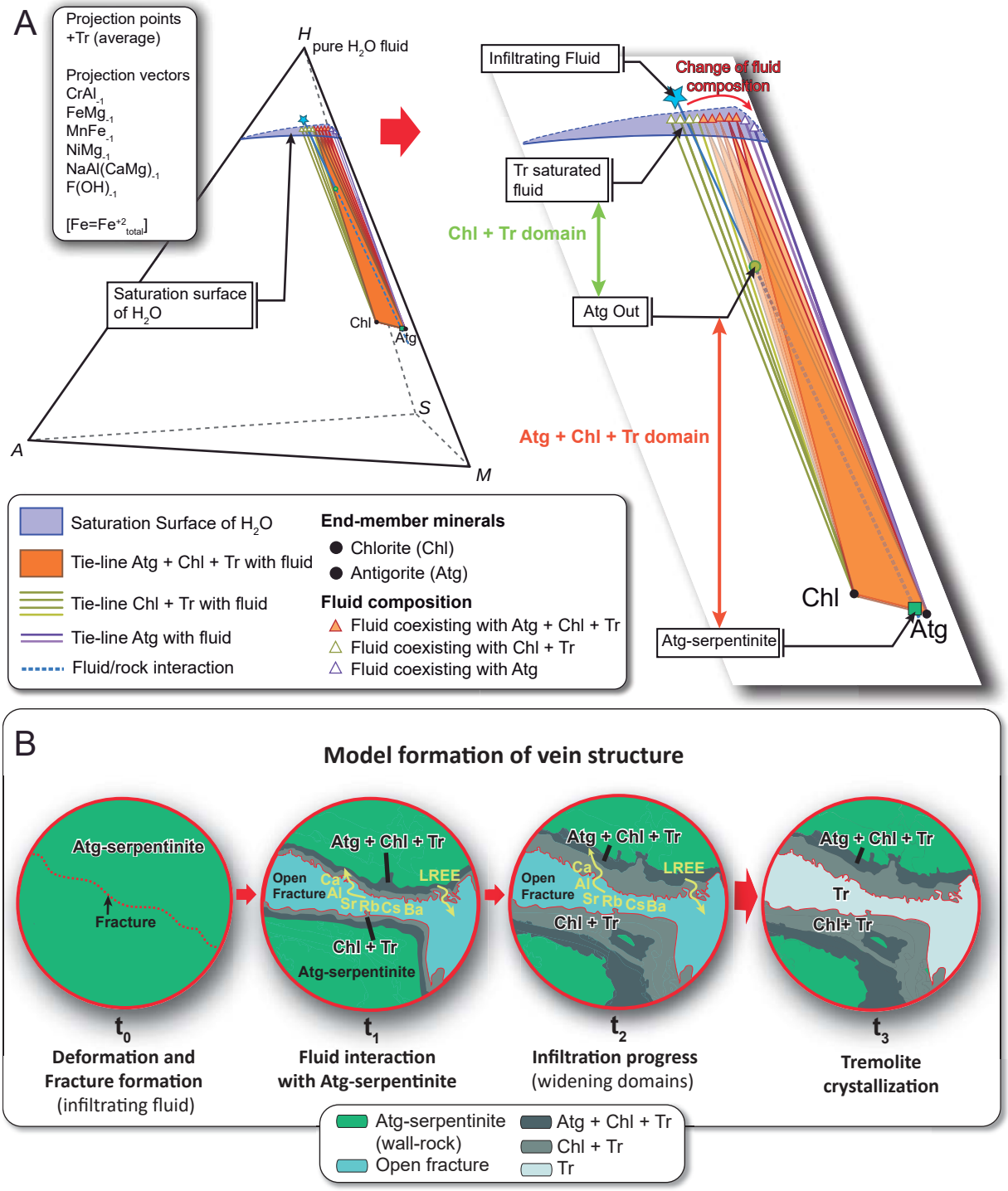

Figure. C6_15 *Model of blackwall assemblage formation. A) Phase diagram in MASH system showing phase relations and metasomatic zone development. All relations involving the composition of the fluid are hypothetical. The diagram was projected from Tr (average) and along the exchange vectors indicated; Fe is considered as Fe^{2+}total (more details of phase diagram in chapter 3.7). Green tie-lines and orange tie-triangles correspond to the fields of Chl + Tr + Fluid and Atg + Chl + Tr + Fluid, respectively. Note that infiltration of fluid (blue star) in Atg-serpentinites (Atg + Chl, green square) would drive the bulk composition towards the fluid, with the development of the indicated assemblages as a function of rock/fluid ratio. Reaction progress triggers decrease in Al (as indicated by triangles of fluid composition) and Ca (not shown) in the fluid. B) Vein formation events. t_0: deformation creates fractures that trigger focused fluid flow; t_1 and t_2: progressive formation of the Atg + Chl + Tr and Chl + Tr domains; t_3: tremolite crystallization in the open fracture and migration of remaining fluid out of the system. See text for details.*

A more "dynamic" scenario is described as follows. Upon onset of fluid infiltration, a large amount of fluid infiltrated into the region adjacent to the fracture (t_1, Fig. C6_15B), triggering large compositional changes in the system up to the point of reaching total consumption of antigorite by means of a reaction such as:

Antigorite + Fluid 1 → Chlorite + Tremolite + Fluid 2.

This represents formation of the metasomatic domain Chl + Tr. Because part of Al dissolved in the fluid is incorporated in newly formed chlorite in this domain, the reaction drives the composition of the remaining fluid (Fluid 2) towards Al-poorer composition. In the MASH diagram, this translates into the displacement of the composition of the remaining fluid away from the A apex within the fluid saturation surface (Fig. C6_15A, green triangles: fluid coexisting with Chl + Tr domain). For similar arguments involving Ca and tremolite, Fluid 2 would be poorer in Ca (not shown). Upon infiltration further into the wallrock of such a remaining Ca-Al-poorer fluid, fluid-consuming metasomatic reactions such as:

Antigorite + Fluid 2 → Chlorite + Tremolite + Fluid 3

would form an outer rim of Atg + Chl + Tr, as expected owing to topological relations (Fig. C6_15A). This process would drive the composition of fluid towards still poorer Ca-Al-compositions (Fluid 3, Fig. C6_15A orange triangles: fluid coexisting with Atg + Chl + Tr). As long as Fluid 3 is saturated in Atg + Chl + Tr, this assemblage does not depend on the rock/fluid ratio. However, for mass-balance and geometrical reasons a higher rock/fluid ratio is expected in the Chl + Tr domain (i.e., system composition would be closer to the Atg-Chl tie-line in Fig. C6_15A), as described in the "static" model above. The progressive decrease in Ca and Al in the fluid upon reaction progress would eventually reach compositions in equilibrium with antigorite and chlorite only (i.e., with Atg-serpentinite at the reaction front), preventing further formation of tremolite and arresting metasomatic transformations irrespective of the rock/fluid ratio (though lower ratios are expected).

The "static" and "dynamic" scenarios described above involve a single instantaneous batch of infiltrated fluid. Yet in an even more dynamic scenario, continuous progress of infiltration of the external Ca-Fe-Mg-Al-Si fluid would trigger progressive consumption of antigorite from the earlier formed Atg + Chl +Tr domain and displacement of the reaction front away the vein, in all cases causing widening of the two metasomatic domains until cessation of fluid infiltration (t_2 in Fig. C6_15B). Finally, tremolite precipitation formed the vein, while the remaining fluid infiltrated the rock or flowed upwards along fractures in the subduction channel (t_3, in Fig. C6_15B)

6.6.4. Exchange of matter

In the described model of blackwall formation, a continuous fluid phase is distributed from the wallrock to the vein via interconnected grain boundaries and brittle (micro-) fractures (c.f. Plümper et al., 2017). This transport allows not only the transfer of matter from the vein fluid towards the wallrock by means of fluid advection, but also the potential transfer of matter from the blackwall to the vein fluid by means of diffusion in the pore fluid.

Figure C6_16 shows the composition of the metasomatic zones normalized to Atg-serpentinite wallrock. As would be expected, metasomatic domain Atg + Chl + Tr is less influenced by the fluid than the inner and more intensely fluxed Chl + Tr domain. Both domains, however, are strongly enriched in CaO and Sr, as a consequence of tremolite crystallization. Subtler enrichments are observed in Al_2O_3 (chlorite formation), while FeO and MgO are slightly depleted. LILE show variable behaviour; while Rb, Cs and Ba are slightly enriched, U and Pb are depleted (Th is uncertain). A similar contrasted behaviour is observed in HFSE, with enrichment in Y and depletion in Ti, Hf and Nb (the latter observed in one domain). LREE are depleted (La, Ce, Pr), while MREE and HREE are moderately to slightly enriched (except Lu, which appears unchanged, and Eu, which shows modest depletion). This contrasting behaviour indicates that the fluid was rich in LILE and perhaps also in REE, but in any case it further enriched in LREE and some HFSE after blackwall formation (Fig. C6_15B), pointing to both advection of matter from fluid to the wallrock and pore fluid diffusion of the latter elements towards the vein fluid. The contrasted behaviour of elements is controlled, mostly, by the compatible/incompatible behaviour in blackwall minerals and fluid at the temperature and pressure conditions of blackwall formation and fluid composition. Available experimental data for element fractionation and transport in hydrous fluids (Adam et al., 2014) indicate that LREE in amphibole are incompatible and tend to be fractionated in the fluid, while LILE are compatible and are incorporated into amphibole, in agreement with our observations and inferences.

The observed concentration of elements in the blackwall contrasts with the strong enrichments in LILE, HFSE and REE observed in metasomatic blackwalls associated with blueschist and eclogite in subduction zone environments around the world, which typically contain HFSE-rich minerals (e.g. rutile, titanite, apatite) not present in the studied metasomatic domains (Figs. C6_12B and C6_12D; e.g. Sorensen, 1988; Sorensen et al., 1997; Sorensen and Grossman, 1989; Saha et al., 2005; John et al., 2008; Penniston-Dorland et al., 2012; Ukar and Cloos, 2013; Angiboust et al., 2014; Penniston-Dorland et al., 2014; Taetz et al., 2016). These distinctive characteristics are explained by the contrasted source of fluids and chemical composition of wallrocks. In blueschist and eclogite fluids derived from nearby subducted sediments and/or altered oceanic crust interacted with subducted metabasaltic rocks. Very strong enrichment in fluid-mobile lithophile elements in these fluids trigger their fractionation into newly formed minerals of metasomatic rinds. Again, the composition of the studied blackwall and vein poorer in LILE, HFSE and REE, would indicate a slab fluid mixture as the main factor responsible for serpentinization and metasomatism.

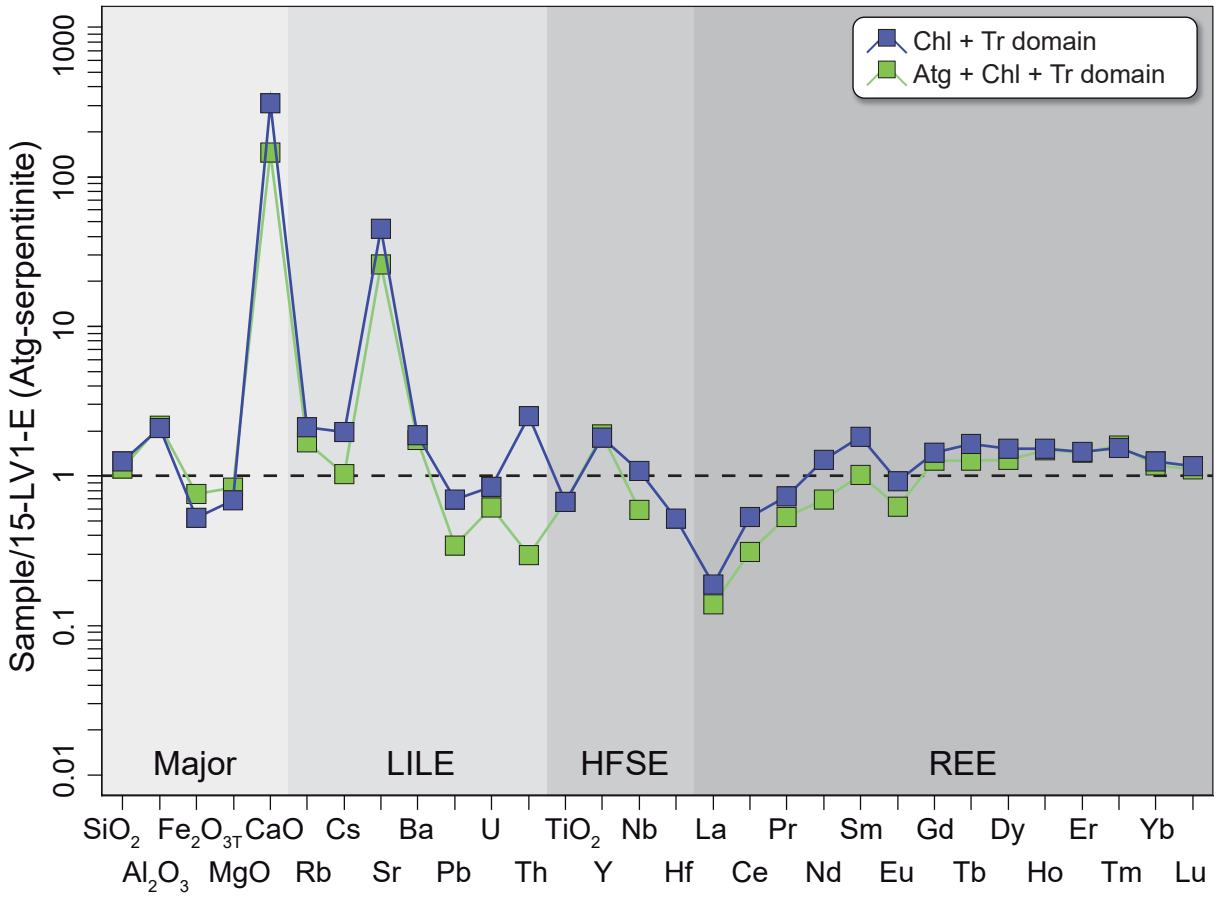

Figure. C6_16 *Major, LILE, HFSE and REE composition of Atg + Chl + Tr and Chl + Tr domains normalized to wallrock Atg-serpentinite (sample:15-LV-1E).*

Chapter 7

General Discussion

7.1. Petrogenesis of serpentinitic matrix and mafic crust rocks of the VCSM

7.2. Ocean-floor metamorphism and supra-subduction zone metasomatism in VCSM

7.3. Geodynamic setting evolution of VCSM

7. General discussion

This PhD thesis is focused on the serpentinitic matrix, mafic crust and exotic blocks of ultramafic sub-oceanic lithospheric mantle of the Villa Clara serpentinitic mélange in central Cuba. The results obtained from field relations, mineral assemblages, mineral chemistry, whole-rock composition and isotope systematics allowed us to track slab-mantle interactions and melting and post-melting metasomatic and alteration processes that took place during the evolution from mid-ocean ridge to subduction zone settings. These observations and inferences can be conceptualized within the framework of the petrogenesis of ophiolites and the geodynamic evolution of the Caribbean realm.

The general discussion of this PhD thesis is constituted by three main parts: 1) Petrogenesis of serpentinitic matrix and mafic crust of the VCSM, 2) Post melting processes of ultramafic and mafic rocks and 3) Geodynamic evolution of Villa Clara serpentinitic mélange in the context of the Caribbean realm evolution.

7.1. Petrogenesis of serpentinitic matrix and mafic crust rocks of the VCSM

The sub-volcanic rocks of tholeiitic affinity of the VCSM may be traced to melts generated after partial melting of a depleted mantle source that corresponds to the protolith of serpentinized peridotite and serpentinite.

The serpentinitic matrix of the VCSM displays a heterogeneous composition that allows two different groups of peridotites to be defined (A and B). The groups are genetically related (see full explanation in chapter 4.5.3). Group A displays a fertile composition (e.g., low Cr# in Cr-spinel, Al-rich pyroxenes and depleted mantle REE pattern) similar to fertile MORB-like abyssal/fracture zone peridotites (Figs. C4_6 to C4_8; C4_11 to C4_13 and C4_15). In contrast, group B shows a refractory composition (e.g., high Cr# in Cr-spinel, low Al in pyroxenes and depleted REE pattern) that fits with forearc peridotites (Figs. C4_6 to C4_8; C4_11 to C4_13 and C4_15). These compositions evidence heterogeneous partial melting process: Group A constitutes the first melting step of a depleted mantle source, while group B resulted from re-melting group A peridotites (chapter 4.5.3). The sub-volcanic unit of the mafic crust also has a heterogeneous composition: Group 1 is basaltic in composition and displays a typical forearc basalt signature, whereas group 2 is basaltic-andesite in composition, displaying an evolved island arc tholeiite signature. Both groups are related to a subduction zone setting (see chapter 5.4.1.2).

All melting models converge in 4-8% of partial melting of a depleted mantle in group A peridotites and 14-22% melting in group B peridotites (chapter 4.5.3). Here we evaluate two melting models in order to genetically link the protolith of serpentinitic matrix and mafic crust: A) three-step melting in the spinel and garnet facies in the first step, and B) two-step melting in the spinel facies. These models were discussed independently for ultramafic and mafic rocks in the respective chapters 4.5.3 and 5.4.1.3.

Case X melting explains group A peridotite compositions in the second step of melting and group B peridotite composition in the third step of melting (Fig. C7_1A). The P-T diagram of figure C7_2A shows that the first step of case X melting (1-light blue star in Fig. C7_2A) should take place at *c.* 1500 ºC in a mid-ocean ridge (MOR) geotherm (1 Ma MOR-geotherm; Dumitru, 1991), in order to allow adiabatic melting in the garnet lherzolite stability field, and the second step of melting in the spinel lherzolite field (2-light blue star in Fig. C7_2A). The second step of melting accounts for group A peridotite compositions upon crossing the dry solidus lherzolite (Fig. C7_1A). However, as expected, the resulting melts do not fit with the primitive composition of the forearc basalts of the sub-volcanic unit (Fig.C7_1A). A third step of melting, related to subduction initiation, would be needed to account for group B peridotites (Fig. C7_1A). Nonetheless, the melts modelled fail to explain composition of the sub-volcanic unit. Hence, case X modelling is rejected.

On the other hand, two step case Y model at the spinel-peridotite facies (Fig. C7_1B) allows for explaining the compositions of group A peridotites in the first step (*c.* 4-8% melting of depleted spinel lherzolite) and group B peridotite compositions in the second step (*c.* 14-22% total melting, first 4% melting and second 10-18% melting, Fig. C7_1B). Moreover, sub-volcanic unit compositions can be accounted for by this model in the second step (*c.* 8-10% total melting, 4% melting in the first step and 4-6% in the second one, Fig. C7_1B). Hence, this model allows one to conclude that group B peridotites and the sub-volcanic unit are genetically related: group B harzburgites are the residue of forearc basalts. Further, evidence such as marked LREE enrichment in group B peridotites indicates melt/rock interaction with basaltic liquid, which is most likely represented by the forearc basalts. This model is illustrated in the P-T diagram of Fig. C7_2A.

In our two step case Y model, the second step of melting affected group A harzburgite. This implies that the P-T phase diagram of lherzolite composition (Fig. C7_2A) is not suitable for describing the process, as long as changes in bulk composition affect the P-T distribution of stable mineral assemblages. For the harzburgitic composition used to calculate the mineral assemblages of Fig. C7_2B, a plagioclase-bearing field is not stable and the spinel-harzburgite field expands. For the harzburgitic composition with only a small quantity of calcium, all Ca is diluted in orthopyroxene and clinopyroxene is not formed (see more details of pseudosection calculation in chapter 3.1.5). Group A peridotites (2-dark blue star, Fig. C7_2B) cooled down isobarically after melt extraction in a mid-ocean ridge because mantle flows laterally away from the spreading center, crossing colder isotherms (green line in Fig. C7_2B). Later, upon subduction initiation, peridotites are exhumed to shallower levels in the upper plate mantle, decreasing pressure and increasing temperature as asthenospheric mantle flows to fill the gap left by the downgoing plate (see below). Subduction initiation triggers devolatilization of the downgoing slab, decreasing the solidus of upper plate harzburgite A (HZ in Fig. C7_2B). The intersection of hydrated group A harzburgite solidus along the subduction initiation geotherm triggers a second melting event in the field spinel-harzburgite facies, forming group B harzburgite (residue, 4-red star in Fig.C7_2B) and group 1 sub-volcanic unit (melt). Sequential melt extraction (open system behaviour) cannot be modelled in Fig. C7_2B, but it would yield higher melting

degrees in the residue (group B peridotites), while group 1 (sub-volcanic unit) would represent the first melt to be extracted (lower degrees of melting).

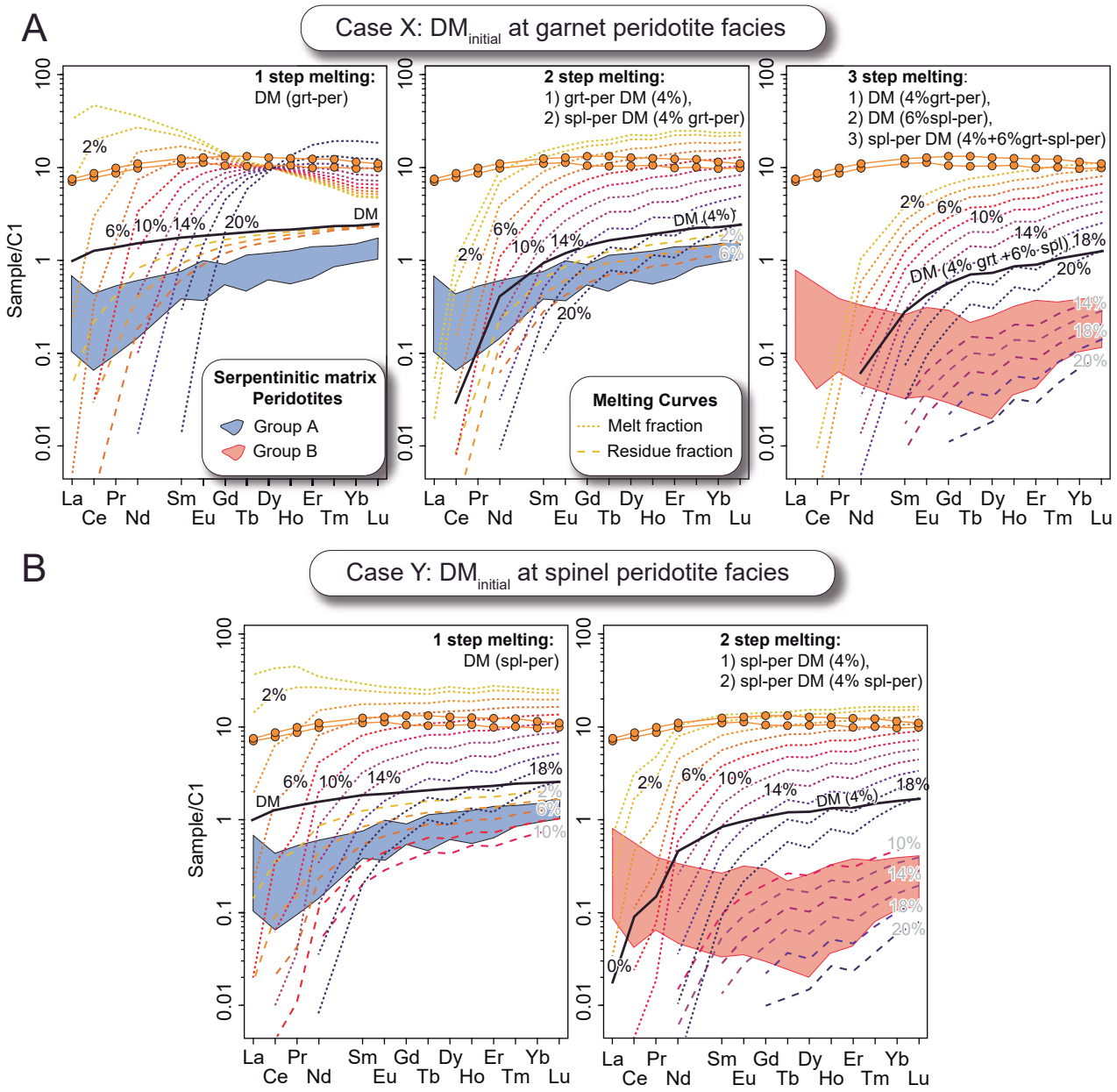

Figure. C7_1 *Non-modal fractional melting modelling of serpentinitic matrix and sub-volcanic unit from VCSM. Chondrite-normalized REE patterns of primitive melts of sub-volcanic unit and fields of peridotites of the serpentinitic matrix of the VCSM. A) Initial melting at garnet facies (case X). B) Initial melting at spinel facies (case Y). Dashed lines are melting curves of solid residues and melt. Source of melting is depleted mantle (DM) composition from Salters and Stracke (2004). Melting modelling calculated using equation of Shaw (2000). Source and melting modes and partition coefficients are as in chapter 3.9 and Table C3_2. Percentages indicate degree of melting.*

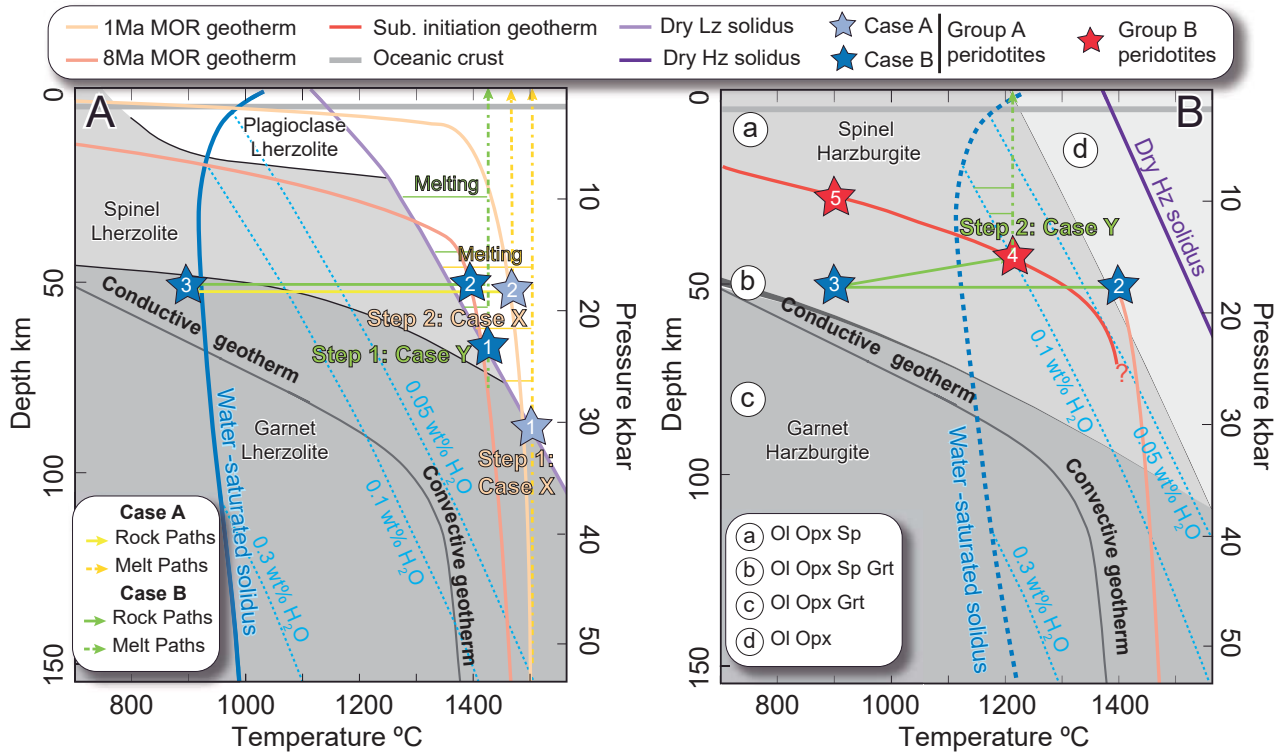

Figure. C7_2 *P-T Phase diagrams of peridotites in the system SiO_2-MgO-CaO-FeO-Al_2O_3. A) Lherzolite phase diagram. B) Harzburgite phase diagram. Stars indicate peridotite residues, light blue stars are case X melting modelling, dark blue stars case Y melting modelling, and red stars indicate group B peridotites. Numbers inside the stars indicate order of formation. Dashed arrows indicate melt path upon extraction from source peridotite. Solid arrows indicate melting residue paths. Fields of plagioclase, spinel and garnet lherzolite in diagram A and conductive/convective geotherm from Gill (2010). Dry and hydrated lherzolite solidus (dry Lz solidus) from Green (2015). Mid-ocean ridge geotherms (1 Ma and 8 Ma) from Dumitru (1991). P-T diagram B was calculated by means of Theriak-Domino with a bulk composition of 39.64 Si, 7 Al, 51.69 Mg, 0.06 Ca, 5.58 Fe and 1.1 H (molar units, see chapter 3.8 for details of pseudosection calculation). Dry harzburgite solidus from MaalØe (2004). Hydrated harzburgite solidus from Green (2015) is modified in consonance with dry harzburgite solidus. Theoretical subduction initiation geotherm is displayed with a slope lower than 8 Ma MOR geotherm. See text for further explanation.*

7.2. Ocean-floor metamorphism and supra-subduction zone metasomatism in VCSM

In this section we will discuss the effects of post-melting ocean-floor metamorphism and supra-subduction zone metasomatism in the chemical composition of the serpentinitic matrix and mafic crust of the VCSM using trace elements, stable and radiogenic isotopes. Moreover, subduction-related ultramafic blocks of VCSM are considered in order to decipher the influence of fluids in the subduction channel-supra and subduction zone contexts.

In slow spreading ridges and fracture zones, a limited amount of oceanic crust is formed and, during amagmatic episodes, extensional tectonic forces favour the formation of oceanic core complexes (Cannat, 1993; Tucholke et al., 1998; Ildefonse et al., 2007; Escartín et al., 2017 and references therein). These complexes expose portions of the lower crust and upper mantle due to the effects of detachment faults, which favour, in turn, fluid flow and fluid/rock interaction in the oceanic crust and shallow mantle. Ocean floor metamorphism near ridges involves cooling and hydration that transform primary metamorphic/magmatic minerals in the mantle and crust (olivine, pyroxenes, plagioclase, spinel) into low to medium temperature metamorphic assemblages that include prehnite, chlorite, amphibole, serpentine group minerals, talc, epidote, etc. Evidence of such transformations occurs in the mafic crust of the VCSM (chapter 5.2.1 and 5.4.1.1). The sub-volcanic unit records changes in mineral composition, such as plagioclase, which become more albitic (from bytownite to albite) and the formation of new minerals, such as epidote (mostly, after plagioclase), amphibole (after pyroxenes) with retrograde zoning (pargasite cores and magnesio-hornblende/tremolite rims) and prehnite, which typically occurs in late veins that crosscut primary and medium-low metamorphic mineral assemblages (chapter 5.2). Taken together, these assemblages and textures indicate a retrograde path and hydration at relatively low P from amphibolite to greenschists facies (chapters 5.4.1.1 and 5.4.2). High fluid/rock ratios are inferred from samples completely transformed into amphibolite. The plutonic unit, on the other hand, displays similar changes in mineral composition but they are less intensely transformed, with only local small areas that record ocean-floor metamorphism as a likely consequence of lower fluid/rock ratios (chapter 5.3). The effects of seawater are clearly indicated by the chlorine-rich composition in the higher-T cores of amphibole (chapter 5.2.2.2). In addition, Nd and Sr isotopes can be used to quantitatively track the effects of seawater. The isotopic signature of the sub-volcanic unit attest to $^{143}Nd/^{144}Nd$ depletion and high values of $^{87}Sr/^{86}Sr$, which support seawater contribution to low fluid/rock ratios (c. <1-10, Fig. C7_4).

These inferences cannot be readily applied to serpentinites, for the serpentinization events probably likely took place at different settings, including a low-P ocean-floor and higher-P subduction channel. In fact, the isotopic signature of the serpentinitic matrix does not display typical signatures of peridotites serpentinized by seawater (e.g. Delacour et al., 2008; Fig. C4_16A chapter 4.4.4), clearly pointing to additional reservoirs and complexities in the serpentinization process. Partial melting of the ultramafic rocks of the VCSM in a

forearc setting suggests supra-subduction zone metasomatism as a potential process that affected these rocks. Various source reservoirs are implied in a subduction zone setting, including slab devolatilization (e.g. Rüpke et al., 2004 and references therein), which is controlled by the thermal state of the subduction zone (e.g. Syracuse et al., 2010 and references therein), the age and velocity of subduction, different types and amounts of lithologies, and key devolatilization reactions (e.g. Atg-out, phengite-out, chlorite-out, and amphibole-out). Diverse authors have studied slab fluids and water recycling in subduction zones (Schmidt and Poli, 1998 and 2003; Wallmann, 2001; Rüpke et al., 2002 and 2004; Jarrard, 2003; Zack and John, 2007; Cannaò et al., 2016; Bebout and Penniston-Dorland, 2016 and references therein). Three main fluid sources are responsible for slab signature: hydrated mantle, igneous crust and sedimentary rocks. Hacker (2008) estimated that major fluid release takes place at shallow levels where pore fluid is expelled while the amount of evolved fluid decreases with depth (Fig. C7_3).

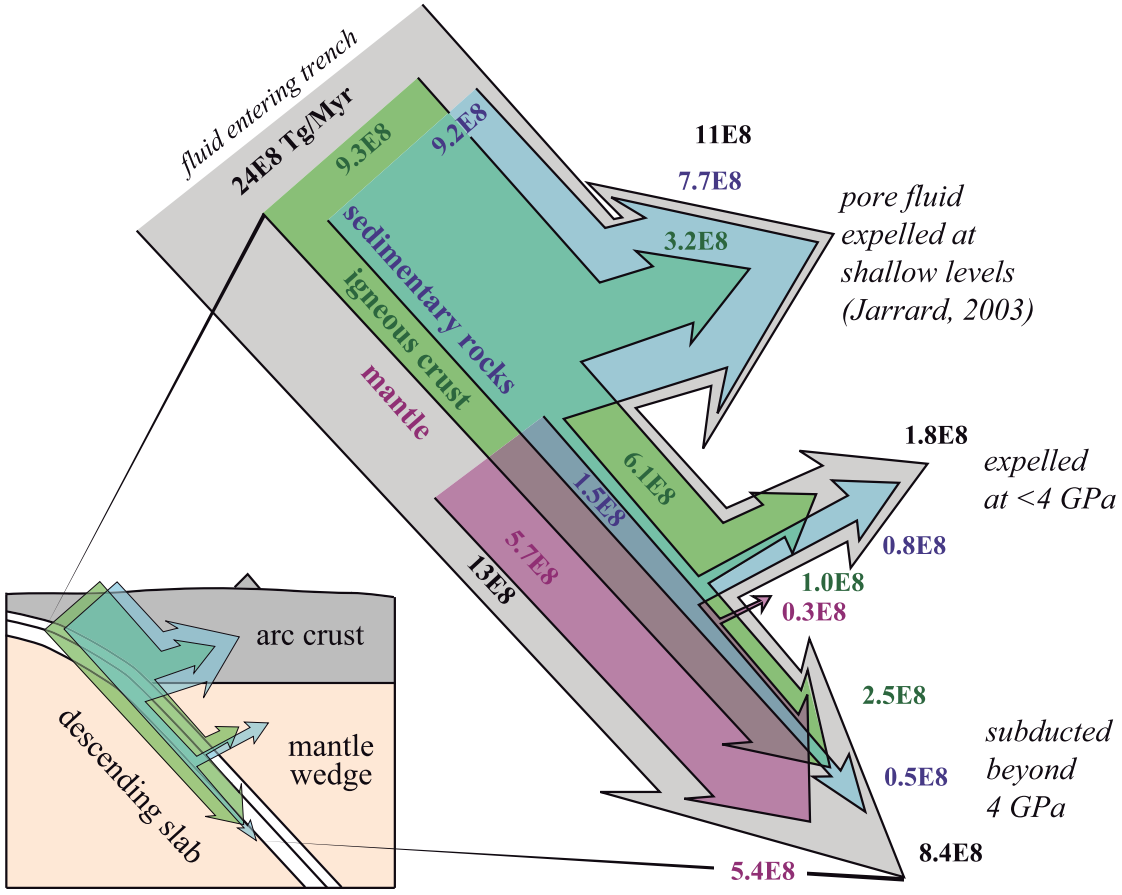

Figure. C7_3 *Fluid release from shallow forearc to arc depths of oceanic lithosphere from Hacker (2008). Numbers are fluid flux of different lithologies during subduction given in Tg/Ma.*

Self-organization of flow patterns in the subduction channel favours physical and geochemical mixture of slab fluids (Baitsch-Ghirardello et al., 2014; Bebout and Penniston-Dorland, 2016). In chapters 4.5.2 and 6.6.2 we concluded that the main types of rock involved in the generation of fluid at the subduction environment are altered oceanic crust (AOC; Kelley et al., 2003), global subducting sediment (GLOSS: pelagic, altered sediments, see Plank, 2014) and terrigenous sediment (TER from unaltered crustal

sediments; Poli and Schmidt, 2002; Rudnick and Gao, 2003), which mix in variable extent to form a heterogeneous slab fluid reservoir. This reservoir interacted with already slightly/completely serpentinized mantle (seawater serpentinization), resulting in the resetting of the primary signature of serpentinized mantle. Enrichments in LILE, U and Pb and similar isotopic signature in exotic ultramafic blocks (Pelo Malo Atg-serpentinite megablock) and the serpentinitic matrix evidence supra-subduction zone metasomatism (chapters 4.5.1 and 6) and indicate that the serpentinitic matrix and exotic ultramafic blocks were mixed together at the subduction channel (i.e., subduction channel mélange; chapter 6.6.2). Slab fluids that interacted with the ultramafic blocks are represented by tremolite veins; associated metasomatic domains with the same isotopic compositions as the Atg-serpentinites and serpentinitic matrix (Fig C7_4), however evidence variable proportions of AOCF-GLOSSF-TERF in the supra-subduction metasomatic agent. Vein and metasomatic domains in Atg-serpentinites represent discrete fluid paths in the subduction channel mélange (e.g. Peacock, 2001; Gerya et al., 2002; Van Keken et al., 2011).

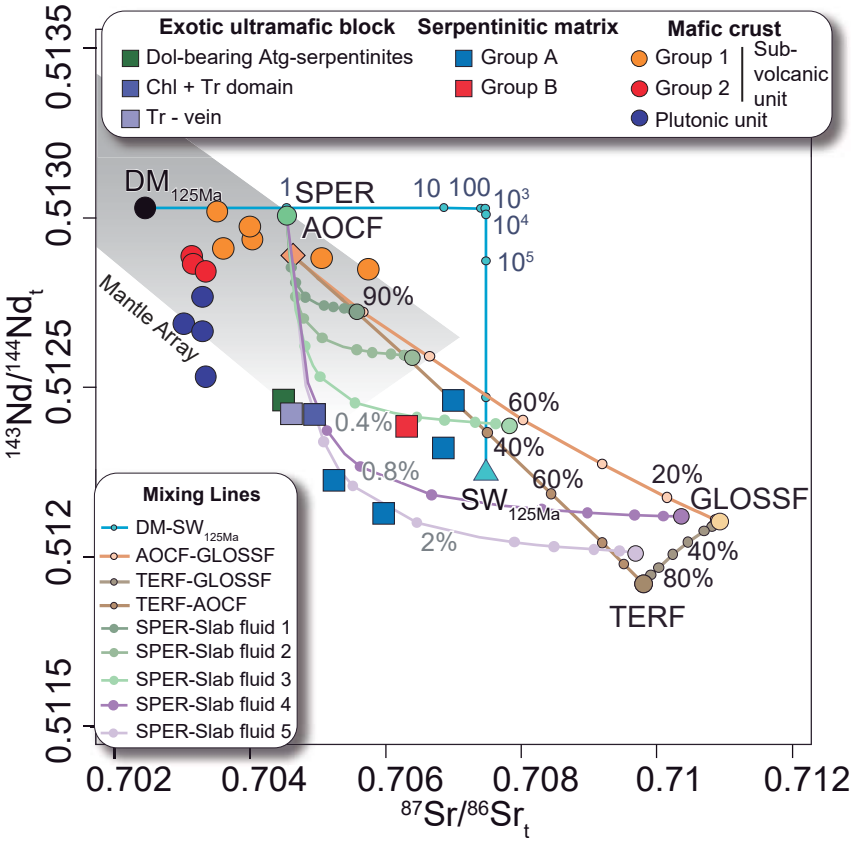

Figure. C7_4 *$^{143}Nd/^{144}Nd_t$ vs $^{87}Sr/^{86}Sr_t$ of the serpentinitic matrix, mafic crust and exotic ultramafic block and vein domains of the VCSM. Endmember compositions used for the isotopic mixing lines modelling are DM (Depleted Mantle), AOCF (altered oceanic crust fluid), GLOSSF (global subducting sediment fluid), TERF (terrigenous fluid), SW (seawater) and SPER (serpentinized peridotite). For more information on endmembers see chapter 3.10 and Table C3_3. Seawater-DM mixing line was calculated following the equations of McCulloch et al. (1981) at 125 Ma (pre-Aptian subduction Garcia-Casco et al., 2002). AOCF-GLOSSF, TERF-GLOSSF, TERF-AOCF and SPER-Slab fluids 1 to 5 were calculated using the equation of isotopic mixture of Faure and Mensing (2005). The endmember proportions of slab fluids as in Fig. C6_13 in chapter 6.4.2.*

7.3. Geodynamic setting evolution of VCSM: from fracture zone to subduction zone setting

Above, we have discussed the petrogenesis of the serpentinitic matrix and mafic crust of the mélange and the post melting processes (ocean floor metamorphism and supra-subduction zone metasomatism) that affected primary bulk compositions. Here we offer a time-integrated model that combines petrogenetic processes in the context of the geodynamic evolution of the Caribbean realm. This model puts together mineral assemblages and whole-rock geochemical and isotopic data from all units studied in this PhD.

The formation of the Caribbean realm started upon the breakup of Pangea in Jurassic times and the development of the Proto-Caribbean basin in between the Americas (e.g. Pindell and Kennan, 2009 and references therein). During the late Jurassic and Early Cretaceous, this basin was most likely separated from the Pacific (Farallon) plate by the Inter-American transform (Fig. C7_5A e.g., Pindell et al., 2012). The transform fault juxtaposed older (colder lithosphere) vs younger (hotter lithosphere) as a consequence of the activity of the Proto-Caribbean ridge. Partial melting degrees indicated by the geochemical composition of fracture zone peridotites are similar to abyssal peridotites (Figs. C4_11 to C4_13; e.g. Warren, 2016). The geochemical composition of group A peridotites, the calculated 4-8% melting of a depleted mantle source (chapter 7.1; Fig. C7_1B) for this type of rock, and serpentinization and high $^{87}Sr/^{86}Sr$ values (see SPER endmember in Fig C7_6A) may be related to the development of Proto-Caribbean oceanic lithosphere in a fracture zone. A similar scenario was envisaged by Cárdenas-Párraga et al. (2017) for the eastern Cuba Sierra del Convento serpentinitic mélange.

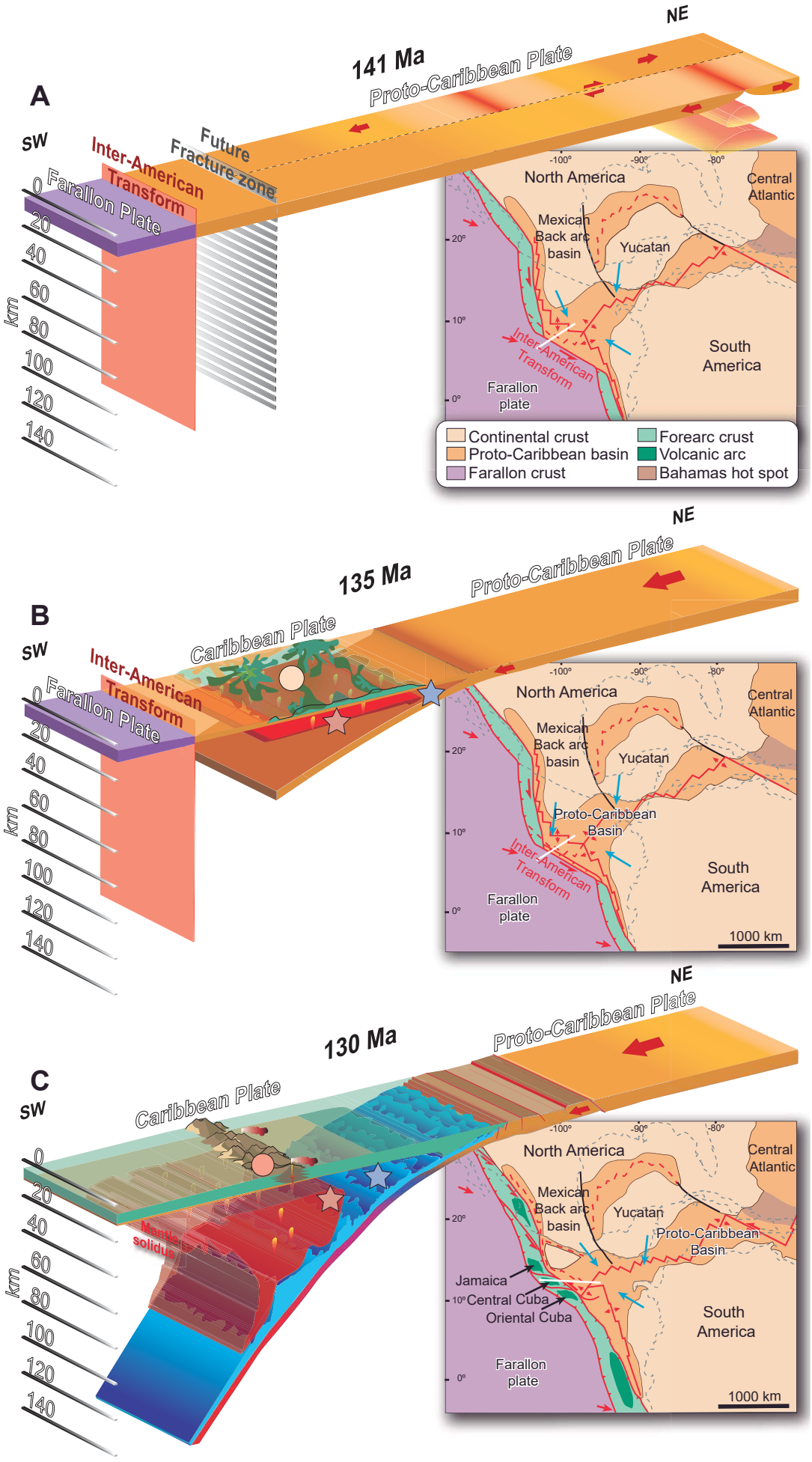
A
141 Ma
NE
SW
Proto-Caribbean Plate
Future
Fracture zone
Inter-American
Transform
Farallon Plate
km
0
20
40
60
80
100
120
140
North America
Central
Atlantic
Mexican
Back arc
basin
Yucatan
South
America
Inter-American
Transform
Farallon
plate
Continental crust
Proto-Caribbean basin
Farallon crust
Forearc crust
Volcanic arc
Bahamas hot spot
B
135 Ma
NE
SW
Proto-Caribbean Plate
Caribbean Plate
Inter-American
Transform
Farallon Plate
Proto-Caribbean
Basin
1000 km
C
130 Ma
NE
SW
Proto-Caribbean Plate
Caribbean Plate
Mantle
solidus
Jamaica
Central Cuba
Oriental Cuba

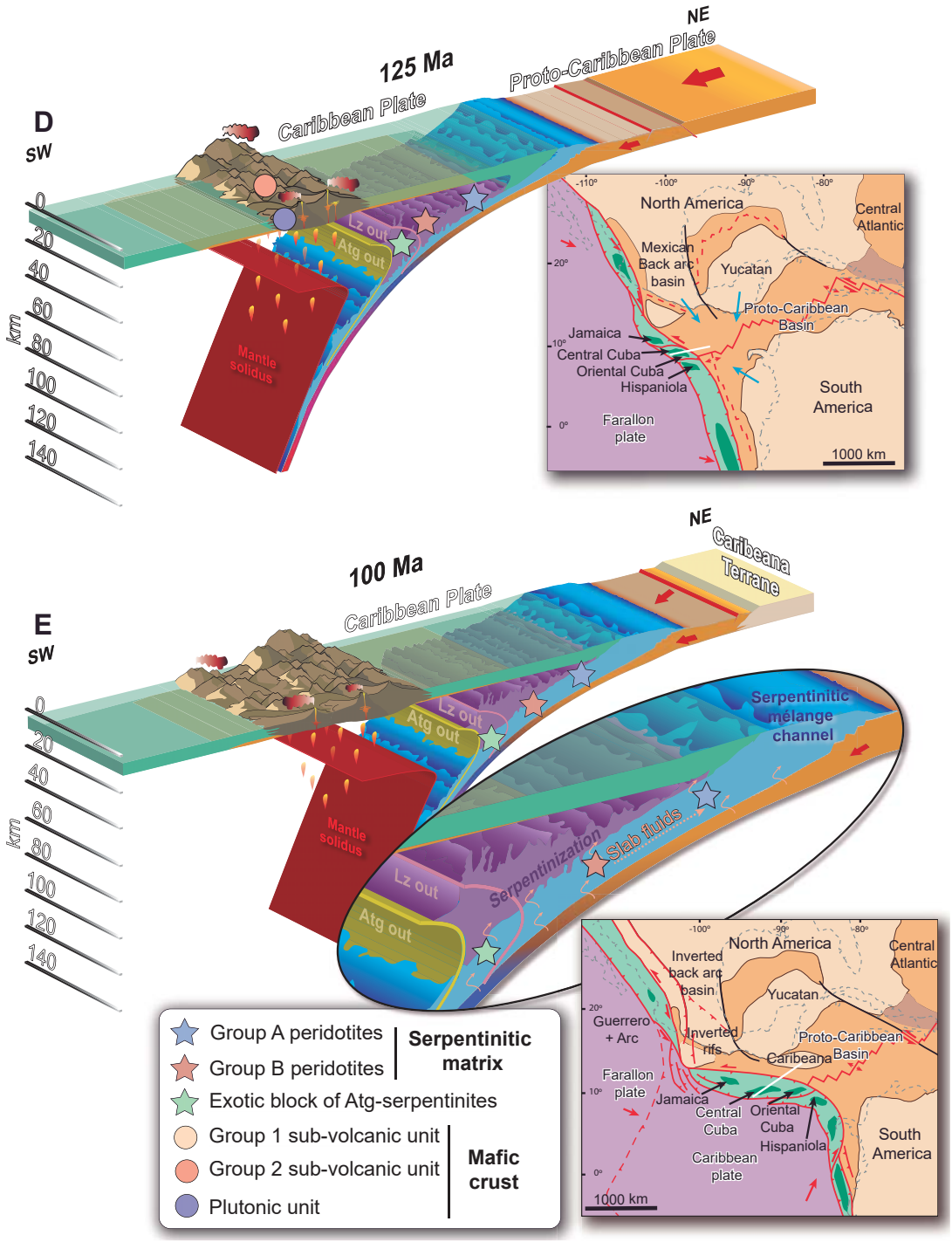

Figure C7_5 *Geodynamic model and palaeogeographic reconstructions of the Caribbean domain addressing the formation of the VCSM, based on Pindell and Kennan (2009) and Pindell et al. (2012). A) At 141 Ma, initial stage of development of the Proto-Caribbean and the Inter-American transform between Farallon plate and Proto-Caribbean basin. Group A peridotites (blue star) constitute the residue of partial melting of depleted mantle which formed the Proto-Caribbean lithosphere in a ridge-fracture zone setting. B) At 135 Ma, subduction initiation of the Proto-Caribbean under the Farallon plate and creation of a forearc. Extension in the forearc triggered re-melting of group A peridotites in the mantle wedge and formation of group B peridotites (red star) and group 1-FAB of the mafic crust (yellow circle). Seawater infiltrated shortly after intrusion (during cooling) and triggered ocean-floor metamorphism in the sub-volcanic unit. C) At 130 Ma, subsequent melting in the mantle at sub-arc depths triggered the formation of a volcanic arc and the formation of group 2-IAT of the mafic crust (red circle). Also at this stage, ocean-floor metamorphism affected these rocks and a subduction channel mélange (shades of blue) started to form as trench retreat progressed towards the Northeast. D) At 125 Ma, shift of the subduction zone towards the Northeast expanded the volcanic arc. The subduction channel expanded and slab fluids metasomatized the*

mantle wedge, creating a wide serpentinized region (purple area). Slab fluids/melts influenced the formation of the plutonic section of the mafic crust at this stage. E) At 100 Ma, widening of the subduction channel reached group A and B peridotites, forming the serpentinitic matrix of the mélange in a relatively shallow region within the lizardite stability field. At this time slab-derived fluids produced by devolatilization reactions were channelized along the subduction channel matrix and the mantle wedge, while exotic blocks of Atg-serpentinites were serpentinized in the antigorite stability field. Partial melting field, mantle solidus and subduction channel are from modelling by Baitsch-Ghirardello et al. (2014) and Gerya et al. (2008). The antigorite- and lizardite-out surfaces are from Ulmer and Trommsdorff (1995) and Bonatti et al. (1984). Blue arrows in paleogeographic sketches show sources of terrigenous sediment of the Proto-Caribbean basin and white lines indicate cross-section locations at 141, 135, 130, 125 and 100 Ma. The whole oceanic ensemble collided with the Caribeana terrane and the Bahamas Platform during the latest Cretaceous-Eocene (not shown; Garcia-Casco et al., 2008a; Iturralde-Vinent et al., 2008).

The onset of SW-directed subduction of the Proto-Caribbean below the Caribbean (Farallon) plate at *c.* 135-130 Ma (Figs. C7_5B and C7_5C; e.g. Garcia-Casco et al., 2006; Pindell and Kennan, 2009; Rojas-Agramonte et al., 2011, 2016; Pindell et al., 2012; Boschman et al., 2014) triggered creation of the Caribbean forearc, which underwent extension, partial melting of peridotite group A, and related basaltic magmatism as a result of trench-retreat. Subduction zone numerical modelling (e.g. Blanco-Quintero et al., 2011b; Baitsch-Ghirardello et al., 2014) predicts intense devolatilization and partial melting events during the first stages of subduction (Fig. C7_5B) as a result of partial distortion of stable oceanic geothermal gradient. The initial anhydrous mantle wedge started to hydrate upon slab-fluid fluxing, triggering partial melting a temperature slightly above the hydrated solidus of harzburgite (Fig.C7_2B), which formed group B peridotites of the serpentinitic matrix (refractory residue, red star, Fig. C7_5C and chapter 4.5.3) and group 1-FAB of the mafic crust (melt, red circle, Fig C7_5C and chapter 5.4.1.2).

Upon approaching a dynamic and thermal steady state subduction zone (135-125 Ma, Fig. C7_5C and 5D), slab devolatilization/melting triggered mantle wedge melting and the formation of IAT melts (group 2 sub-volcanic unit with Th-Nb anomalies and medium Ti/V ratios; Fig. C7_6B and Fig. C7_6C; see chapter 5.4.1.2). The isotopic signature of the plutonic unit indicates a slab signature involving melt-GLOSS and/or fluid GLOSS (Fig. C7_6B; chapter 5.4.2), pointing to formation of this unit at this stage. At 100 Ma (Fig. C7_5E), progressive development of the subduction zone allowed for the progressive release of slab-derived fluids (see chapter 4.5.2 and Fig. C7_6C) into the subduction channel mélange and the mantle wedge (inset in Fig. C7_5E purple area of serpentinization, from Baitsch-Ghirardello et al., 2014) and the incorporation of mantle wedge group A and B peridotites into the subduction channel. The original isotopic signature of the seawater-altered serpentinitic matrix (i.e., depleted mantle/serpentinized mantle; blue/green circle in Fig. C7_6C) shifted to lower $^{143}Nd/^{144}Nd$ and higher $^{87}Sr/^{86}Sr$ ratios following SPER-slab fluid mixing line (Fig. C7_6C). During this period, the sub-volcanic and plutonic units were affected by seawater interaction, which resulted in increasing $^{87}Sr/^{86}Sr$ ratios (orange circle; Fig. C7_6C) and formation of amphibolite and greenschist facies mineral assemblages typical of ocean floor metamorphism (see chapter 5). Tectonic blocks of the crustal section of the Cajálbana ophiolite within serpentinite (western Cuba) attest to amphibolite

facies metamorphism at 129.8 Ma ($^{40}Ar/^{39}Ar$ plateau ages on amphiboles; Garcia-Casco et al., 2003b), which is in line with observations in the VCSM.

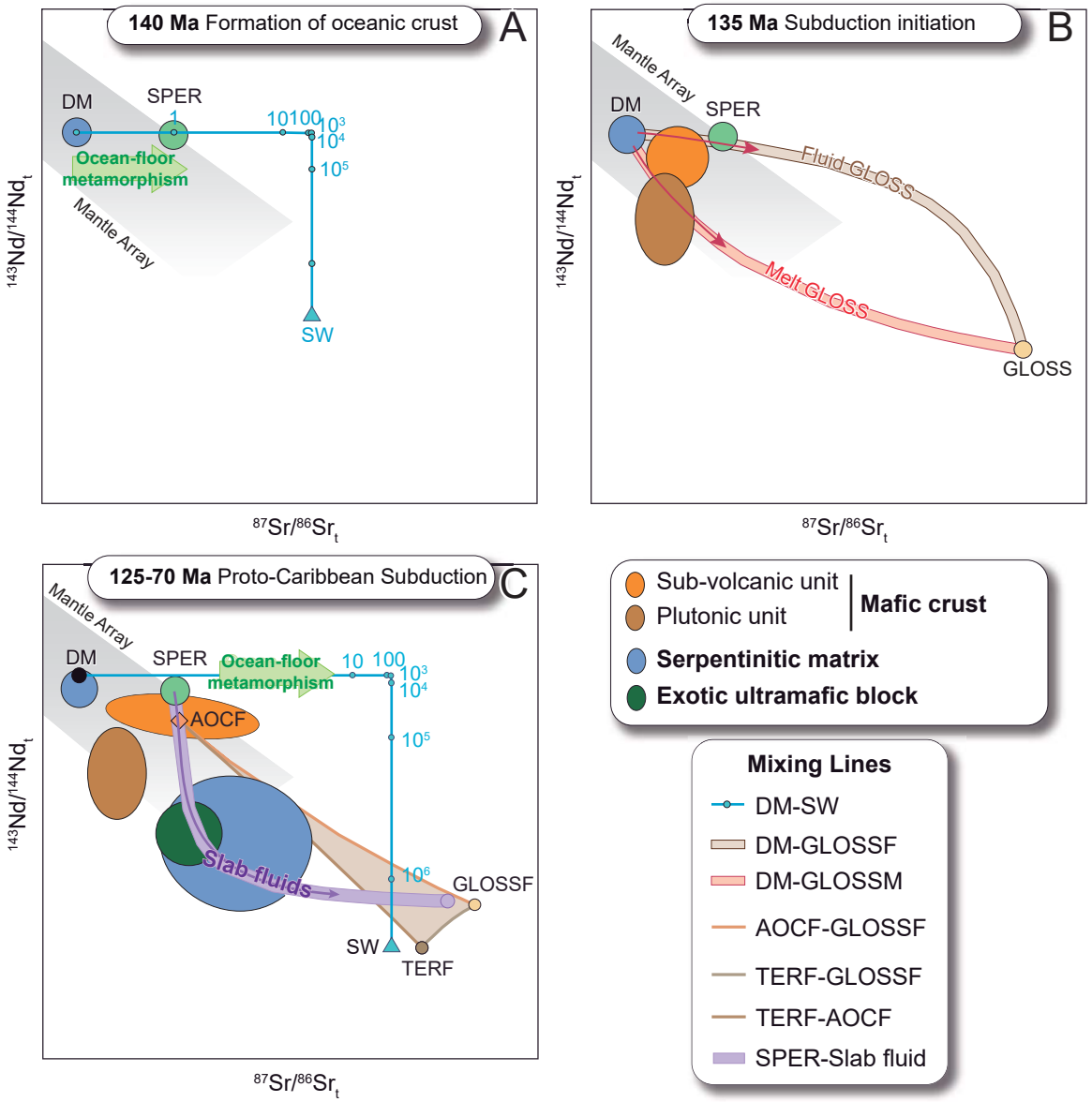

Figure C7_6 *Theoretical Nd and Sr isotopic evolution of serpentinitic matrix, mafic crust and exotic ultramafic blocks in the VCSM. A) Ocean floor metamorphism of the serpentinitic matrix at 140 Ma. The isotopic compositions of the mantle rocks change along the depleted mantle-Creteceous seaweater (DM-SW) mixing line reaching SPER endmember. B) At 135-125 Ma, subduction initiation formed the forearc sub-volcanic and plutonic units with isotopic compositions along the DM-GLOSSF or DM-GLOSSM (global subducting sediment fluid and global subducting sediment melt, respectively) mixing lines. C) At 125-70 Ma, steady state subduction of the Proto-Caribbean formed slab fluids after devolatilization of altered oceanic crust (AOCF), global subducting sediment (GLOSSF) and terrigenous sediments (TERF) that interacted with ultramafic rocks. At 135-125 Ma the mafic crust of the VCSM experienced sea floor metamorphism that modified its isotopic composition (DM-SW mixing line). Note the change in composition of the serpentinitic matrix (blue circle) and exotic ultramafic block (dark green), reaching similar isotopic composition. All endmember and mixing lines as in Fig. C7_3.*

Long lasting subduction (*c.* 135-75 Ma; Fig. C7_5, e.g. Iturralde-Vinent et al., 1996c; Rojas-Agramonte et al., 2011 and 2016) led to the expansion of the subduction channel and the shift of the trench towards the Northeast (Fig. C7_5E). During this stage, the subduction channel mélange included blocks of eclogite, garnet amphibolite and blueschist, as well as the Pelo Malo Atg-serpentinite megablock within the serpentinitic matrix. The protolith of the Atg-serpentinites was serpentinized by slab fluids at temperatures higher than 350ºC (consumption of lizardite; lizardite-out area in Fig. C7_5E; Evans, 2004). Tremolite veins and associated metasomatic domains within the Atg-serpentinite megablock represent the path of the slab fluid fluxing along the subducting plate and overriding subduction channel (e.g. Peacock, 2001; Gerya et al., 2002; Van Keken et al., 2011). At this stage, group A and B peridotites from the upper plate mix together with exotic blocks in a shallow channel mélange.

The serpentinitic mélange was finally constituted after a long period, *c.* 75-40 Ma, during collision of the arc-trench system with the subducting Caribeana terrane first (*c.* 75-60 Ma, Escambray complex in central Cuba; Garcia-Casco et al., 2008a; Despaigne-Díaz et al., 2016 and references therein), followed by collision with the Bahamas Platform (Iturralde-Vinent et al., 2008; van Hinsbergen et al., 2009). The Cretaceous volcanic activity ended by the latest Cretaceous (Iturralde-Vinent, 1994; Hall et al., 2004; Kesler et al., 2004) as a result of subduction/accretion of the Caribeana metasedimentary terrane (García-Casco et al., 2008). The collision of the Caribbean plate with the North American passive margin sequences (Bahamas platform) continued until *c.* 40 Ma (van Hinsbergen et al., 2009). During this stage, the overriding subduction channel mélange incorporated non-metamorphosed blocks of the passive margin and the volcanic arc, reworking pre-existent blocks and the serpentinitic matrix. During collision, synorogenic basins were formed and filled with volcanic arc, passive margin and subduction channel-related material. Since the late Eocene the Cuban sector of the Caribbean orogen is wedged to the North American plate and only local subsidence formed post-orogenic basins (Meyerhoff and Hatten, 1968; Knipper and Cabrera, 1974).

The ophiolitic bodies and serpentinitic mélanges of the Caribbean realm are excellent examples on fracture zone-subduction initiation processes (e.g. Cardenas-Párraga et al., 2017). The dynamic setting described above is the result of magmatic and post-melting geochemical and geodynamic processes that resulted in the complex geochemical and isotopic signatures of the studied rock bodies. A progressive change from fracture zone to subduction is documented in other regions, such as the Franciscan Complex (Coast Range ophiolite, Choi et al., 2008; Wakabayashi, 2011), Kings-Kaweah ophiolite belt (California, Saleeby, 2011), Turkey ophiolite complexes (Dilek et al., 2007; Aldanmaz et al., 2012; Uysal et al., 2016), Loma Caribe peridotite (Marchesi et al., 2016) and South Albanian ophiolites (Hoeck et al., 2002). This PhD Thesis documents a significant new case of the dynamic evolution of an intra-oceanic convergent/fracture-zone active margin.

Chapter 8

Conclusions

8. Conclusions

The Villa Clara serpentinitic mélange (VCSM), central Cuba, is formed by a serpentinitic matrix representing hydrated oceanic mantle, mafic crust and exotic high-pressure blocks of antigorite-serpentinite. Geochemical fingerprints preserved in the relict mantle phases, whole rock major and trace element compositions evidence fertile (group A) and refractory (group B) peridotites in the serpentinized matrix. Melting models converge in 4-8 % of partial melting of a depleted mantle in group A peridotites and 14-22% melting in group B peridotites, which is in line with the composition of relict phases. The field relations and geochemical signatures of both groups point to a genetic relation between them, being group B the result of melting of group A peridotites.

Late enrichment processes attested by whole rock compositions (major and trace elements) and isotopic data (stable and radiogenic) overprinted the primary geochemical signature of both peridotite protoliths and evidence:

1. Post-melting refertilization of group B peridotite by basaltic melts (i.e., LREE enrichment) and

2. Repeated serpentinization events in group A and B peridotites by seawater and slab fluids in a context of abyssal/fracture zone and subduction settings, respectively. Isotope modelling points to slab fluids in the subduction channel as the main serpentinization agent, formed by a mixture of altered oceanic crust fluid (AOCF), global subducting sediment fluid (GLOSSF) and terrigenous fluid (TERF).

The mafic crust in the VCSM includes sub-volcanic (diabase and microgabbro) and plutonic (cumulate gabbro and Ol-gabbro) units. The sub-volcanic unit can be separated in two rock types: group 1 with basaltic compositions typical of forearc basalt and group 2 of basaltic andesite composition characteristic of island arc tholeiite. All types of rock show greenschist to amphibolite facies assemblages developed at low pressure during low to medium temperature ocean floor metamorphism. The sub-volcanic and plutonic units have a subduction-related signature (<2%; slab fluids/melts) as evidenced by radiogenic isotopes. Variable slab input likely resulted in heterogeneous enrichment of suprasubduction magma source(s).

Melting modelling evidence a genetic relationship between group B peridotites of the serpentinitic matrix and sub-volcanic crust group 1 rocks, produced after *c.* 8-10 % melting leaving a residue of group B peridotites. Additional evidence such as the marked LREE enrichment of group B peridotites indicates melt/rock interaction with basaltic liquid, which is most likely represented by forearc basalts (group 1).

The protolith of exotic ultramafic blocks of the VCSM represents subducted peridotite that developed heterogeneous composition (CaO-enriched and Ca-poor compositions) during interaction with a H_2O-CO_2 fluid mixture, forming dolomite-bearing Atg-serpentinites and Atg-serpentinites. Thermodynamic calculations indicate infiltration of a H_2O-rich H_2O-CO_2 fluid at *c.* 450 ºC and *c.* 10 kbar. The fluid channelized along fractures, favouring fluid/rock interaction that developed blackwall domains (Atg + Chl + Tr and Chl + Tr) Atg-serpentinite

wall rock adjacent to tremolite veins. Upon infiltration, the rock/fluid ratios varied across the metasomatic blackwall and the fluid changed composition towards Al- and Ca-poorer compositions outward the vein. The observed exchange of matter from the Atg-serpentinite wallrock through the blackwall domains towards the tremolite vein allows characterizing the metasomatic fluid as rich in Ca, Al and LILE (mostly Sr, Rb, Cs and Ba). Because the serpentinized matrix and exotic ultramafic block of VCSM display similar isotopic signatures, the main responsible of serpentinization and blackwall formation are slab fluids formed by variable proportion of altered oceanic crust fluid (AOCF), global subducting sediment fluid (GLOSSF) and terrigenous fluid (TERF).

Data and models presented in this PhD suggest the involvement of abyssal/fracture zone and subduction zone settings in the generation of the ultramafic protoliths of serpentinites, the mafic crust and exotic high-pressure ultramafic block of the VCSM. Abyssal/fracture zone setting where group A peridotites were formed is consistent with break up of Pangea and continental drift (i.e., formation of the Proto-Caribbean oceanic lithosphere in between the Americas) during Upper Jurassic-Lower Cretaceous times. SW-directed subduction initiation of the Proto-Caribbean likely started along the inter-American fracture zone (*c.* 135 Ma), creating of a forearc where subduction-initiation related extension triggered re-melting of group A peridotites in the mantle wedge and formation of group B peridotite and group 1-FAB of the mafic crust. Seawater infiltrated after intrusion, triggering ocean-floor metamorphism in the sub-volcanic unit and, to some extent, in peridotites. Continuous devolatilization of the slab during Cretaceous time allowed subsequent melting that formed group 2 (IAT-like) sub-volcanic and plutonic rocks. The subsequent development of the subduction zone involved the incorporation of group A and B peridotites in a widening subduction channel after the continued infiltration of slab-derived fluids produced by devolatilization reactions, forming the serpentinitic matrix in a relatively shallow region within the stability field of lizardite, while exotic blocks of Atg-serpentinites were serpentinized in the antigorite stability field. The final constitution of the VCSM took place during *c.* 75-40 Ma, when collision of the arc-trench system took place, first with the subducting Caribeana terrane followed by collision with the Bahamas Platform.

References

9. References

Adam, J., Locmelis, M., Afonso, J.C., Rushmer, T., Fiorentini, M.L., 2014. The capacity of hydrous fluids to transport and fractionate incompatible elements and metals within the Earth's mantle. Geochemistry, Geophysics, Geosystems 15, 1-13.

Aldanmaz, E., 2012. Trace element geochemistry of primary mantle minerals in spinel-peridotites from polygenetic MOR-SSZ suites of SW Turkey: constraints from an LA-ICP-MS study and implications for mantle metasomatism. Geological Journal 47, 59-76.

Allan, J.F., Forsythe, L., Natland, J.H., 1999. 11 Determination of primitive melt composition in the North Atlantic seaward-dipping reflector sequences from cr-rich spinel compositions, in: Larsen, H.C., Duncan, R.A., Allan, J.F., Brooks, K., (Eds.), Proceedings of the Ocean Drilling Program, Scientific Results, 163: College Station, Texas (Ocean Drilling Program), pp. 119-134.

Allen, D.E., Seyfried Jr., W.E., 2003. Compositional controls on vent fluids from ultramafic-hosted hydrothermal systems at mid-ocean ridges: an experimental study at 400◦C, 500 bars. Geochimica et Cosmochimica Acta 67, 1531–1542.

Álvarez, H., Millán, G., Mainegra, V., Bernal, L., 1991. Significado Geotectónico de las Rocas Eclogíticas de Cuba Central. (Unpublished).

Andó, J., Harangi, S., Szakmany, B., Dosztaly, L., 1996. Petrología de la asociación ofiolítica de Holguín, in: Iturralde-Vinent, M.A., (Ed.), Ofiolitas y Arcos volcánicos de Cuba. International Geological Correlation Program (IGCP) Project 364, Miami,pp. 154-176.

Angiboust, S., Langdon, R., Agard, P., Waters, D., Chopin, C., 2011. Eclogitization of the Monviso ophiolite (W. Alps) and implications on subduction dynamics. Journal of metamorphic geology 30, 37-61.

Angiboust, S., Wolf, S., Burov, E., Agard, P., Yamato, P., 2012. Effect of fluid circulation on subduction interface tectonic processes: Insights from thermo-mechanical numerical modelling. Earth and Planetary Science Letters 357-358, 238-248.

Angiboust, S., Pettke, T., De Hoog, J.C.M., Caron, B., Oncken, O., 2014. Channelized Fluid Flow and Eclogite-facies Metasomatism along the Subduction Shear Zone. Journal of Petrology 55, 883-916.

Anonymous, 1972. Penrose Field Conference on ophiolites. Geotimes 17, 24–25.

Auzende., A.L., Bertrand, D., Guillot, S., Daniel, I., Baronnet, A., Lardeaux, J.M., 2002. Serpentinites from Central Cuba: petrology and HRTEM study: European Journal of Mineralogy, v.14, p. 905-9014, doi:10.1127/0935-1221/2002/0014-0905.

Ayers, J., 1998. Trace element modelling of aqueous fluid - peridotite interaction in the mantle wedge of subduction zones. Contributions Mineral Petrology 132, 390-404.

Baitsch-Ghirardello, B., Stracke, A., Connolly, J.A.D., Nikolaeva, K.M., Gerya, T.V., 2014. Lead transport in intra-oceanic subduction zones: 2D geochemical–thermo-mechanical modeling of isotopic signatures. Lithos 208-209, 265-280.

Bebout, G.E., 1991. Field-Based Evidence for Devolatilization in Subduction Zones: Implications for Arc Magmatism. Science 251, 413-416.

Bebout, G.E. Barton, M.D., 2002. Tectonic and metasomatic mixing in a high-T, subduction-zone mélange—insights into the geochemical evolution of the slab–mantle interface. Chemical Geology 187, 79-106.

Bebout, G.E., 2007. Metamorphic chemical geodynamics of subduction zones. Earth and Planet Science Letters 260, 373-393.

Bebout, G.E., 2014. Chemical and Isotopic Cycling in Subduction Zones, in Holland, H.D., and Turekian, K.K., eds., Treatise on Geochemistry (Second Edition): Oxford, Elsevier 4, pp. 703-747.

Bebout, G.E. and Penniston-Dorland, S.C., 2016. Fluid and mass transfer at subduction interfaces-the field metamorphic record. Lithos 240-243, 228-258.

Bédard, J.H., 1999. Petrogenesis of Boninites from the Betts Cove Ophiolite, Newfoundland, Canada: Identification of Subducted Source Components. Journal of Petrology 40, 1853-1889.

Blanco-Quintero, I.F., García-Casco, A., Rojas-Agramonte, Y., Rodríguez-Vega, A., Lázaro, C., Iturralde-Vinent, M.A., 2010.

Metamorphic evolution of subducted hot oceanic crust, La Corea mélange, Cuba. American Journal of Science 310, 889–915.

Blanco-Quintero, I.F., Proenza, J.A., Garcia-Casco, A., Tauler, E., Galí, S., 2011a. Serpentinites and serpentinites within a fossil subduction channel: La Corea mélange, eastern Cuba. Geologica Acta 9, 389-405.

Blanco-Quintero, I.F., Gerya, T.V., Garcia-Casco, A., Castro, A., 2011b. Subduction of young oceanic plates: A numerical study with application to aborted thermal-chemical plumes. Geochemistry Geophysics Geosystems 12, 1-14.

Blanco-Quintero, I.F., Rojas-Agramonte, Y., Garcia-Casco, A., Kröner, A., Mertz, D.F., Lázaro, C., Blanco-Moreno, J., Renne, P.R., 2011c. Timing of subduction and exhumation in a subduction channel: Evidence from slab melts from La Corea mélange (eastern Cuba). Lithos 127, 86-100.

Blanco-Quintero, I.F., Lázaro, C., Garcia-Casco, A., Proenza, J., Rojas-Agramonte, Y., 2011d. Barium-rich fluids and melts in the subduction environment (La Corea and Sierra del Convento mélanges, eastern Cuba). Contributions to Mineralogy and Petrology 162, 395-413.

Blein, O., Guillot, S., Lapierre, H., Mercier-de-Lépinay, B., Lardeaux, J.M., Millán Trujillo, G., Campos, M., García, A., 2003. Geochemistry of the Mabujina Complex. Central Cuba: Implication on the Cuban Cretaceous arc rocks. The Journal of Geology 111, 89–101.

Bodinier, J.L., Merlet, C., Bedini, R.M., Simien, F., Remaidi, M., Garrido, C.J., 1996. Distribution of niobium, tantalum, and other highly incompatible trace elements in the lithospheric mantle: the spinel paradox. Geochimica et Cosmochimica Acta 60, 545–550.

Bodinier, J-L. Godard, M., 2014. 3.4 Orogenic, Ophiolitic, and Abyssal Peridotites, in Holland, H.D., Turekian, K.K. (Eds.), Treatise on Geochemistry (Second Edition). Elsevier, Oxford, pp.103-167.

Bence, A.E., Albee, A.L., 1968. Empirical correction factors for the electron microanalysis of silicate and oxides. Journal of Geology 76, 382-403.

Bonatti, E., Lawrence, J.R., Morandi, N., 1984. Serpentinitzation of oceanic peridotites: temperature dependence of mineralogy and boron content. Earth and Planetary Science Letters 70, 88-94.

Bonev, N., Stampfli, G., 2008. Petrology, geochemistry and geodynamic implications of Jurassic island arc magmatism as revealed by mafic volcanic rocks in the Mesozoic low-grade sequence, eastern Rhodope, Bulgaria. Lithos 100, 210-233.

Boschi, C., Dini, A., Früh-Green, G.L., Kelley, D.S., 2008. Isotopic and element exchange during serpentinization and metasomatism at the Atlantis Massif (MAR 30°N): Insights from B and Sr isotope data. Geochimica et Cosmochimica Acta 72, 1801–1823.

Boschi, C., Bonatti, E., Ligi, M., Brunelli, D., Cipriani, A., Dallai, L., D'Orazio, M., Früh-Green, G. L., Tonarini, S., Barnes, J.D., Bedini, R. M., 2013. Serpentinization of mantle peridotites along an uplifted lithospheric section, Mid Atlantic Ridge at 11° N. Lithos 178, 3-23.

Boschman, L.M., Van Hinsbergen, D.J.J., Torsvik, T.H., Spakman, W., Pindell, J.L., 2014. Kinematic reconstruction of the Caribbean region since the Early Jurassic. Earth Science Review 138, 102-136.

Bouilhol, P., Burg, J.P., Bodinier, J.L., Schmidt, M.W., Bernasconi, S.M., Wood, H., 2012. Gem Olivine and Calcite mineralitzation precipitated from subduction-derived fluids in The Kohistan arc mantle (Pakistan). Canadian Mineralogist 50, 1291-1304.

Cannaò, E., Agostini, S., Scambelluri, M., Tonarini, S., Godard, M., 2015. B, Sr and Pb isotope geochemistry of high-pressure Alpine metaperidotites monitors fluid-mediated element recycling during serpentinite dehydration in subduction mélange (Cima di Gagnone, Swiss Central Alps). Geochimica et Cosmochimica Acta 163, 80-100.

Cannaò, E., Scambelluri, M., Agostini, S., Tonarini, S., Godard, M., 2016. Linking serpentinite geochemistry with tectonic evolution at the subduction plate-interface: The Voltri Massif case study (Ligurian Western Alps, Italy). Geochimica et Cosmochimica Acta 190, 115-133.

Cannat, M., 1993. Emplacement of 750 Mantle rocks in the Seafloor at Mid-Ocean Ridges. Journal of Geophysical Research 98, 4163-4172.

Cao, Y., Song, S., Su, L., Jung, H., Niu, Y., 2016. Highly refractory peridotites in Songshugou, Qinling orogen: Insights into partial melting and melt/fluid–rock reactions in forearc mantle. Lithos 252-253, 234-254.

Cárdenas-Párraga, J., García-Casco, A., Harlow, G.E., Blanco-Quintero, I.F., Rojas-Agramonte, Y., Kröner, A., 2012. Hydrothermal origin and age of jadeitites from Sierra del Convento Mélange (Eastern Cuba): European Journal of Mineralogy 24, 313–331.

Cárdenas-Párraga, J., García-Casco, A., Proenza, J.A., Harlow, G.E., Blanco Quintero, I.F., Lázaro, C., Villanova-de-Benavent, C., Núñez Cambra, K., 2017. Trace element geochemistry of transform-fault serpentinite in high-pressure subduction mélanges (Eastern Cuba): Implications for subduction initiation. International Geology Review, 1-24.

Catanzaro, E.J., Champion, C.E., Garner, E.L., Malinenko, G., Sappenfield, K.M., Shields, W.R., 1970. Boric acid, isotopic, and assay standard reference materials. U.S. National Bureau Standards Special Publication 260-17, 1-70.

Cazañas, X., Proenza, J.A., Kysar-Mattietti, G., Lewis, J., Melgarejo, J.C., 1998. Rocas volcánicas de las series inferior y media del Grupo El Cobre en la Sierra Maestra (Cuba oriental): volcanismo generado en un arco de islas toleiítico. Acta Geologica Hispanica 33, 57-74.

Chan, T.K., Finch, I.J., (2001). Determination of platinum-group elements and gold by inductively coupled plasma mass spectrometry. In: Australian Platinum Conference, Perth, Western Australia:1-9

Chaussidon, M., Marty, B., 1995. Primitive Boron Isotope Composition of the Mantle. Science 269, 383-386.

Choi, S.H., Shervais, J.W., Mukasa, S.B., 2008. Supra-subduction and abyssal mantle peridotites of the Coast Range ophiolite, California. Contributions Mineral Petrology 156, 551-576.

Cintron Franqui, N.O., Choi, S.H., LEE, D-C., 2017. Peridotites and basaltic rocks within an ophiolitic mélange from the SW igneous province of Puerto Rico: relation to the evolution of the Caribbean Plate. Geological Magazine 154, 96-118.

Cloos, M., Shreve, R.L., 1988a. Subduction-channel model of prism accretion, melange formation, sediment subduction, and subduction erosion at convergent plate margins: 1. Background and description. Pure and Applied Geophysics 128 (3-4), 455-500.

Cloos, M., Shreve, R.L., 1988b.Subduction-channel model of prism accretion, melange formation, sediment subduction, and subduction erosion at convergent plate margins: 2. Implications and discussion. Pure and Applied Geophysics 128 (3-4), 501-545.

Cobiella, J., 1988. El vulcanismo paleogénico cubano. Apuntes para un nuevo enfoque. Tecnológica 18(4), 25-32.

Colás, V., González-Jiménez, J.M., Griffin, W.L., Fanlo, I., Gervilla, F., O'Reilly,S.Y., Pearson, N.J., Kerestedjian, T., Proenza, J.A., 2014. Fingerprints of metamorphism in chromite: New insights from minor and trace elements, Chemical Geology 389,137-152.

Connolly, J., 1990. Multivariable phase-diagrams - an algorithm based on generalized thermodynamics. American Journal of Science 290, 666-718.

Connolly, J., 2005. Computation of phase equilibria by linear programming: A tool for geodynamic modeling and its application to subduction zone decarbonation. Earth Planet Science Letters 236, 524-541.

Cowan, D.S., 1985. Structural styles in Mesozoic and Cenozoic mélanges in the western Cordillera of North America. Geological Society of America Bulletin 96, 451–462.

Debret, B., Andreani, M., Godard, M., Nicollet, C., Schwartz, S., Lafay, R., 2013. Trace element behavior during serpentinization/de-serpentinization of an eclogitized oceanic lithosphere: A LA-ICPMS study of the Lanzo ultramafic massif (Western Alps). Chemical Geology 357, 117–133.

Debret, B., Andreani, M., Muñoz, M., Bolfan-Casanova, N., Carlut, J., Nicollet, C., Schwartz, S., Trcera, N., 2014. Evolution of Fe redox state in serpentine during subduction. Earth and Planetary Science Letters 400, 206-218.

De Capitani C., Petrakakis K., 2010. The computation of equilibrium assemblage diagrams with Theriak/Domino software. American Mineralogist 95, 1006-1016.

Delacour, A., Früh-Green, G., Frank, M, Gutjahr, M., Kelley, D. S., 2008. Sr- and Nd-isotope geochemistry of the Atlantis Massif (30°N, MAR): Implications for fluid fluxes and lithospheric heterogeneity. Chemical Geology 254, 19-35.

Deschamps, F., Guillot, S., Godard, M., Chauvel, C., Andreani, M., Hattori, K., 2010. In situ characterization of serpentinites from forearc mantle wedges: Timing of serpentinization and behavior of fluid-mobile elements in subduction zones. Chemical Geology 269, 262-277.

Deschamps, F., Guillot, S., Godard, M., Andreani, M., Hattori, K., 2011. Serpentinites act as sponges for fluid-mobile ele-

ments in abyssal and subduction zone environments. Terra Nova 23, 171-178.

Deschamps, F., Godard, M., Guillot, S., Chauvel, C., M., Andreani, M., Hattori, K., Wunder, B., France, L., 2012. Behavior of fluid-mobile elements in serpentines from abyssal to subduction environments: Examples from Cuba and Dominican Republic. Chemical Geology 312-313, 93-117.

Deschamps, F., Godard, M., Guillot, S., Hattori, K., 2013. Geochemistry of subduction zone serpentinites: A review. Lithos 178, 96-127.

Despaigne-Díaz, A.I., Garcia-Casco, A., Cáceres Govea, D., Jourdan, F., Wilde, S.A., Millán Trujillo, G., 2016. Twenty-five million years of subduction-accretion-exhumation during the Late Cretaceous-Tertiary in the northwestern Caribbean: the trinidad dome, escambray complex, central Cuba. American Journal of Science 316, 203-204.

Díaz de Villalvilla, L., Milia, I., Cruz Pacheco, M.S., Aguirre, G., 2003. Formación los pasos: Geología, Geoquímica y su comparación con el Caribe. In: Instituto de Geología y Paleontología de Cuba (Eds.), Estudios sobre los Arcos Volcánicos de Cuba, Centro Nacional de Información Geológica, La Habana, pp. 1-22.

Dick, H.J.B., 1989. Abyssal peridotites, very slow spreading ridges and ocean ridge magmatism. Geological Society, London, Special Publications 42, 71-105.

Dick, H.J.B., Bullen, T., 1984. Chromian spinel as a petrogenetic indicator in abyssal and alpine-type peridotites and spatially associated lavas. Contributions Mineral Petrology 86, 54-76.

Dick, H.J.B., Lissenberg, J., Warren, J.M., 2010. Mantle Melting, Melt Transport, and Delivery Beneath a Slow-Spreading Ridge: The Paleo-MAR from 23º15'N to 23º45'N. Journal of Petrology 51, 425-467.

Dilek, Y., Furnes, H., 2011. Ophiolite genesis and global tectonics: Geochemical and tectonic fingerprinting of ancient oceanic lithosphere. Geological Society of America Bulletin 123, 387-411.

Dilek, Y., Furnes, H., 2014. Ophiolites and their origins. Elements 10, 93-100.

Dilek, Y., Furnes, H., Shallo, M., 2007. Suprasubduction zone ophiolite formation along the periphery of Mesozoic Gondwana. Gondwana Research 11, 453-475.

Dublan, L., Álvarez-Sánchez, H., Mlcoch, B., Mañour, J., LLedíaz, P., Molak, B., Vázquez, C., Snopkova, P., De los Santos, E., Soucek, J., Pérez, M., Mihailova, A., Bernal, I., Zoubek, J., Ordoñez, M., Soucek, J., Morousek, J., Svetska, J., Marshall, W., Pérez-Conde, R., González, E., and Rodríguez, R., 1986. Informe final del levantamiento geológico y evaluación de minerales útiles, a escala 1:50 000, del polígono CAME I, zona Centro: La Habana, Cuba, Fondo Geológico Nacional, Oficina Nacional de Recursos Minerales, Ministerio de Industria Básica, 1402 p., 250 maps (unpublished report).

Ducloz, C., Vuagnat, M., 1962. Apropose de l'age des serpentinites de Cuba. Archives de Sciences de Physique et d'Histoire Naturelle 15, 309–332.

Duggen, S., Hoernle, K., Klügel, A., Geldmacher, J., Thirlwall, M., Hauff, F., Lowry, D., Oates, N., 2008. Geochemical zonation of the Miocene Albora´n Basin volcanism (westernmost Mediterranean): geodynamic implications. Contribution to Mineral Petrology 156, 577-593.

Dupuis, C., Hébert, R., Dubois-Côté, V., Guilmette, C., Wang, C.S., Li, Y.L., Li, Z.J., 2005. The Yarlung Zangbo Suture Zone ophiolitic mélange (southern Tibet): new insights from geochemistry of ultramafic rocks. Journal of Asian Earth Sciences 25, 937-960.

Dumitru, T.A., 1991. Effects of subduction parameters on geothermal gradients in forearcs, with an application to Franciscan subduction in California. Journal of Geophysical Research 96, 621-641.

Escartín, J., Mével, C., Petersen, S., Bonnemains, D., Cannat, M., Andreani, M., Augustin, N., Bezos, A., Chavagnac, V., Choi, Y., Godard, M., Haaga, K., Hamelin, C., Ildefonse, B., Jamieson, J., John, B., Leleu, T., MacLeod, C. J., Massot-Campos, M., Nomikou, P., Olive, J. A., Paquet, M., Rommevaux, C., Rothenbeck, M., Steinfuhrer, A., Tominaga, M., Triebe, L., Campos, R., Gracias, N., Garcia, R., 2017. Tectonic structure, evolution, and the nature of oceanic core complexes and their detachment fault zones (13°20'N and 13°30'N, Mid Atlantic Ridge). Geochemistry, Geophysics, Geosystems 18, 1-31.

Escuder-Viruete, J., Díaz de Neira, A., Hernáiz Huerta, P.P., Monthel, J., García Senz, J., Joubert, M., Lopera, E., Ullrich, T., Friedman, R., Mortensen, J., Pérez-Estaún, A., 2006. Magmatic relationships and ages of Caribbean island-arc tholeiites, boninites and related felsic rocks, Dominican Republic. Lithos 90, 161–186.

Escuder-Viruete, J., Contreras, F., Stein, G., Urien, P., Joubert, M., Pérez-Estaún, A., Friedman, R., Ullrich, T., 2007. Mag-

matic relationships and ages between adakites, magnesian andesites and Nb-enriched basalt-andesites from Hispaniola: Record of a major change in the Caribbean island arc magma sources. Lithos 99, 151-177.

Escuder-Viruete, J., Friedman, R., Castillo-Carrión, M., Jabites, J., Pérez-Estaún, A., 2011. Origin and significance of the ophiolitic high-P mélanges in the northern Caribbean convergent margin: Insights from the geochemistry and large-scale structure of the Río San Juan metamorphic complex. Lithos 127, 483-504.

Escuder-Viruete, J., Castillo-Carrión, M., Pérez-Estaún, A., 2014. Magmatic relationships between depleted mantle harzburgites, boninitic cumulate gabbros and subduction-related tholeiitic basalts in the Puerto Plata ophiolitic complex, Dominican Republic: implications for the birth of the Caribbean Island-arc. Lithos 196-197, 261–280.

Evans, B.W., 2004. The Serpentinite Multisystem Revisited: Chrysotile is Metastable. International Geology Review 46, 479–506.

Faure, G., Mensing, T.M., 2005. Isotopes Principles and Applications, third ed. Willey and Sons, Hoboken, New Jersey.

Festa, A., Dilek, Y., Pini, G.A., Codegone, G., Ogata, K., 2012. Mechanisms and processes of stratal disruption and mixing in the development of mélanges and broken formations: Redefining and classifying mélanges. Tectonophysics 568-569, 7-24.

Fisher, G.W., 1989. Matrix analysis of metamorphic mineral assemblages and reactions. Contributions Mineral Petrology 102, 69-77.

Fisher, G.W., 1993. An improved method for algebraic analysis of metamorphic mineral assemblages. American Mineralogist 78, 1257-1261.

Frisby, C., Bizimis, M., Mallick, S., 2016. Seawater-derived rare earth element addition to abyssal peridotites during serpentinization. Lithos 248–251, 432–454.

Furnes, H., Dilek, Y., 2017. Geochemical characterization and petrogenesis of intermediate to silicic rocks in ophiolites: A global synthesis. Earth- Science Reviews 166, 1-37.

Garcia-Casco, A., 2007. Magmatic paragonite in trondhjemites from the Sierra del Convento mélange, Cuba. American Mineralogist 92, 1232-1237.

Garcia-Casco, A., Torres-Roldán, R.L., Millán, G., Monié, P., Schneider, J., 2002. Oscillatory zoning in eclogitic garnet and amphibole, Northern Serpentinite Melange, Cuba: a record of tectonic instability during subduction?. Journal of Metamorphic Geology 20, 581–598.

Garcia-Casco, A., Pérez de Arce, C., Millán, G., Iturralde-Vinent, M., Fonseca, E., Torres-Roldán, R., Nuñez, K., Morata, D., 2003a. Metabasites from the northern serpentinite belt (Cuba) and a metamorphic perspective of plate tectonic models for the Caribbean region. Memorias Geomin, 24–28.

Garcia-Casco, A., Pérez de Arce, C., Millán, G., Iturralde-Vinent, M.A., Fonseca, E., Torres-Roldán, R., Núnez, K., Morata, D., 2003b. Metabasites from the northern serpentinite belt (Cuba) and a metamorphic perspective of the plate tectonic models for the Caribbean region. Memorias GEOMIN, La Habana, pp. 9.

Garcia-Casco, A., Torres-Roldán, R. L., Iturralde-Vinent, M. A., Millán, G., Núñez Cambra, K., Lázaro, C., Rodríguez Vega, A., 2006. High pressure metamorphism of ophiolites in Cuba. Geologica Acta 4, 63–88.

Garcia-Casco, A., Iturralde-Vinent, M.A., Pindell, J., 2008a. Latest Cretaceous collision/accretion between the Caribbean Plate and Caribeana: Origin of metamorphic terranes in the Greater Antilles. International Geology Review 50, 781–809.

Garcia-Casco, A., Lázaro, C., Rojas-Agramonte, Y., Kröner, A., Torres-Roldán, R.L., Núñez, K., Neubauer, F., Millán, G., Blanco-Quintero, I., 2008b. Partial melting and counterclockwise P-T path of subducted oceanic crust (Sierra del Convento Mélange, Cuba). Journal of Petrology 49, 129-161.

García-Delgado, D. E., Delgado Damas, R., Millán Trujillo, G., Díaz de Villalvilla, L., Sukar Sastroputro, K., Llanes, I., Bernal, L., 1998, Mapa geológico de Cuba Central (Provincias Cienfuegos, Villa Clara y Sancti Spiritus), scale 1: 100000, 1 sheet. Memorias del Congreso Cubano de Geología, p. 263-266.

Gervilla, F., Proenza, J.A., Frei, R., González-Jiménez, J.M., Garrido, C.J., Melgarejo, J.C., Meibom, A., Díaz-Martínez, R., Lavaut, W., 2005. Distribution of platinum-group elements and Os isotopes in chromite ores from Mayarí-Baracoa Ophiolitic Belt (eastern Cuba). Contributions to Mineralogy and Petrology 150, 589–607.

Gerya, T.V., Stöckhert, B., Perchuk, A.L., 2002. Exhumation of high-pressure metamorphiv rocks in a subduction channel:

a numerical simulation. Tectonics 21, 1-15.

Gerya, T.V., Connolly, J.A.D., Yuen, D.A., 2008. Why is terrestrial subduction one-sided?. Geology 36, 43-46.

Gill, R., 2010. Igneous Rocks and Processes A Practical Guide, first ed. Wiley-Blackwell, Malaysia.

Godard, M., Lagabrielle, Y., Alard, O., Harvey, J., 2008. Geochemistry of the highly depleted peridotites drilled at ODP Sites 1272 and 1274 (Fifteen-Twenty Fracture Zone, Mid-Atlantic Ridge): Implications for mantle dynamics beneath a slow spreading ridge. Earth and Planetary Science Letters 267, 410-425.

Govindaraju, K., 1994. Compilation of Working values and Sample description for 383 Geostandards. Geostandards Newsletter 18, 1-158.

Grafe, F., Stanek, K.P., Baumann, A., Maresch, W.V., Hames, W.E., Grevel, C., and Millán, G., 2001. Rb-Sr and 40Ar/39Ar mineral ages of granitoid intusives in the Mabujina unit, Central Cuba: Thermal exhumation history of the Escambray massif. Journal of Geology 109, 615–631.

Green, T.H., 1994. Experimental studies of trace-element partitioning applicable to igneous petrogenesis-Sedona 16 years later. Chemical Geology 117, 1-36.

Green, E.C.R., Holland, .T.J.B., Powell, R., 2007. An order-disorder model for omphacitic pyroxenes in the system jadeite-diopside-hedenbergite-acmite, with applications to eclogite rocks. American Mineralogist 92, 1181-1189.

Green, D.H., 2015. Experimental petrology of peridotites, including effects of water and carbon on melting in the Earth's upper mantle. Physics and Chemistry of Minerals 42, 95–122.

Green, D.H., Hibberson, W.O., Rosenthal, A., Kovács, I., Yaxley, G.M., Falloon, T.J., Brink, F., 2014. Experimental Study of the Influence of Water on Melting and Phase Assemblages in the Upper Mantle. Journal of Petrology 55, 2067-2096.

Groppo, C., Rinaudo, C., Cairo, S., Gastaldi, D., Compagnoni, R., 2006. Micro-Raman spectroscopy for a quick and reliable identification of serpentine minerals from ultramafics. European Journal of Mineralogy 18, 319-329.

Guillot, S., Hattori, K., Agard, P., Schwartz, S., Vidal, O., 2009. Exumation processes in oceanic and continental subduction contexts: a review. In: Lallemand, S., Funiciello, F., eds., 175-204, Subduction Zone Geodynamics. Frontiers in Earth Sciences. Springer, Berlin, Heidelberg.

Guillot, S., Schwartz, S., Reynard, B., Agard, P., Prigent, C., 2015. Tectonic significance of serpentinites. Tectonopysics 646, 1-9.

Gurenko, A.A., Chaussidon, M., Boron concentrations and isotopic composition of the Icelandic mantle: evidence from glass inclusions in olivine. Chemical Geology 135, 21-34.

Hacker, B.R., 2008. H2O subduction beyond arcs. Geochemistry, Geophysics, Geosystems 9, 1-24.

Hall, C.M., Kesler, S.E., Russell, N., Piñero, E., Sánchez, R., Pérez, M., Moreira, J., Borges, M., 2004. Age and tectonic setting of the Camaguey Volcanic-Intrusive Arc, Cuba: Late Cretaceous extension and uplift in the Western Greater Antilles. The Journal of Geology 112, 521–542.

Hart, S.R., Blusztajn, J., Dick, H.J.B., Meyer, P.S., Muehlenbachs, K., 1999. The fingerprint of seawater circulation in a 500-meter section of ocean crust gabbros. Geochimica et Cosmochimica Acta 23-24, 4059-4080.

Harlow, G.E., Hemming, S.R., Avé Lallemant, H.G., Sisson, V. B., Sorensen, S.S., 2004. Two high-pressure–low-temperature serpentinite-matrix mélange belts, Motagua fault zone, Guatemala: A record of Aptian and Maastrichtian collisions. Geology 32, 17-20.

Harlow, G.E., Sorensen, S.S., 2005. Jade (nephrite and jadeitite) and serpentinite: metasomatic connections. International Geology Review 47, 113-146.

Harlow, G.H., Tsujimori, T., Sorensen, S.S., 2015. Jadeitites and Plate Tectonics. Annual Review of Earth and Planetary Sciences 43, 105-138.

Hattori, K.H., Guillot, S., 2007. Geochemical character of serpentinites associated with high- to ultrahigh-pressure metamorphic rocks in the Alps, Cuba, and the Himalayas: Recycling of elements in subduction zones. Geochemistry Geophysics Geosystems 8, 1525-2027.

Hauff, F., Hoernle, K., Schmidt, A., 2003. Sr-Nd-Pb composition of Mesozoic Pacific oceanic crust (Site 1149 and 801, ODP Leg 185): Implications for alteration of ocean crust and the input into the Izu-Bonin-Mariana subduction system.

Geochemistry Geophysics Geosystems 4, 1-30.

Hawthorne, F.C., Oberti, R., Harlow, G.E., Maresch, W.V., Martin, R.F., Schumacher, J.C., Welch, M.D., 2012. Nomenclature of amphibole supergroup. American Mineralogist 97, 2031-2048.

Hellebrand, E., Snow, J.E., Hoppe, P., Hofmann, A.W., 2002. Garnet-field melting and Late-stage Refertilitzation in "Residual" abyssal peridotites from the Central Indian Ridge. Journal of Petrology 43, 2305-2338.

Herzberg, C., 2004. Geodynamic information in Peridotite Petrology. Journal of Petrology 45, 2507-2530.

Hirahara, Y., Kimura, J.-I., Senda, R., Miyazaki, T., Kawabata, H., Takahashi, T., Chang, Q., Vaglarov, B. S., Sato, T., Kodaira, S., 2015. Geochemical variations in Japan Sea back-arc basin basalts formed by high-temperature adiabatic melting of mantle metasomatized by sediment subduction components. Geochemistry Geophysics Geosystems 16, 1324–1347.

Hirth, G., Kohlstedt, D.L., 1996. Water in the oceanic upper mantle: implications for rheology, melt extraction and the evolution of the lithosphere. Earth and Planetary Science Letters 144, 93-108.

Hoeck, V., Koller, F., Meisel, T., Onuzi, K., Kneringer, E., 2002. The Jurassic South Albanian ophiolites: MOR- vs. SSZ-type ophiolites. Lithos 65, 143-164.

Hoeck, V., Ionescu, C., Balintoni, I., Koller, F., 2009. The Eastern Carpathians "ophiolites" (Romania): remnants of a Triassic ocean. Lithos 108, 151-171.

Holland, T.J.B., Powell, R., 1996. Thermodynamics of order-disorder in minerals. 2. Symmetric formalism applied to solid solutions. American Mineralogist 81, 1425-37.

Holland, T.J.B., Powell, R., 1998. An internally consistent thermodynamic data set for phases of petrological interest. Journal of Metamorphic Geology 16, 309-343.

Holland, T.J.B., Powell, R., 2011. An improved and extended internally consistent thermodynamic dataset for phases of petrological interest, involving a new equation of state for solids. Journal of Metamorphic Geology 29, 333-383.

Holland, T.J.B., Baker, J.M., Powell, R., 1998. Mixing properties and activity- composition relationships of chlorites in the system MgO-FeO-Al2O3-SiO2-H2O. European Journal of Mineralogy 10, 395-406.

Ildefonse, B., Blackman, D.K., John, B.E., Ohara, Y., Miller, D.J., MacLeod, C.J., 2007. Oceanic core complexes and crustal accretion at slow-spreading ridges. Geological Society of America 35, 623-626.

Irvine, T.N., Baragar, W.R.A., 1971. A guide to the chemical classification of the common volcanic rocks. Canadian Journal Earth and Science 8, 523-548.

Ishii, T., Robinson, P.T., Maekawa, H. and Fiske, R., 1992. Petrological studies of peridotites from diapiric serpentinite seamounts in the Izu-Ogasawara-Mariana Forearc, Leg 125. Proceedings of the Ocean Drilling Program, Scientific Results 125, 445-485.

Ishizuka, O., Tani, K., Reagan, M.K., Kanayama, K., Umino, S., Harigane, Y., Sakamoto, I., Miyajima, Y., Yuasa, M., Dunkley, D.J., 2011. The timescales of subduction initiation and subsequent evolution of an oceanic island arc. Earth and Planetary Science Letters 306, 229-240.

Iturralde-Vinent, M.A., 1994. Cuban geology: A new plate tectonic synthesis. Journal of Petroleum Geology 17, 39–70.

Iturralde-Vinent, M.A., 1996a. Introduction to Cuban geology and geophysics, in: Iturralde-Vinent, M.A., (Eds.), Cuban ophiolites and volcanic arcs, International Geological Correlation Program (IGCP) Project 364, Miami, pp. 3–35.

Iturralde-Vinent, M.A., 1996b. Cuba: El arco de islas volcánicas del Cretácico, in: Iturralde-Vinent, M.A., (Eds.), Ofiolitas y Arcos Volcánicos de Cuba, International Geological Correlation Program (IGCP) Project 364, Miami, pp. 179–189.

Iturralde-Vinent, M.A., 1996c. Geología de las ofiolitas de Cuba, in: Iturralde-Vinent, M.A., (Eds.), Ofiolitas y Arcos Volcánicos de Cuba, International Geological Correlation Program (IGCP) Project 364, Miami, pp. 83–120.

Iturralde-Vinent, M., 1998. Sinopsis de la constitución geológica de Cuba. Acta Geológica Hispánica 33, 9-59.

Iturralde-Vinent, M.A., 2006a. Meso-Cenozoic Caribbean Paleogeography: Implications for the Historical Biogeography of the Region. International Geology Review 48, 791-827.

Iturralde-Vinent, M.A., Díaz-Otero, C., Rodríguez-Vega, A., Díaz-Martínez, R., 2006b. Tectonic implications of paleontologic dating of Cretaceous-Danian sections of Eastern Cuba. Geologica Acta 4, 89-102.

References

Iturralde-Vinent, M.A., Díaz Otero, C., Garcia-Casco, A., Van Hinsbergen, D.J.J., 2008. Paleogene Foredeep Basin Deposits of North-Central Cuba: A Record of Arc-Continent Collision between the Caribbean and North American Plates. International Geology Review 50, 863-884.

Iturralde-Vinent, M.A., Garcia-Casco, A., Rojas-Agramonte, Y., Proenza, J.A., Murphy, J.B., Stern, R.J., 2016. The geology of Cuba: A brief overview and synthesis. GSA Today 26, 4-10.

Iyer, K., Austrheim, H., John, T., Jamtveit, B., 2008. Serpentinization of the oceanic lithosphere and some geochemical consequences: constraints from the Leka Ophiolite Complex, Norway. Chemical Geology 249, 66–90.

Jarrard, R.D., 2003. Subduction fluxes of water, carbon dioxide, chlorine, and potassium. Geochemistry, Geophysics, Geosystems 4.

Janecky, D.R., Seyfried Jr., W.E., 1986. Hydrothermal serpentinization of peridotite within the oceanic crust: experimental investigations of mineralogy and major element chemistry. Geochimica et Cosmochimica Acta 50, 1357–1378.

Jean, M.M., Shervais, J.W., Choi, S.H., Mukasa, S.B., 2010. Melt extraction and melt refertilization in mantle peridotite of the Coast Range ophiolite: an LA–ICP–MS study. Contributions to Mineralogy Petrology 159, 1-113.

John, T., Klemd, R., Gao, J., Garbe-Schönberg, C-D., 2008. Trace-element mobilization in slabs due to non steady-state fluid–rock interaction: Constraints from an eclogite-facies transport vein in blueschist (Tianshan, China). Lithos 103, 1-24.

Johnson, K.T.M., Dick, H.J.B. and Shimizu, N., 1990. Melting in the Oceanic Upper Mantle: An ion Microprobe Study of Diopsides in Abyssal Peridotites. Journal of Geophysical research 95, 2661-2678.

Johnson, K.T.M., Dick, H.J.B., 1992. Open system melting and temporal and spatial variation of peridotite and basalt at the Atlantis II fracture zone. Journal of Geophysical Research 97, 9219-9241.

Johnson, M.C., Plank, T., 1999. Dehydration and melting experiments constrain the fate of subducted sediments. Geochemistry Geophysics Geosystems 1, 1-26.

Jolly, W.T., Lidiak, E.G., Dickin, A.P., Wu, T-W., 2002. Recycling in the Puerto Rican mantle wedge, Greater Antilles Island Arc. The Island Arc 11, 10-24.

Jolly, W.T., Lidiak, E.G., 2006. Role of crustal melting in petrogenesis of the Cretaceous Water Island Formation (Virgin Islands, northeast Antilles Island arc). Geologica Acta 4, 7-33.

Kamenov, G.D., Perfit, M.R., Lewis, J.F., Goss, A.R., Arévalo, R., Shuster, R.D., 2011. Ancient lithospheric source for Quaternary lavas in Hispaniola. Nature Geoscience 4, 554-557.

Kanchev, Il., Boyanov, Iv., Popov, N., Cabrera, R., Goranov, Al., Iolkicev, N., Kanazirski, M., Stancheva, M., 1978. Informe Geología de la Província de Las Villas. Academia de las Ciencias de Bulgaria (Instituto de Geología) y Academia de Ciencias de Cuba (Instituto de Geología y Paleontología) eds., Sofía-Habana, 1119 p.

Kelemen, P.B., Hanghøj, K., Greene, A.R., 2003. One view of the Geochemistry of Subduction-related Magmatic Arcs, with an Emphasis on Primitive Andesite and Lower Crust, in: Holland, H.D., Turekian, K.K., (Eds.), Treatise on Geochemistry. Elsevier, Oxford, pp. 593-659.

Kelley, K.A., Plank, T., Ludden, J., Staudigel, H., 2003. Composition of altered oceanic crust at ODP Sites 801 and 1149: Geochemistry Geophysics Geosystems 4, 1-21.

Kendrick, M.A., Honda, M., Vanko, D.A., 2015. Halogens and noble gases in Mathematician Ridge meta-gabbros, NE Pacific: implications for oceanic hydrothermal root zones and global volatile cycles. Contributions to Mineral Petrology 170-43, 1-20.

Kerr, A.C., Saunders, A.D., Babbs, T.L., Tarney, J., 1999. New plate tectonic model of the Caribbean: Implications from a geochemical reconnaissance of Cuban Mesozoic volcanic rocks. Geological Society of America Bulletin 111, 1-19.

Kesler, S.E., Hall, C.M., Russell, N., Piñero, E., Sánchez, C.R., Pérez, R.M., Moreira, J., 2004. Age of the Camagüey gold-silver district, Cuba: tectonic evolution and preservation of epithermal mineralization in volcanic arcs. Economic Geology 99, 869–886.

Kesler, S. E., Campbell, I. H., Allen, C. M., 2005. Age of the Los Ranchos Formation, Dominican Republic: timing and tectonic setting of primitive island arc volcanism in the Caribbean region. Geological Society of American Bulletin 117, 987-995.

Keto, L.S., Jacobsen S.B., 1988. Nd isotopic variations of Phanerozoic paleoceans. Earth and Planetary Science Letters 90,

395-410.

King, R.L., Bebout, G.E., Moriguti, T., Nakamura, E., 2006. Elemental mixing systematics and Sr–Nd isotope geochemistry of mélange formation: Obstacles to identification of fluid sources to arc volcanics. Earth and Planetary Science Letters 246, 288-304.

Knipper, A., Cabrera, R., 1974. Tectónica y geologia histórica de la zona de articulación entre el mio- y eugeosinclinal y del cinturon de hiperbasitas, in: Academia de Ciencias de Cuba, Instituto de Geología (Eds), Contribución a la Geología de Cuba., La Habana, pp. 15–77.

Kodolányi, J., Pettke, T., Spandler, C., Kamber, B.S., Gméling, K., 2012. Geochemistry of Ocean Floor and Fore-arc Serpentinites: Constraints on the Ultramafic Input to Subduction Zones. Journal of Petrology 53, 235-270.

Kogiso, T., Tatsumi, Y., Nakano, S., 1997. Trace element transport during dehydration processes in the subducted oceanic crust: 1. Experiments and implications for the origin of ocean island basalts. Earth and Planetary Science Letters 148, 193–205.

Konrad-Schmolke, M., O'Brien, P.J., and Zack T., 2011. Fluid migration above a subducted slab-constraints on amount, pathways and major element mobility from partially overprinted eclogite-facies rocks (Sesia Zone, Western Alps). Journal of Petrology 52, 457-486.

Korzhinskii, D.S., 1959. Physicochemical basis of the analysis of the paragenesis of minerals, ed. consultants Bureau, New York, 142 p.

Kovács, I., Green, D.H., Rosenthal, A., Hermann, J., O'Neill, H.St.C., Hibberson, W.O., Udvardi, B., 2012. An experimental study of water in nominally anhydrous minerals in the upper mantle near the water-saturated solidus. Journal of Petrology 53, 2067-2093.

Kysar-Mattietti, G., 2001. The role of Paleogene Magmatism in the evolution of the northern Caribbean margin. The Sierra Maestra (southern Cuba). Unpublished Ph.D. thesis. George Washington University 187p.

Lázaro, C., García-Casco, A., Rojas-Agramonte, Y., Kröner, A., Neubauer, F., Iturralde-Vinent, M., 2009. Fifty-five-million-year history of oceanic subduction and exhumation at the northern edge of the Caribbean plate (Sierra del Convento mélange, Cuba). Journal of Metamorphic Geology 27, 19–40.

Lázaro, C., Blanco-Quintero, I.F., Marchesi, C., Bosch, D., Rojas-Agramonte, Y., Garcia-Casco, A., 2011. The imprint of subduction fluids on subducted MORB-derived melts (Sierra del Convento Mélange, Cuba). Lithos 126, 341-354.

Lázaro, C., García-Casco, A., Blanco-Quintero, I.F., Rojas-Agramonte, Y., Corsini, M., Proenza, J.A., 2015. Did the Turonian–Coniacian plume pulse trigger subduction initiation in the Northern Caribbean? Constraints from 40Ar/39Ar dating of the Moa-Baracoa metamorphic sole (eastern Cuba). International Geology Review 57, 919–942.

Lázaro, C., Blanco-Quintero, I.F., Proenza, J.A., Rojas-Agramonte, Y., Neubauer, F., Núñez-Cambra, K., García-Casco, A., 2016. Petrogenesis and 40Ar/39Ar dating of proto-forearc crust in the Early Cretaceous Caribbean arc: The La Tinta mélange (eastern Cuba) and its easterly correlation in Hispaniola. International Geology Review 58, 1020–1040.

Laird, J., Albee, A.L., 1981. Pressure-temperature and time indicators in mafic schist: their application to reconstructing the polymetamorphic history of Vermont. American Journal of Science 281, 127-175.

Laird, J., Lanphere, M.A., Albee, A.L., 1984. Distribution of Ordovician and Devonian Metamorphism in Mafic and Pelitic Schists from Northern Vermont. American Journal of Science 284, 376-413.

Lafay, R., Deschamps, F., Schwartz, S., Guillot, S., Godard, M., Debret, B., Nicollet, C., 2013. High-pressure serpentinites, a trap-and-release system controlled by metamorphic conditions: Example from the Piedmont zone of the western Alps. Chemical Geology 343, 38-54.

Leeman, W.P., Tonarini, S., Chan, L. H., Borg, L.E., 2004. Boron and lithium isotopic variations in a hot subduction zone—the southern Washington Cascades. Chemical Geology 212, 101-124.

Lehnert, K., Su, Y., Langmuir, C., Sarbas, B., Nohl, U. A., 2000. Global geochemical database structure for rocks. Geochemistry Geophysics Geosystems 1-5.

Le Maître, R.W., Streckeisen, A., Zanettin, B., Le Bas, M.J., Bonin, B., Bateman, P., Bellieni, G., Dudek, A., Efremova, S., Keller, J., Lameyre, J., Sabine, P.A., Schmid, R., Sørensen, H., Woolley, A.R., 2002. Igneous Rocks A classification and glossary of terms, ed. Cambridge University Press, Cambridge.

References

Le Roux, V., Dick, H.J. B., Shimizu, N., 2014. Tracking flux melting and melt percolation in supra-subduction peridotites (Josephine ophiolite, USA). Contributions to Mineralogy and Petrology 168 (1064).

Lewis, J.F., Draper, G., Proenza, J.A., Espaillat, J., Jiménez, J., 2006. Ophiolite-related ultramafic rocks (serpentinites) in the Caribbean region: A review of their occurrence, composition, origin, emplacement and Ni-laterite soil formation. Geologica Acta 1-2, 237-263.

Lidiak, E.G., Jolly, W.T., Dickin, A.P., 2011. Pre-arc basement complex and overlying early island arc strata, Southwestern Puerto Rico: overview, geologic evolution, and revised data bases. Geologica Acta 9, 273-287.

Lidiak, E.G., Anderson, T.H., 2015. Evolution of the Caribbean plate and origin of the Gulf of Mexico in light of plate motions accommodated by strike-slip faulting. Geological Society of America Special Paper 513, 1-89.

Lindsley, D.H., 1983. Pyroxene thermometry. American Mineralogist 68, 477-493.

Llanes, A. L., García, D. E., Meyerhoff, D. H., 1998. Hallazgo de fauna Jurásica (Tithoniano) en ofiolitas de Cuba central: La Habana, in: Sociedad Cubana de Geología (Eds.), III Congreso Cubano de Geología y Minería 2, Memorias, La Habana, pp. 241–244.

Llanes, A.I., Proenza, J.A. Zaccarini, F., Garuti, G., Santa Cruz Pacheco, M., 2016. Al- and Cr-rich chromitites from the Eastern Havana-Matanzas ophiolites (Western Cuba). Episodes 38, 334-343.

MaalØe, S., 2004. The solidus of harzburgite to 3 GPa pressure: the composition of primary abyssal tholeiite. Mineralogy and Petrology 81, 1-17.

Malvoisin, B., 2015. Mass transfer in the oceanic lithosphere: Serpentinization is not isochemical. Earth and Planetary Science Letters 430, 75-85.

Marchesi, C., Garrido, C.J., Godard, M., Proenza, J.A., Gervilla, F., Blanco-Moreno, J., 2006. Petrogenesis of highly depleted peridotites and gabbroic rocks from the Mayarí-Baracoa Ophiolitic Belt (eastern Cuba). Contributions Mineral Petrology 151, 717-736.

Marchesi, C., Garrido, C.J., Bosch, D., Proenza, J.A., Gervilla, F., Monie, P., Rodriguez-Vega, A., 2007. Geochemistry of Cretaceous magmatism in eastern Cuba: Recycling of North American continental sediments and implications for subduction polarity in the Greater Antilles Paleo-arc. Journal of Petrology 48, 1813–1840.

Marchesi, C., Jolly, W.T., Lewis, J.F., Garrido, C.J., Proenza, J.A., Lidiak, E.G., 2011. Petrogenesis of fertile mantle peridotites from the Monte del Estado massif (Southwest Puerto Rico): a preserved section of Proto-Caribbean lithospheric mantle?. Geologica Acta 3-4, 289-306.

Marchesi, C., Garrido, C.J., Padrón-Navarta, J.A., López Sánchez-Vizcaíno, V., Gómez-Pugnaire, M.T., 2013. Element mobility from seafloor serpentinization to high-pressure dehydration of antigorite in subducted serpentinite: Insights from the Cerro del Almirez ultramafic massif (southern Spain). Lithos 178, 128-142.

Marchesi, C., Garrido, C.J., Proenza, J.A., Hidas, K., Varas-Reus, M.I., Butjosa, L., Lewis, J.F., 2016. Geochemical record of subduction initiation in the sub-arc mantle: Insights from the Loma Caribe peridotite (Dominican Republic). Lithos 252-253, 1-15.

Martin, C., Flores, K.E., Harlow, G.E., 2016. Boron isotopic discrimination for subduction-related serpentinites. Geology 1-4.

Mével, C., 2003. Serpentinitzation of abyssal peridotites at mid-ocean ridges. Comptes Rendus Geoscience 335, 825-852.

Meyerhoff, A.A., Hatten, C.W., 1968. Diapiric structure in Central Cuba. Memoir of the American Association of Petroleum Geologists 8, 315–357.

McDonough, W.F., Sun, S.S., 1995. The composition of the Earth. Chemical Geology 120, 223-253.

McCulloch, M.T., Gregory, R.T., Wasserburg, G.J., Taylor, H.P., 1981. Sm-Nd, Rb-Sr and 18O/16O Isotopic Systematics in an Oceanic Crustal Section: Evidence From the Samail Ophiolite. Journal of Geophysical Research 86, 2721-2735.

Millán, G., 1996a. Metamorfitas de la asociación ofiolítica de Cuba, in: Iturralde-Vinent, M.A. (Ed.), Cuban ophiolites and volcanic arcs, International Geological Correlation Program (IGCP) Project 364, Miami, pp 131-146.

Millán, G., 1996b. Geología del complejo de Mabujina in: Iturralde-Vinent, M.A. (Ed.), Cuban ophiolites and volcanic arcs, International Geological Correlation Program (IGCP) Project 364, Miami, pp 147–153.

Miranda, E.A. and Dilek, Y., 2010. Oceanic Core Complex Development in Modern and Ancient Oceanic Lithosphere:

Gabbro-Localized versus Peridotite-Localized Detachment Models. Journal of Geology 118, 95-109.

Miyashiro, A., 1975. Petrology and plate tectonics. Reviews of Geophysics 13, 94-98.

Molina, J.F., Poli, S., 2000. Carbonate stability and fluid composition in subducted oceanic crust: An experimental study on H2O-CO2-bearing basalts. Earth and Planetary Science Letters 176, 295-310.

Montero, P., Bea, F., 1998. Accurate determination of 87Rb/86Sr and 147Sm/144Nd ratios by inductively-coupled-plasma mass spectrometry in isotope geoscience: an alternative to isotope dilution analysis. Analytica Chimica Acta 358, 227–233.

Morimoto, N., Fabries, J., Ferguson, A.K., Ginzburg, I.V., Ross, M., Seifert, F.A., Zussman, J., Aoki, K., Gottardi, G., 1988. Nomenclature of pyroxenes. American Mineralogist 73, 1123-1133.

Niu, Y., 2004. Bulk-rock Major and Trace Element Compositions of Abyssal Peridotites: Implications for Mantle Melting, Melt Extraction and Post-melting Processes Beneath Mid-Ocean Ridges. Journal of Petrology 45, 2423-2458.

O'Hanley, D.S., 1996. Serpentinites: Records of Tectonic and Petrological History, ed. Oxford University Press, New York.

O'Hara, M. J., 1967 Mineral facies in ultrabasic rocks, in: Wyllie, P. J. (Ed.), Ultramafic and related rocks, New York, London, Sydney.

Padrón-Navarta, J.A., Tommasi, A., Garrido, C.J., Sánchez-Vizcaíno, V.L., Gómez-Pugnaire, M.T., Jabaloy, A., Vauchez, A., 2010. Fluid transfer into the wedge controlled by high-pressure hydrofracturing in the cold top-slab mantle. Earth and Planetary Science Letters 297, 271-286.

Padrón-Navarta, J.A., Sánchez-Vizcaíno, V.L., Garrido, C.J., Gómez-Pugnaire, M.T., 2011. Metamorphic record of high-pressure dehydration of antigorite serpentinite to chlorite harzburgite in a subduction setting (Cerro del Almirez, Nevado-Filábride complex, Southern Spain). Journal of Petrology 52, 2047-2078.

Padrón-Navarta, J.A., Tommasi, A., Garrido, C.J., López Sánchez-Vizcaíno, V., 2012. Plastic deformation and development of antigorite crystal preferred orientation in high-pressure serpentinites. Earth and Planetary Science Letters 349-350, 75-86.

Padrón-Navarta, J.A., Sánchez-Vizcaíno, V.L., Hermann, J., Connolly, J.A.D., Garrido, C.J., Gómez-Pugnaire, M.T., Marchesi, C., 2013. Tschermak's substitution in antigorite and consequences for phase relations and water liberation in high-grade serpentinites. Lithos 178, 186-196.

Palandri, J. L., Reed, M. H., 2004. Geochemical models of metasomatism in ultramafic systems: Serpentinization, rodingitization, and sea floor carbonate chimney precipitation. Geochimica et Cosmochimica Acta 68, 1115-1133.

Palmer, M.R., Edmond, J.M., 1989. The strontium isotope budget of the modern ocean. Earth and Planetary Science Letters 92, 11–26.

Parkinson, I.J., Pearce, J.A., Thirlwall, M.F., Johnson, K.T.M., Ingram, G., 1992. Trace element geochemistry of peridotites from the Izu-Bonin-Mariana Forearc, Leg 125. Proceedings of the Ocean Drilling Program, Scientific Results 125 487-506.

Parkinson, I.J., Pearce, J.A., 1998. Peridotites from the Izu–Bonin–Mariana Forearc (ODP Leg 125): Evidence for Mantle Melting and Melt–Mantle Interaction in a Supra-Subduction Zone Setting. Journal of Petrology 39, 1577-1618.

Paul, M., Bridgestock, L., Rehkämper, M., Van DeFlierdt, T., Weiss, D., 2015. High-precision measurements of seawater Pb isotope compositions by double spike thermal ionization mass spectrometry. Analytica Chimica Acta 863, 59-69.

Paulick, H., Bach, W., Godard, M., De Hoog, J.C.M., Suhr, G., Harvey, J., 2006. Geochemistry of abyssal peridotites (Mid-Atlantic Ridge, 15°20'N, ODP Leg 209): Implications for fluid/rock interaction in slow spreading environments. Chemical Geology 234, 179-210.

Pearce, J.A., 1982. Trace element characteristics of lavas from destructive plate boundaries. Andesites: Orogenic Andesites and Related Rocks, 525-548.

Pearce, J.A., 1992. Boninite and harzburgite from Leg 125 (Bonin-Mariana Forearc): a case study of magma genesis during the initial stages of subduction. Proceedings and Scientific Results, ODP Leg 125, 623-662.

Pearce, J.A., 2008. Geochemical fingerprinting of oceanic basalts with applications to ophiolite classification and the search for Archean oceanic crust. Lithos 100, 14-48.

Pearce, J.A., 2014. Immobile elements fingerprinting of ophiolites. Elements 10, 101–108.

References

Pearce, J.A., Cann, J.R., 1971. Ophiolite origin investigated by discriminant analysis using Ti, Zr and Y. Earth and Planetary Science Letters 12, 339-349.

Pearce., J.A., Barker, P.F., Edwards, S. J., Parkinson, I. J., Leat, P. T., 2000. Geochemistry and tectonic significance of peridotites from the South Sandwich arc-basin system, South Atlantic. Contributions Mineral Petrology 139, 36-53.

Peacock, S.M., 2001. Are the lower planes of double seismic zones caused by serpentine dehydration in subducting oceanic mantle? Geology 29, 299-302.

Peacock, S.M., Wang, K., 1999. Seismic Consequences of Warm Versus Cool Subduction Metamorphism: Examples from Southwest and Northeast Japan. Science 286, 937-939.

Penniston-Dorland, S.C., Sorensen, S.S., Ash, R.D., Khadke, S.V., 2010. Lithium isotopes as a tracer of fluids in a subduction zone mélange: Franciscan Complex, CA. Earth and Planetary Science Letters 292, 181–190.

Penniston-Dorland, S.C., Bebout, G.E., Pogge von Strandmann, P.A.E., Elliot, T., Sorensen, S.S., 2012. Lithium and its isotopes as tracers of subduction zone fluids and metasomatic processes: Evidence from the Catalina Schist, California, USA. Geochimica et Cosmochimica Acta 77, 530-545.

Penniston-Dorland, S.C., Gorman, J.K., Bebout, G.E., Piccoli, P.M., Walker, R.J., 2014. Reaction rind formation in the Catalina Schist: Deciphering a history of mechanical mixing and metasomatic alteration. Chemical Geology 384, 47–61.

Piepgras, D.J., Wasserburg, G.J., 1987. Rare-earth element transport in the western North-Atlantic inferred from Nd isotopic observations. Geochimica et Cosmochimica Acta 51, 1257–1271.

Pindell, J. L, Kennan, L., Maresch, W.V., Stanek, K.P., Draper, G., Higgs, R., 2005. Plate-kinematics and crustal dynamics of circum-Caribbean arc-continent interactions: Tectonic controls on basin development in Proto-Caribbean margins. Geological Society of America Special Paper 394, 7–52.

Pindell, J., Kennan L., 2009, Tectonic evolution of the Gulf of Mexico, Caribbean and northern South America in the mantle reference frame: an update, in: James, K., Lorente, M. A., Pindell, J., (Eds.), The Origin and Evolution of the Caribbean Plate: London, Geological Society Special Publications 328, London.

Pindell, J., Maresch, W. V., Martens, U., Stanek, K., 2012. The Greater Antillean Arc: Early Cretaceous origin and proposed relationship to Central American subduction mélanges: Implications for models of Caribbean evolution. International Geology Review 54, 131-143.

Plank, T., Langmuir, C. H., 1998. The chemical composition of subducting sediment and its consequences for the crust and mantle. Chemical Geology 145, 325-394.

Plank, T., 2014. 4.17- The Chemical Composition of Subducting Sediments, in: Holland, H.D., Turekian, K.K., (Eds.), Treatise on Geochemistry (second Edition). Elsevier, Oxford, pp. 607-629.

Plümper, O., John, T., Podladchikov, Y.Y., Vrijmoed, J.C., Scambelluri, M., 2017. Fluid escape from subduction zones controlled by channel-forming reactive porosity. Nature Geoscience 10, 150-156.

Poli, S., Schmidt, M,W., 2002. Petrology of subducted slabs. Annual Reviews of Earth and Planetary Science 30, 207-235.

Proenza, J.A., Gervilla, F., Melgarejo, J.C., 1999. La Moho Transition Zone en el Macizo Ofiolítico Moa-Baracoa: un ejemplo de interacción magma/peridotita. Revista de la Sociedad Geológica de España 12, 309–327.

Proenza, J.A., Ortega-Gutiérrez, F., Camprubí, A., Tritlla, J., Elías-Herrera, M., Reyes-Salas, M., 2004. Paleozoic serpentinite-enclosed chromitites from Tehuitzingo (Acatlán Complex, southern Mexico): a petrological and mineralogical study. Journal of South American Earth Sciences 16, 649-666.

Proenza, J.A., Díaz-Martínez, R., Iriondo, A., Marchesi, C., Melgarejo, J.C., Gervilla, F., Garrido, C.J., Rodríguez-Vega, A., Lozano-Santacruz, R., Blanco-Moreno, J.A., 2006. Primitive Cretaceous island-arc volcanic rocks in eastern Cuba: the Téneme Formation. Geologica Acta 4, 103-121.

Pszczólkowski, A., 1987. Contribución a la geología de la província de Pinar del Río, ed. Científico-Técnica, La Habana, 253 p.

Puscharovski, Yu., Mossakovsky, A., Nekrasov, G., Sokolov, S., Iturralde-Vinent, M.A., 1989.Geology of Cuba. Explanatory note to the 1:250 000 geological map of cuba: Geological institute of USSR Academy of Sciences, Ed. Nauka, Moscow, pp. 55.

Rampone, E., Hofmann, A.W., 2012. A global overview of isotopic heterogeneities in the oceanic mantle. Lithos 148,

247-261.

Ranero, C., Morgan, J.P., McIntosh, K., Reichert, C., 2003. Bending-related faulting and mantle serpentinization at the Middle America trench. Nature 425, 367–373.

Raymond, L.A., 1984. Classification of melanges. In: Raymond, L.A. (Ed.), Melanges: Their nature, origin and significance. Boulder, ColoradoGeological Society of America Special Papers 198, 7–20.

Reagan, M.K., Ishizuka, O., Stern, R.J., Kelley, K.A., Ohara, Y., Blichert-Toft, J., Bloomer, S.H., Cash, J., Fryer, P., Hanan, B.B., Hickey-Vargas, R., Ishii, T., Kimura, J-I., Peate, D.W., Rowe, M.C., Woods, M., 2010. Fore-arc basalts and subduction initiation in the Izu-Bonin-Mariana system. Geochemistry Geophysics Geosystems 11(3), 1-17.

Reagan,M.K., Pearce, J.A., Petronotis, K., Almeev, R.R., Avery, A.J., Carvallo, C., Chapman, T., Christeson, G.L., Ferré, E.C., Godard, M., Heaton, D.E., Kirchenbaur,M., Kurz, W., Kutterolf, S., Li, H., Li,Y., Michibayashi,K., Morgan, S., Nelson, W.R., Prytulak, J., Python, M., Robertson, A.H.F., Ryan, J.G., Sager, W.W., Sakuyama, T., Shervais, J.W., Shimizu, K., Whattam, S.A., 2017. Subduction initiation and ophiolite crust: new insights from IODP drilling. International Geology Review 59, 1439-1450.

Rehkämper, M., Hofmann, A.W., 1997. Recycled ocean crust and sediment in Indian Ocean MORB. Earth and Planetary Science Letters 147, 93-106.

Ribeiro, J.M., Stern, R.J., Kelley, K.A., Martinez, F., Ishizuka, O., Manton, W.I., Ohara, Y., 2013. Nature and distribution of slab-derived fluids and mantle sources beneath the Southeast Mariana forearc rift. Geochemistry Geophysics Geosystems 14, 1-24.

Ribeiro, J.M., Stern, R.J., Kelley, K.A., Shaw, A.M., Martinez, F., Ohara, Y., 2015. Composition of the slab-derived fluids released beneath the Mariana forearc: Evidence for shallow dehydration of the subducting plate. Earth and Planetary Science Letters 418, 136-148.

Rickwood, P.C., 1989. Boundary lines within petrologic diagrams which use oxides and minor elements. Lithos 22, 247-263.

Rinaudo, C., Gastaldi, D., Belluso, E., 2003. Characterization of chrysotile, antigorite and lizardite by FT-Raman spectroscopy. Canadian Mineralogist 41, 883-890.

Roehrig, E.E., Laó-Dávila, D.A., Wolfe, A.L., 2015. Serpentinitzation history of the Río Guanajibo serpentinite body, Puerto Rico. Journal of South American Earth Sciences 62, 195-217.

Rojas-Agramonte, Y., Neubauer, F., Bojar, A.V., Hejl, E., Handler, R., García-Delgado, D., 2006. Geology, age and tectonic evolution of the Sierra Maestra Mountains, southeastern Cuba. Geologica Acta 4, 123-150.

Rojas-Agramonte, Y., Kröner, A., Pindell, J., Garcia-Casco, A., García-Delgado, D., Liu, D., Wang, Y., 2008. Detrital zircon geochronology of Jurassic sandstones of western Cuba (San Cayetano Formation): Implications for the Jurassic paleogeography of the NW Proto-Caribbean. American Journal of Science 308, 639-656.

Rojas-Agramonte, Y., Kröner, A., Garcia-Casco, A., Kemp, T., Hegner, E., Pérez, M., Barth, M., Liu, D., Fonseca-Montero, A., 2010. Zircon ages, Sr-Nd-Hf Isotopic Compositions, and Geochemistry of Granitoids associated with the Northern Ophiolite Mélange of Central Cuba: Tectonic Implication for Late Cretaceous Magmatism in the Northwestern Caribbean. American Journal of Science 310, 1453-1479.

Rojas-Agramonte, Y., Kröner, A., Garcia-Casco, A., Somin, M., Iturralde-Vinent, M., Mattison, J.M., Millán Trujillo, G., Sukar, K., Pérez Rodríguez, M., Carrasquilla, S., Wingate, M. T. D., Liu, D.Y., 2011. Timing and Evolution of Cretaceous Island Arc Magmatism in Central Cuba: Implications for the History of Arc Systems in the Northwestern Caribbean. Journal of Geology 119, 619-640.

Rojas-Agramonte, Y., Garcia-Casco, A., Kröner, A., Herwartz, D., Despaigne, A.I., Wilde, S., 2012. New geochronological ages (U-Pb/Lu-Hf) from high-pressure rocks of the Escambray terrane and Santa Clara serpentinite mélange, central Cuba. Regional correlations and geodynamic implications. In: abstract volume EGU General Assembly, Geophysical research abstracts 14.

Rojas-Agramonte, Y., Garcia-Casco, A., Kröner, A., and Kemp, T., 2013. On the origin of Precambrian to Triassic zircon grains from the Cuban juvenile intra-oceanic arc formations and ophiolitic complexes. In: abstract volume of International Meeting on Precambrian Evolution and Deep Exploration of the Continental Lithosphere, IAGR conference series 15, pp. 85-86.

Rojas-Agramonte, Y., Garcia-Casco, A., Kemp, A., Kröner, A., Proenza, J.A., Lázaro, C., Liu, D., 2016. Recycling and transport of continental material through the mantle wedge above subduction zones: A Caribbean example. Earth

and Planetary Science Letters 436, 93-107.

Rudnick, R.L., Gao, S., 2003. 3.01- Composition of the Continental Crust, in: Holland, H.D., Turekian, K.K., (Eds.), Treatise on Geochemistry. Elsevier, Oxford.

Ruiz, J., Tosdal, R. M., Restrepo, P.A., Murillo-Muñetón, G., 1999. Pb isotope evidence for Colombia-southern México connections in the Proterozoic. Geological Society of America Special Paper 336, 183-197.

Rutten, M.G., Rutten, L.M.R., Gillavoy, H.J.M., Thiadens, A.A. and Vermunt, L.W.J., 1938. Geología de la parte norte de la Província de Santa Clara: Secretaria de Agricultura, Dirección de Montes Minas y Aguas, República de Cuba 42, 1-86.

Rüpke, L.H., Morgan, J.P., Hort, M., Connolly, J.A.D., 2002. Are the regional variations in Central American arc lavas due to differing basaltic versus peridotitic slab sources of fluids? Geology 30, 1035–1038.

Rüpke, L.H., Morgan , J.P., Hort , M., Connolly , J.A.D., 2004. Serpentine and the subduction zone water cycle . Earth and Planetary Science Letters 223, 17 – 34.

Saccani, E., 2015. A new method of discriminating different types of post-Archean ophiolitic basalts and their tectonic significance using Th-Nb and Ce-Dy-Yb systematics. Geoscience Frontiers 6, 481-501.

Saha, A., Basu, A.R., Wakabayashi, J., Wortman, G. L., 2005. Geochemical evidence for a subducted infant arc in Franciscan high-grade-metamorphic tectonic blocks. Geological Society of American Bulletin 117, 1318-1335.

Saka, S., Uysal, I., Melih Akmaz, R., Kaliwoda, M., Hochleitner, R., 2014. The effects of partial melting, melt–mantle interaction and fractionation on ophiolite generation: Constraints from the late Cretaceous Pozantı-Karsantı ophiolite, southern Turkey. Lithos 202-203, 300-316.

Saleeby, J., 2011. Geochemical mapping of the Kings-Kaweah ophiolite belt, California-Evidence for progressive mélange formation in a large offset transform-subduction initiation environment. Geological Society of America 480, 31-73.

Salters, V.J.M., Stracke, A., 2004. Composition of the depleted mantle. Geochemistry, Geophysics, Geosystems 5.

Saumur, B-M., Hattori, K.H., Guillot, S., 2010. Contrasting origins of serpentinites in a subduction complex, northern Dominican Republic. Geological Society of American Bulletin 122, 292-304.

Savov, I.P., Ryan, J.G., D'Antonio, M., Kelley, K., Mattie, P., 2005. Geochemistry of serpentinized peridotites from the Mariana Forearc Conical Seamount, ODP Leg 125: Implications for the elemental recycling at subduction zones. Geochemistry Geophysics Geosystems 6, 1-24.

Scambelluri, M., Rampone, E., Piccardo, G. B., 2001a. Fluid and Element cycling in subducted serpentinite: a Trace-Element study of the Erro-Tobbio High-Pressure Ultramafites (Western Alps, NW Italy). Journal of Petrology 42, 55-67.

Scambelluri, M., Bottazzi, P., Trommsdorff, V., Vannucci, R., Hermann, J., Gómez-Pugnaire, M.T., López-Sánchez Vizcaíno, V., 2001b. Incompatible element-rich fuids released by antigorite breakdown in deeply subducted mantle. Earth and Planetary Science Letters 192, 457-470.

Scambelluri, M., Fiebig, J., Malaspina, N., Müntener, O., Pettke, T., 2004a. Serpentinite Subduction: Implications for Fluid Processes and Trace-Element Recycling. International Geology Review 46, 595-613.

Scambelluri, M., Müntener, O., Ottolini, L., Pettke, T., Vannucci, R., 2004b. The fate of B, Cl and Li in the subducted oceanic mantle and in the antigorite breakdown fluids. Earth and Planetary Science Letters 222, 217-234.

Scambelluri, M., Tonarini, S., 2012. Boron isotope evidence for shallow fluid transfer across subduction zones by serpentinized mantle. Geology 10, 907-910.

Schmidt, M.W., Poli, S., 1998. Experimentally based water budgets for dehydrating slabs and consequences for arc magma generation. Earth and Planetary Science Letters 163, 361–79.

Schmidt, M.W. and Poli, S., 2003. 3.17- Generation of Mobile Components during Subduction of Oceanic Crust, in Heinrich, D., Holland, H.D., and Turekian, K.K., eds., Treatise on Geochemistry: Oxford, Elsevier, p. 567-591.

Schmidt, M.W., Poli, S., 2014. Devolatilization During Subduction, in Holland, H.D., and Turekian, K.K., eds., Treatise on Geochemistry (Second Edition): Oxford, Elsevier 4, p. 669-701.

Schmidt, M.W., Jagoutz, O., 2017. The global systematics of primitive arc melts. Geochemistry Geophysics Geosystems

18, 2817–2854.

Schneider, J., 2000. Origines et chemins P, T, t d'éclogites de Cuba (Cara) exhumes en contexte de subduction, Montpellier [DEA report]: Montpellier, University of Montpellier II, 43 pp.

Shreve, R.L., Cloos, M., 1986. Dynamics of sediment subduction, melange formation, and prism accretion. Journal of Geophysical Research, Solid Earth 91, 10229-10245.

Secchiari, A., Montanini, A., Bosch, D., Macera, P., Cluzel, D., 2016. Melt extraction and enrichment processes in the New Caledonia lherzolites: Evidence from geochemical and Sr-Nd isotope data. Lithos 260, 28-43.

Seyler, M., Toplis, M.J., Lorand, J.P., Luguet, A., Cannat, M., 2001. Clinopyroxene microtextures reveal incompletely extracted melts in abyssal peridotites. Geology 29, 155-158.

Shaw, D.M., 2000. Continuous (Dynamic) melting theory revisited. The Canadian Mineralogist 38, 1041-1063.

Shervais, J.W., 1982. Ti-V plots and the petrogenesis of modern and ophiolitic lavas. Earth and Planetary Science Letters 59(1), 101-118.

Shervais, J.W., Choi, S.H., Sharp, W.D., Ross, J., Zoglman-Schuman, M., Mukasa, S.B., 2011. Serpentinite matrix mélange: Implications of mixed provenance for mélange formation. Geological Society of America Special Paper 480, 1-30.

Snow, J.E., Hart, S.R., Dick, H.J.B., 1994. Nd and Sr isotope evidence linking mid-ocean-ridge basalts and abyssal peridotites. Nature 371, 57-60.

Sobolev , A.V., Chaussidon, M., 1996 . H2O concentrations in primary melts from supra – subduction zones and mid - ocean ridges: implications for H2O storage and recycling in the mantle. Earth and Planetary Science Letters 137, 45-55.

Sobolev, A.V., Hofmann, A.W., Kuzmin, D.V., Yaxley, G.M., Arndt, N.T., Chung, S.-L., Danyushevsky, L.V., Elliott, T., Frey, F.A., Garcia, M.O., 2007. The amount of recycled crust in sources of mantle-derived melts. Science 316, 412–417.

Somin, M., Millán, G., 1981. Geology of the metamorphic complexes of Cuba. Moscow, pp. 218.

Somin, M.L., Arakelyants, M.M., Kolesnikov, E.M., 1992. Age and tectonic significance of high-pressure metamorphic rocks of Cuba. International Geology Review 34, 105-118.

Sorensen, S.S., 1988. Petrology of amphibolite-facies mafic and ultramafic rocks from the Catalina Schist, southern California: metasomatism and migmatization in a subduction zone metamorphic setting. Journal Metamorphic Geology 6, 405-435.

Sorensen, S.S., Grossman, J.N., 1989. Enrichment of trace elements in garnet amphibolites from a paleo-subduction zone: Catalina Schist, southern California. Geochimica et Cosmochimica Acta 55, 3155-3177.

Sorensen, S.S., Grossman, J.N., Perfit, M.R., 1997. Phengite-hosted LILE Enrichment in Eclogite and Related Rocks: Implications for Fluid-Mediated Mass Transfer in Subduction Zones and Arc Magma Genesis: Journal of Petrology 38, 3-34.

Sorensen, S.S., Sisson, V.B., Harlow, G.E., Avé Lallemant, H.G., 2010. Element residence and transport during subduction-zone metasomatism: evidence from a jadeitite-serpentinite contact, Guatemala. International Geology Review 52, 899-940.

Spandler, C., Pettke, T., Rubatto, D., 2011. Internal and External Fluid Sources for Eclogite-Facies Veins in the Monviso Meta-ophiolite, Western Alps: Implications for Fluid Flow in Subduction Zones. Journal of Petrology 52, 1207-1236.

Spandler, C., Pirard, C., 2013. Element recycling from subducting slabs to arc crust: A review. Lithos 170-171, 208-223.

Spear, F.S., 1993. Metamorphic Phase Equilibria and Pressure-Temperature-Time paths, first ed. Mineralogical Society of America Monograph, Washington.

Spivack, A.J. and Edmond, J.M., 1987. Boron isotope exchange between seawater and the oceanic crust. Geochimica et Cosmochimica Acta 51, 1033-1043.

Staudigel, H., Davies, G. R., Hart, S. R., Marchant, K. M., Smith, B.M., 1995. Large scale isotopic Sr, Nd and O isotopic anatomy of altered oceanic crust: DSDP/ODP sites 417/418: Earth and Planetary Science Letters 130, 169-185.

Stern, R.J., Reagan, M., Ishizuka, O., Ohara, Y., Whattam, S., 2012. To understand subduction initiation, study forearc

crust: to understand forearc crust, study ophiolites. Lithosphere 4, 469-483.

Stracke, A., Bizimis, M., Salters, V.J.M., 2003a. Recycling oceanic crust: Quantitative constraints. Geochemistry Geophysics Geosystems 4(3), 1-33.

Stracke, A., Zindler, A., Salters, V.J.M., McKenzie, D., Blichert-Toft, J., Albarède, F., Grönvold, K., 2003b. Theistareykir revisited. Geochemistry Geophysics Geosystems 4(2), 1-49.

Sun, S.S., McDonough, W.F., 1989. Chemical and isotopic systematics of oceanic basalts: implications for mantle composition and processes. Geological Society Special publications 42, 313-345.

Syracuse, E.M., Van Keken, P.E., Abers, G.A., 2010. The Global range of subduction zone thermal models. Physics of the Earth and Planetary Interiors 183, 73-90.

Tachikawa, K., Jeandel, C., Roy-Barman, M., 1999. A newapproach to the Nd residence time in the ocean: the role of atmospheric inputs. Earth and Planetary Science Letters 170, 433-446.

Taetz, S., John, T., Bröcker, M., Spandler, C., 2016. Fluid-rock interaction and evolution of a high-pressure/low-temperature vein system in eclogite from New Caledonia: insights into intraslab fluid flow processes. Contributions to Mineralogy and Petrology 171-90, 1-27.

Todt, W., Cliff, R.A., Hanser, A., Hofmann A.W., 1993. Recalibration of NBS lead standards using a 202Pb/205Pb double spike. Terra Abstracts 5(1), 396.

Tonarini, S., Pennisi, M., Leeman, W.P., 1997. Precise boron isotopic analysis of complex silicate (rock) samples using alkali carbonate fusion and ion-exchange separation. Chemical Geology 142, 129-137.

Tonarini, S., Agostini, S., Doglioni, C., Innocenti, F., Manetti, P., 2007. Evidence for serpentinite fluid in convergent margin systems: The example of El Salvador (Central America) arc lavas. Geochemistry Geophysics Geosystems 8, 1-18.

Torres-Roldán, R.L., Garcia-Casco, A., DWImager: una implementación para el procesamiento de Matrices de intensidades de Rayos X (unpublished).

Torres-Roldán, R.L., Garcia-Casco, A., García-Sánchez, P.A., 2000. CSpace: An integrated workplace for the graphical and algebraic analysis of phase assemblages on 32-bit Wintel platforms. Computer and Geoscience 26, 779-793.

Trommsdorff, V., Evans, B.W., 1997. Antigorite-Ophicarbonates: Phase Relations in a Proportion of the System CaO-MgO-SiO2-H2O-CO2. Contributions to Mineralogy and Petrology 60, 39-56.

Torró, L., Proenza, J.A., Marchesi, C., Garcia-Casco, A., Lewis, J.F., 2017. Petrogenesis of meta-volcanic rocks from the Maimón Formation (Dominican Republic): Geochemical record of the nascent Greater Antilles paleo-arc. Lithos 278-281, 255-273.

Tucholke, B.E., Lin, J., and Kleinrock, M.C., 1998. Megamullions and mullion structure defining oceanic metamorphic core complexes on the mid-Atlantic ridge. Journal of Geophysical Research 103, 9857–9866.

Ukar, E., Cloos, M., 2013. Actinolitic rinds on low-T mafic blueschist blocks in the Franciscan shale-matrix mélange near San Simeon: Implications for metasomatism and tectonic history. Earth and Planetary Science Letters 377-378, 155-168.

Ulmer, P., Trommsdorff, V., 1995. Serpentine Stability to Mantle Depths and Subduction-Related Magmatism. Science 268, 858-861.

Uysal, I., Ersoy, E. Y., Dilek, Y., Kapsiotis, A., Sarifakioğlu, E., 2016. Multiple episodes of partial melting, depletion, metasomatism and enrichment processes recorded in the heterogeneous upper mantle sequence of the Neotethyan Eldivan ophiolite, Turkey. Lithos 246-247, 228-245.

Vanko, D.A., 1986. High-chlorine amphiboles from oceanic rocks: product of highly-saline hydrothermal fluids? American Mineralogist 71, 51-59.

Van Keken, P.E., Hacker, B.R., Syracuse, E.M., Abers, G.A., 2011. Subduction factory: 4. Depth-dependent flux of H2O from subducting slabs worldwide. Journal of geophysical research 116, 1-15.

Van Hinsbergen, D. J. J., Iturralde-Vinent, M. A., Van Geffen, P. W. G., Garcia-Casco, A., Van Benthem, S., 2009. Structure of the accretionary prims and the evolution of the Paleogene northern Caribbean subduction zone in the region of Camaguey, Cuba. Journal of Structural Geology 31, 1130–1144.

Veizer, J., Ala, D., Azmy, K., Bruckschen, P., Buhl, D., Bruhn, F., Carden, G.A.F., Diener, A., Ebneth, S., Godderis, Y., Jasper,

T., Korte, K., Pawellek, F., Podlaha, O.G., Strauss, H., 1999. 87Sr/86Sr, δ13C and δ 18O evolution of Phanerozoic seawater. Chemical Geology 161, 59-88.

Vils, F., Pelletier, L., Kalt, A., Müntener, O., Ludwig, T., 2008. The Lithium, Boron and Beryllium content of serpentinized peridotites from ODP Leg 209 (Sites 1272A and 1274A): Implications for lithium and boron budgets of oceanic lithosphere. Geochimica et Cosmochimica Acta 72, 5475-5504.

Vils, F., Tonarini, S., Kalt, A., Seitz, H.M., 2009. Boron, lithium and strontium isotopes as tracers of seawater–serpentinite interaction at Mid-Atlantic ridge, ODP Leg 209. Earth and Planet Science Letters 286, 414-425.

Vils, F., Müntener, O., Kalt, A., Ludwig, T., 2011. Implications of the serpentine phase transition on the behaviour of beryllium and lithium–boron of subducted ultramafic rocks. Geochimica et Cosmochimica Acta 75, 1249–1271.

Vitale Brovarone, A., Alard, O., Beyssac, O., Martin, L., Picatto, M., 2014. Lawsonite metasomatism and trace element recycling in subduction zones. Journal of Metamorphic Geology 32, 489–514.

Wakabayashi, J., 2011. Mélanges of the Franciscan Complex, California: Diverse structural settings, evidence for sedimentary mixing, and their connection to subduction processes. Geological Society of America Special Papers 480,117-141.

Wallmann, K., 2001. The geological water cycle and the evolution of marine d18O values. Geochimica et Cosmochimica Acta 65, 2469-2485.

Warren, J.M., 2016. Global variations in abyssal peridotite compositions. Lithos 248-251, 193-219.

Weber, B., Scherer, E.E., Schulze, C., Valencia, V.A., Montecinos, P., Mezger, K., Ruiz, J., 2010. U–Pb and Lu–Hf isotope systematics of lower crust from central–southern Mexico-geodynamic significance of Oaxaquia in a Rodinia realm. Precambrian Research 182, 149-162.

White, R.W., Powell, R., Holland, T.J.B., 2007. Progress relating to calculation of partial melting equilibria for metapelites. Journal of Metamorphic Geology 25, 511-527.

White, R.W., Powell, R., Holland, T.J.B., Johnson, T.E., Green, E.C.R., 2014a. New mineral activity–composition relations for thermodynamic calculations in metapelitic systems. Journal of Metamorphic Geology 32, 261-286.

White, R.W., Powell, R., Johnson, T.E., 2014b. The effect of Mn on mineral stability in metapelites revisited: new a–x relations for manganese-bearing minerals. Journal of Metamorphic Geology 32, 809–828.

Whitney, D.L., Evans, B.W., 2010. Abbreviations for names of rock-forming minerals. American Mineralogist 95, 185-187.

Willbold, M., Stracke, A., 2006. Trace element composition of mantle endmembers: Implications for recycling of oceanic and upper and lower continental crust. Geochemistry, Geophysics, Geosystems 7, 1-30.

Winchester, J.A., Floyd, P.A., 1977. Geochemical Discrimination of Different Magma series and their differentiation products using immobile elements. Chemical Geology 20, 325-343.

Wood, D.S., 1974. Ophiolites, mélanges, blue schists, and ignimbrites: early Caledonian subduction in Wales? In: Dott, R.H., Shaver, R.H. (Eds.). Modern and Ancient Geosynclinal Sedimentation SEPM Special Publications 19, 334–343.

Wunder, B., Schreyer, W., 1997. Antigorite: High-pressure stability in the system MgO-SiO2-H2O (MSH). Lithos 41, 213-227.

You, C.-F., Castillo, P.R., Gieskes, J.M., Chan, L.H., Spivack, A.J., 1996. Trace element behaviour in hydrothermal experiments: implications for fluid processes at shallow depths in subduction zones. Earth and Planetary Science Letters 140, 41–52.

Zack, T., John, T., 2007. An evaluation of reactive fluid flow and trace element mobility in subducting slabs. Chemical Geology 239, 199-216.

Zelepuguin, V., Fonseca, E., Díaz de Villavilla, L., 1982. Asociaciones vulcanógenas de la provincia de Pinar del Río. Serie Geológica, Instituto de Geología y Paleontología, Academia de Ciencias de Cuba 6, 45-74.

UNIVERSITAT DE BARCELONA

Departament de Mineralogia Petrologia i geologia aplicada

Facultat de Ciències de la Terra

B:KC Barcelona Knowledge Campus

Campus d'Excel·lència Internacional

Programa de doctorat de Ciències de la Terra